Structure, activity, and stability of platinum alloys as catalysts for the oxygen reduction reaction

Vej-Hansen, Ulrik Grønbjerg

Publication date:
2015

Document Version
Publisher's PDF, also known as Version of record

Structure, activity, and stability of platinum alloys as catalysts for the oxygen reduction reaction

PhD thesis

Ulrik Grønbjerg Vej-Hansen

Structure, activity, and stability of platinum alloys as catalysts for the oxygen reduction reaction

PhD thesis

Ulrik Grønbjerg Vej-Hansen

November 2015

Supervisor:
Professor Jakob Schiøtz, DTU Physics

Co-supervisors:
Associate Professor Ifan E. L. Stephens, DTU Physics
Professor Jan Rossmeisl, KU Chemistry

DTU Physics
Center for Individual Nanoparticle Functionality
Center for Atomic-scale Materials Design

Preface

This thesis is submitted in candidacy for the PhD degree in physics from the Technical University of Denmark. The work was carried out between July 2012 and November 2015 in the section for Theoretical Atomic-scale Physics (CAMD) and in close collaboration with the the DNRF Center for Individual Nanoparticle Functionality (CINF), both at the Department of Physics. The project was supevised by professor Jakob Schiøtz, as well as associate professor Ifan E. L. Stephens and professor Jan Rossmeisl, and funded by DTU.

I am especially grateful to Jakob for being an always enthusiastic and helpful supervisor, helping me steer this project to the destination. I would also like to thank Ifan and Jan for bringing distinct and invaluable input to the project, heightening the quality of the final result.

I would like to thank my many collaborators, including of course my supervisors, for their efforts on our common projects. Science is definitely a team effort. Theoretical collaborators; Martin H. Hansen, Vladimir Tripkovic, Simon H. Brodersen, and Mikkel Jørgensen. Experimental collaborators: Maria Escudero-Escribano, Brian P. Knudsen, Arnau Verdaguer-Casadevall, Paolo Malacrida, Amado Velázquez-Palenzuela, Elisabeth T. Ulrikkeholm, Anders F. Pedersen, Jakob N. Riedel and professor Ib Chorkendorff. It has been very rewarding to experience the synergy between theory and experiment.

Furthermore, I would also like to thank the rest of my colleagues at CAMD and CINF for creating a nice working environment, and especially my office mates through the years, Simon H. Brodersen, Mohammedreza Karamad, Rizwan Ahmed and Jacob Madsen. I also appreciate the efforts of the many students I have supervised over the years, as I also learned quite a few things from these projects.

I would also like to thank the technical and administrative staff for always being quick to help and allowing me to get back to doing research: Marianne Ærsøe, Tine H. Klitmøller, Jytte F. Mikkelsen, Ole H. Nielsen, Jens Jørgen Mortensen and Marcin Dulak. In the same vein, I am grateful to professor Andrew Peterson and his group for hosting me at Brown, and taking good care of me while I was there.

A special thanks is due to the people who helped me in the grueling task of proofreading this thesis; Brian P. Knudsen, Rasmus Frydendal, Jacob Madsen and Simon H. Brodersen.

And last, but definitely not least, my wife Cecilie and the rest of our family, for keeping things together while I was busy condensing 3 years of work into this document.

Ulrik Grønbjerg Vej-hansen
Kgs. Lyngby, November 2015

Abstract

In this thesis I present our work on theoretical modelling of platinum alloys as catalysts for the Oxygen Reduction Reaction (ORR). The losses associated with the kinetics of the ORR is the main bottleneck in low-temperature fuel cells for transport applications, and more active catalysts are essential for wide-spread use of this technology. platinum alloys have shown great promise as more active catalysts, which are still stable under reaction conditions.

We have investigated these systems on multiple scales, using either Density Functional Theory (DFT) or Effective Medium Theory (EMT), depending on the length and time scales involved.

Using DFT, we show how diffusion barriers in transition metal alloys in the $L1_2$ structure depend on the alloying energy, supporting the assumption that an intrinsically more stable alloy is also more stable towards diffusion-related degradation and dealloying due to kinetic barriers, despite the thermodynamic driving force for dissolution.

This is followed by our results on trying to decouple the strain and ligand effects for platinum skin structures, and determining whether there is any correlation between adsorption energy and surface stability in these systems. We find that there is such a correlation for some adsorbates, indicating that there exists a limit for the stability of an overlayer for a given adsorption strength.

Finally, we introduce our work on platinum alloy nanoparticles, and our attempt to isolate the features which result in the increased activity that has been seen experimentally. We show how the platinum-platinum distance at the surface is decreased for a variety of alloy phases in the core, with greater compression of the overlayer for core phases with lattice parameters which are either much smaller or much larger than pure platinum.

Resumé

I denne afhandling præsenterer jeg vores arbejde med teoretisk modellering af platin legeringer som katalysatorer for Oxygen Reduktions Reaktionen (ORR). Tabene relateret til denne reaktions kinetik er den primære flaskehals i lav-temperatur brændselsceller til transport formål og mere aktive katalysatorer er essentielle for udbredt brug af denne teknologi. Platin legeringer har udvist stort potentiale som mere aktive katalysatorer, som stadig er stabilie under reaktionsbetingelser.

Vi har undersøgt disse systemer på flere skalaer ved brug af enten Tætheds Funktional Teori (DFT) eller effektiv Medium Teori (EMT), afhængig af de involverede længde- og tids-skalaer.

Ved brug af DFT viser vi hvordan diffusionsbarrier i overgangsmetal legeringer i $L1_2$ strukturen afhænger af legeringsenergien, hvilket støtter antagelsen om at intrinsisk mere stabile legeringer også er mere stabile overfor diffusions-relateret degradering og af-legering på grund af kinetiske barrier, på trods af den termodynamiske drivkraft mod opløsning.

Dette efterfølges af vores resultater fra vores forsøg på at afkoble tøjning og ligand effekter for platin-skind strukturer og afgøre om der korrelation mellem adsorptionsenergien og overfladestabiliteten i disse systemer. Vi finder at der er en sådan korrelation for nogle adsorbater, hvilket indikerer at der er en grænse for stabiliteten af et overlag for en given adsorptionsstyrke.

Endeligt præsenterer vi vores arbejde med nanopartikler af platin legeringer og vores forsøg på at isolere de egenskaber der resulterer i den øgede aktivtet der er set eksperimentelt. Vi viser hvordan platin-platin afstande ved overfladen bliver sænket for flere forskellige legeringsfaser i kernen, med større kompression i overlaget for kernefaser med gitter parametre der er enten meget mindre eller meget større end ren platin.

List of papers

Paper I

Correlation between diffusion barriers and alloying energy in binary alloys

Ulrik Grønbjerg Vej-Hansen, Jan Rossmeisl, Ifan E. L. Stephens and Jakob Schiøtz

Accepted, Physical Chemistry Chemical Physics, 2015

Paper II

A modernized Effective Medium Theory potential for metals and intermetallics

S. H. Brodersen, U. G. Vej-Hansen, R. E. Christiansen, K. W. Jacobsen, and J. Schiøtz

In preparation, 2015

Paper III

Pt_xGd alloy formation on Pt(111): Preparation and structural characterization

Elisabeth T. Ulrikkeholm, Anders F. Pedersen, Ulrik G. Vej-Hansen, Maria Escudero-Escribano, Ifan E. L. Stephens, Daniel Friebel, Apurva Mehta, Jakob Schiøtz, Robert K. Feidenhansl', Anders Nilsson and Ib Chorkendorff

Submitted, 2015

Paper IV

This paper is not attached due to journal guidelines.

Tuning the activity of Pt alloy electrocatalysts by means of the lanthanide contraction

María Escudero-Escribano, Paolo Malacrida, Martin H. Hansen, Ulrik G. Vej-Hansen, Amado Velázquez-Palenzuela, Vladimir Tripkovic, Jakob Schiøtz, Jan Rossmeisl, Ifan E.L. Stephens, Ib Chorkendorff

Submitted, 2015

Papers not part of the thesis

Paper i

My contribution to this paper was part of my master project and it is therefore not included here.

Understanding the electrocatalysis of oxygen reduction on platinum and its alloys

Ifan E. L. Stephens, Alexander S. Bondarenko, Ulrik Grønbjerg, Jan Rossmeisl and Ib Chorkendorff.

Energy and Enviromental Science, 2012, **5**, 6744

Paper ii

My contribution to this paper was predominantly directly related to my master thesis and it is therefore not included here.

Pt_5Gd as a highly active and stable catalyst for oxygen electroreduction

María Escudero-Escribano, Arnau Verdaguer-Casadevall, Paolo Malacrida, Ulrik Grønbjerg, Brian P. Knudsen, Anders K. Jepsen, Jan Rossmeisl, Ifan E. L. Stephens and Ib Chorkendorff

Journal of the American Chemical Society, 2012, 134, 16476-16479

Paper iii

The essentials of this paper was included as a confidential addendum in my master thesis and is therefore not included in this thesis.

New Platinum alloy catalysts based on abundant alkaline earth metals

Ulrik Grønbjerg Vej-Hansen, Maria Escudero-Escribano, Paolo Malacrida, Jan Rossmeisl, Ifan E. L. Stephens, Ib Chorkendorff, Jakob Schiøtz

In preparation, 2015

Paper iv

The theoretical part of this paper is principally the result of a master project which I assisted in supervising. The contents are therefore not included as such in this thesis.

H_2/D_2 exchange reaction on monodispersed Pt clusters and enhanced activity from minute O_2 concentrations

Jakob N. Riedel, Marian Rötzer, Mikkel Jørgensen, Ulrik Grønbjerg Vej-Hansen, Thomas Pedersen, Béla Sebök, Florian F. Schweinberger, Ole Hansen, Jakob Schiøtz, Ulrich Heiz, Ib Chorkendorff

In preparation, 2015

List of Patents

Patent I

Electrode used for fuel cell e.g. electrochemical fuel, comprises alloy containing noble metal(s) chosen from platinum and/or palladium, and lanthanide metal(s) chosen from cerium to lutetium, supported on conductive support material

I. E. L. Stephens, M. Escudero-Escribano, A. Verdaguer-Casadevall, P. Malacrida, U. G. Vej-Hansen, B. P. Knudsen, A. K. Jepsen, J. Rossmeisl, I. Chorkendorf

Patent Number(s): WO2014005599-A1 ; CA2877617-A1 ; KR2015036435-A ; EP2870649-A1

Patent II

Electrode used as electrocatalyst used for fuel cell comprises binary alloy containing noble metal chosen from palladium and platinum, and alkaline earth metal in which alloy is supported on conductive support material

I. E. L. Stephens, M. Escudero-Escribano, A. Verdaguer-Casadevall, P. Malacrida, U. G. Vej-Hansen, J. Schiøtz, J. Rossmeisl, I. Chorkendorf

Patent Number(s): WO2014079462-A1 ; CA2891134-A1

Contents

List of Figures

List of Tables

Chapter 1

Introduction

1.1 The global energy challenge

Producing enough energy will be a global challenge in the coming years. The near perspective is that we need to reduce CO_2 emissions immediately in order to counteract climate change. This is a well-established scientific fact and as it, and its consequences, has been treated extensively elsewhere I will not go into detail here[1, 2]. However, if that is not motivation enough, an even greater energy challenge lurks on the horizon. Looking at current, proven, reserves and current production, we have oil and natural gas for the next 50 years and coal for the next 110[3]. However, the demand will certainly increase in the near future if it is not mitigated, due to increased living standards in the developing economies, and this will make the current reserves last shorter than this. The reserves may also increase somewhat in that period, but fossil fuels are a limited resource - at some point they will run out. It is thus absolutely necessary to move away from fossil fuels, in order to secure the world energy supply, and by extension, the global political stability. The numbers mentioned above are global averages, and due to the inhomogeneous distribution of reserves, it is likely that some regions will deplete their resources faster than others, and will need to get them elsewhere. This must be expected to be a destabilising influence if the global reserves are running low[4].

In order to elaborate on the connection between living standards and energy consumption, I show in figure 1.1 values of the United Nations Human Development Index (HDI) vs. the energy consumption of that particular country. HDI is a measure of the overall development of a society, aggregating parameters describing life expectancy, education and per capita income. The figure shows that most countries are actually consuming very little energy per capita. However, the majority of the countries with a low energy consumption are also evaluated to have an HDI value significantly lower than 0.9, which means there is room for improvement - an improvement which will be powered by an increased energy consumption. It should also be noted that the two most populated countries in the world are situated at HDI values below 0.8, resulting in a large increase in energy consumption when they rise in HDI. A rough estimate is that the total energy consumption will double if the population in the developing countries should all rise to the minimum energy required for a HDI above 0.9.

However, all of the above is based on a static population. In figure 1.2 I show the United Nations population projections until year 2100. It shows that within the 95% confidence interval, the best-case scenario is a slow increase to just below 10 billion people in 2080 and a very slow decline after that, while the worst-case scenario is a steady increase to more than 13 billion people in 2100. Unfortunately, even the best-case scenario will increase the world population by more than a third, increasing energy consumption even further. In fact, the

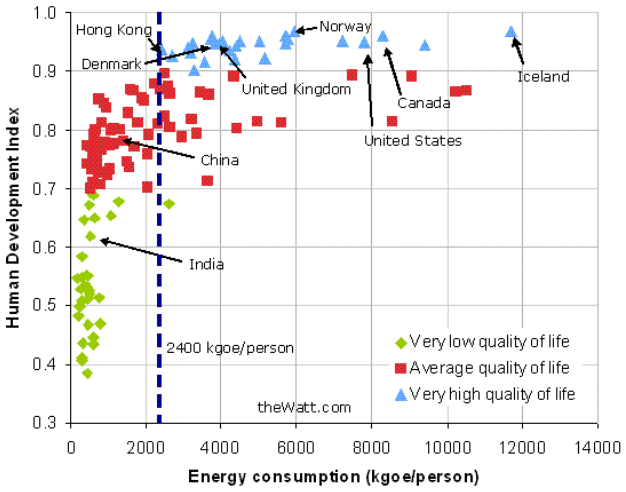

Figure 1.1: *Plot of the Human Development Index (HDI) as a function of the energy consumption for various countries, based on data from 2003. The vertical dashed line shows the energy consumption which seems to be sufficient to achieve a very high standard of living. Reproduced from reference [5].*

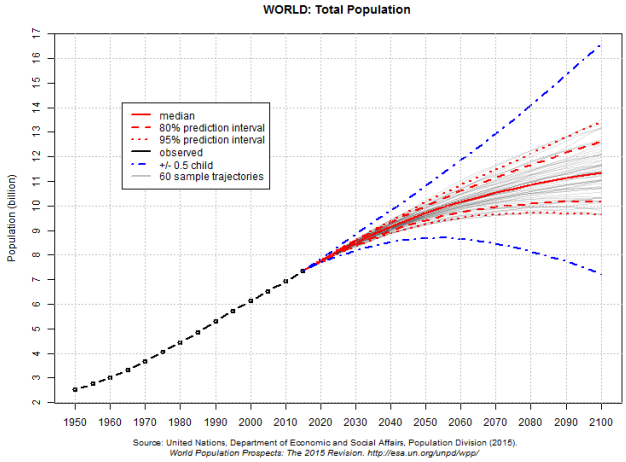

Figure 1.2: *Plot of world population as a function of time. Black is historical data, and the red dotted line is the 95% confidence interval of the UN projection. The dashed blue line is the best and worst-case scenarios for the projection. Reproduced from reference [7].*

International Energy Agency (IEA) expects global energy demand to grow by 37% by 2040, and this includes the current focus on energy efficiency[6].

There are at least two ways to mitigate this problem, of which one is also a possible long-term solution. We can try to use energy more efficiently, slightly lowering the consumption every year, while keeping our standard of living. However, this strategy is only really effective in the developed economies, which already have a high standard of living. In the developing economies, the energy demand will increase together with the standard of living. So this strategy will only postpone the problem, and likely not even by much as the global distribution of energy consumption will change.

The second strategy, and only viable long-term solution, is to move away from fossil fuels

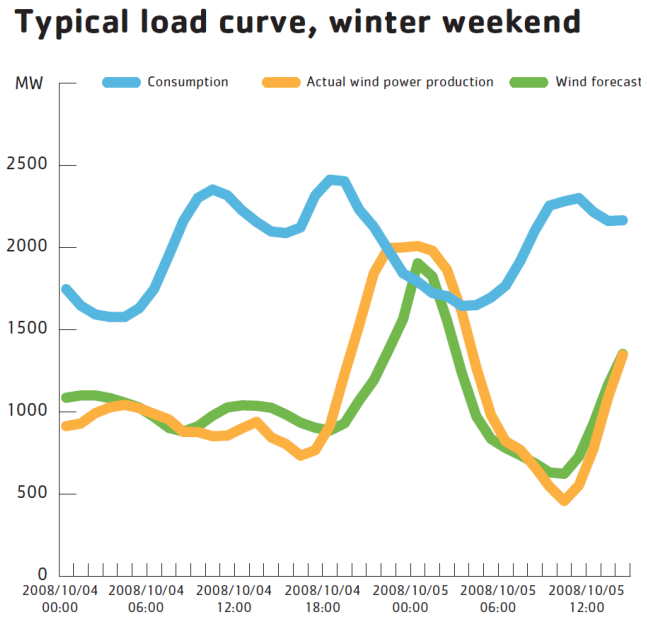

Figure 1.3: *Plot of electricity consumption in blue, forecast of electricity generated from wind power in green, and the actual production in yellow, for a period of approximately 36 hours. Reproduced from reference [8].*

as an energy source, and instead use renewable sources, such as sun, wind and hydroelectricity. Today, renewable energy accounts for about 9 % of the global energy consumption, nuclear energy for 4.5 % and fossil fuels make up the rest[3]. It should be noted that the renewables here include hydroelectricity, which is very dependent on appropriate natural landscapes, and as such it has a definite limit to the potential increase.

1.2 Integrating renewables in the energy infrastructure

However, aside from political, economic and ideological obstacles for the introduction of renewable energy sources in the global energy supply, there are some practical constraints. The major renewables, such as wind and solar power, both suffer from intermittency, meaning they are dependent on phenomena which fluctuate on both short and long time-scales. These fluctuations are in general difficult to predict accurately in advance, and they are in no way correlated to the fluctuations in demand. I show two such examples in figure 1.3 for a single day including the forecast and in figure 1.4 for an entire month. It is clearly seen in figure 1.3 how there is substantial deviation between the forecast and the actual production, making balancing the electricity grid a real-time challenge. It is also quite obvious that while the entire electricity consumption can at times be covered by wind power, it is still necessary to have other power sources to supplement with, and even if the wind power could be averaged without losses, it would not be adequate to cover consumption.

1.2.1 Energy intermittency and storage

As discussed above, the intermittency of wind is a problem if wind power is supposed to cover a large part of the electricity consumption, and must be compensated in some way. This also applies to photovoltaics, the other major renewable today. There are two basic ways to

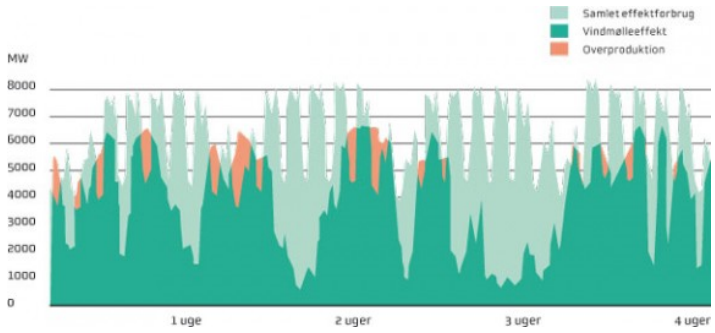

Figure 1.4: *Plot of electricity consumption in light green and the wind power production in dark green. The x-axis is in weeks, covering a total of about a month. The orange areas represent overproduction, meaning that wind power alone produced more electricity than was consumed at that time. Reproduced from reference [9].*

handle this, with the best solution probably being a combination of the two. One is to have alternate energy sources which can be controlled with a very small time constant, and simply turn these up or down depending on the production of the intermittent sources. However, this does not solve the problem of overproduction, and the best example today is probably a gas-fired power plant, which is reliant on fossil fuels. The second solution is to store the energy when there is a surplus and then release it back into the grid when needed. This is already done to some extent using hydropower facilities, but they are limited to selected areas where natural landscape makes it possible. It is not obvious how to supplement this storage, as the various mechanisms each have drawbacks. The most obvious solution is to install huge batteries and simply charge or discharge them depending on the situation. However, as seen from figure 1.5, such batteries would be both huge and massive, as well as very expensive. Additionally, other problems might appear as a result of the huge scale we are discussing here. An alternative would be to use the electric power to produce some sort of chemical fuel, and then convert that back into electricity when needed. The combination of electrolysers, fuel cells and electric motors are superior to internal combustion engines in efficiency, and this process would have about 50 % efficiency for the round-trip, depending on the hydrogen storage technology. This way, using the excess electricity to produce a chemical fuel could help in integrating renewables in the transport sector, which also accounts for a sizeable portion of the energy consumption.

1.2.2 Transport applications

A major challenge in the conversion from a fossil fuels based energy supply to one based on renewable sources is the transportation sector. Liquid fossil fuels have very high energy densities both volumetric and gravimetric, which become extremely important when we are looking at transport applications. It is difficult to reproduce this in a different way based on renewables. In figure 1.5 I show the energy densities for various materials. Note how diesel and gasoline both have a very high density on both axes. Hydrogen also has a high gravimetric density, but the volumetric density is extremely low for the gas at standard conditions, and even liquid hydrogen has a low volumetric density compared to hydrocarbons.

While it is possible to produce hydrocarbons using electrochemistry[12], which would be a viable path towards integrating renewables in the transport sector, it is not yet a mature technology, and still require intense research efforts in the field [13–17]. The infrastructure and the automotive technology already exists, though the efficiency of the internal combus-

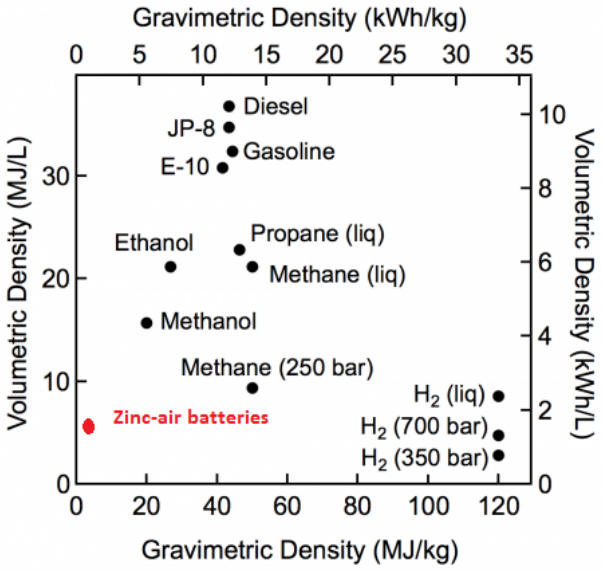

Figure 1.5: *Plot of the gravimetric vs. volumetric energy density for various materials. The most desirable ones are in the top-right corner. Adapted from reference [10], with the red point added on the basis of reference [11].*

tion engine would probably drive the overall efficiency down. Another material with a high gravimetric energy density, depending on the form, is hydrogen, which can be produced from electricity and water with about 80 % efficiency[18] and then converted back to electricity with a fuel cell. According to Honda [19], this can be done with 60 % efficiency using current technology, giving a electricity-to-wheels efficiency of nearly 50 %. This can be contrasted with the up to 30 % fuel-to-wheels efficiency of gasoline vehicles, which does not take losses during extraction and processing of the fuel into account[20].

1.3 Fuel cells

A fuel cell makes it possible to convert hydrogen, or other fuels, to electricity. There are several different fuel cell technologies available, but here I will focus on Polymer Electrolyte Membrane Fuel Cells (PEMFCs), which operate at less than 100 °C and use pure hydrogen as a fuel. I show a sketch of a PEMFC in figure 1.6. The low temperature makes them suitable for transport applications. Due to the high efficiency of electric motors, this is a viable way to keep the current range characteristics of personal cars, if a few challenges can be overcome. One is the storage of hydrogen in the car, which presents a set of problems since hydrogen needs to be either compressed, liquefied or stored in a solid material, in order to make the volumetric density practical for transport applications. This can be seen in figure 1.5. However, I will not go further into the problem of storage; instead I will focus on a specific challenge related to the electrocatalytic process of converting hydrogen and oxygen into water.

As stated above, energy efficiency will become even more important over time, and it is therefore of the utmost importance to optimize the efficiency of fuel cells. It turns out that a very big part of the loss is related to the poor kinetics of the Oxygen Reduction Reaction (ORR) at the cathode[22]. This means that the potential that can be drawn from the fuel cell is much lower than the ideal case, and this difference is known as the overpotential. This

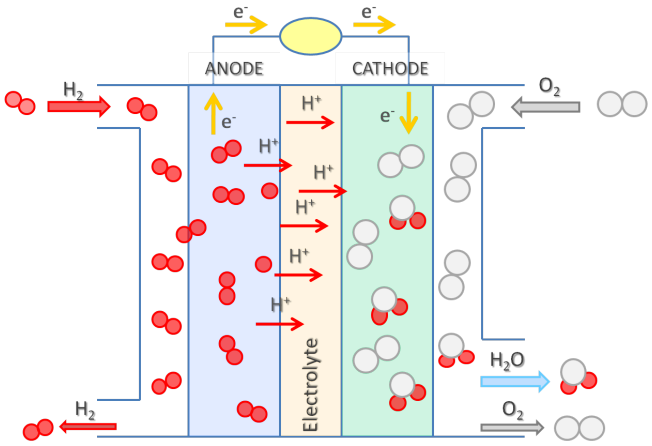

Figure 1.6: *Overview sketch of a fuel cell. Hydrogen comes in from the left and is split at the anode, while oxygen comes in from the right and is split at the cathode, where it is then combined with hydrogen ions to form water. Electrons travel through the circuit at the top, providing usable work. Reproduced from reference [21].*

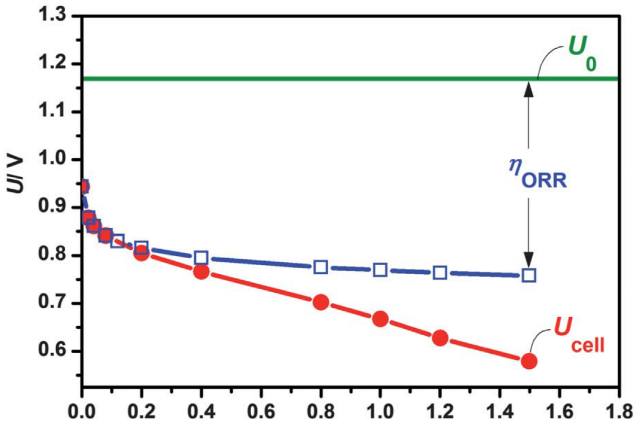

Figure 1.7: *Voltage as a function of current in a fuel cell. Note the large overpotential associated with the ORR. Reproduced from reference [23], originally from reference [22].*

can be seen in figure 1.7.

This large overpotential is observed with even the state-of-the-art Pt catalyst available in 2005 when these experiments were published. However, this presents a problem, as the usage of Pt per fuel cell is fairly large. If the annual global production of Pt of 200 tons[24] went to fuel cells, only 6 million cars could be produced annually, assuming a Pt loading of 30 g per fuel cell[25]. It is therefore necessary to develop better catalysts, if fuel cells are to be more than a niche technology for automotive applications. There are two obvious routes to take in this regard; one is to modify the existing Pt catalyst in order to use less Pt and/or get better performance, while the other is to avoid Pt altogether. Here I will focus on the first strategy, while the interested reader may consult the recent review by Nie et al.[26] for an overview of both fields.

However, first I will mention the very corrosive environment of a fuel cell, which is the main reason for restricting research to improving Pt instead of looking at Pt-free catalysts. In figure 1.8 I show the Pourbaix diagram for Pt. This illustrates which phase is stable

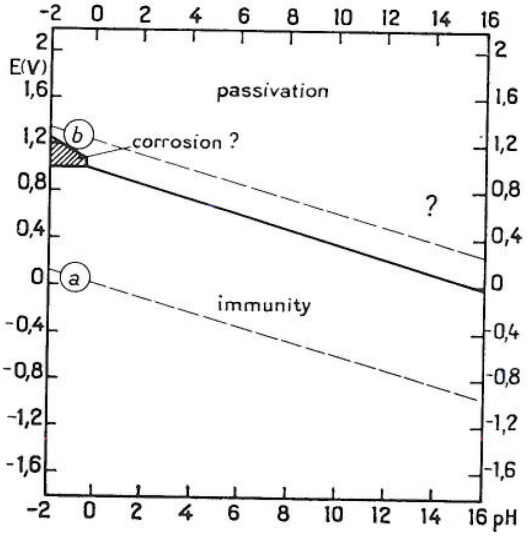

Figure 1.8: *Pourbaix diagram for Pt. Reproduced from reference [27].*

under a given combination of potential and pH. A PEMFC normally operates with a pH of 0 and a potential of up to 1 V, and it is seen that Pt is just beginning to corrode under those circumstances. However, just about every other material will corrode long before that, making Pt one of the few materials which are still marginally stable under these conditions. The Pourbaix diagram is based on static considerations, and the dynamics of potential cycling make things more complicated.

1.4 Overview of this thesis

Chapter 2 gives a more detailed introduction to the Oxygen Reduction Reaction, specifically as it takes place on Pt and its alloys. I will describe which properties of the alloys influence the activity and how to model it.
Chapter 3 gives an introduction to Density Functional Theory (DFT), which is an *ab initio* method used to calculate many results in this thesis. It is also related to Effective Medium Theory (EMT), which is used and introduced in chapter 6.
Chapter 4 presents our results on correlating diffusion barriers in alloys with their thermodynamic stability, specifically their Heat of Formation or alloying energy. This is related to their resistance to diffusion-related degradation mechanisms.
Chapter 5 describes how the strain and ligand effects influence activity and overlayer stability, and how they correlate. This is important for alloys where both effects are expected to be present at the same time.
Chapter 6 explores the the Pt-Pt distance on the surface of Pt alloy nanoparticles, and how it depends on the minority element and the structure of the core.
Chapter 7 will summarise the thesis and present an outlook for the future of the projects presented here.

Chapter 2

Platinum alloys for the Oxygen Reduction Reaction

In order to design new and better catalysts for the Oxygen Reduction Reaction (ORR) in fuel cells, it is necessary to understand the reaction in detail. In this chapter I will introduce the concept of catalysis of a chemical reaction, and then go into more detail with the ORR. Finally I will present some strategies for increasing the activity, including a thorough presentation of the previous work on Pt alloy catalysts at DTU Physics.

2.1 Catalysis in general

Catalysis is the concept of introducing an additional substance to a chemical reaction, separate from the reactants and products, which makes the reaction proceed faster towards equilibrium without being consumed in the process. There are two traditional categories of catalysts, homogeneous and heterogeneous. The first type exists in the same phase as the reactants, while the second does not. In general, a catalyst acts by lowering the activation barrier of a reaction, increasing the probability that the reactants will have enough energy to overcome it and react. This is depicted in figure 2.1. This lowering is extremely important, as up to 90 % of the products in the chemical industry are manufactured using a catalysed process[28].

In the case of a heterogeneous catalyst, the reaction typically happens on a (metal) surface. This opens up another pathway where the reaction can proceed in a different way than it otherwise could, and in the case of electrocatalysis, transport electrons between the reactants and the catalyst.

2.2 Specific kinetics of the ORR

The ORR is given by the overall reaction seen in equation (2.1). Compared to many other chemical reactions, this is a fairly simple example, but the four electrons involved show that it is actually a four-step process. These four steps have a total of 3 intermediates, and I show the four elementary steps for the associative mechanism in equations (2.2) to (2.5). $*$ signifies an adsorbed species, while (l) and (g) indicate liquid phase and gas phase, respectively.

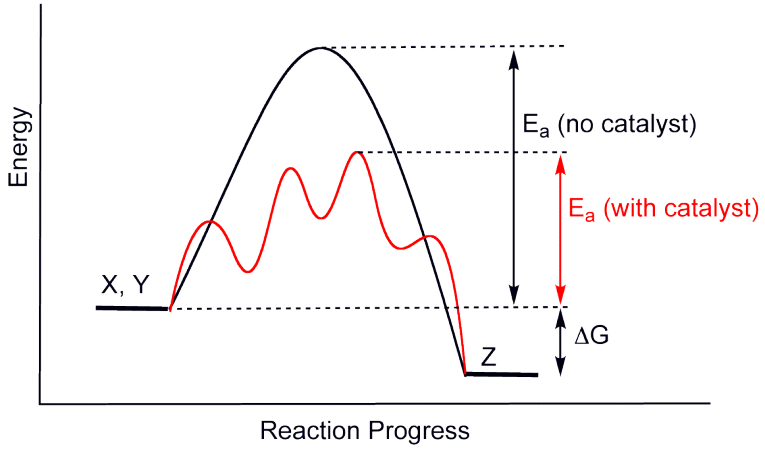

Figure 2.1: *Sketch of the energy barrier for a reaction with (in black) and without (in red) a catalyst. Reproduced from reference [29].*

$$O_2(g) + 4H^+ + 4e^- \leftrightarrow 2H_2O(l) \quad (2.1)$$
$$O_2(g) + H^+ + e^- \leftrightarrow *OOH \quad (2.2)$$
$$*OOH + H^+ + e^- \leftrightarrow *O + H_2O(l) \quad (2.3)$$
$$*O + H^+ + e^- \leftrightarrow *OH \quad (2.4)$$
$$*OH + H^+ + e^- \leftrightarrow H_2O(l) \quad (2.5)$$

The entire process has been modelled in detail by the group of J. K. Nørskov [30–32]. The Gibbs free energy diagram for the reaction is shown in figure 2.2. They found that the potential-determining step on Pt is the hydrogenation of adsorbed OH shown in equation (2.5), caused by OH being too strongly bound to the surface for optimal activity. Specifically, optimal activity should be achieved by a catalyst binding OH about 0.1 eV weaker than Pt[32], which has also been experimentally verified[33].

However, from figure 2.2 it can be seen that hydrogenation of O_2 to form adsorbed OOH is also uphill in free energy, indicating that OOH is bound too weakly to the surface. This presents a major problem, as it has been shown that the adsorption energies of molecules with the same major component, in this case O, scale linearly[34, 35]. Thus, it is probably not possible to find a material with a regular surface which binds OH more weakly than Pt, and OOH more strongly. Nevertheless, it is still possible to achieve much better activity within these constraints, and in figure 2.3 I show a plot of experimentally measured activities versus calculated OH adsorption energies. While the agreement with the Sabatier model is not perfect, there is definitely a trend towards higher activities at slightly weaker binding than pure Pt. It should also be noted that the very severe outlier of Pt/Au(111) have since been explained by inconsistency between the surface under experimental conditions and what was modelled[36].

2.3 How to change adsorption energies

As detailed above, we should look for a catalyst material, based on Pt, which binds OH about 0.1 eV weaker than pure Pt, in order to achieve optimal activity for the ORR. I will therefore

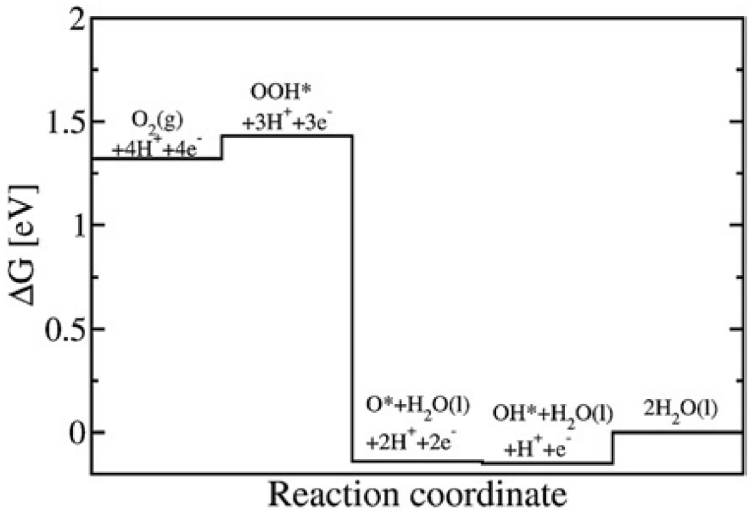

Figure 2.2: *Gibbs free energy diagram using the associative mechanism for the ORR. Reproduced from reference [32].*

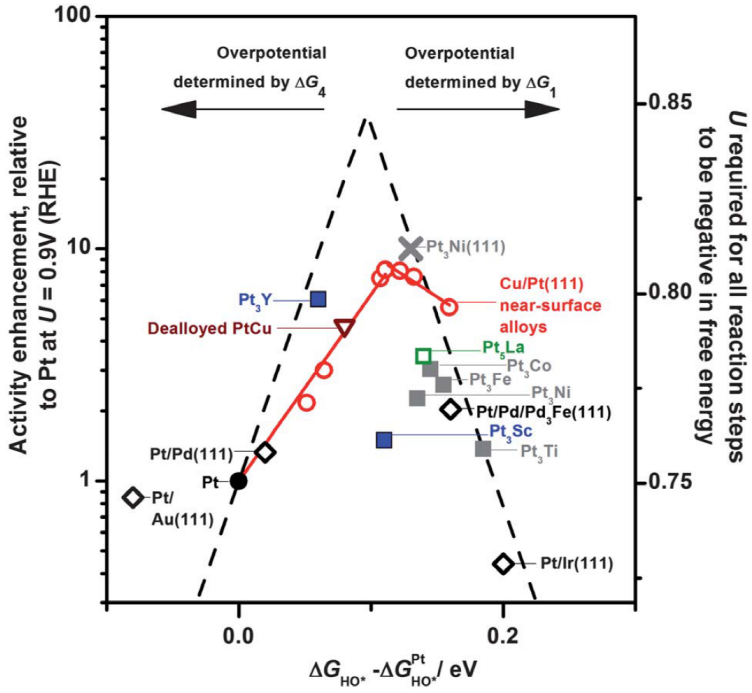

Figure 2.3: *The Sabatier volcano shown as dashed line, with measured activites and theoretically calculated OH binding energies. Reproduced from reference [23].*

present the two major phenomena affecting adsorption properties on metal surfaces, according to the so-called d-band model, which has been highly successful in describing adsorption properties of transition metals[37–40]. The d-band model describes how the adsorption properties of transition metals are closely related to the position and filling of the metal d-band, as it dominates the interaction with adsorbates. The adsorption properties can then be influenced by changing the d-band, though e.g. strain and ligand effects.

2.3.1 Strain effects

One way to change the d-band of the surface metal atoms, is by the so-called strain effect, which was coupled to the d-band model by Mavrikakis et al.[41]. The strain effect is caused by the movement of the metal d-band when the surface experiences a strain, moving the interatomic distance away from equilibrium. An expansion leads to a thinner band, which must then move up in energy in order to keep the filling constant, which will lead to stronger interaction with the adsorbate and stronger bonding to the surface. Conversely, a compression of the surface moves the d-band down in energy, causing the interaction between the surface and the adsorbate to lessen, making the bonding weaker. Note that this effect can also be found for under-coordinated atoms, such as corner atoms compared to surface atoms, an effect which might be important in gold catalysis[42]. In order to get an adsorption energy for OH which is about 0.1 eV weaker than for pure Pt, it is necessary to compress Pt about 2 % if no other effects modify the adsorption[23].

2.3.2 Ligand effects

The second major way to modify the adsorption properties of transition metal surfaces, is through the ligand effect[43]. The ligand effect appears when atoms of another element are present near the surface, usually in the layer just below, and influences the surface atoms through direct electronic interaction. This effect can also both strengthen and weaken the adsorption at the surface, but it is in general more complicated than the strain effect, making it harder to predict its effect in real systems, though some success has been shown for model systems[44]. I will return to the strain and ligand effects in chapter 5.

2.4 Pt alloy ORR catalysts

The obvious route when modifying the properties of a metal is to alloy it with another, and alloys of Pt and late transition metals, such as Co, Cu, Fe and Ni were first implemented as cathode catalysts in fuel cells more than two decades ago and are used commercially today[45–49]. However, these commercial catalysts tend to degrade over time under operating conditions. The minority element tends to diffuse to the surface where it is then dissolved into the electrolyte, a process known as dealloying. This causes the catalytic activity to decrease towards that of pure Pt, negating the advantage gained from alloying in the first place[22, 49–51]. This activity decrease is shown in figure 2.4 for Pt_3Co.

This degradation obviously limits the lifetime of the catalyst, but recent reports show exceptional activity and stability for novel nanoparticulate forms of Pt-Ni alloys[52–55]. However, these are all based on accelerated degradation tests, and it is therefore still unknown if this performance is also stable under long periods of time[56]. So far, there is no consensus on how to measure stability of the catalysts under laboratory conditions, and many different definitions of stability can be found in the literature[53, 56–58]. This is at least partly due

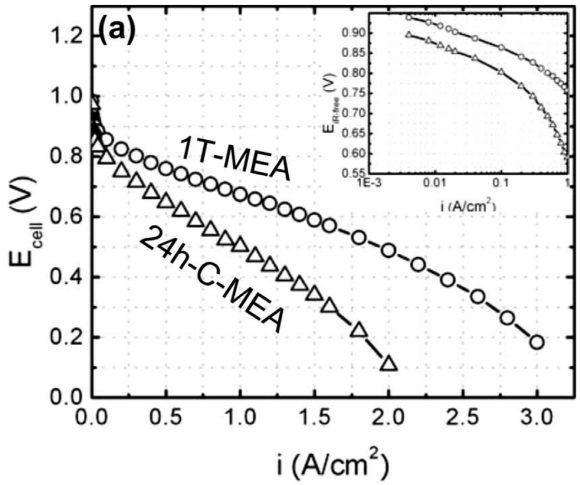

Figure 2.4: *Voltage vs. current for a Membrane Electrode Assembly (MEA) with a Pt_3Co cathode catalyst. The freshly prepared MEA is shown as circles, while the triangles are after 24 hours of cycling. Reproduced from reference [49].*

to the degrading mechanisms being poorly understood, making it difficult to know how to replicate true operating conditions in the laboratory.

2.4.1 Pt alloys with a high alloying energy

In order to overcome the problem of dealloying, earlier work at DTU Physics proposed the use of the alloying energy for an alloy as a descriptor for stability under operating conditions[59]. This initially led to the discovery of catalysts with very negative alloying energies and high activity such as polycrystalline Pt_3Y [59]. Continued work in this direction and related insights into the structure of these materials led to the discovery of several alloys of lanthanides and Pt, such as polycrystalline Pt_5La [23], Pt_5Y [60], Pt_5Gd [61] and Pt_5Ce [62]. These alloys all form a structure which it is possible to match a compressed Pt overlayer to, even though the minority elements are much larger than Pt[63]. I show this for Pt_5La in figure 2.5. As mentioned above, this compression will lead to a weaker binding of adsorbates and thereby an increased activity for the ORR. However, while figure 2.5 shows that it is possible to do this, it is necessary to investigate in more detail to determine if it actually happens in real systems.

Previous work has shown that the exact nature of the Pt surface is important in order to understand the activity of a given material, specifically whether it is a thin and well-defined "Pt-skin" structure or a more thick and rough "Pt-skeleton" structure[65]. This is of course dependent on the precise interaction with the electrolyte. Angle-Resolved X-ray Photoelectron Spectroscopy (ARXPS) is a technique capable of determining the composition of a sample in the region closest to the surface. It has been used extensively to study these samples, before and after exposure to the corrosive electrolyte, in order to determine whether an overlayer was formed and to give an indication of its thickness. In figure 2.6 I show such a measurement for Pt_5Gd, taken before and after exposure to reaction conditions. Before exposure there is a uniform distribution of the two elements, corresponding to the bulk ratio of the alloy. After ORR activity measurements, Gd is depleted from the surface region, which is now entirely Pt for a distance corresponding to 2-3 layers.

We expect this overlayer to form quickly upon exposure to reaction conditions, indicating

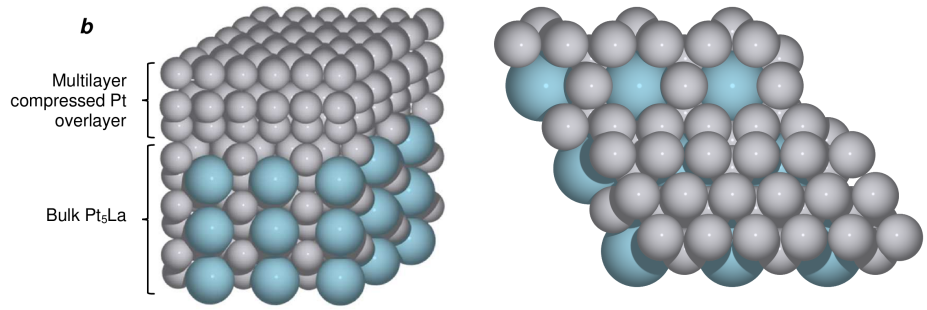

(a) *Reproduced from reference [23].* **(b)** *Reproduced from reference [64].*

Figure 2.5: *Bulk structure of Pt_5La with a compressed Pt(111) layer on top. Note how the symmetry is matched between the two structures.*

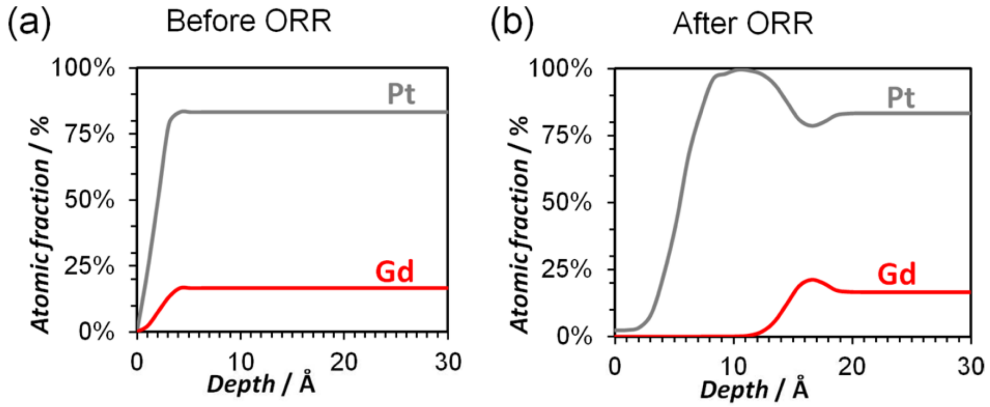

Figure 2.6: *ARXPS measurements on a polycrystalline Pt_5Gd electrode before (a) and after (b) exposure to ORR conditions. Adventitious contamination has been omitted for clarity. Reproduced from reference [61].*

that this is the active surface. This would seem to rule out the ligand effect as an influence on the surface reactivity, which we have previously confirmed with DFT calculations[23]. It therefore seems that the activity of these alloys should be determined exclusively by the lattice parameter, which would control the strain in the surface, and thereby the activity. We explore this notion further in Paper IV[66].

However, even though the alloys mentioned above have a large, negative, alloying energy, they are thermodynamically less stable than alloys such as Pt_3Ni under operating conditions. It has even been shown that the dissolution potential of the minority transition metal tends to scale with the alloying energy[67]. Thus it is still undetermined whether the dissolution potential or the alloying energy has the greater influence on the long term stability of Pt alloy catalysts under operating conditions in a fuel cell. I will return to this in chapter 4.

Nevertheless, ARXPS measurements after an electrochemical stability test, which in this case is cycling 10,000 times between 0.6 and 1.0 V, shows that the composition is virtually unchanged, as shown in panels c) and d) in figure 2.7. Panels a) and b) in the same figure are a bit more technical, and show the Pt:La and Pt:Ce ratios as a function of electron emission angle, which is the basis for the plots in panel c) and d). They show how the ratio is constant and uniform during the sputter cleaning, before exposure to electrochemistry, and how the

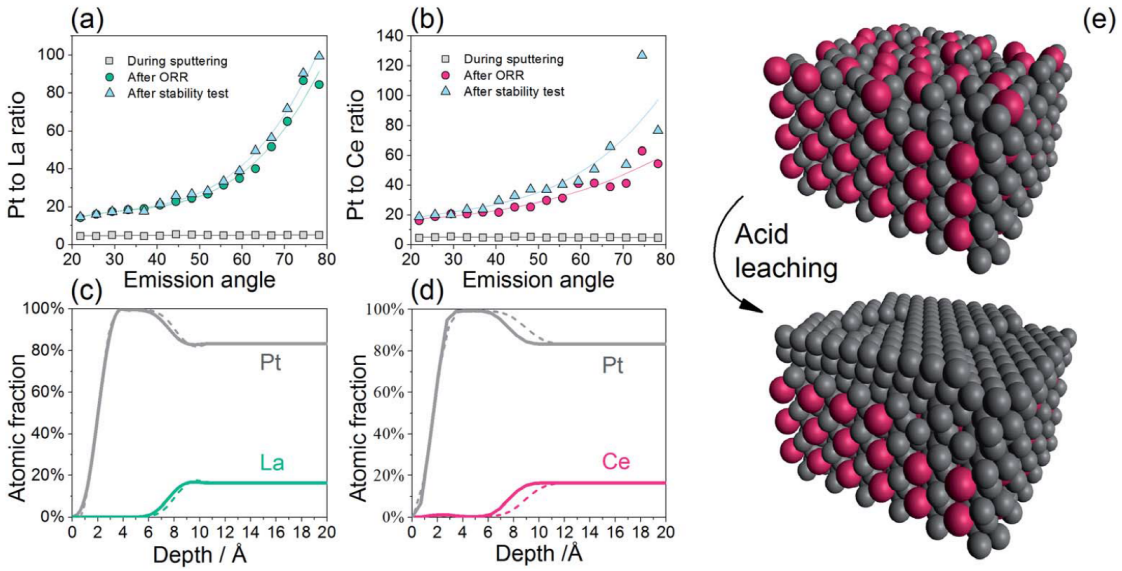

Figure 2.7: *ARXPS measurements of Pt_5La (a) and c)) and Pt_5Ce electrodes (b) and d)). Panels a) and b) show the Pt:X atomic ratio as a function of emission angle of the electrons, and panels c) and d) show the depth profiles which can be constructed from these data, with the fulle line being after ORR and the dashed line being after a stability test. Panel e) is a sketch of the atomic surface based on the depth profiles. Reproduced from reference [62].*

significant shift happens after exposure to reaction conditions for just a short time, with the stability test making very little difference. Finally, panel e) is a sketch of the surface as seen before and after exposure to ORR conditions.

2.5 Pt alloys in nanoparticulate form

Catalysts used in a fuel cell need to be in nanoparticulate form in order to maximize the surface area, and thereby the activity by mass of the catalyst. Of the Pt alloys mentioned in the previous section with a high alloying energy, Pt_xY [68, 69] and Pt_xGd [70] have successfully been synthesized with a physical method and tested in nanoparticulate form. Both showed excellent activity as shown in figure 2.8 on the following page. In addition, there are several ways in which the two systems seem very different compared to the pure Pt reference particles. Pure Pt has a maximum in the mass activity for particles of about 3 nm, whereas Pt_xGd nanoparticles have a maximum for the much larger 8 nm particles, and Pt_xY could be even larger, as it was not found in the investigated range of up to 9 nm. It is also somewhat surprising that the largest Pt_xY nanoparticles show a higher specific activity than the polycrystalline sample, in contrast to the two other materials, which converge to this value in the range investigated. This, coupled with the strain measurements in the paper, indicates that the Pt surface of a large Pt_xY nanoparticle is under a higher strain than polycrystalline Pt_3Y.

In order to investigate whether compressive strain could be the mechanism increasing the activity of these particles, the authors carried out Extended X-ray Absorption Fine Structrue (EXAFS) measurements[72–75]. This gives the average Pt-Pt distance in the particle, shown in figure 2.9 vs. the specific activity. However, according to the theoretical model, the

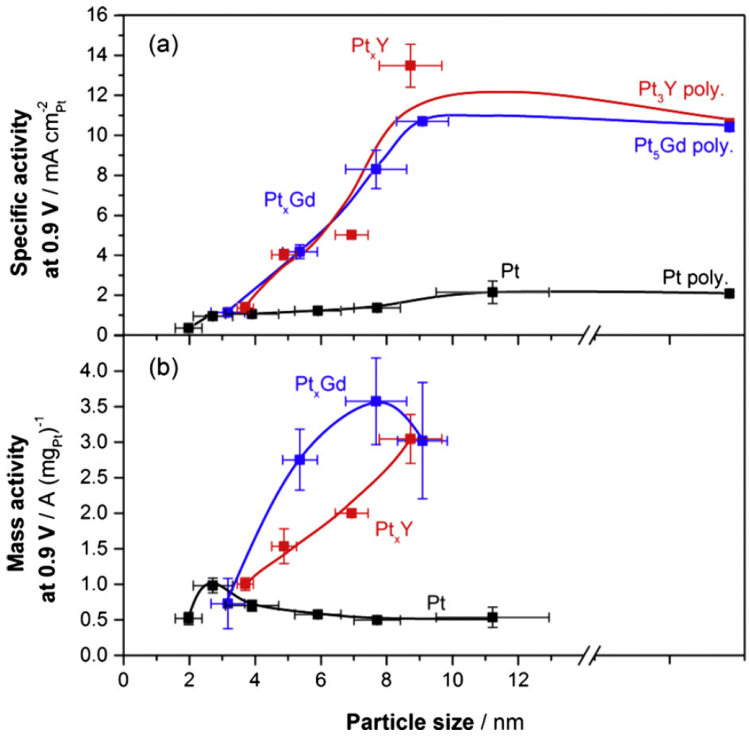

Figure 2.8: *Specific activity (per surface area of catalyst) and mass activity (per mass of catalyst) vs. particle diameter, for Pt_xY and Pt_xGd nanoparticles, as well as pure Pt as a reference. The lines serve to guide the eye. Reproduced from reference [70] with original data from references [69, 71].*

interesting property is not the average strain in the whole particle, but only at the surface, and indeed only at (111)-like surface facets. It would therefore be very beneficial to model these nanoparticles theoretically, in order to understand their high activity in detail. I will return to this in chapter 6.

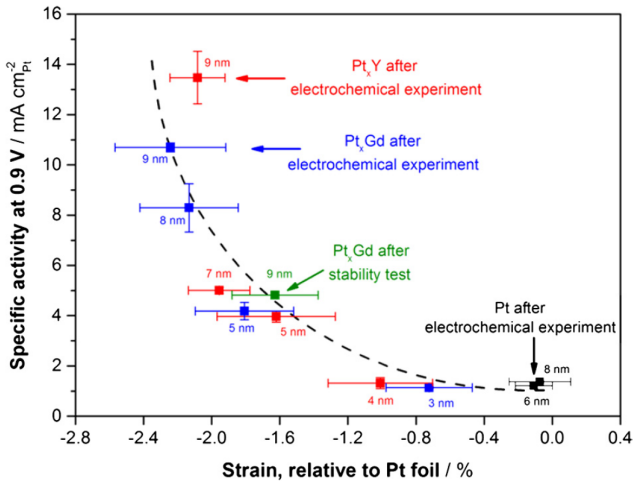

Figure 2.9: *Specific activity vs. strain measured with EXAFS for Pt_xY and Pt_xGd nanoparticles, as well as pure Pt. EXAFS measurements on a Pt foil is used as a reference for the strain. The lines serve to guide the eye. Reproduced from reference [70] with original data from references [69, 71].*

Chapter 3

Density Functional Theory

In this chapter I will introduce the workhorse method of my project, Density Functional Theory. In section 3.1 I will introduce the basic problem of the electronic structure of materials and in section 3.2, explain how DFT can be used to solve it. This approach follows that of the textbook by Kohanoff [76]. This is followed by section 3.3 about Exchange-Correlation functionals, an essential part of DFT, and also the main limitation. Finally in section 3.4 I will explain how all of this is carried out in practice. Other methods I have used will be presented in the relevant chapters.

3.1 The Electronic Structure Problem

The electronic structure of a material is in principle all you need to know in order to calculate a host of properties of interest. However, even though the problem is in principle solvable by using the deceptively simple Schrödinger equation, it is in practice very difficult for all but the simplest systems. The Schrödinger equation is an eigenvalue equation for the Hamiltonian operator, shown here as equation (3.1). The Hamiltonian is shown in expanded form for a system of P atomic nuclei and N electrons as equation (3.2)[76].

$$\mathcal{H}\psi = E\psi \tag{3.1}$$

$$\begin{aligned}\mathcal{H} = & -\sum_{I=1}^{P}\frac{\hbar^2}{2M_I}\nabla_I^2 - \sum_{i=1}^{N}\frac{\hbar^2}{2m}\nabla_i^2 + \frac{e^2}{2}\sum_{I=1}^{P}\sum_{J\neq I}^{P}\frac{Z_I Z_J}{|\mathbf{R}_I - \mathbf{R}_J|} \\ & + \frac{e^2}{2}\sum_{i=1}^{N}\sum_{j\neq i}^{N}\frac{1}{|\mathbf{r}_i - \mathbf{r}_j|} - e^2\sum_{I=1}^{P}\sum_{i=1}^{N}\frac{Z_I}{|\mathbf{R}_I - \mathbf{r}_i|}\end{aligned} \tag{3.2}$$

The two-body nature of the Coulomb interaction makes every particle dependent on all the others. The system must therefore be treated as a many-body wavefunction, which is a function of the positions of all particles, making it impossible to solve even numerically.

3.1.1 The Born-Oppenheimer approximation

In order to make the problem more tractable, it is usual to use the Born-Oppenheimer approximation, which was proposed already in 1927, almost immediately after the Schrödinger equation was proposed in 1926. The Born-Oppenheimer approximation is essentially to separate the many-body wavefunction into two, one for the electrons and one for the nuclei. This includes the adiabatic approximation, which uses that nuclei are much heavier than electrons, and electrons therefore operate on a much shorter time scale than the nuclei. This means that

the electrons will almost instantaneously enter the new ground state due to any movement of the nuclei. A second element of this approximation is the treatment of the nuclei as classical, which is valid in most situations[76].

The Born-Oppenheimer approximation allows us to focus on the electrons when solving equation (3.2) on the previous page, giving the simpler expression shown here as equation (3.3). Here the electrostatic potential from the nuclei is simply given as an arbitrary external potential V_{ext}.

$$\mathcal{H} = -\sum_{i=1}^{N} \frac{\hbar^2}{2m} \nabla_i^2 + \frac{e^2}{2} \sum_{i=1}^{N} \sum_{j \neq i}^{N} \frac{1}{|\mathbf{r}_i - \mathbf{r}_j|} + V_{ext} \tag{3.3}$$

However, the second term in equation (3.3) is still very complex, as it is dependent on the interaction between every pair of electrons. A traditional strategy is then to separate it into two terms. The Hartree energy U_H, which is the electrostatic energy of a classical charge distribution corresponding to the total distribution of electrons, and the exchange-correlation energy E_{xc} which includes the quantum mechanical effects. These are chiefly the exchange-energy, whose primary effect is to increase the energy if two electrons with the same spin are close together, and the correlation energy, which is usually defined as whatever effects are not captured by the other terms. Unfortunately, the Hartree energy includes self-interaction for each electron, which needs to be compensated for in the exchange-correlation term. The energy can now be written as shown in equation (3.4), where T_e is the kinetic energy of the electrons, corresponding to the first term in equation (3.3). In this formulation, the complex parts of the problem have been isolated in the exchange-correlation term, which eases the solving of this equation in the next section.

$$E_{elec} = E_{ext} + T_e + U_H + E_{xc} \tag{3.4}$$

3.2 The Kohn-Sham formulation of Density Functional Theory

The next step in the development of DFT was the Hohenberg-Kohn theorems[77], which introduces the electronic density as a fundamental property of the system. Specifically, Hohenberg and Kohn prove that for a given electronic density, the external potential is uniquely determined, which in turn determines the wavefunction of the system.

This was further developed by Kohn and Sham[78]. They proposed using the kinetic energy of a non-interacting electron gas, instead adding the interaction part to the exchange-correlation term defined previously. This leads to a very simple Hamiltonian for this non-interacting reference system, which is given in equation (3.5). Here the external potential is defined as the potential which reproduces the density of the real, interacting system. This Hamiltonian operates not on the full many-body wavefunction, but on one-electron pseudo-wavefunctions, which in total reconstruct the full density. This gives rise to the Kohn-Sham equations, shown in equation (3.6), which are a series of eigenvalue equations of the Hamiltonian in equation (3.5) acting on the various one-electron pseudo-wavefunctions.

$$\mathcal{H}_R = \sum_{i=1}^{N} \left(-\frac{\hbar^2}{2m} \nabla_i^2 + v_R(\mathbf{r}_i) \right) \tag{3.5}$$

$$\mathcal{H}_R \phi_i = \epsilon_i \phi_i \tag{3.6}$$

The density can then be constructed from the one-electron pseudo-wavefunctions, allowing the full energy to be calculated from equation (3.7). The energy is now a function of the density, where the first three terms of equation (3.7) can be calculated exactly, while all approximations are collected in the final term. The first term is the electrostatic energy of the electrons due to the external potential, the second term is the kinetic energy of the reference system of non-interacting electrons, the third term is the classical electrostatic energy of the electronic charge distribution and the fourth term includes the quantum mechanical exchange and correlation effects.

$$E[\rho] = E_{ext}[\rho] + T_R[\rho] + U_H[\rho] + \tilde{E}_{XC}[\rho] \tag{3.7}$$

However, it is not possible *a priori* to determine the external potential which results in the correct electron density. It is therefore necessary to solve equation (3.6) iteratively, where the density is constructed from the one-electron wavefunctions using equation (3.8). This density is then used to determine the external potential, which is put into equation (3.6) until the results are self-consistent to the specified precision.

$$\rho(\mathbf{r}) = \sum_{n=1}^{N} |\phi(\mathbf{r})|^2 \tag{3.8}$$

3.3 Exchange-Correlation functionals

As described above, all the approximations in the calculation of the total energy of the system are collected in the exchange-correlation term, which is also defined as a functional of the density. The overall accuracy of DFT is thus dependent on good approximations of the exchange-correlation term. While there are a very large number of available functionals, most of them can be divided into a few categories depending on the basic strategy used to construct them. This was presented using a Jacob's Ladder analogy by Perdew and Schmidt[79], ranking various models based on their accuracy. I will present some of the most widely used categories below.

3.3.1 Local Density Approximation (LDA)

The simplest approximation is to use the exchange-correlation energy of a homogeneous electron gas, with a density corresponding to the density at the point in question. Thus the exchange-correlation energy is calculated as if the electronic density is everywhere locally homogeneous. The exchange-correlation energy for the homogeneous electron gas is known to good accuracy. This is a very simple, but also very rough approximation. It is known to give excellent values for lattice constants in solids, but this is due to some rather fortunate error cancellation. It is therefore not a reliably good approximation, especially for non-homogeneous systems. In the LDA, the exchange-correlation energy is calculated using equation (3.9).

$$\tilde{E}_{XC}^{LDA}[\rho] = \int \rho(\mathbf{r})\tilde{\epsilon}_{XC}^{LDA}[\rho(\mathbf{r})]d\mathbf{r} \tag{3.9}$$

$$\tilde{\epsilon}_{XC}^{LDA}[\rho] = \epsilon_X^{LDA}[\rho] + \tilde{\epsilon}_C^{LDA}[\rho] \tag{3.10}$$

The exchange-correlation energy density $\tilde{\epsilon}_{XC}^{LDA}[\rho(\mathbf{r})]$ is found through equation (3.10). The reader may consult equations (5.1) and (5.2) in reference [76] for the precise expressions of the two terms if so inclined.

3.3.2 Generalised Gradient Approximations (GGAs)

The natural progression from the LDA is to include also the gradient of the density, which is the starting point for the GGAs. They are usually generated by making an expansion in the gradient and then imposing some of the known exact conditions in order to find the coefficients of the expansion. The general form is akin to the one for the LDA in equation (3.9), and is shown in equation (3.11). Here the enhancement factor F_{XC} is a functional of the gradient expansion, which should go to one for the homogeneous electron gas, as the LDA should be recovered in this limit. ϵ_{XC} can be chosen in many ways depending on the exact exchange-correlation functional, but will often be close to the LDA expression shown earlier.

$$E_{XC}[\rho] = \int \rho(\mathbf{r})\epsilon_{XC}[\rho(\mathbf{r})]F_{XC}[\rho(\mathbf{r}), \nabla\rho(\mathbf{r})]d\mathbf{r} \tag{3.11}$$

As not all of the exact conditions can be fulfilled at the same time, a lot of different GGA's have been constructed, with various sets of exact constraints. This is mostly done in order to optimize the functional for a specific class of systems, usually worsening the description of others. This has led to a very large number of available GGA functionals, most of them optimised with a specific set of criteria in mind.

3.3.3 Specific GGA functionals

All exchange-correlation functionals used in this thesis are of the GGA variety and in this section I will give a short introduction to each of them.

PBE

PBE[80] was constructed to satisfy as many formal properties and limits, known from the exact theory, as possible. This makes it a functional with a solid theoretical grounding and no fitting parameters, and has also resulted in a well-performing and generally applicable functional, as evidenced by the more than 40,000 citations of the original paper.

BEEF-vdW

BEEF-vdW (Bayesian Error Estimation Functional - van der Waals)[81] is a very recent GGA exchange-correlation functional designed to minimise the total errors on a variety of material properties. Most notably, it breaks the so-called GGA-line, which is a connection between the descriptions of chemisorption properties and surface energies. This means that you generally cannot optimise one without sacrificing accuracy in the other when using a GGA functional. This is illustrated in figure 3.1. This line also shows why some GGA functionals have been optimised with a specific set of properties in mind, as none of them are close to the experimental point on both axes. This functional also includes a vdW-component, which allows it to describe van der Waals interactions, which are otherwise not included in the semi-local GGA description.

A second feature of this functional is the capacity for error estimation. The BEEF-vdW functional is based on the best fit to a number of properties, but also includes a large ensemble of alternative functionals. In this way it is possible to compute error bars for a given property, showing how sensitive it is to the exact choice of exchange-correlation functional. These are also shown on figure 3.1.

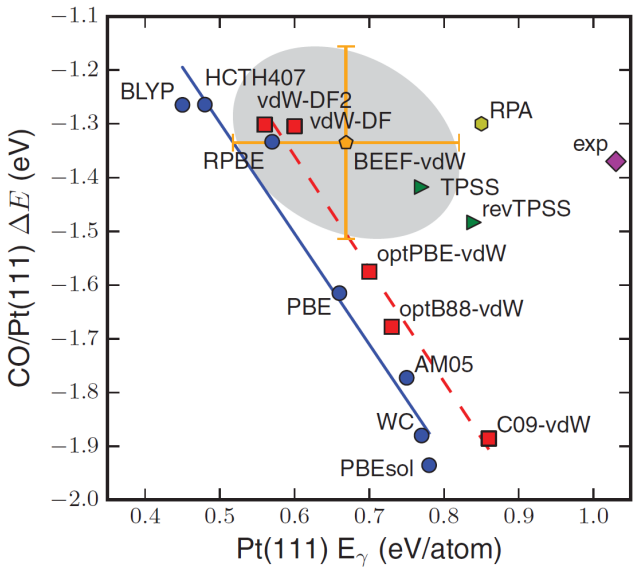

Figure 3.1: *Plot of CO adsorption energy on Pt(111) vs. the surface energy of the Pt(111) surface. Values calculated with GGA functionals are blue, GGA-vdW-functionals are red, meta-GGA are green and RPA (Random Phase Approximation) is yellow. The orange point with error bars is the BEEF-vdW functional. The experimental point is purple. Reproduced from reference [81].*

RPBE

RPBE[82] is a PBE-like functional which has a slightly different enhancement factor in order to improve the description of chemisorption. As can be seen from figure 3.1, it has succeeded in this, but at the cost of an even worse description of surface energies as compared to the original PBE. It is definitely more of a niche functional compared to PBE, with a little more than 2,500 citations of the original paper.

PBEsol

PBEsol[83] is optimised in the opposite direction of RPBE, aiming to describe lattice constants and surface energies as accurately as possible. However, as can be seen from figure 3.1, this comes at the cost of a large error in the adsorption energies, and the surface energies are still too small compared to experiment. However, if the system is a solid, PBEsol should be significantly more accurate than standard PBE. It is also a niche functional compared to PBE, with a little more than 1,100 citations, but at only 7 years old, it might very well increase in popularity in the future.

3.3.4 Beyond GGA

While GGA exchange-correlation functionals are used in a large portion of present DFT calculations, more advanced exchange-correlation functionals are gaining ground. One such class of functionals is the meta-GGA, where further terms in the gradient expansion is taken into account[84]. This gives improved general accuracy, but also somewhat decreased computational performance, depending on implementation.

A different way to go beyond standard GGA is to replace a fraction of the exchange part with exact Hartree-Fock theory, leading to a so-called hybrid functional[85]. In this way the

exchange-correlation term will be given by equation (3.12). However, it has not yet been established what the optimum way of determining α is, leaving it an arbitrary or fitting parameter, giving a large number of functionals building on different philosophies.

$$E_{XC}^{hyb} = \alpha E_X^{HF} + (1-\alpha)E_X^{DFT} + E_C^{DFT} \tag{3.12}$$

3.4 DFT in practice

I have now presented the overall strategy of solving the Schrödinger equation, and will continue with some matters that must be dealt with before the above solution can be implemented in practice. All DFT calculations presented in this project have been made with the GPAW code[86, 87] in the ASE framework[88].

3.4.1 Treating the core electrons - the PAW formalism

So far, we have been treating all electrons equally and fully. However, most of the time only the valence electrons interact with the environment around the atom, while the core electrons are so tightly bound that they are unaffected by the chemical environment. In most cases it is therefore not necessary to treat them explicitly, which can save a lot of time, especially for elements with high atomic numbers.

There are mainly two ways to do this today, and both of them work by replacing the core electrons with their aggregated influence on the valence electrons. One such method is ultrasoft pseudopotentials[89] and the other is the Projector Augmented Wave (PAW) formalism[90, 91]. As GPAW uses the PAW method to treat the core electrons, I will not go further into pseupotentials, but go into more detail with the PAW method below.

The main idea of the PAW method is to split space into two regions: augmentation spheres centred on each atom, and the interstitial region between the atoms. It then defines pseudo (PS) wavefunctions that are identical to the true (Kohn-Sham) one-electron wavefunctions outside the augmentation spheres, but smooth inside, where the true wavefunctions exhibit strong oscillations due to the strong potential from the nucleus. The expression linking the true all-electron (AE) wavefunction with the PS wavefunctions is shown in equation (3.13). Here $|\Psi\rangle$ is the AE wavefunction, $|\tilde{\Psi}\rangle$ is the PS wavefunction, $|\phi_i\rangle$ are partial waves of the AE wavefunction, $|\tilde{\phi}_i\rangle$ are partial waves of the PS wavefunction and $\langle\tilde{p}_i|$ is a projector function for the corresponding PS partial wave. Generally two partial waves for each angular momentum is sufficient, and having a few more actually leads to undesired ghost states. The AE and PS partial waves corresponding to the same electron coincide outside the augmentation sphere. The partial waves are only different inside the augmentation sphere, so the equation uses this difference and the projector functions to make the transformation from the PS wavefunction to the AE wavefunction around the nucleus.

$$|\Psi\rangle = |\tilde{\Psi}\rangle + \sum_i \left(|\phi_i\rangle - |\tilde{\phi}_i\rangle\right)\langle\tilde{p}_i|\tilde{\Psi}\rangle \tag{3.13}$$

The AE partial waves are found by radial integration of the Schrödinger equation inside the augmentation sphere, while it is assumed that the potential here is spherically symmetric. Another notable approximation that is often invoked, is that the core electrons are treated as a frozen core, meaning that they behave in the same way, no matter which environment the atom is placed in. It is very important to note that due to the transformation between the PS and AE wavefunctions described above, the PAW method provides access to the true (Kohn-Sham) wavefunctions, in contrast to pseudopotential methods.

3.4.2 Spin polarization

In order to treat magnetic systems containing spin-polarized electrons, the density is divided into two independent parts, as shown in equation (3.14). These two densities are then treated separately, leading to a doubling of computing time, but no other fundamental changes in the treatment of the problem, though it does lead to a few practical complications, which I will not go into detail with.

$$\rho = \rho_{\uparrow} + \rho_{\downarrow} \tag{3.14}$$

3.4.3 Solving the Kohn-Sham equations in practice

In order to actually solve the Kohn-Sham equations, the wavefunctions need to be represented in some way. In this subsection I will introduce the three modes which have been used in this project and are all available in the GPAW code. They each have some different advantages and disadvantages, meaning they are not equally well suited to all systems, and it is beneficial to take the specific system into account when choosing calculational mode. There are of course many more technical details in actually doing the calculations, which are described on the webpages of the various DFT codes.

Plane waves - PW mode

The traditional way of solving the Kohn-Sham equations is by using an expansion of plane waves to represent the wavefunction. This is a natural choice for solids, whose natural periodicity lends itself well to this description. Using a plane wave basis set, it is possible to systematically improve the accuracy by increasing the size of the basis set. However, parallelization is not as straightforward or efficient as for the methods discussed below, making plane waves unwieldy for large systems.

Linear Combination of Atomic Orbitals - LCAO mode

Instead of expanding the wavefunction in plane waves, it is also possible to expand it in local atomic orbitals. As the basis sets require some construction by hand, it is not as simple to achieve systematic improvement of the accuracy as for the PW method. The implementation in GPAW is described in reference [92]. It is usually a good deal faster than the other methods described here, but it does suffer from accuracy issues under some circumstances, such as adsorption. More details can be found in the reference.

Finite Difference - FD mode

A very different way of approaching the problem, is to simply represent the wavefunctions on a real-space grid and solve numerically. The accuracy is determined by the fineness of this grid, but due to the grid points moving in space depending on the exact number of points, the energy will not change monotonically as can be seen for the PW method when the basis set is expanded. Another issue is that the energy of the system will depend very slightly on the configuration of the system with regard to the grid, known as the eggbox effect. However, it is much easier to parallelize, as the grid can simply be divided into several domains which are then distributed among the available CPU cores. The introduction of this method of solving the Kohn-Sham equations was the original reason for the introduction of the GPAW code.

3.5 Chapter summary

In this chapter I have introduced the basic theory of Density Functional Theory and some of the exchange-correlation functionals and calculational modes which are available in the GPAW code. Both exchange-correlation functionals and calculational modes have different properties, and some are thus more suited than others to a specific system. In later chapters I will explain my choice in relation to the systems investigated in that specific chapter.

Chapter 4

Correlation between diffusion barriers and alloying energy in binary alloys

As detailed in section 2.4, it has previously been assumed that a very negative alloying energy, indicating a very stable alloy, provides better stability under harsh conditions, such as the operating conditions for the Oxygen Reduction Reaction (ORR) in a Polymer Electrolyte Membrane Fuel Cell (PEMFC). This assumption is also known from the so-called Ni_3Al "superalloys", where a large diffusion resistance contributes to reducing creep formation, which would limit the lifetime of the turbine blades in jet engines[93].

In this chapter we will investigate this assumption further, by looking at whether or not there is a correlation between a high alloying energy and diffusion barriers in alloys.

4.1 Methods

First off, we assume that the relevant transport mechanism for the minority element from the bulk of the alloy to the surface is diffusion. The electrolyte is unlikely to interact directly with atoms below the surface layer[94]. Normally, diffusion in metals take place along dislocations or grain boundaries, and there is no reason to believe this is not the case in the alloys presented in this work. However, we take the view that any trend found in defect-free, single-crystalline systems, will also apply in more realistic situations. Additionally, commercial Pt-based catalysts are often crystalline, in which case bulk vacancy diffusion is the most relevant process.

Most of the alloys in this work has the $L1_2$ structure, which is one of the simplest possible structures for alloys. It is simply an FCC structure with one atom changed to another element. Even so, modelling the full diffusion process is computationally very expensive, and we only do this for a small number of alloys. We then show that the barrier is correlated with a specific energy along the path, which can be calculated an order of magnitude faster than the full barrier.

We investigate vacancy diffusion where a minority atom is replaced by a vacancy. A certain number of vacancies will always exist due to entropy, but we also expect some number of vacancies to be created due to the reaction conditions. The simplest possible complete path consists of six steps before the crystal is returned to the initial state, taking translational symmetry into account. Our proposed path is shown on the left in figure 4.1. We note that the path is symmetric and the steps are pairwise mirror images of each other.

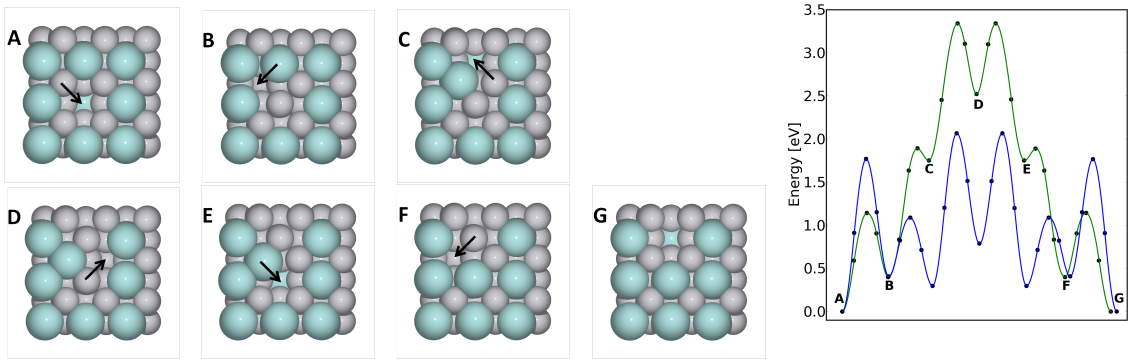

Figure 4.1: *The overall diffusion path. On the left we show, for each step along the path, a top view of the computational unit cell, which has a depth of two crystal unit cells. Here is shown Pt_3Y specifically, but it is equivalent for all alloys. To the right, the energy along the diffusion path is shown for both Pt_3Y in green and for Pt_3Cu in blue, calculated with the Nudged Elastic band method (NEB).*

We calculated the barrier for each step using the Nudged Elastic Band (NEB) method[95–99], which is detailed in section 4.1.1. The total barrier is then simply the energy difference between the initial configuration and the transition state with highest energy along the path. We show two examples of the energy along the path on the right of figure 4.1. The end points were relaxed initially, and their geometries were locked during the NEB calculation, which then structurally relaxed the intermediate points under constraints.

The calculations were done using DFT in the LCAO mode with the PBE exchange-correlation functional. LCAO allowed us to save a significant amount of computational time, and has been shown to be very accurate for structural geometries[92]. We chose the PBE functional due to its good all-round properties. For further calculational details see the attached paper and for explanations of the various abbreviations see chapter 3.

As mentioned before, the full path is demanding to calculate, so we initially did it for a small set of alloys, chosen to be diverse with regard to alloying energy and lattice parameter. We expected those two parameters to be the most important for describing the diffusion process. The alloying energy describes the strength of the atomic interactions and the lattice parameter describes the geometric space along the path.

When atoms diffuse across a surface it is often seen that concerted motion of several atoms results in a lower barrier[100, 101]. We tested if the same could happen in our case, by using the NEB method to calculate the full path from configuration A to D in one go, with simultaneous motion of the three involved atoms as the initial guess. As this calculation is very demanding to carry out, we did it for Pt_3Y and Pt_3Cu only, chosen because they have very different alloying energies and lattice parameters. In both cases the calculation split the motion into the three elemental steps we were already considering, validating this approach.

Finally, we also investigated the direct diffusion path, where the minority atom moves directly from its initial position to the vacancy. This corresponds to going directly from configuration A to G without the accomodative motion of the Pt atoms. This involves an obvious geometric restriction and we would expect this path to be relevant for only the smallest of atoms. It turns out that even for these, the barrier is much greater than for the longer path detailed above. For Pt_3Cu the barrier for this motion is found to be 3.641 eV compared to 2.067 eV for the 6-step path. Due to the exponential dependence of the rate on the barrier, this alternative path is very unlikely, even at elevated temperatures.

4.1.1 Nudged Elastic Band

The Nudged Elastic Band method (NEB) is a method designed to find the path between two known configurations of a system of atoms, including the saddle point on the potential energy surface, which is the maximum on this path. It was originally described by Mills et al. [95–97] with later additions by Henkelman et al. [98, 99] and Smidstrup et al. [102], though the latter improvement is too recent to have been used in this work.

The NEB method requires knowledge of the configuration in the two endpoints, which will normally be local minima, such as the reactants and the products of a reaction. The algorithm then creates a series of intermediate configurations, called images, between the two endpoints. These are connected by fictive spring forces, ensuring that they can be relaxed without dumping down into one of the two minima. This spring force also replaces the parallel component of the true force, leaving only the component of the true force which is orthogonal on the path. The force on each image is given by equation (4.1), where the spring force is defined in equation (4.2) and the orthogonal component of the true force is shown in equation (4.3). $\hat{\tau}_i$ is a unit vector in the direction of the path for image i.

$$F_i = F_i^s|_{\parallel} - \nabla V(R_i)|_{\perp} \tag{4.1}$$

$$F_i^s|_{\parallel} = k(|R_{i+1} - R_i| - |R_i - R_{i-1}|)\hat{\tau}_i \tag{4.2}$$

$$\nabla V(R_i)|_{\perp} = \nabla V(R_i) - \nabla V(R_i) \cdot \hat{\tau}_i \tag{4.3}$$

One of the improvements by Henkelman et al. was to introduce the so-called "climbing image" to the NEB algorithm. In the original formulation, the images were spaced evenly along the path, and there was no guarantee that one of them would coincide with the saddle point itself, necessitating interpolation. The "climbing image" modification solves this by selecting the image which is believed to be closest to the saddle point, removing the spring force, and then reversing the force component parallel to the path. In this way, the image will be dragged up to the saddle point, ensuring that it is sampled directly. The force on the specific image, usually chosen to be the one with the highest energy, is then replaced by the one shown in equation (4.4).

$$F_{i_max} = -\nabla V(R_{i_{max}}) + 2\nabla V(R_{i_{max}})|_{\parallel} \tag{4.4}$$

4.2 Results

We calculated the full barrier for eight alloys, and pure Pt, which we show in figure 4.2 as they relate to the alloying energy and the lattice parameter of the alloys. There is a clear correlation in both cases, which is not so surprising as both of them vary systematically through the periodic table, meaning that they correlate with each other. It is thus difficult to conclude from this small dataset whether one or the other is the better descriptor for the diffusion barrier. However, generating a very large dataset of diffusion barriers is too computationally expensive.

This means that a simpler descriptor is needed in order to increase the size of the dataset significantly. Looking at figure 4.1 it seems that the energy difference between configuration A and D is a possible descriptor, as the barriers of the individual steps are about the same height, but the intermediate minima have very different energies for Pt_3Y and Pt_3Cu. This scaling of the barrier with the difference in energy between the states is known as a Brønsted-Evans-Polanyi relation, and it is well-known in chemistry[103, 104]. We have plotted the barriers versus this energy difference, $E_{A\to D}$, in figure 4.3.

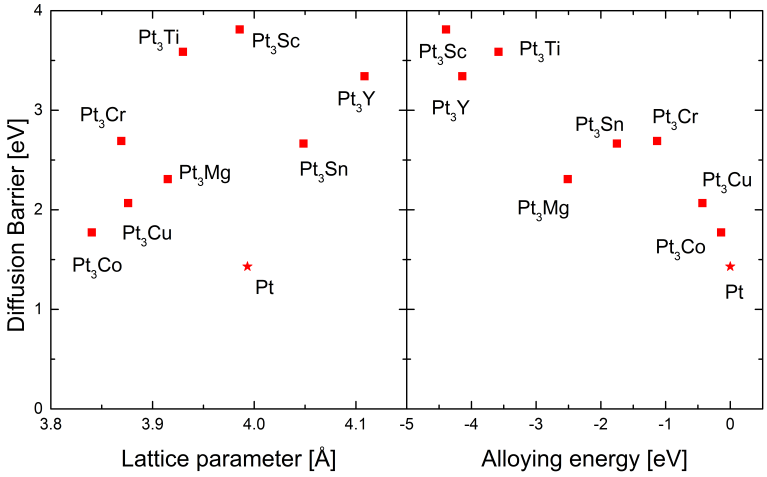

Figure 4.2: *Plot of the total barrier height vs. the lattice parameter of the alloy (left) and the alloying energy (right).*

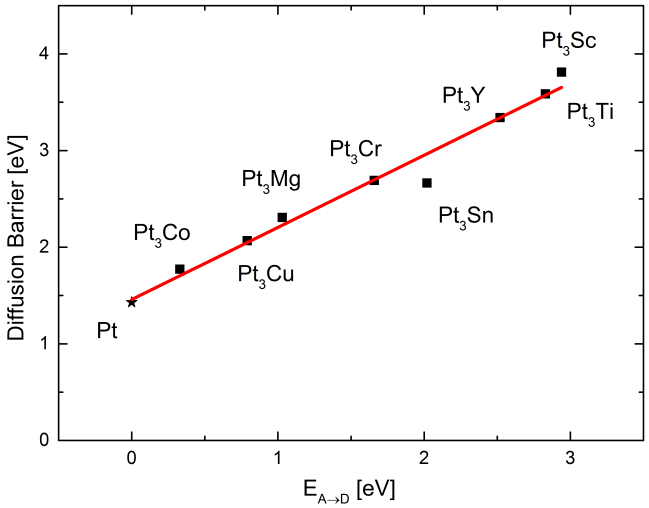

Figure 4.3: *The barrier height as a function of the energy difference between the initial and middle configurations on the diffusion path. These are shown as A and D in figure 4.1. The red line is a best linear fit with a slope of* 0.75 ± 0.04 *and an intercept of* 1.46 ± 0.08 *eV. It is seen that the correlation is very clear, indicating that this energy difference is a good descriptor for the barrier.*

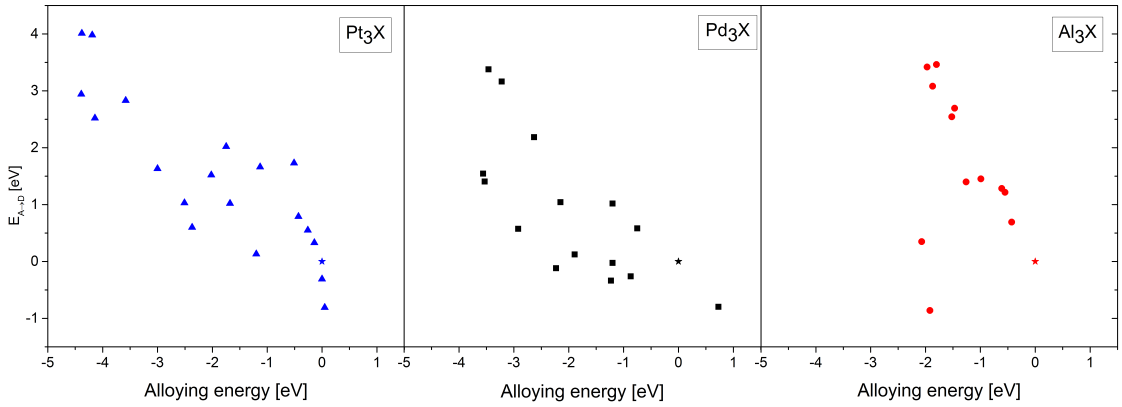

Figure 4.4: *The energy difference describing the diffusion barrier correlated with the alloying energy for Pd_3X (squares), Al_3X (circles) and Pt_3X (triangle) alloys. The autodiffusion for each main element is shown as a star and is by definition zero in this plot. In all three cases, we see a clear correlation. The outliers in the Al_3X set are Al_3Ir and Al_3Pt.*

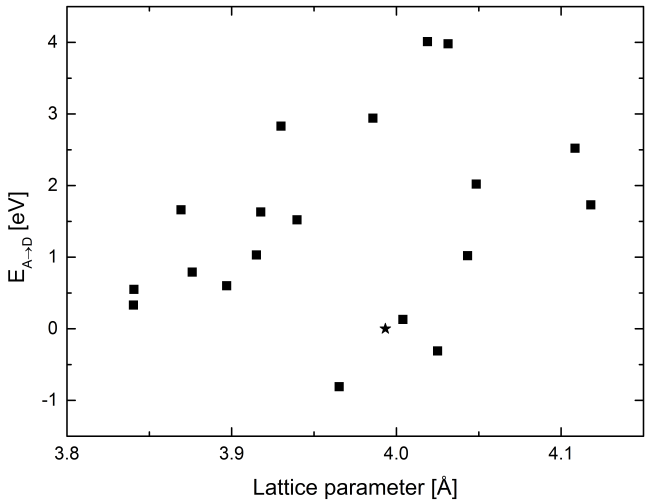

Figure 4.5: *The energy difference $E_{A\to D}$ vs. the lattice parameter of the alloy for Pt_3X alloys. Autodiffusion in Pt is included as a star-shaped point.*

It is seen that $E_{A\to D}$ is a very good descriptor for the full barrier, while being more than an order of magnitude faster to calculate. This is because a lot of energy is gained from the interaction between the two elements in the very stable alloys, and so there is also a prohibitive energy cost associated with breaking this arrangement. We therefore calculated $E_{A\to D}$ for a large number of Pt_3X alloys, where the results are shown in figures 4.4 and 4.5.

It is seen from the left-most part of figure 4.4 that there is clearly a correlation between the alloying energy and $E_{A\to D}$ for Pt_3X alloys, showing that more stable alloys also have higher diffusion barriers. However, there is also a definite amount of scatter, indicating that other parameters also have a significant impact on the diffusion barrier. Even so, the correlation with the alloying energy is strong enough to allow this property to be used as a predictor for diffusion barriers. We note that self-diffusion is included as star-shaped points.

Figure 4.5 shows the relationship between $E_{A\to D}$ and the lattice parameter for Pt_3X, and exhibits much less correlation than figure 4.4, indicating that the influence of the lattice

parameter on the diffusion barrier is much smaller than for the alloying energy. However, it seems there is a division into two groups, and closer inspection of the alloys indicate that this might indeed be the case. The small group in the lower right comprises Pt alloyed with Ag, Cd, Hg, In, Pb, Sn, and Y, as well as pure Pt. All of these, apart from Y, belong to a group of metals in the 4^{th} and 5^{th} rows, spanning the end of the transition metals and the early p-block metals. The other group includes Cu, Ga, Ni and Zn, indicating a clear division between the 3^{rd} and 4^{th} rows.

In order to ascertain whether the observed correlation between the alloying energy and $E_{A\to D}$ is limited to Pt, we calculated $E_{A\to D}$ and alloying energies for a number of Pd_3X and Al_3X alloys. These elements were chosen because Pd is chemically similar to Pt, while Al is not, and both of them form a significant number of 3:1 alloys. We investigated alloys which either have the $L1_2$ structure, or something very similar, in the sense that the local order is the same, while the overall order is different. This is similar to the difference between hcp and fcc, where the nearest neighbour environment is the same, but the next-nearest neighbours are arranged differently in the two structures. In all cases the calculation is done with the $L1_2$ structure, as for Pt. These results are shown in figure 4.4. Both series show correlation between the two properties, though Al_3X also exhibits two clear outliers in Al_3Ir and Al_3Pt. These two minority elements are closely related, indicating that there might be some unknown effect in their interaction with Al.

4.3 Discussion

This work deals with one of the simplest ordered structures for alloys, but we speculate that the relation between alloying energy and diffusion barrier is a general principle. There is no obvious reason why it should be dependent on the exact crystal structure, though the exact strength of the correlation may vary. It is similar to the well-known correlation between the melting point of a pure metal and its barrier for auto-diffusion[93].

These results are consistent with the experimental work of Johansson et al.[105] and Schumacher et al.[106]. They investigated the behaviour of Y and Cu, respectively, at elevated temperatures, when deposited on a single-crystalline Pt(111) substrate. The experiments were carried out under ultra-high vacuum, and they saw that Y diffused into the surface at 800 K[105], while Cu diffused into the surface already at 460 K[106]. In both cases the substrate is pure Pt instead of an alloy, meaning that the lattice parameter is not affected by the minority element, which could cause an additional geometric contribution when compared to our results. A third example from a different group is the experiment by Tang et al.[107] for Ce on Pt(111), where they found that Ce alloyed with Pt at 770 K. However, it is not clear if the process started at a lower temperature. Ce-Pt has an alloying energy which is very close to Y-Pt, and the two should have similar behaviour according to our results.

We portray the overall dissolution process, specifically for a Pt alloy under fuel cell conditions, in figure 4.6, with energies to scale. Before the minority element can dissolve into the electrolyte, it needs to be transported through the bulk of the alloy and through the Pt overlayer to the surface where it can interact with the electrolyte. The exact structure of the overlayer is currently not well understood and thus the exact process of diffusion through the overlayer and dissolution at the surface is beyond the scope of this study. Nevertheless, we anticipate that the diffusion barriers in the bulk are equal to or greater than the barrier for transport to the surface and subsequent dissolution[94]. Due to the initial dissolution process, we expect the near-surface region to have a higher degree of disorder compared to the bulk, which could enhance diffusion rates in this region. The diffusion barrier in the bulk

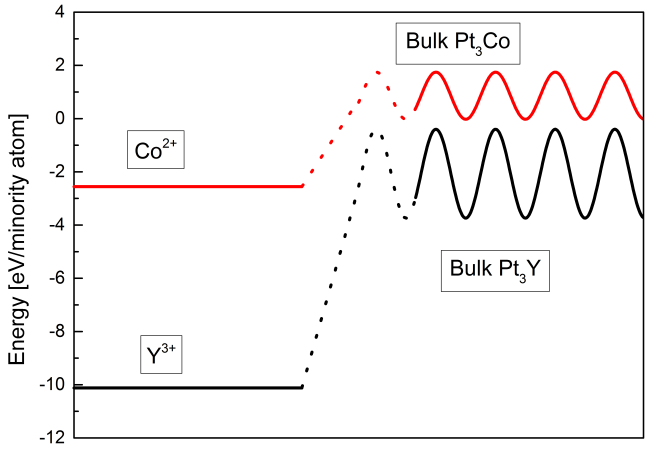

Figure 4.6: *Schematic overview of the energetics of the dealloying process in a PEM fuel cell with an electrode potential of 1 V vs. RHE (Reversible Hydrogen Electrode). The focus of this work is the diffusion energy barrier in the metal. The energy barriers in the alloy, and the energy difference between the alloy and the dissolved atom are shown to scale. The energies of intermediate configurations relating to the dissolution process itself and passage through the near-surface region are unknown, as indicated by the dotted part of the lines. Everything else is under standard conditions with the standard reduction potential from reference [108].*

of the alloy provides it with kinetic stability, despite thermodynamics favouring dissolution. We have shown that this barrier correlates with the alloying energy, making alloys of Pt and early transition metals more stable towards diffusion-related degradation than alloys of Pt and late transition metals. This indicates that they should show at least the same level of stability under operating conditions, despite the greater driving force for dissolution.

4.4 Chapter summary

We have shown that the barrier for vacancy diffusion of the minority element in Pt_3X, Pd_3X and Al_3X alloys correlate with the alloying energy of the alloy. This validates the use of the alloying energy as a key parameter when searching for alloys that are stable against diffusion related degradation. A central example is the discovery of Pt_3Y and Pt_5Y alloys as electrocatalysts for the oxygen reduction reaction in fuel cells[59, 60], where Pt_3Y was predicted to be active while having a large alloying energy, and subsequently shown in electrochemical experiments to be both active and stable. In this case a protective overlayer of pure Pt is formed at the surface of the alloy, limiting the dissolution of the minority element. A high alloying energy turns out to be more important than the thermodynamic driving force for oxidative corrosion of the minority element. This is because the diffusion of the alloying element to the surface is kinetically hindered by the large diffusion barrier.

Experimental alloying energies are known for many compounds, and can be calculated relatively easily and accurately for new materials[109]. Consequently, we confirm the notion that the alloying energy will be useful as a key search parameter when searching for new alloys for applications where the diffusive stability of the alloy is of importance.

Chapter 5

Interplay between adsorption and stability properties of surfaces

When discussing how a metal surface can be used as a catalyst, there are two properties which are very significant for its operation. How the surface interacts with the reactants, intermediates and products, which determines the activity and selectivity, and how stable the surface is under reaction conditions. If the surface is not stable under reaction conditions, it can be very difficult to determine what the catalytically relevant surface is, and that is essential for calculating the relevant adsorption properties. Neglecting this effect could lead to the design of a catalyst which quickly becomes inactive after exposure to reaction conditions.

In this chapter, I will present our work on describing how these two effects, separately and together, affect Pt_3M alloys with a single surface layer of pure Pt. This Pt skin structure is well-known for several catalytically interesting alloys[65, 110, 111].

We have been particularly interested in determining whether there are any fundamental correlations between these two properties, setting a limit on the skin stability which is achievable for a given set of adsorption properties. This could be interesting to the catalyst research community as it would limit the parameter space necessary to search when looking for new catalysts.

We used Density Functional Theory (DFT) to calculate the adsorption energy for different elements on the surface of different Pt_3M alloys, where M is either a transition metal, a p-block metal or Mg. In all cases the top layer is pure Pt, and the adsorption properties are thus modified by both a strain effect due to the lattice constant of the alloys and a ligand effect due to the minority element of the alloy. The effects were introduced in section 2.3, and will be presented further below.

5.1 Strain and ligand effects

In this section we will follow up on the introduction of strain and ligand effects in section 2.3, going into more detail with how they affect each other. Due to their importance for catalytic effects, a lot of effort is currently spent on trying to understand them in more detail. We will mention a few recent examples specifically, starting with strain effects. Du et al. used a NiTi shape memory alloy to study the catalytic activity of a specific Pt sample under both compressive and tensile strain[112]. Sethuraman et al. used in situ stress measurements to correlate the activity of a dealloyed PtCu sample directly to the strain under reaction conditions[113]. Yang et al. used mechanical strain on a PdCuSi metallic glass to investigate the catalytic activity of the Pd-rich surface as a function of strain[114]. Regarding the ligand

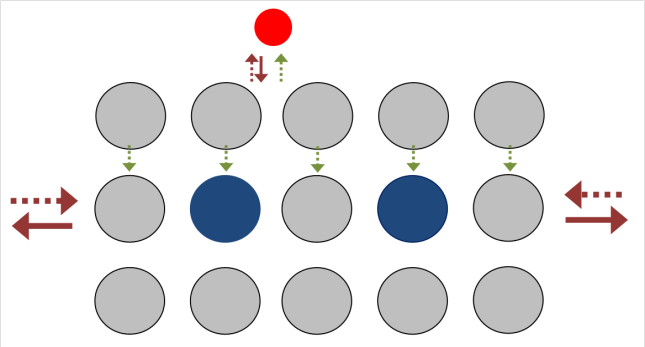

Figure 5.1: *Sketch of a system being affected by both strain and ligand effects. The red arrows indicate the strain effect, while the green arrows represent the ligand effect. Reproduced from reference [118].*

effect, in 2012, Calle-Vallejo et al. showed that counting the number of valence electrons was a good measure for the ligand effect in the investigated alloy-like model system[44]. A year earlier, Stephens et al. made experimental observations of the ligand effect using a Pt/Cu near-surface alloy, using only about a monolayer of Cu[33], which was followed up by Bandarenka et al. in 2012[115].

When alloying Pt with other metals, it is to be expected that both of the above effects will occur simultaneously, in a situation as shown in figure 5.1. In this case we can expect the two effects to interact, complicating the situation. In contrast, all of the examples mentioned in the previous paragraph focused on isolating either the strain or the ligand effect, in order to study it in more detail. An early attempt to deconvolute the two effects were made by Schlapka et al. in 2003, using Pt thin films of varying thickness on a Ru substrate, studying the adsorption energy as a function of film thickness[116]. The following year, Kitchin et al. used DFT to study both strain and ligand effects in monolayers of Ni, Pd and Pt on other transition metals[117]. Based on this, we take the view that the strain effect is fairly well understood, while the ligand effect and their interplay has only been well-described in model systems.

5.2 Methods

Some initial work on studying the relation between skin stability and adsorption was done by A. K. Jepsen[118], and the basic method is described therein. However, there are some changes between this preliminary work, and the work presented here, so we will describe my methods in detail below.

Platinum is a material that is interesting for a lot of catalytic applications and forms alloys with many transition metals. We have therefore used this as our starting point. Most of the alloys form the $L1_2$ structure, and in order to study trends, we have used this structure in all cases. Both the $L1_2$ structure and bulk Pt in the fcc structure can be seen in figure 5.2. Five different adsorbates in two different sites were used, in order to determine if there were any adsorbate- or site-specific effects. We have used C, H and O in the fcc site, as well as CO and OH in the ontop site. Our choice of adsorbates partly reflects the overall goal of modelling the ORR, and partly a desire to have a broad range of relevant adsorbates.

(a) **(b)**

Figure 5.2: *a) Bulk Pt_3Y in the $L1_2$ structure and b) bulk Pt. Both are a 3x3 supercell.*

5.2.1 Calculational details

All the calculations in this chapter has been done with the BEEF-vdW functional, as it gives the best compromise between surface and adsorption energies among the GGA functionals, as described in section 3.3. All calculations have made use of the setups and basis sets distributed as GPAW setups 0.9.11271 and used a Fermi temperature of $k_BT = 0.1$ eV, with the results extrapolated to 0 K.

All calculations involving strained Pt have been done with the PW mode, as the incremental strain makes them especially susceptible to the eggbox effect. We used an energy cutoff of 1000 eV in all cases, with a 10x10x10 Monkhorst-Pack k-point grid[119] for bulk Pt in the orthorhombic cell and 8x8x1 for the 2x2 Pt(111) slabs.

All calculations involving alloys, including reference calculations with pure Pt with the equilibrium lattice constant, used the FD mode and were spin-polarized. For the bulk alloys we used a 10x10x10 k-point grid and a 40x40x40 real-space grid. For the alloy slabs we used an 8x8x1 k-point grid and a grid spacing of 0.15 Å.

5.2.2 Stability

While activity is usually the most interesting property of a new catalyst material, stability is also of great importance if the material is to have any practical significance. It is therefore relevant to determine if the stability and activity properties have any relationship.

We define the stability as the energy which is gained by terminating a slab with pure Pt instead of one more layer of the alloy, with bulk Pt and the bulk alloy being used as the reference. The 111-planes of the $L1_2$ structure are all equivalent. This means we can calculate the stability of the overlayers using equation (5.1). A negative number means Pt atoms would prefer forming this skin compared to aggregating as bulk Pt somewhere else, while a positive number shows the opposite.

$$E_{skin} = E_{slab,Pt/Pt_3M} + E_{bulk,Pt_3M} - E_{slab,Pt_3M} + E_{bulk,Pt} \tag{5.1}$$

Here E_{skin} is the energy of the skin with reference to bulk Pt, $E_{slab,Pt/Pt_3M}$ is the energy of the alloy slab with a Pt overlayer, E_{bulk,Pt_3M} is the bulk energy of the alloy, E_{slab,Pt_3M} is the energy of the pure alloy slab and $E_{bulk,Pt}$ is simply the bulk energy of equilibrium Pt. The atomic configurations corresponding to $E_{slab,Pt/Pt_3M}$ and E_{slab,Pt_3M} are shown in figure 5.3, E_{bulk,Pt_3M} in figure 5.2a, and $E_{bulk,Pt}$ in figure 5.2b.

In this case it is quite straightforward to correct the stability for strain, in order to isolate the influence of the ligand effect on the stability of the Pt skin. We calculate the difference

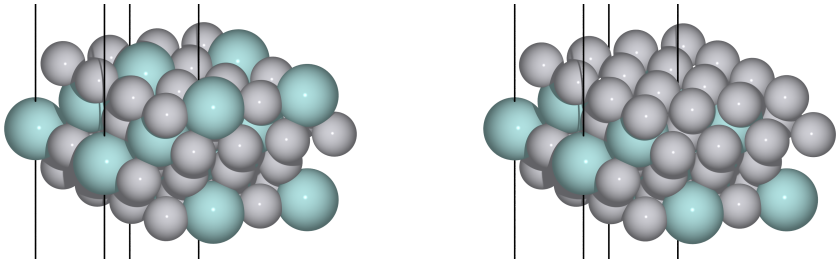

(a) **(b)**

Figure 5.3: *a) Pt alloy slab without Pt skin, corresponding to the term E_{slab,Pt_3M}. b) Pt alloy slab with Pt skin, corresponding to the term $E_{slab,Pt/Pt_3M}$. The black lines are the corners of the computational unit cell.*

between bulk Pt with the lattice parameter of the alloy and bulk Pt with the equilibrium lattice constant, and denote it $\Delta E^{corr}_{bulk,Pt}$. We then simply add this correctional term to the previously calculated skin energy, as shown in equation (5.2). We need to do it this way as all calculations with alloys, as well as the original $E_{bulk,Pt}$ term, are calculated using FD mode, while all calculations with strained Pt have used the PW mode. By calculating the strain-corrected stability in this way, we do not mix total energies calculated with different methods, but only ΔE values.

$$E^{corr}_{skin} = E_{skin} + \Delta E^{corr}_{bulk,Pt} \tag{5.2}$$

Here E^{corr}_{skin} is the strain-corrected energy of the skin, E_{skin} is the same as before and $\Delta E^{corr}_{bulk,Pt}$ is the difference in bulk energy of Pt with a Pt-Pt distance equivalent to the Pt overlayer on the alloy and Pt with the equilibrium distance.

5.2.3 Adsorption energies

Adsorption energies are calculated with stable molecules, specifically H_2O, CO and H_2, as references. These are shown for each adsorbate in equations (5.3) to (5.7). Taking CO as an example, E^{CO}_{ads} is the adsorption energy, $E_{slab,CO}$ is the energy of the slab with CO adsorbed, E_{slab} is the energy of the slab without CO and E_{CO} is the energy of CO in the gas phase. For O, we use H_2O as a reference due to the problems DFT has with describing oxygen in the gas phase. We have not included zero-point energies, as we assume that any variation here will be insignificant, which is supported by calculations on strained Pt.

$$E_{ads,O} = E_{slab,O} - E_{slab} - E_{H_2O} + E_{H_2} \tag{5.3}$$
$$E_{ads,C} = E_{slab,C} - E_{slab} - E_{CO} - E_{H_2} + E_{H_2O} \tag{5.4}$$
$$E_{ads,H} = E_{slab,H} - E_{slab} - 1/2E_{H_2} \tag{5.5}$$
$$E_{ads,OH} = E_{slab,OH} - E_{slab} - E_{H_2O} + 1/2E_{H_2} \tag{5.6}$$
$$E_{ads,CO} = E_{slab,CO} - E_{slab} - E_{CO} \tag{5.7}$$

The atomic configurations corresponding to $E_{slab,X}$ are shown in figures 5.4 and 5.5.

In this case it is trivial to correct for the effect of strain on the adsorption energy, as the shift in adsorption energy is easily calculated for Pt slabs with various lattice parameters. The expression for the corrected adsorption energies are then simply calculated as shown in

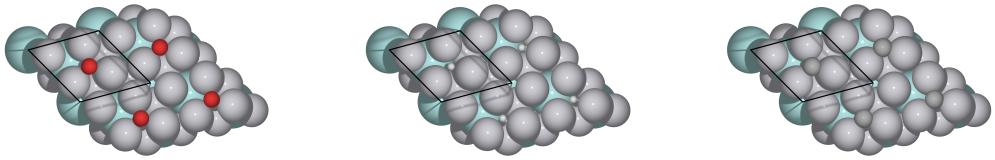

(a) *Oxygen (O)* **(b)** *Hydrogen (H)* **(c)** *Carbon (C)*

Figure 5.4: *The three mono-atomic adsorbates in fcc sites. The black box is the computational unit cell.*

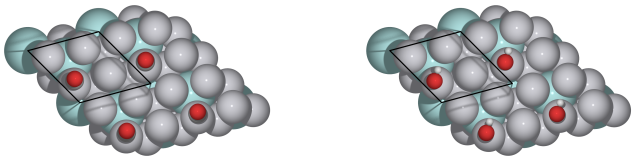

(a) *Carbon Monoxide (CO)* **(b)** *Hydroxide (OH)*

Figure 5.5: *The two diatomic adsorbates in ontop sites. The black box is the computational unit cell.*

equation (5.8), equivalent to the bulk correction in equation (5.2).

$$E^{corr}_{ads,X} = E_{ads,X} + \Delta E^{strain}_{ads,Pt} \tag{5.8}$$

5.3 Strained Pt

In this section we will present our results for the bulk stability and adsorption energies for strained Pt. This will be used to strain-correct the corresponding values for the alloys in section 5.4.

5.3.1 Bulk Pt

In order to use equations (5.1) and (5.2), we need to calculate the activity of Pt with various lattice constants deviating from the equilibrium value. These results are shown in figure 5.6, and shows how Pt is destabilised by strain effects. In order to interpolate between these values to a specific strain value, we fit a third-order polynomial to the deviation from equilibrium, with the expression shown in equation (5.9). It is well-known that a third-order fit is a good approximation of the energy as a function of the lattice parameter in one dimension[120, 121]. Here x is the strain in percent and E_{Pt} is the energy of equilibrium bulk Pt. The parameters of the fit are shown in table 5.1. The low values and relatively large uncertainties of a and b simply show that these terms do not contribute significantly to the fit.

$$E(x) - E_{Pt} = a + bx + cx^2 + dx^3 \tag{5.9}$$

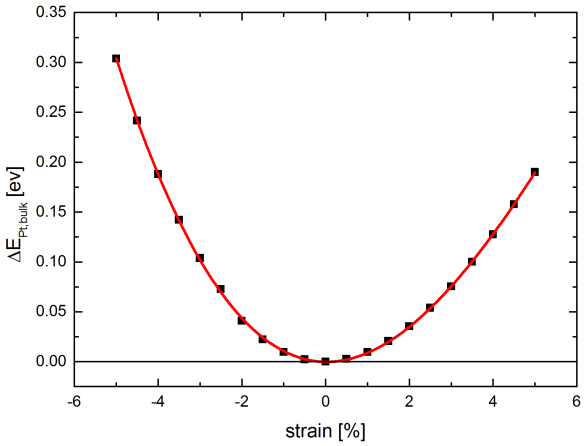

Figure 5.6: *Bulk energy of Pt at various lattice constants, referenced to equilibrium. The fit is a 3^{rd} degree polynomial with the parameters given in table 5.1.*

Table 5.1: *Parameters for the 3^{rd} order polynomial fit to the bulk energies of strained Pt, shown in figure 5.6. The expression defining the parameters is: $a + bx + cx^2 + dx^3$.*

System	a [meV]	b [meV]	c [meV]	d [meV]
Bulk Pt	-0.190 ± 0.4312	-0.433 ± 0.239	9.68 ± 0.0351	-0.441 ± 0.0133

5.3.2 Adsorption on strained Pt

We have also done calculations for the reference system of strained Pt slabs, which will later be used to correct the alloy values for strain. We plot in figure 5.7 adsorption energies for strain in the range of -5.0 % to +5.0 %. At greater absolute values of strain, the slab might start to reconstruct, leading to system-specific and uncontrollable effects, muddying the overall trend due to the strain itself. This was not found to be the case within this range. This range adequately covers the range of the alloys, where the maximum absolute strain is found to be 3.97 %, for Pt_3Pb. Early work on adsorption energies as a function of strain found a linear relationship, but this was over a shorter range of strains than what we have used here[41]. Instead, we have used a 3^{rd} order polynomial in order to capture the non-linear contribution, but still avoid overfitting[122]. It could be viewed as the lowest order polynomial that we found to give a very good interpolation between the data points for the adsorption energies. We note that we know of no underlying reason for the strain effect to be cubic, and we regard our choice entirely as a practical matter of interpolating between the calculated points. The parameters for the various fits are given in table 5.2.

In figures 5.7a, 5.7b and 5.7c we show the adsorption energy of the adsorbates in the fcc sites on pure Pt with different lattice parameters. For H the energy difference between the different sites is very small, but it has been shown to bind in the fcc site when the zero-point energy is taken into account[123, 124].

In order to investigate the influence of the type of adsorption, we have also looked at CO and OH, both binding ontop. These results are shown in figures 5.7d and 5.7e.

In all five cases there is an overall linear tendency, as predicted by Mavrikakis et al.[41]. However, it is also obvious that there is a slight non-linearity, especially when going beyond the ±2.5 % strain that was investigated in that paper. In the case of hydrogen, the deviation

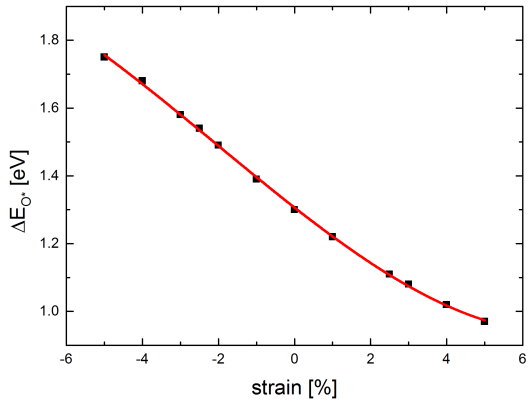

(a) *O adsorped in the fcc site.*

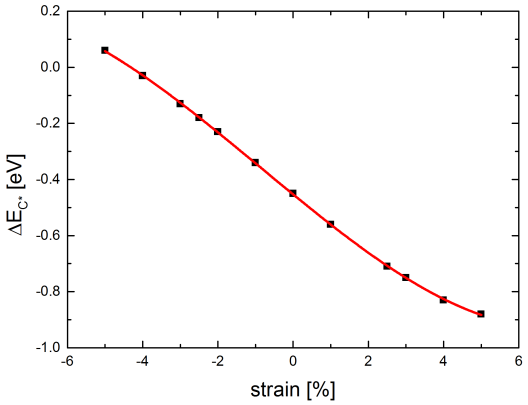

(b) *C adsorped in the fcc site.*

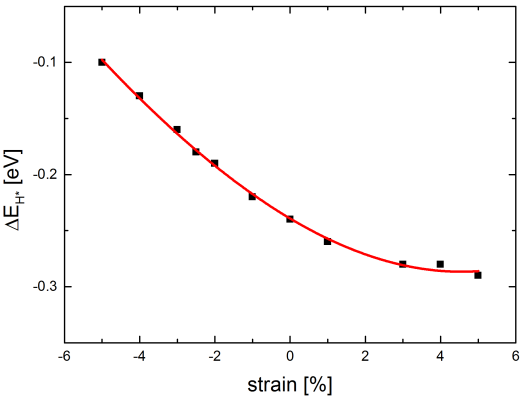

(c) *H adsorped in the fcc site.*

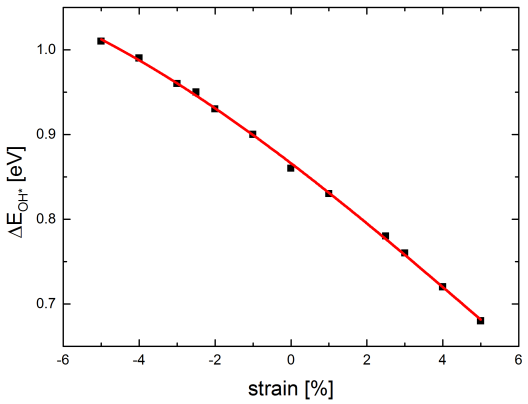

(d) *OH adsorped in the ontop site.*

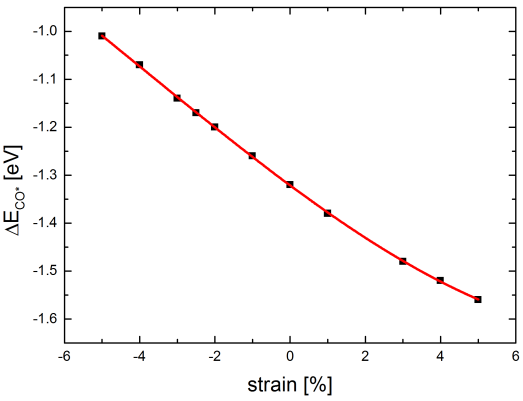

(e) *CO adsorped in the ontop site.*

Figure 5.7: *Adsorption energies as a function of strain for the five different adsorbates on strained Pt. The red curves are the best 3^{rd} order polynomial fit.*

Table 5.2: *Parameters for 3^{rd} order polynomial fits to the adsorption energies on strained Pt, shown in figure 5.7. Note the change in units between the a parameter and the rest. The expression defining the parameters is: $a + bx + cx^2 + dx^3$.*

Adsorbate	Site	a [eV]	b [meV]	c [meV]	d [meV]
O	fcc	1.307 ± 0.003	-88.5 ± 1.4	2.36 ± 0.21	0.385 ± 0.073
C	fcc	-0.453 ± 0.001	-109.8 ± 0.7	1.61 ± 0.11	6.31 ± 0.037
H	fcc	-0.239 ± 0.002	-19.9 ± 0.9	1.89 ± 0.13	0.0433 ± 0.048
OH	ontop	0.866 ± 0.001	-34.1 ± 0.7	-0.77 ± 0.12	0.0425 ± 0.039
CO	ontop	-1.321 ± 0.001	-58.1 ± 0.6	1.49 ± 0.08	0.124 ± 0.030

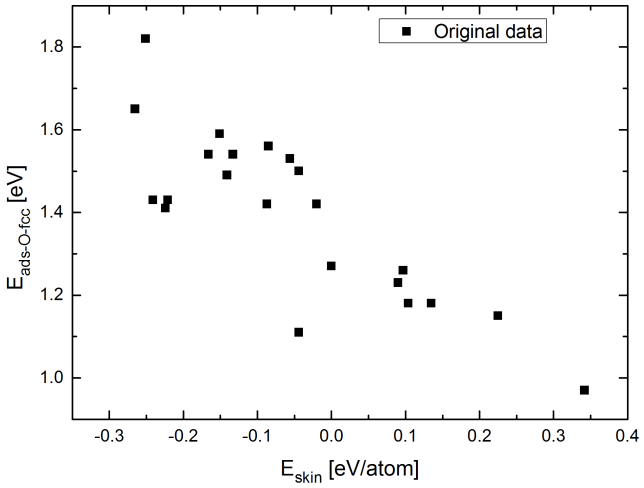

Figure 5.8: *Adsorption energy of O on alloys as a function of the Pt skin stability.*

from a straight line is quite drastic for large positive strains. Considering the size of the hydrogen atom, we speculate that this is at least partly due to a geometric effect where the distance between Pt atoms starts to play a role, putting constraints on the bond length.

5.4 Adsorption on alloys

We have calculated the adsorption energy of a pure Pt layer on different Pt_3M alloys and these results are shown for O in the fcc site in figure 5.8. We see a weak trend with more stable skins also binding the O adsorbate more weakly. However, in the case of alloys there are two contributing effects. If we correct the data for strain effects we can isolate the ligand effect, and see if this changes the relationship between the two variables. This is shown in figure 5.9a along with a best linear fit to both datasets. We choose a linear fit as this is the simplest possible model, and are not aware of any underlying theory suggesting a specific functional form.

It is obvious from visual inspection that there is now a much stronger linear relationship between the adsorption energy and the stability of the overlayer. The red circles, representing the strain-corrected data set, are clustered much more tightly together around the line. This is in contrast to the adjusted R^2 value for the fit, shown in table 5.3, which is a little bit smaller for the strain-corrected fit. Adjusted R^2 is a measure of the explanatory power of the model, where the adjustment is a penalty related to the complexity of the model, designed

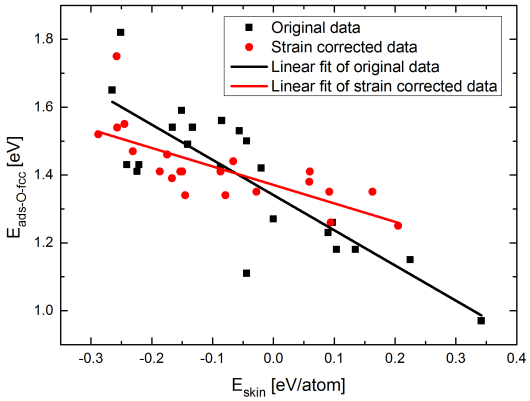

(a) *O adsorped in the fcc site.*

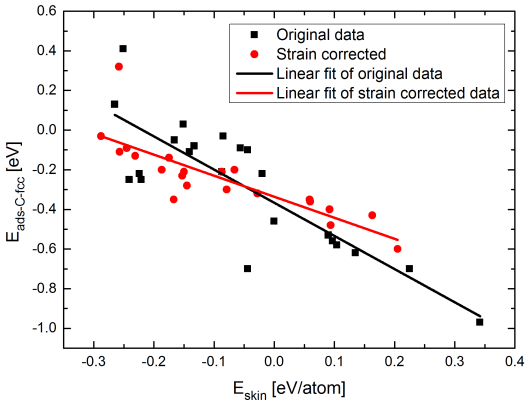

(b) *C adsorped in the fcc site.*

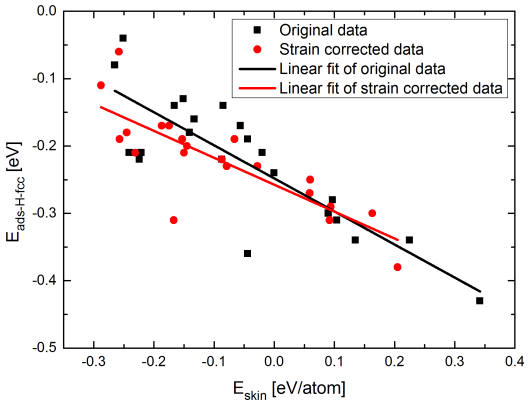

(c) *H adsorped in the fcc site.*

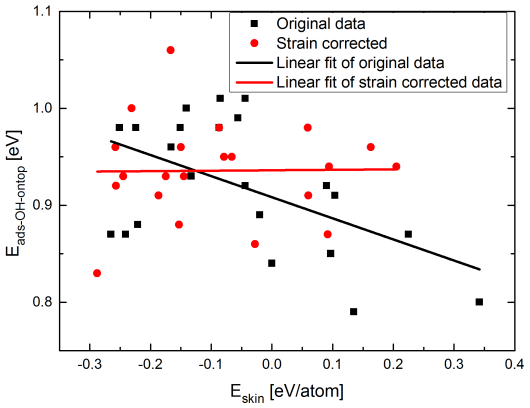

(d) *OH adsorped in the ontop site.*

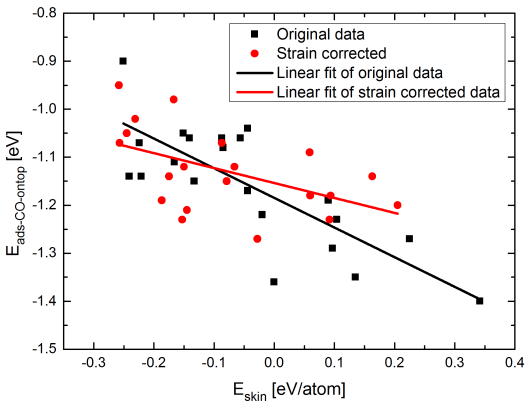

(e) *CO adsorped in the ontop site.*

Figure 5.9: *Adsorption energy vs. skin stability for the five different adsorbates on Pt_3M alloys with a Pt skin. Black squares denote properties as calculated directly with DFT, while the red circles are corrected for strain a described in section 5.2. Straight lines are best linear fits to the dataset with the same colour.*

Table 5.3: *Parameters for linear fits to the adsorption energies on the Pt alloys shown in figure 5.9. The expression is defined as $a + bx$.*

Adsorbate	Site	Strain corr.	a [eV]	b [eV]	Adj. R^2
O	fcc	No	1.341 ± 0.026	-1.037 ± 0.157	0.67
O	fcc	Yes	1.371 ± 0.019	-0.544 ± 0.115	0.52
C	fcc	No	-0.366 ± 0.041	-1.674 ± 0.243	0.69
C	fcc	Yes	-0.336 ± 0.028	-1.062 ± 0.165	0.67
H	fcc	No	-0.248 ± 0.012	-0.491 ± 0.073	0.68
H	fcc	Yes	-0.257 ± 0.011	-0.399 ± 0.064	0.66
OH	ontop	No	0.908 ± 0.013	-0.218 ± 0.079	0.24
OH	ontop	Yes	0.936 ± 0.013	0.005 ± 0.079	-0.05
CO	ontop	No	-1.185 ± 0.018	-0.618 ± 0.112	0.60
CO	ontop	Yes	-1.154 ± 0.019	-0.311 ± 0.121	0.23

to avoid overfitting. However, this partly reflects the lowering of the slope, indicating that the overall dependence of the adsorption energy on the skin stability is lower after correction. This lowers the difference between the linear fit and a simple mean of the data, which leads to a lowering of the adjusted R^2 value. This is not surprising as we have just removed an effect coupling the two, and this must be kept in mind when comparing the adjusted R^2 values. It should also be noted that the dataset is overall shifted to the left and compressed in the horizontal direction, as correcting for strain in all cases make the overlayer more stable. Finally, we would like to draw attention to the two data points representing Pt_3Ti, in the upper left corner. The strain-corrected point seems like a clear outlier, but as we have been unable to find a specific reason for this, it is included in all fits.

In order to check if this effect is dependent on the adsorbate, we did the same for C and H in fcc sites, and these results are shown in figures 5.9b and 5.9c.

For C in figure 5.9b the overall picture is the same as for O, with the strain-corrected values clustering more tightly around the linear fit, while for H in figure 5.9c not much is changed when correcting for strain. This is due to the overall weaker interaction of H with the metal surface, as the adsorption energy only changes about 200 meV for H when going from 5 % compression to 5 % expansion. For O, it changes about 800 meV.

Ontop sites

In order to test if the type of adsorption site is important for the relationship between the adsorption energy and the overlayer stability, we have done the same for calculations for CO and OH. They are situated in the ontop position and the results are shown in figures 5.9d and 5.9e.

While a very slight tendency is seen in the original data for OH in figure 5.9d, this trend completely disappears in the strain-corrected data set. For CO there is still a very weak correlation in the strain-corrected data seen in figure 5.9e, but it is not particularly convincing. This becomes especially clear if the two adsorption sites are seen as groups, in which case the trend is clearly much stronger for the adsorbates in the fcc site, while it is almost non-existent for the ontop site. This is further signified by the negative value of adjusted R^2 for OH, which, broadly speaking, shows that a linear fit includes more variables than needed to describe the correlation; a constant would have been enough. This indicates

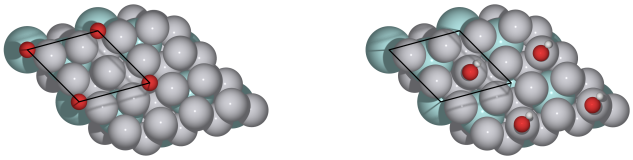

(a) (b)

Figure 5.10: *O in an fcc site and CO in an ontop site. These sites are placed differently with respect to the second layer when compared to figures 5.4 and 5.5, giving a different composition in the second layer below the adsorbate. Specifically, 3 Pt atoms instead of 2 Pt and one M. The black box is the computational unit cell.*

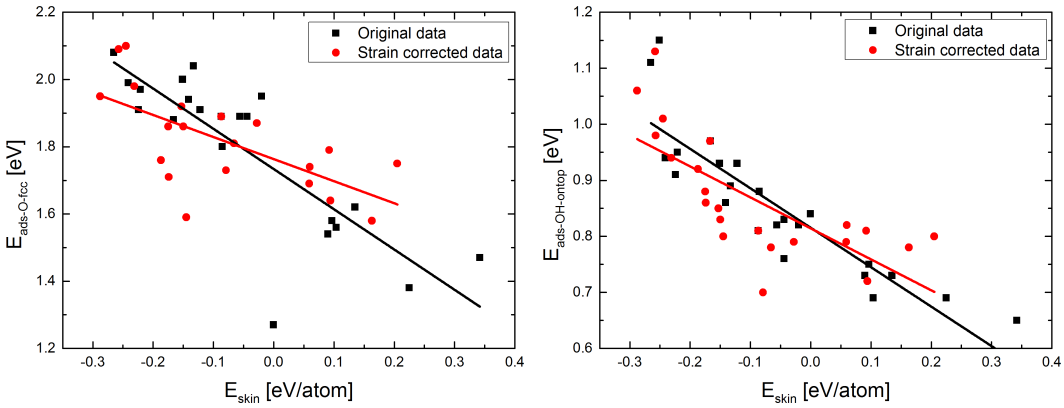

(a) (b)

Figure 5.11: *Both original and strain-corrected values for the adsorption energy of O in a different FCC site and OH in a different ontop site on an alloy as a function of the skin energy. The straight lines are the best linear fit to each dataset. a) O in the 3-Pt fcc site. b) OH in the 3-Pt ontop site.*

that there is no correlation between skin stability and and adsorption energy for the ligand effect.

5.4.1 Changing the site

The inclusion of the other element in the Pt-alloy breaks the symmetry of the adsorption sites on the surface, resulting in a larger number of different sites, compared to a regular Pt(111) surface. In this section we will investigate the difference between the sites investigated above, and superficially similar sites on the same slab, but with a different composition in the second layer. The atomic configurations are shown in figure 5.10.

We show the adsorption energies and skin stabilities for O in the 3-Pt fcc site and OH in the 3-pt ontop site in figure 5.11. Pt_3Ti and Pt_3Y are missing from the O datasets due to convergence problems. The straight lines are again the best linear fit to the respective datasets, with the parameters shown in table 5.4. In figure 5.11a the trend for the strain-corrected data is much weaker compared to what was seen in figure 5.9a. This is not really surprising, as there is no longer an atom of element M in the second layer directly below the

Table 5.4: *Parameters for linear fits to the adsorption energies in the 3-Pt sites shown in figure 5.11. The expression is defined as $a + bx$.*

Adsorbate	Site	Strain corr.	a [eV]	b [eV]	Adj. R^2
O	fcc	No	1.734 ± 0.031	-1.197 ± 0.191	0.66
O	fcc	Yes	1.763 ± 0.029	-0.657 ± 0.178	0.40
OH	ontop	No	0.815 ± 0.013	-0.704 ± 0.079	0.78
OH	ontop	Yes	0.814 ± 0.019	-0.553 ± 0.115	0.51

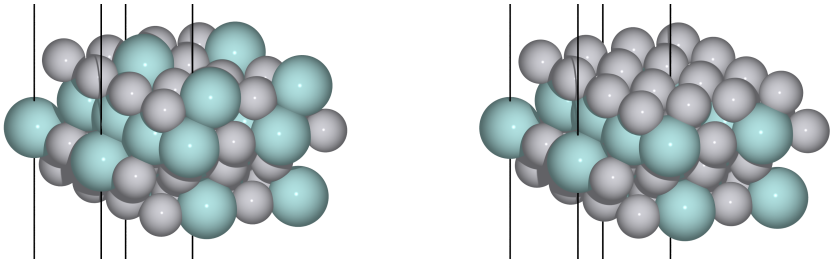

(a) **(b)**

Figure 5.12: *Pt alloy slabs without and with Pt skin, now with 50 % of the minority element in the second layer. The black lines are the corners of the computational unit cell. a) Depiction of E_{slab,Pt_3M} and b) Depiction of $E_{slab,Pt/Pt_3M}$.*

adsorbate, making the overall interaction weaker. On the other hand, figure 5.11b shows a much stronger trend in both the original and strain corrected data compared to figure 5.9d. This indicates that there is a qualitative difference between the interaction of O in the fcc site and OH in the ontop site on a Pt-alloy surface.

5.4.2 Effect of concentration in second layer

Different alloys have different concentrations of the minority element in the second layer[111, 125, 126]. In this section we investigate what this means for the adsorption properties and the stability of the skin. We have again used the two test cases of O in the fcc site and OH in the ontop site, now with 50 % of element M in the second layer. The skin energy is defined analogously, by having a pure slab with 50 % M in the second layer. The bare slabs are shown in figure 5.12, and including adsorbates in figure 5.13. Pt_3Co is missing from the O-fcc datasets and Pt_3V are missing from both O-fcc and OH-ontop due to convergence problems, while Pt_3Pb are missing from the OH datasets due to surface deformation making the result incomparable.

In figure 5.14 we show the adsorption energies as a function of the skin stability for O in the fcc site and OH in the ontop site with 50 % of the minority element in the second layer. Parameters for the linear fits can be found in table 5.5. In this case the strain correction seems to have less effect than what has been seen previously, with less movement of the data points and an almost unchanged slope of the linear fits. This indicates that the strain effect is less important in this system, which is not surprising as the ligand effect must be relatively more important with double the concentration of the minority atom in the subsurface layer. This also indicates that the inverse correlation between skin stability and adsorption energy of O observed earlier, is a general manifestation of the ligand effect, as it seems to be stronger

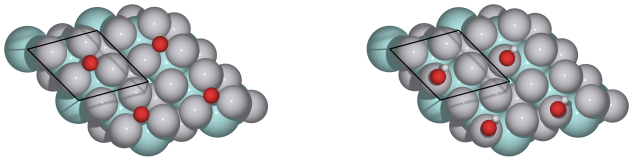

(a) (b)

Figure 5.13: *O in an fcc site and OH in an ontop site. The concentration of the minority element has been increased to 50 % in the second layer compared to figures 5.4 and 5.5, and as shown in figure 5.12. This gives a different composition in the second layer below the adsorbate. The black box is the computational unit cell. a) O in fcc site and b) OH in ontop site*

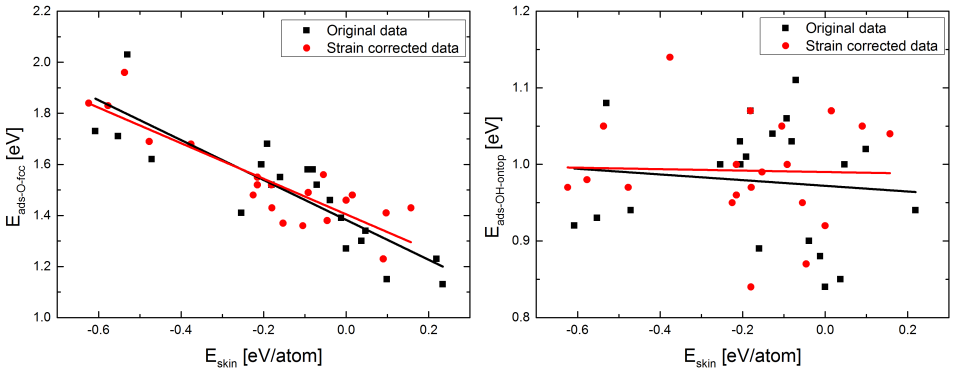

(a) (b)

Figure 5.14: *Both original and strain-corrected values for the adsorption energy on an alloy with 50% minority element in the second layer as a function of the skin energy. The straight lines are the best linear fit to each dataset. a) O in an FCC site and b) OH in an ontop site.*

here. Despite OH also binding to the surface through an O atom, the effect is not seen in this case, again indicating that the nature of the bond is qualitatively different, or at the very least, that their interaction with the ligand is.

5.5 Discussion

According to the d-band theory[37], this change in the adsorption properties should correlate with a shift of the d-band center of the Pt atoms at the surface. We investigated this, and in figure 5.15 we show the adsorption energy for O vs. the calculated the d-band center. There seems to be a weak trend in the original dataset, but not in the strain-corrected one. The d-band center is calculated using the standard method for the GPAW code and is strain corrected by subtracting the strain-induced difference on pure Pt slabs. We speculate that this lack of correlation is due to the shift being relatively small compared to noise factors in the data, which makes the approximation of looking only at the center of the d-band invalid.

While it is difficult to make a direct comparison of the magnitudes of the strain and ligand effects, we can get an indication of their relative strength for a specific system, by looking at

Table 5.5: *Parameters for linear fits to the adsorption energies with 50 % M in the second layer, which are shown in figure 5.14. The expression is defined as $a + bx$.*

Adsorbate	Site	Strain corr.	a [eV]	b [eV]	Adj. R^2
O	fcc	No	1.383 ± 0.029	-0.781 ± 0.107	0.72
O	fcc	Yes	1.405 ± 0.027	-0.696 ± 0.092	0.75
OH	ontop	No	0.972 ± 0.022	-0.037 ± 0.081	-0.04
OH	ontop	Yes	0.990 ± 0.022	-0.009 ± 0.076	-0.05

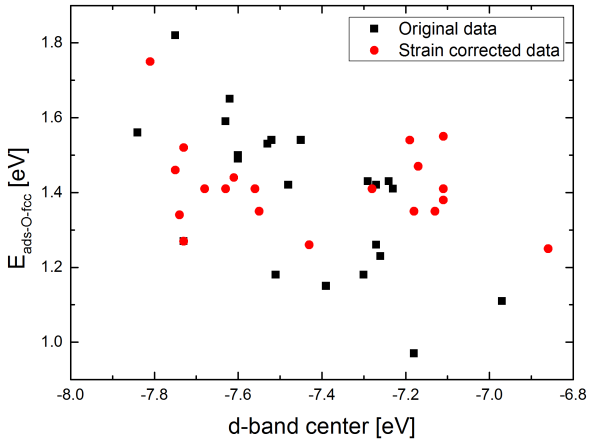

Figure 5.15: *Adsorption energy of O in the fcc site vs. d-band center.*

the range of adsorption energies in the different datasets. In table 5.6 we show the range in adsorption energies for the original and strain corrected datasets for the different adsorbates, as well as the range for adsorption on the pure, strained Pt slabs. One way of looking at these data is to compare the original and strain corrected ranges. If the strain corrected range is much smaller than the original range, it suggests that the ligand effect is relatively weaker than the strain effect in these systems. On the other hand, if the two ranges are equal, it suggests that the two effects are of equal importance, or that the ligand effect is dominant. We also see a general trend of the absolute size of all three ranges scaling with each other, suggesting that both effects depend on the nature of the interaction between the adsorbate and Pt.

We would like to point out that our procedure for strain correction neglects any hybridisation or interaction between the strain and ligand effects. This means that what we here describe as the ligand effect is, strictly speaking, a superposition of the isolated ligand effect, and any interaction terms.

5.6 Chapter summary

In this chapter we have investigated how the adsorption energy of 5 different adsorbates correlate with the stability of a Pt skin on many different Pt_3M alloys. We have proposed a method for isolating the ligand effect, and used it to show how the adsorption strength is strongly correlated with the skin stability for some adsorbates, and completely unaffected for others. Generally speaking, we saw that the adsorption of atomic adsorbates in the fcc site were weakened when the skin became more stable, while diatomic adsorbates in the

Table 5.6: *Range of adsorption energies for the various adsorbates, including both original and strain corrected data. The last column is the range in adsorption energies for strained Pt in the range of -5.0 % to 5.0 %.*

Adsorbate	Site	System	Original range [eV]	Strain corr. range [eV]	Pure strain range [eV]
O	fcc	Regular	0.85	0.49	0.79
C	fcc	Regular	1.38	0.93	0.94
H	fcc	Regular	0.39	0.33	0.19
OH	ontop	Regular	0.22	0.23	0.33
CO	ontop	Regular	0.50	0.41	0.55
O	fcc	3-Pt	0.80	0.82	0.79
OH	ontop	3-Pt	0.50	0.42	0.33
O	fcc	50 % M	0.91	0.73	0.79
OH	ontop	50 % M	0.27	0.30	0.33

ontop sites showed little (CO) or no (OH) such effect. This indicates a qualitatively different nature of the binding, suggesting that the ligand effect could be used to circumvent the scaling relation for the adsorption energy between O and OH.

Chapter 6

MD simulations of Pt_xM nanoparticles

The work summarised in chapter 2, based mostly on references [23, 59–62, 66, 127], deal with polycrystalline alloys, which is not the form of the actual catalysts in a fuel cell. We therefore need to know if the observed activity improvements also appear when the alloy is in nanoparticulate form. It is, however, very difficult and time-consuming to do experimental series on nanoparticles of these alloys of Pt and early transition metals or lanthanides, though it can and has been done [69, 70]. It is therefore of great value to look into these systems with simulations, as a larger number of alloys can be investigated in this way.

In this chapter we will look for trends in the Pt-Pt distance in the overlayer of nanoparticles of a number of different Pt_5X and Pt_3X alloys, to see how the surface strain depends on the alloy phase in the bulk. The lanthanides, including lanthanum itself, is difficult to describe accurately with computational methods, due to the very localised nature of the f-states exacerbating the self-interaction error in DFT. Methods have been proposed to circumvent this problem, but are not without issues[128, 129]. We have therefore chosen to focus on alloying Pt with other relevant metals. Of the alloys mentioned in the previous references, we choose to work with Ca, Mg, Sc, Sr, and Y. In addition to these, we will also look at alloys of Pt and Cu, where Cu is one of the traditional metals for EMT and Pt_xCu is a well-known ORR catalyst[130–133].

6.1 Methods

We investigate these systems using Langevin Molecular Dynamics simulations [134, Sec. 9.3] where we calculate the energies and forces with an EMT potential [135–137] fitted to the metals used in this project [138]. In this section we will give a short introduction to these methods, and to the various analysis methods we use to analyse the data output from the simulations. At the end we will give a more specific account of the computational procedure.

6.1.1 Molecular Dynamics

Molecular Dynamics are essentially a system of atoms where you; find the forces, solve Newton's 2. law, propagate the system a small time-step forward, and repeat from the beginning for a specified number of time-steps. However, in practice, things get a bit more complicated. Obtaining the energies and forces of the system is a world unto itself, and I will get back to this in section 6.2. In order to get meaningful results, a statistical mechanics ensemble must

be chosen. We choose the canonical ensemble, keeping the number of particles (N), volume of the system (V) and the temperature (T) constant (NVT). Other possibilities could be to keep the energy constant instead of the temperature, or the pressure instead of the volume. The discretization of the system into finite time-steps is a prerequisite for solving the problem on a computer, but also introduces numerical issues that must be taken care of when designing algorithms. We will now go into more detail with the Langevin algorithm, designed to do NVT simulations numerically.

Langevin algorithm

The general idea of Langevin dynamics, is to couple each atom to a heat bath with a specified temperature, in order to keep the total temperature constant. This heat bath can be thought of as the electron gas of the system. This coupling is done through the introduction of both a fluctuating force $\dot{\mathbf{p}}_{rand}(t)$ and a friction term $-\xi\mathbf{p}(t)$, in addition to the true force $\mathbf{f}(t)$ from the potential. This is shown in equation (6.1). The friction coefficient ξ is an arbitrary parameter, which can cause the temperature to fluctuate too much if it is too low and artificially hamper movement in the system if it is too high.

$$\dot{\mathbf{p}}(t) = -\xi\mathbf{p}(t) + \mathbf{f}(t) + \dot{\mathbf{p}}_{rand}(t) \tag{6.1}$$

6.1.2 Analysis methods

Radial Distribution Function

The Radial Distribution Function (RDF) describes the relative probability for finding an atom at a distance r from another. It is presented in many textbooks on statistical mechanics, where we would recommend the treatment by Gould and Tobochnik[139]. The RDF is normalized to unity in the limit of very far away if the density is uniform, and the density used for this normalization is calculated within the volume of the particle.

Common Neighbour Analysis

Common Neighbour Analysis (CNA)[140–143] is a technique used to study the local crystallinity of a system. A very common use-case is to study the prevalence of FCC and HCP phases in a system of metal atoms. It works by cataloguing the bonds between the neighbours of a specific atom. More specifically, if we look at an atom n with a nearest neighbour m, CNA will analyse the neighbours common to n and m, count how many there are, how many bonds these common neighbours form, and how long the longest chain of bonds between them is. These three numbers are then found for each neighbour to n, and this can, in many cases, define the crystallinity, if any, of the local environment of atom n. As the algorithm only takes nearest neighbours into account, it us unable to distinguish crystal structures were the variation has a longer range than this. The CNA algorithm is known to be very sensitive to the specific atomic environment, and in slightly disordered systems, such as our nanoparticles, it should be taken as a lower bound for the crystallinity of the system.

Layering algorithm

In this project, it is important to distinguish between atoms at or near the surface, as opposed to those which are closer to the core. In order to make this identification, we use an algorithm which uses the center of the particle and the coordination numbers of the atoms to identify which atoms are at the surface of the particle, and defining these as layer 1. Layer 2 is then

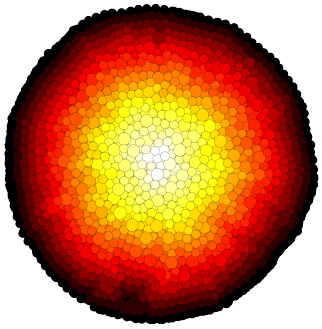

Figure 6.1: *Pt_5Y nanoparticle coloured according to layer numbers, with black signifying the surface.*

defined as the neighbours of atoms in layer 1, which are not already assigned to layer 1, and so on. The combination of distance to the center of the particle and coordination number makes identification of the outermost layer very robust, though not infallible, as can be seen by the dark spot at the bottom of the example particle shown in figure 6.1.

Calculating the diameter

The diameter is difficult to define for a nanoparticle, as it is only approximately spherical. One method could be to look at its width in the different crystallographic directions, but as we introduce a certain degree of disorder with the overlayer, this could be misleading in this case. Instead, we calculate it as an average over 500 different directions, equally spaced over the surface of a unit sphere centred on the geometric centre of the nanoparticle. To ensure these points are equally distributed, we follow the procedure of Saff and Kuijlaars[144].

6.1.3 Simulation procedure

We have investigated nanoparticles created from a variety of alloys and structures, which we will go into more detail with in section 6.3. First, we set up a big bulk crystal and the nanoparticle is then created by removing all atoms further from the centre of the particle than its chosen radius. This makes the initial particle rather spherical, which was an acceptable solution compared to the complexity that would be introduced by making Wulff-like constructions[145, 146] for the complicated structures detailed in section 6.3. Furthermore the thermal equilibration should make the specific starting configuration unimportant. Next, minority element atoms are removed from the outer layers, at a distance from the surface defined by the radius minus the desired shell thickness. This will in general give a slightly thinner shell than specified, due to subsequent relaxation of the Pt atoms removing the created vacancies. However, the shell thickness is not a well-defined quantity, neither here nor in experiments, making this difference unimportant. The energy is now minimized by the MDMin algorithm, which is a minimization algorithm using a Molecular Dynamics approach. This was done in order to avoid complications, such as vaporization of single atoms due to high-energy local configurations, primarily caused by the removal of the minority element from the shell.

We run the Langevin MD at 300 K for 10 million steps, which have previously been shown to be enough to reach thermal equilibrium[147]. Next, we run 100,000 steps starting from the already equilibrated nanoparticle, while sampling the positions every 100 steps. These

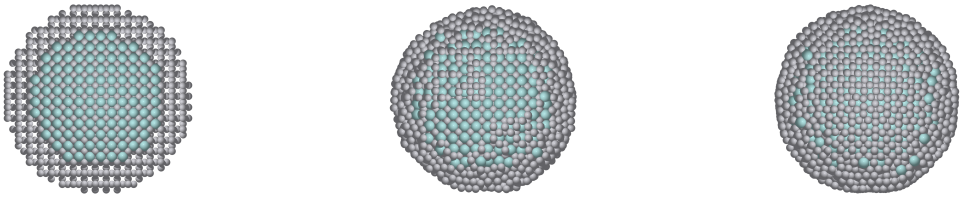

(a) **(b)** **(c)**

Figure 6.2: *Nanoparticles at various stages of the procedure. a) After deletion of M in the shell, b) after initial minimization with MDMin, and c) after thermal equilibration with Langevin dynamics.*

1,000 samples are then analysed using the various methods outlined above. We will describe this in further detail in the following sections when presenting the results of these analyses. In figure 6.2 we see an example nanoparticle at various stages of the procedure.

6.2 Effective Medium Theory

Molecular Dynamics simulations are, as described above, dependent on an external method to calculate the forces of the system. As MD simulations often involve many thousands of atoms and millions of time-steps, the forces must usually be calculated by a method which is much faster than DFT. This requires a semi-empirical approach, where some choices are made about the class of systems to be described accurately. However, there is still room for variation after this choice has been made, as the large number of potentials for describing close-packed metals can attest to. This includes, but is not limited to, the Embedded Atom Method (EAM)[148], the glue model[149], the Gupta potential [150], the Finnis-Sinclair potential [151] and the Effective Medium Theory[135–137].

We have chosen to use the Effective Medium Theory (EMT) and in this section we will give an introduction to EMT, closely based on the approach by Jacobsen et al.[137]. EMT is a semi-empirical potential built on quantum mechanical arguments and using parameters calculated using a quantum mechanical approach[136] or fitted to experimental data. The basic idea is to make an exact calculation of the energy associated with placing an atom in a reference system, and then adding the difference in energy between the reference system and the real system, as shown in equation (6.2). Here, E is the true energy of the system and $E_{c,i}$ is the energy of the i'th atom when placed in the reference system, and is known as the cohesive energy. In the following we have used that the systems under consideration in this thesis are metals.

$$E = \sum_i E_{c,i} + \left(E - \sum_i E_{c,i} \right) \tag{6.2}$$

The trick is now to construct the reference system in such a way that the term in the parentheses can be estimated using perturbation theory. Using DFT, the correction term in the parentheses in equation (6.2) can be rewritten to the more enlightening form shown in equation (6.3).

$$E = \sum_i E_{c,i} + \Delta E_{AS} + \Delta E_{1el} \tag{6.3}$$

There are now two correctional terms, the first of which is known as the atomic-sphere correction ΔE_{AS}, and represents the change in electrostatic and exchange-correlation energy for the atoms in the real system, compared to the reference system. This can be implemented as a difference of pair interaction energies in the two systems. The second correctional term is the one electron correction ΔE_{1el}, which can be calculated ab initio. If the second correctional term is small, which is definitely not true in general, equation (6.3) can be rewritten to a form including the reference energy and a pair-potential, as shown in equation (6.4). However, even if the second term is not small, the pair-potential can be modified to include the one-electron correction, and we will therefore focus on the cohesive energy and the atomic sphere correction.

$$E = \sum_i \left(E_{c,i}(n_i) + \frac{1}{2} \left(\sum_{j \neq i} V_{ij}(r_{ij}) - \sum_{j \neq i}^{\text{ref}} V_{ij}(r_{ij}) \right) \right) \tag{6.4}$$

Now the correctional energy term has the form of a classical pair-potential, assuming both potentials and the cohesive energy $E_{c,i}(n_i)$ are known. It is now assumed that the electron density n_i is a superposition of exponential tails of the electron density from other atoms, as shown in equation (6.5). Here r_{ij} is the distance between atoms number i and j, and s_i is the neutral sphere radius, the radius of the sphere around atom i where the total charge is zero.

$$n_i = \sum_{j \neq i} \Delta n_j(s_i, r_{ij}) \tag{6.5}$$

This neutral sphere radius can then be calculated using Density Functional Theory and the general expression is shown here as equation (6.6). Here s_0 is the equilibrium neutral sphere radius, η_2^{-1} is the distance over which the electron density becomes insignificant, and β is the geometrical factor between the neutral sphere radius and the nearest neighbour distance, using the approximation that the neutral sphere is identical to the Wigner-Seitz sphere. This approximation is made under the assumption that the reference system is a perfect fcc crystal, which is a very common reference system.

$$\begin{aligned} s_i &= s_0 - \frac{1}{\beta \eta_2} \ln \left(\frac{\sigma_{1,i}}{12} \right) \\ \sigma_{1,i} &= \sum_{j \neq i} \exp\left(-\eta_2 (r_{ij} - \beta s_0) \right) \end{aligned} \tag{6.6}$$

The cohesive energy and the atomic-sphere correction can then be written as functions of the neutral sphere radius, using the expressions in equation (6.7) and equation (6.8).

$$\begin{aligned} E_{c,i}(s) &= E_0 f[\lambda(s_i - s_0)] \\ f[x] &= (1 + x) \exp(-x) \end{aligned} \tag{6.7}$$

$$\begin{aligned} \Delta E_{AS}(s) &= \frac{1}{2} \sum_i \left(\sum_{j \neq i} V(r_{ij}) - 12 V(\beta s_i) \right) \\ V(r) &= -V_0 \exp\left(-\kappa (r/\beta - s_0) \right) \end{aligned} \tag{6.8}$$

The pair-potential from equation (6.4) has now been rewritten to be a function of a series of parameters. All of these can in principle be calculated from Density Functional Theory, but the best results are achieved when they are fitted to a diverse set of properties for each element, as briefly described below.

6.2.1 Revised EMT

As described previously, EMT contains several parameters which govern the pairwise interactions between atoms in the system. The best results for these parameters are found when they are fitted to high-quality data from either experiments or DFT calculations[138, 152–154]. However, care must be taken to balance the quality of the description of the specific systems and properties with the possible loss of transferability. This happens when the potential is fitted to too specific systems. It might still give a good description of this specific class of systems, but a much worse description of everything not explicitly accounted for in the fitting procedure.

This project makes use of a revised formulation of EMT and a new set of parameters, which are fitted to the elements and alloys that are relevant in this context. In this section we will give a brief presentation of the most important features, while further details can be found in the attached paper[138].

We have created a set of general EMT potential parameters to an extended number of elements, by fitting first to the pure elements of the original EMT formulation and then to various properties of alloys between these elements. Afterwards we introduce a new set of elements, which all crystallise in a close-packed structure, either hcp or fcc, and then fit the parameters to properties of these and their alloys. We make this distinction as EMT inherently favours close-packed structures and thus gives a poorer description of more open structures such as the bcc. The parameters from this set is shown in table (I) in the attached paper and they are used for Pt and Cu in the calculations in this chapter.

The calculations in this chapter are all focused on Pt alloys, and we have therefore produced a potential optimised to this situation. This was done by starting with the parameters in table (I) in the paper, and then fitting to an additional set of Pt alloy phases, as well as the pure elements. These phases included both the Pt-rich phases which are interesting as catalysts for the ORR, but also Pt-poor phases, to ensure an overall good description of the systems. The parameters for Pt were not allowed to vary, to ensure a good description in the catalytically important regions of pure Pt. The resulting parameters are shown in table (III) of the attached paper, and are used in all calculations involving Ca, Mg, Pt, Sc, Sr and Y.

While these potentials are fitted to the systems and properties of interest in this project, there is still an inherent inaccuracy in EMT due to the various approximations. Furthermore, the parameters used in this project are new, and therefore not yet thoroughly tested. As mentioned above, EMT systematically favours close-packed systems, and does not include finite-size effects arising from quantum mechanics. However, it is a good approximation for close-packed metals, and has shown good results in many applications since its formulation.

6.3 Alloy structures

Before we can model the nanoparticles, we need some knowledge about the structure of the alloys, in order to set up the nanoparticles in a relevant structure and shape. Due to evidence of corrosion of Pt_2M alloys under experimental conditions[60], we restrict ourselves to alloys with at least a 3:1 Pt:M ratio. Several alloys including the minority elements Ca, Cu, Mg, Sc, Sr, and Y have well-known structures, such as Pt_5Ca in the $CaCu_5$ structure[155], Pt_3Mg in the $L1_2$[155, 156], Pt_5Sr in the $CaCu_5$[157], Pt_5Y in the $AuBe_5$[60, 158], Pt_3Cu, Pt_3Y and Pt_3Sc in the $L1_2$[159–161]. Pt_3Sr also appears in a proposed phase diagram for the Pt-Sr system, but without crystallographic data[162]. Some of these have not been investigated thoroughly and their structures are therefore somewhat uncertain. We will now investigate

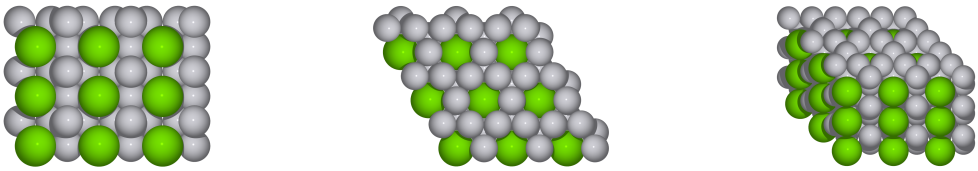

(a) (b) (c)

Figure 6.3: *The hexagonal Pt_5M structure, here shown specifically for Pt_5Ca. Also called the $CaCu_5$ structure. All three figures depict a $3x3x3$ supercell. a) Seen from the side, b) seen from above, and c) seen at an angle.*

some different structures which are found for the Pt_5M alloys, and present our results for the bulk structures.

6.3.1 Description of the Pt_5M structures

During our initial simulations with Pt_5Sc, we discovered that it could transition from the initial $CaCu_5$ structure into a different, and to us, unknown, structure. It was therefore obvious that we needed to investigate the relations between the different alloys and these various structures.

Pt_5Ca, Pt_5Sr, and many other Pt_5M alloys are known to form the $CaCu_5$ structure. This structure has hexagonal symmetry and a unit cell of six atoms. We show it from three different angles in figure 6.3. Note how the structure is constructed from alternating layers of Pt_3 and Pt_2M, with a vacancy in the Pt_3 layers to accommodate the much larger atom of element M. In figure 6.3c this becomes especially obvious as there are clear holes in the topmost Pt layer. This structure is known as a *kagomé* lattice[163], and the addition of the vacancy is what causes the Pt-Pt distances in these structures to be much lower than in bulk Pt.

Pt_5Y has been found to form the $AuBe_5$ structure, which has cubic symmetry and 24 atoms in the unit cell. The Y atoms are arranged in an FCC lattice and the Pt atoms are then distributed in the space between the Y atoms. We show it in figure 6.4. Note the fcc-lattice of the Y atoms in figure 6.4a, which causes the hexagonal symmetry in the topview of the 111-slab in figure 6.4c. Even though it has cubic symmetry, as opposed to the hexagonal symmetry of $CaCu_5$, it turns out to be very similar to $CaCu_5$ on closer inspection, as seen in the sideview of the slab in figure 6.4b. Both have alternating layers of Pt_2M and Pt_3, with the main difference being an ABC stacking in the 111-direction in $AuBe_5$ instead of the AAA stacking in the 001-direction found in $CaCu_5$. This equivalence of structures, apart from different stacking sequences, is also known for the Pt_2M compounds; the class of structures known as Laves phases [164–167]. This also fits with data in the literature for e.g. Pt_5Gd and Pt_5Y showing a cell of comparable dimensions to $CaCu_5$ in the a and b directions, but much larger in the c direction, indicating a long stacking sequence[158, 168].

The new structure is closely related to the $CaCu_5$ structure, and involves elimination of the vacancy from the Pt_3 layers as the Pt reorganize into a full 111-like layer. This also increases the Pt-Pt distances in this layer, and causes a slight expansion in the c-direction of the unit cell, in order to accommodate the larger atoms after removal of the vacancy. In our case, every other Pt_3 layer reconstructed differently, leading to an ABAC stacking, instead of the ABAB stacking from the original structure. This stacking makes the structure similar to

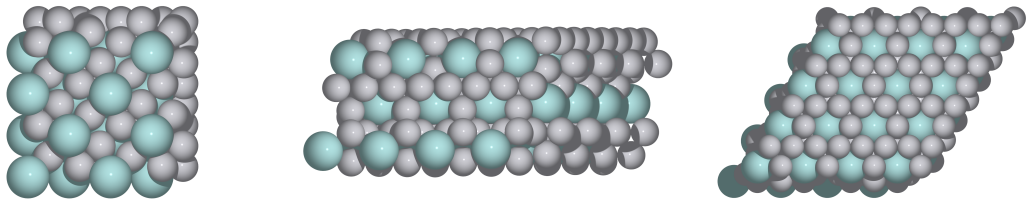

(a) (b) (c)

Figure 6.4: *The fcc-like Pt_5M structure, here shown specifically for Pt_5Y. Also called the $AuBe_5$ structure. a) A 2x2x2 bulk supercell. b) and c) A 2x2 supercell of a slab cut in the (111) direction.*

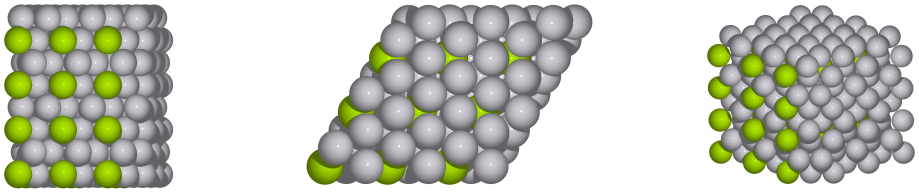

(a) (b) (c)

Figure 6.5: *The bulk structure Pt_5M in the double-axis hexagonal close-packed (dhcp) structure, shown specifically for Pt_5Mg. All three figures depict a 3x3x2 supercell. a) Seen from the side, b) seen from above, and c) seen at an angle.*

what is known as the double-axis hexagonal close-packed (dhcp) structure for pure elements, and we will use that name for this structure. We show it in figure 6.5 for Mg. The elimination of the vacancies in the, now, close-packed 111-like Pt layers is easily seen in figures 6.5b and 6.5c, while the new stacking sequence is seen in figure 6.5a.

In the remainder of this chapter we will denote the $CaCu_5$ structure as the hexagonal (hex) structure and the $AuBe_5$ as the fcc structure in order to make the names more descriptive of their respective properties. The new structure will be denoted as the double-axis hexagonal close-packed (dhcp) structure.

6.3.2 Relative stability of the Pt_5M structures

We calculated the alloying energy for each of the alloys in each of the three structures, using DFT with the PBEsol exchange-correlation functional, as well as the EMT potential. The PBEsol exchange-correlation potential was chosen as it describes bulk properties very well. The DFT calculations have made use of the PBE-setups distributed as GPAW 0.9.11271. We used a 4x4x4 k-point grid for the fcc structure, 6x6x4 for the dhcp structure and 8x8x8 for the hex structure. This gave approximately the same k-point density in the Brillouin zone, due to the different unit cell sizes in the three structures. We used a plane wave cutoff of 600 eV in all three cases. We show the results of these calculations in figure 6.6. We note that neither Pt_5Mg or Pt_5Sc are present in the phase diagrams of their respective systems[155, 162].

The important features of figure 6.6 is which structure is lowest in energy for a given alloy, and to what degree there is correspondence between the EMT and DFT results. These results are summarised in table 6.1. The figure shows that the DFT energy of the three different structures for Pt_5Y are almost equal, making it unclear which structure is truly

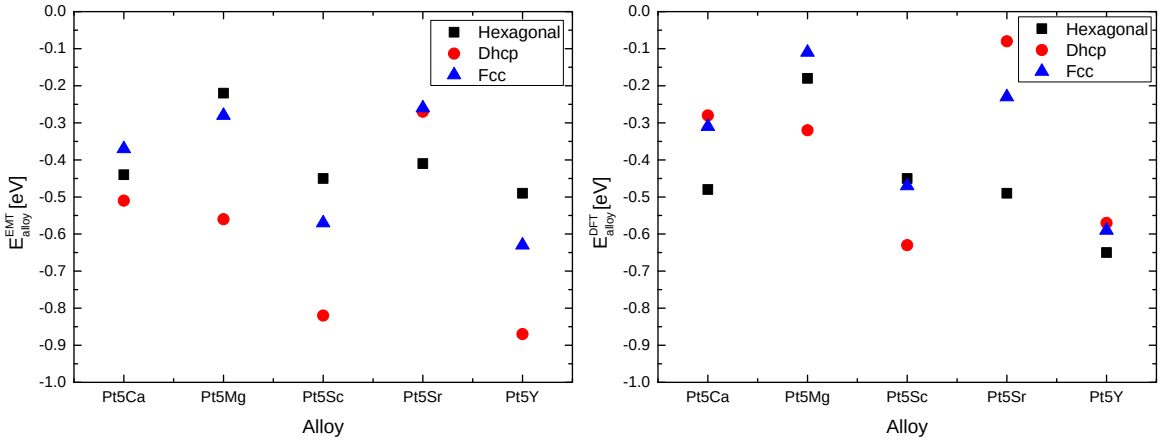

Figure 6.6: *Alloying energies for the three different Pt_5M structures, hexagonal, fcc and dhcp. a) Calculated with EMT, and b) calculated with DFT.*

Table 6.1: *Summary of the data presented in figure 6.6 with respect to the structure predicted to be most stable by each of the calculational methods.*

Alloy	Pt_5Ca	Pt_5Mg	Pt_5Sc	Pt_5Sr	Pt_5Y
EMT	Dhcp	Dhcp	Dhcp	Hex	Dhcp
DFT	Hex	Dhcp	Dhcp	Hex	Hex

favoured. Unfortunately, the EMT potential clearly favours the dhcp structure, compared to DFT, as can be seen from the alloying energies being much larger for EMT. This is not really surprising, as it is the most close-packed of the three structures. For Pt_5Ca and Pt_5Y it results in the wrong structure being predicted, but for Pt_5Mg and Pt_5Sc only the magnitude is off. However, the latter two are not necessarily stable phases, and the local atomic environment in the dhcp structure most closely resembles fcc/hcp. For Pt_5Sr the hex structure is clearly favoured by both DFT and EMT.

As the hexagonal and dhcp structures are very close, we have investigated whether there is a barrier for transitioning between them. Due to the different stacking in the fcc structure, it is not likely that there is a simple transition between this and one of the other structures, and we have therefore not looked at transitions involving this. As the dhcp cell is very close to being a 1x1x2 version of the hexagonal unit cell, we investigated the possible transition between the hexagonal and dhcp structures by simple linear interpolation between the two. The results of these calculations were that there are no appreciable barriers for transitioning from the high-energy structure to the low-energy structure for a given alloy. Using EMT, the largest barrier we found was 140 meV, for Pt_5Ca going from the hexagonal structure to the rotated. Using DFT we found no barriers above 10 meV/atom, but we did find a local minimum for Pt_5Y nearly midway between the two structures, nearly 25 meV/atom below the hexagonal structure. This is the lowest energy structure in this case. This is a very small difference on the scale of figure 6.6b. This further shows that there are many different structures which are close in energy for Pt_5Y, making it difficult to map out in detail with any certainty.

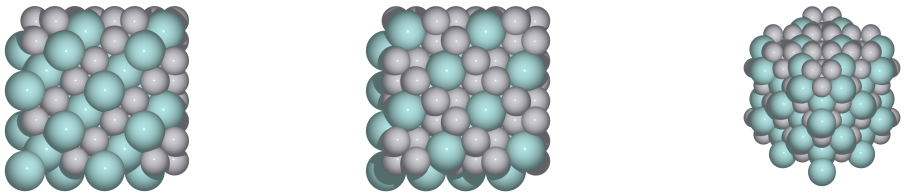

(a) **(b)** **(c)**

Figure 6.7: *The bulk structure of Pt_2M, shown specifically for Pt_2Y. In all cases we show a $2x2x2$ super cell. a) Seen from the side, b) seen from above, and c) seen at an angle.*

The similarity of the hexagonal and dhcp structures also shows if we do a CNA analysis using only the M atoms. As the local environment is a simple hexagonal lattice in both cases, the two structures are indistinguishable to the CNA. On the other hand, the total structures, including Pt, are too complicated for CNA to be an effective analysis tool.

6.3.3 Pt_3M alloy structure

We assume the Pt_3M alloys are all in the $L1_2$ structure, which is consistent with the literature for those alloys where the structure is known. The structure of Pt_3Sr is unknown and Pt_3Ca is not in the phase diagram[169]. As detailed in previous chapters, the $L1_2$ structure is simply an fcc structure with one of the atoms in the conventional unit cell exchanged with a different element. It is therefore also an obvious candidate structure when the majority element is an fcc metal. See also figure 5.2a on page 37 for a picture of the structure.

6.3.4 Pt_2M alloy structure

While the Pt_2M alloys have a too low Pt content to be interesting on their own as ORR catalysts, they could still be relevant for some phenomena that might happen in the nanoparticles. We will therefore present the Cu_2Mg structure, which is known for Pt_2Ca, Pt_2Sr, and Pt_2Y[155, 158, 170]. Mg, Sc and Cu are not known to form Pt_2M alloys with Pt. This structure has cubic symmetry and the M atoms are arranged in two offset fcc lattices with the Pt atoms forming neat rows in between.

6.3.5 Lattice parameters used in this chapter

in this section we will, primarily for reference purposes, present the lattice parameters we have used for our calculations. In table 6.2 we show the lattice parameters we have used for EMT calculations with the three different structure for Pt_5M alloys. This includes the bulk Pt-Pt distance. The dhcp structure actually has an extra internal parameter which describes the deviation of the Pt atoms from the high-symmetry positions of the unit cell, which is still allowed by the overall crystal symmetry. However, it is almost the same for the five alloys, and is in all cases close to 1/3. In table 6.3 we show the equivalent information for DFT calculations.

In table 6.4 we show the lattice parameters we have used for EMT calculations with the Pt_3M alloys, as well as their alloying energy calculated with EMT. We show the equivalent information for the DFT calculations in table 6.5.

Table 6.2: *Pt_5M alloy lattice parameters used in this project for calculations with EMT. The three bulk structures can be seen in figures 6.3, 6.4 and 6.5. Alloying energies are shown in figure 6.6a.*

EMT	Fcc		Hex			Dhcp		
Alloy	a	d_{Pt-Pt}	a	c	d_{Pt-Pt}	a	c	d_{Pt-Pt}
Pt_5Ca	7.4197	2.6233	5.3689	4.2377	2.6845	4.9941	9.2552	2.8834
Pt_5Mg	7.1705	2.5352	5.0789	4.2869	2.5395	4.7969	8.9946	2.7695
Pt_5Sc	7.2073	2.5481	5.1647	4.2641	2.5824	4.8202	9.0404	2.7829
Pt_5Sr	7.6208	2.6944	5.6031	4.1537	2.8015	5.2444	9.2865	3.0279
Pt_5Y	7.3672	2.6047	5.2758	4.3446	2.6379	4.9010	9.1226	2.8296

Table 6.3: *Pt_5M alloy lattice parameters used in this project for calculations with DFT. The three bulk structures can be seen in figures 6.3, 6.4 and 6.5. Alloying energies are shown in figure 6.6b.*

DFT	Fcc		Hex			Dhcp		
Alloy	a	d_{Pt-Pt}	a	c	d_{Pt-Pt}	a	c	d_{Pt-Pt}
Pt_5Ca	7.4321	2.6277	5.3271	4.3633	2.6636	4.9552	9.1200	2.8609
Pt_5Mg	7.3379	2.5943	5.1948	4.4446	2.5974	4.8187	9.0296	2.7821
Pt_5Sc	7.3344	2.5931	5.1912	4.4398	2.5956	4.8621	9.0664	2.8071
Pt_5Sr	7.5218	2.6593	5.4172	4.3351	2.7086	5.1006	9.1345	2.9448
Pt_5Y	7.4226	2.6243	5.2782	4.4129	2.6391	4.9759	9.1684	2.8728

Table 6.4: *Pt_3M lattice parameters used in this project for calculations with EMT.*

$L1_2$	EMT		
Alloy	a	d_{Pt-Pt}	E_{alloy} $[\frac{\text{eV}}{\text{atom}}]$
Pt_3Ca	4.1368	2.9252	-0.66
Pt_3Mg	3.9166	2.7695	-0.66
Pt_3Sc	3.9409	2.7866	-0.97
Pt_3Sr	4.3127	3.0495	-0.35
Pt_3Y	4.0594	2.8704	-0.99
Pt_3Cu	3.8004	2.6873	-0.09

Table 6.5: *Pt_3M lattice parameters used in this project for calculations with DFT.*

$L1_2$	DFT		
Alloy	a	d_{Pt-Pt}	E_{alloy} $[\frac{\text{eV}}{\text{atom}}]$
Pt_3Ca	4.0407	2.8572	-0.53
Pt_3Mg	3.9130	2.7669	-0.56
Pt_3Sc	3.9530	2.7952	-1.06
Pt_3Sr	4.1466	2.9321	-0.27
Pt_3Y	4.0617	2.8720	-0.99
Pt_3Cu	3.8458	2.7194	-0.11

Table 6.6: *Pt_2M lattice parameters used in this project for calculations with EMT.*

Pt_2M	EMT		
Alloy	a	d_{M-M}	E_{alloy} $[\frac{eV}{atom}]$
Pt_2Sr	7.9770	3.4541	-0.85
Pt_2Y	7.5061	3.2503	-1.19

Table 6.7: *Pure element lattice parameters used in this project for calculations with EMT and DFT.*

	EMT		DFT	
Element	a	c	a	c
Pt	3.9131	-	3.9195	-
Ca	5.5614	-	5.4663	-
Mg	3.1904	5.2089	3.1716	5.1719
Sc	3.2934	5.3356	3.2761	5.0846
Sr	6.0447	-	5.9413	-
Y	3.6164	5.8536	3.5986	5.5848
Cu	3.6025	-	3.5790	-

In table 6.6 we show the lattice parameters for the Pt_2M alloys as calculated with EMT. We have not done DFT calculations with these alloys.

In table 6.7 we show the lattice parameters for the pure elements, as calculated with EMT and DFT. The Pt value with EMT is especially relevant, as this what is used as the reference when investigating whether the Pt overlayers in the MD simulations are compressed or not.

6.4 Pt_xY nanoparticles

The main purpose of this chapter is to study the interatomic distance of Pt in Pt_xM nanoparticles. Due to its proven results as an ORR catalyst when in nanoparticulate form, the Pt_xY alloy is of particular interest, and this is where we will begin.

A very powerful way of studying interatomic distances in large systems is through the use of Radial Distribution Functions, as described in section 6.1.2 on page 52. We will start by focusing on the Pt-Pt distances, and in figure 6.8 on the facing page we show these for Pt_5Y in the fcc structure with a 1 nm shell of Pt, as well as pure Pt. In both cases the entire particle has been used to generate the RDF, and the particle diameters are between 3 and 12 nm. The vertical lines denote the bulk values, shown for comparison. We also fit a gaussian function to the top half of the peak, shown in the insets, and use this to extract a mean value. It is seen how the leftmost peak for the pure Pt nanoparticle is slightly offset towards lower values, compared to the bulk value. This shows that the pure Pt nanoparticle, as expected, is actually compressed compared to bulk Pt, and it is therefore important to use this as a reference instead of bulk Pt. The Pt_5Y particle has a peak between the bulk values of Pt_5Y and pure Pt, seemingly showing a greater degree of compression than pure Pt. It is also seen that only the smallest Pt_5Y particle shows clear peaks at the higher bulk Pt values, indicating that it is significantly more Pt-like than the larger particles. This is to be expected, as almost all the Y has been removed in this case. It is also clear that the Pt_5Y

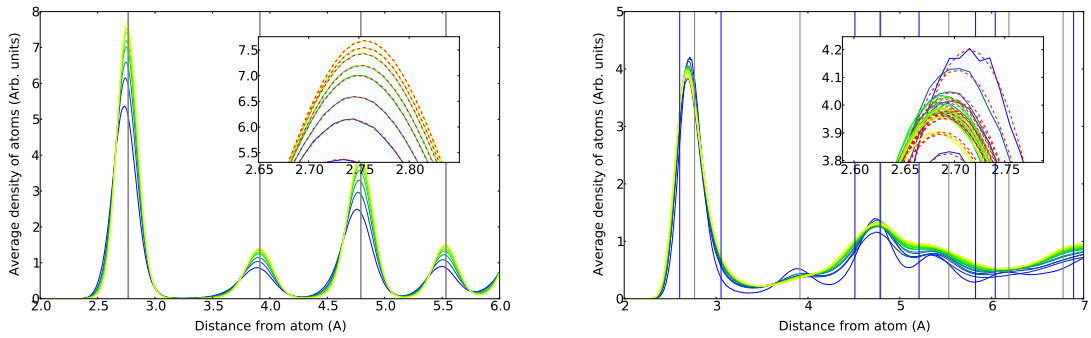

(a) **(b)**

Figure 6.8: *Pt-Pt RDF's for full particles between approximately 3 and 12 nm of a) pure Pt and b) Pt_5Y in the fcc-like structure. The colour scale goes from blue for the smallest particle size to yellow for the largest. The grey lines denote the Pt bulk values, and the blue lines are bulk Pt_5Y-fcc values for the Pt-Pt distance. The inset shows the gaussian fit to the top of the peak.*

nanoparticle has a much higher background, indicating less order among the Pt atoms, as compared to the pure Pt nanoparticle.

For catalytic purposes, the surface of the particles is especially important, and it is therefore particularly relevant to look in more detail here. In figure 6.9 on the next page we show RDF's which are equivalent to those in figure 6.8, except that they are now calculated based on only the three outermost atomic layers. This should cover the region which is almost pure Pt, without including part of the core. However, these boundaries are extremely difficult to define and this is accordingly only an approximate division. We choose to include three layers at this time, in order to get better statistics, and we will go into more detail with the surface atoms further on. Apart from a higher first peak for the Pt_5Y particle, there is very little difference between the plots for the full particle and the shell, indicating that the average properties of the Pt-Pt distances are dominated by the shell.

Trends across structures

In order to determine what influence the precise starting structure has on the Pt-Pt distance, we plot in figure 6.10 the mean Pt-Pt distance, as found from the gaussian fit, in the shell and in the entire particle for all four Pt_xY structures, as well as pure Pt. The bulk Pt-Pt distances of the alloys are either much too large (Pt_3Y and dhcp phases) or much too small (fcc and hexagonal phases) to fit in figure 6.10. See tables 6.2 and 6.4 for the exact values. It is seen on the figure that all structures give rise to a much shorter Pt-Pt distance than pure Pt, both in the full particle and in the shell. This is quite surprising, as both the dhcp phase and the Pt_3Y phase have a larger Pt-Pt distance in the bulk. All the non-Pt datasets are very non-uniform, indicating a large spread in the thermal ensemble. However, there are two tendencies which we will discuss further. When looking at the shell only, Pt_3Y is fairly consistent in having the shortest Pt-Pt distance, despite having the largest Pt-Pt distance in the bulk. However, when looking at the full particle, there is a definite upward trend for the larger Pt_3Y particles, showing that the Pt-Pt distance rises as the particle cores become more and more bulk-like. The second trend is the strange oscillatory behaviour of the hexagonal phase, where every other particle seems to change the Pt-Pt distance quite a bit. More

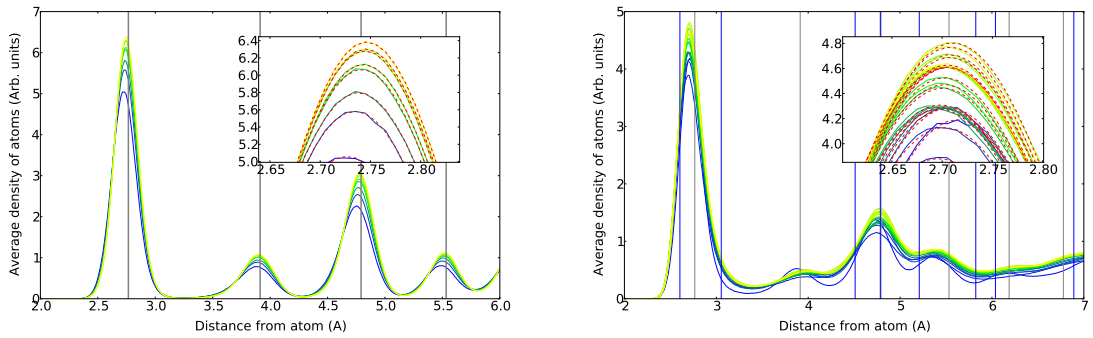

(a) (b)

Figure 6.9: *Pt-Pt RDF's for only the outermost three layers of nanoparticles between approximately 3 and 12 nm of a) pure Pt and b) Pt_5Y in the fcc-like structure. The colour scale goes from blue for the smallest particle size to yellow for the largest. The grey lines denote the Pt bulk values, and the blue lines are bulk Pt_5Y-fcc values for the Pt-Pt distance. The inset shows the gaussian fit to the top of the peak.*

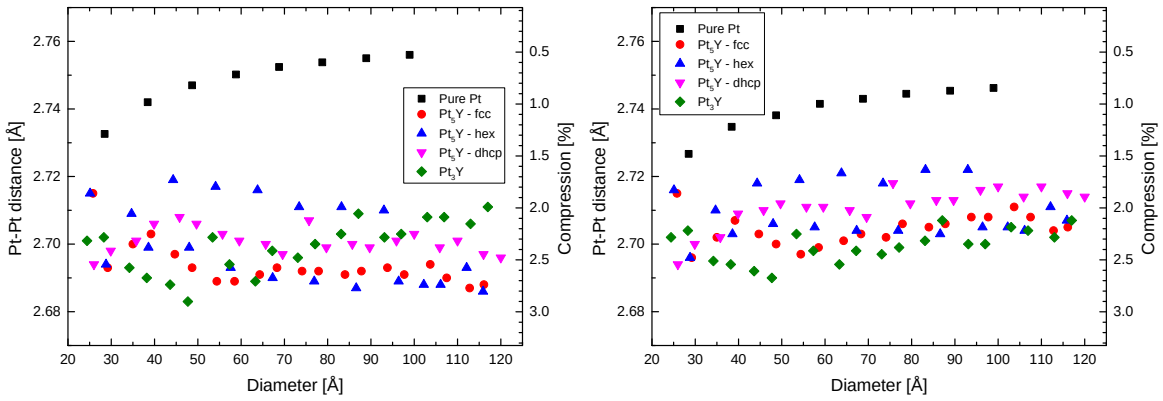

(a) (b)

Figure 6.10: *Mean Pt-Pt distance for nanoparticles created from the four Pt_xY structures, together with Pt nanoparticles. For the full nanoparticles in a) and only the three outermost layers in b). Compression is with reference to bulk Pt.*

specifically, particles created with integer diameters have much larger mean Pt-Pt distance than those with non-integer diameters. This trend is very clear between 4 and 10 nm, and found both in the shell and the full particle. We speculate that it is due to the specifics of how the particle is created initially, giving rise to different terminations and specific compositions. It does not seem to be a general problem, as it is a very small effect for Pt_5Sr (see below), and not found for other elemental combinations, as seen later in this chapter. We conclude that it reflects the spread in Pt_5Y particles created from the hexagonal structure.

Analysis of the surface Pt on Pt_xY nanoparticles

While the average Pt-Pt distance gives a first indication of the reason for the increased activity, it is really only the outermost layer that is important for the activity, and we will

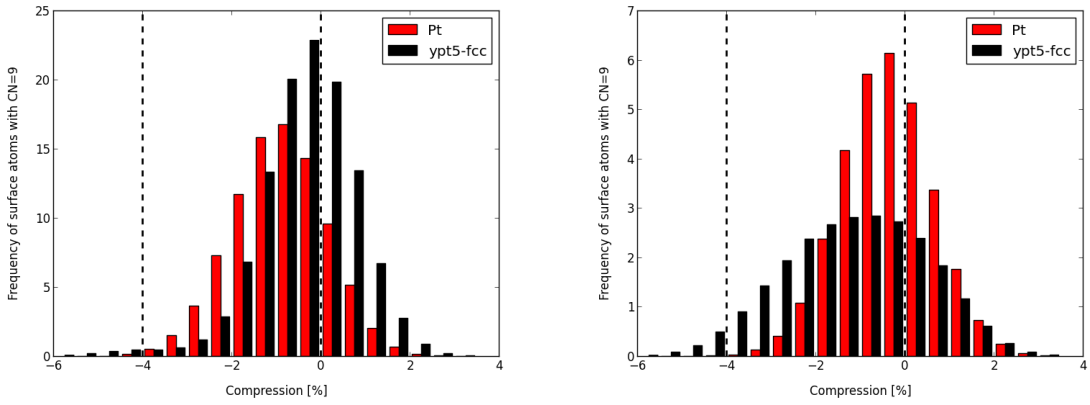

Figure 6.11: *Histograms of the frequency of 9-coordinated surface Pt atoms in Pt_5 Y-fcc (black) and pure Pt (red) nanoparticles. a) Approximately 3 nm in diameter and b) approximately 10 nm in diameter. The frequencies are normalised to the total number of atoms to make them comparable. The dashed lines denote the especially interesting region. The cutoff used to determine the coordination number was 3.0 Å.*

therefore go into more detail with this. Specifically, it has been shown that the active site for the ORR on Pt is the 111 surface, as described in chapter 2. We will therefore focus on the 9-coordinated atoms, as this is what the fcc(111) surface is composed of. Figure 6.11 shows histograms of the frequency of 9-coordinated surface Pt atoms with different compressions compared to bulk Pt, comparing Pt_5Y and pure Pt. The coordination number is simply defined as the number of Pt atoms within an (arbitrary) cutoff distance, and we define the surface atoms through the layering algorithm described in section 6.1.2 on page 52. The frequencies are normalised to the total number of atoms in the particles. As they are based on a sample of 1,000 particles, this means that the frequency is the average permille of 9-coordinated atoms with the specific compression in a particle of the given size and type. We define an interesting region between 0 and 4 % compression, as it has been shown that optimal activity should occur at a compression of about 2 % compared to extended Pt(111) surfaces.

For the Pt_5Y 3 nm particle, compared to the pure Pt particle, there is a small shift towards larger Pt-Pt distances, but also an overall increase in the frequency of 9-coordinated atoms, adding up to an activity which is probably about the same as for the pure Pt particle. However, the 10 nm particle is a very different story, as it shows a shift towards lower Pt-Pt distances, but also a broadening and lowering of the distribution compared to pure Pt. The overall frequency of 9-coordinated atoms in the interesting region is about the same for the two particles, making it hard to deduce the relative activity of the two types of particles.

In an attempt to come closer to quantifying the increase in activity, we will look at the frequency of 9-coordinated atoms in the interesting region defined above, as well as the average compression of the 9-coordinated atoms. We use a cutoff value of 3.0 Å when computing the coordination numbers, to avoid getting a contribution from the disordered background seen on the RDF's. We will return to the influence of the cutoff on the results at the end of this section. On the left of figure 6.12 we show the average compression of 9-coordinated atoms,

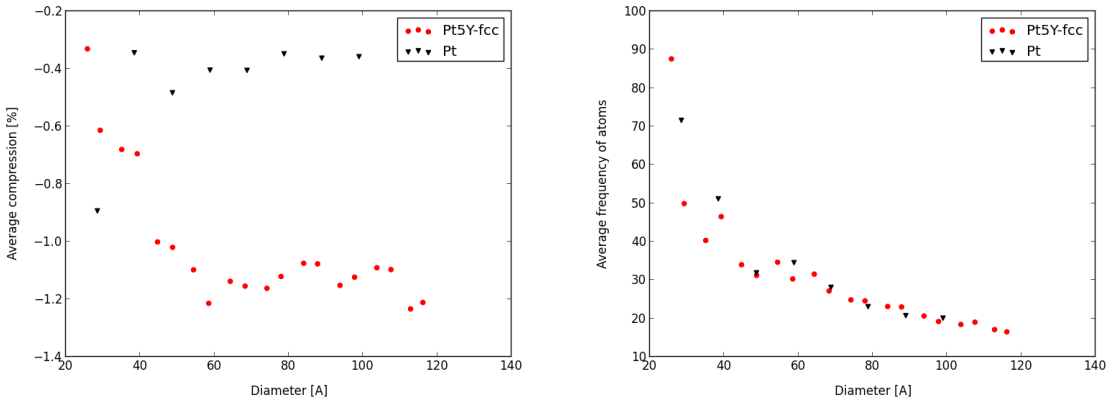

(a) (b)

Figure 6.12: *Aggregation of the information presented for two specific particle sizes in figure 6.11 on the preceding page. a) The average compression of the 9-coordinated surface atoms as a function of size. b) The frequency of 9-coordinated surface atoms with a compression between 0 and 4 %, normalised to the total number of atoms. Here is shown data only for Pt_5Y in the fcc structure.*

with respect to the bulk value for Pt, and compared to pure Pt nanoparticles. It is clearly seen how the Pt_5Y nanoparticle is consistently much more compressed for particles of at least 4 nm. On the right, we show the frequency of 9-coordinated atoms in the interesting region of compression, for Pt_5Y compared to pure Pt, normalised to the total number of atoms in the particle. Here, the difference is less pronounced, being well within the scatter inherent in both datasets.

In figure 6.13 on the next page, we show the average compression of 9-coordinated surface atoms and the frequency of those which have a compression in the interesting range of between 0 and 4 %, for all the Pt_xY alloy structures investigated in this project. We see in figure 6.13a how all four Pt_xY phases show a significant compression for the 9-coordinated Pt atoms on the surface, though there is quite a lot of scatter in the dataset seen as a whole. On the other hand, figure 6.13b shows that all of these nanoparticles have a lower frequency of atoms in the interesting range of compression than pure Pt nanoparticles, indicating fewer active sites for the ORR. However, as there is an exponential dependence of the activity on the barrier, and thus the compression, the overall compression of the surface might more than make up for it. In this case the specific phases show more separation, with the Pt_5Y-fcc phase consistently having the highest number and Pt_3Y having the lowest.

6.4.1 Investigating the importance of the cutoff

All of the above analysis has been made with a cutoff of 3.0 Å when determining the coordination number of the atoms. Considering that the nearest-neighbour distance in pure Pt is 2.77 Å this should be enough to ensure that atoms are still counted despite thermal vibrations or if the local structure is slightly distorted, without also counting atoms which are so far away that they should no longer be considered nearest neighbours. In figure 6.14 we show the same analysis as in figure 6.13, but now with a cutoff of 3.2 Å instead of 3.0 Å when determining the number of nearest neighbours. If we look first at figure 6.14a we see a huge increase in the average Pt-Pt distance. From a compression of about 1 % there is now

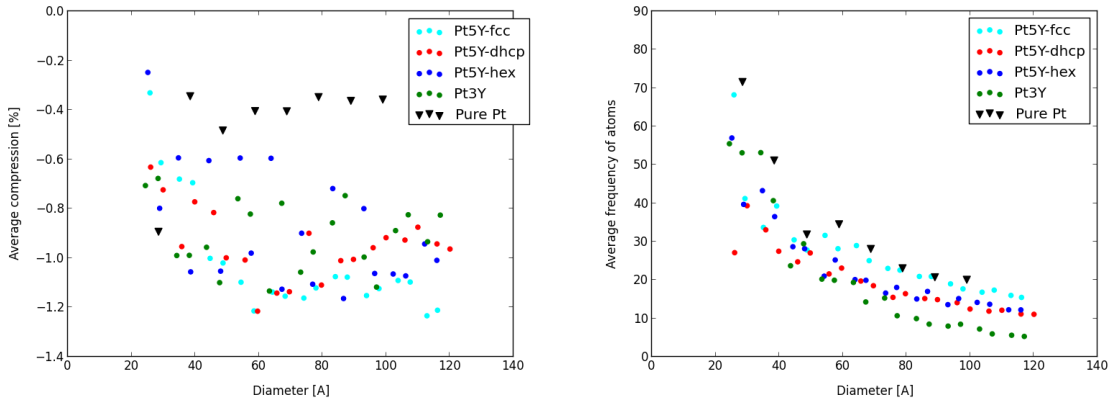

(a) **(b)**

Figure 6.13: *a) Average compression for 9-coordinated surface atoms for all Pt_xY alloy structures and compared to pure Pt. b) Frequency of 9-coordinated surface atoms with a compression between 0 and 4 % for all Pt_xY alloy structures and compared to pure Pt. In both cases are the Pt_5Y-fcc data the same as in figure 6.12 on the preceding page.*

an expansion of slightly smaller magnitude. This measure is therefore very sensitive to the exact choice of cutoff. If we now look at figure 6.14b we see only a slight downward shift in the number of atoms in the interesting range of Pt-Pt distances. This indicates that the main effect of raising the cutoff is to include some extra atoms which had one or more neighbours so far away that they had not previously been counted with a coordination number of 9, while, more or less, keeping the existing number of 9-coordinated atoms. Combined with the information from the RDF's in figures 6.8 on page 63 and 6.9 on page 64, we take the view that these additional 9-coordinated atoms have a disordered local structure, and are therefore not as relevant when trying to predict catalytic performance.

6.4.2 Structure of the core of Pt_5Y-fcc nanoparticles

The results in the previous section of surface Pt being compressed compared to Pt nanoparticles, regardless of the Pt_xY phase used in constructing the nanoparticle, is a bit surprising. Two of the Pt_xY phases have bulk Pt-Pt distances which are larger than pure Pt, but they still lead to an overall compression at the surface. In an attempt to deduce the reason for this, we look first at the RDF's for the Pt-Y and Y-Y distances in the nanoparticles, which are shown in figure 6.15. It is immediately obvious from the Y-Y RDF in figure 6.15b that the core is only vaguely bulk-like. While there is a peak centred around the bulk value of approximately 5.2 Å, it is very broad, and both the position and form is very dependent on the size of the nanoparticle. There is also a clear feature at about 3.4 Å, close to the Pt_2Y value, which we ascribe to Pt_2Y-like dimers of Y, aided by visual inspection. The Pt-Y RDF shows a main peak below the bulk value, indicating deviation from the bulk structure.

However, it is not clear if this restructuring of the core is caused by the introduction of the Pt shell, or if it is simply a result of the nanoparticulate form of the alloy. In order to shed light on this, we show in figure 6.16 on page 69 RDF's for Pt_5Y-fcc particles where the Y has not been leached from the overlayer. These show the same features, if not even more so. This shows that the restructuring in the core is not dependent on the introduction of a

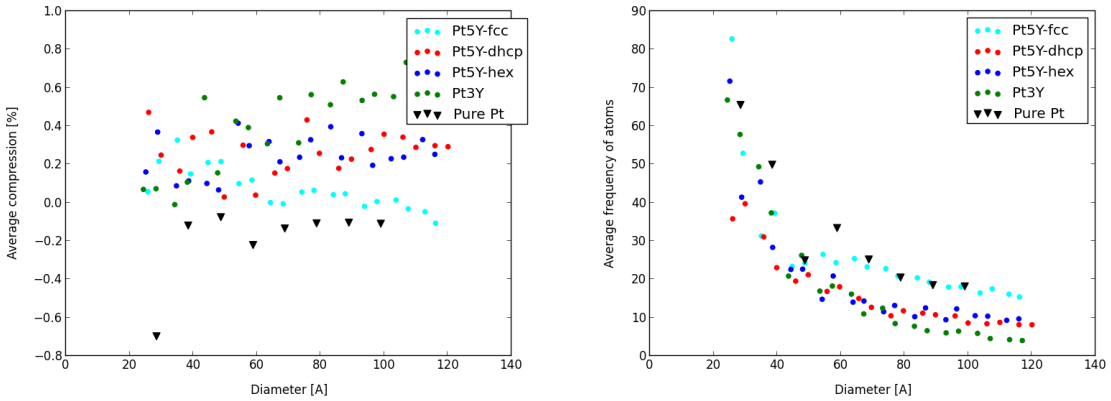

(a) **(b)**

Figure 6.14: *a) Average compression for 9-coordinated surface atoms for all $Pt_x Y$ alloy structures and compared to pure Pt. b) Frequency of 9-coordinated surface atoms with a compression in the interesting region for all $Pt_x Y$ alloy structures and compared to pure Pt. Here the cutoff has been 3.2 Å compared to figure 6.13 on the previous page where it was 3.0 Å.*

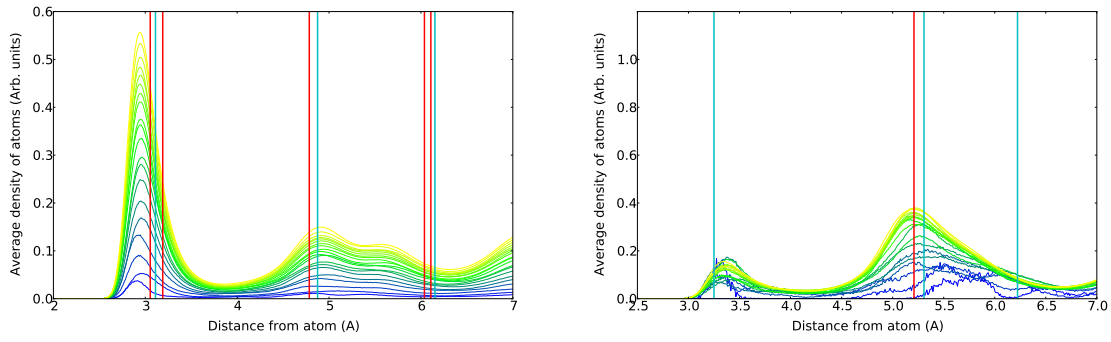

(a) **(b)**

Figure 6.15: *RDF's for $Pt_5 Y$-fcc nanoparticles with a shell of approximately 1 nm, for: a) Pt-Y distances and b) Y-Y distances. Red lines denote the bulk $Pt_5 Y$-fcc values and cyan denote bulk $Pt_2 Y$.*

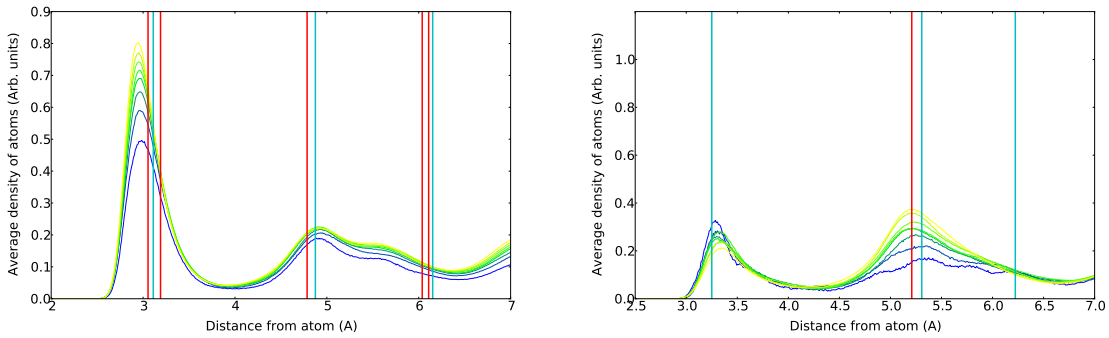

(a) **(b)**

Figure 6.16: *RDF's for Pt_5 Y-fcc nanoparticles without a Pt shell. a) Pt-Y distances and b) Y-Y distances. Red lines denote the bulk Pt_5 Y-fcc values and cyan denote bulk Pt_2 Y.*

(a) **(b)**

Figure 6.17: *Representative Pt_5 Y-fcc nanoparticles with a diameter of about 8 nm: a) with a shell of about 1 nm b) without a shell.*

pure Pt shell. As the various alloys of Pt and Y have almost the same alloying energy per Y atom, it is energetically equivalent for Y to have a local environment corresponding to either of them. We speculate that this, combined with the increased mobility from the relatively open structure of the alloys, is what causes this effect.

The results of the RDF's in figures 6.15 and 6.16, combined with visual inspection on e.g. the nanoparticles shown in figure 6.17, strongly suggests that the core, and especially the edge of it, is not very ordered. This means that there is no bulk crystal symmetry imposed on the Pt overlayers. We speculate that this is what leads to an overall compression of the surface atoms, as they move closer together in order to increase their local electron density, unrestrained by an underlying crystal symmetry.

6.5 Pt_xSr nanoparticles

As we found that EMT correctly predicts the most energetically favourable structure for Pt_5Sr, of the three structures we investigated, we also made MD simulations with this compound. Except for exchanging Y with Sr and doing the corresponding adjustments of lattice parameters, all other details are the same as in the previous section. In figure 6.18 we show

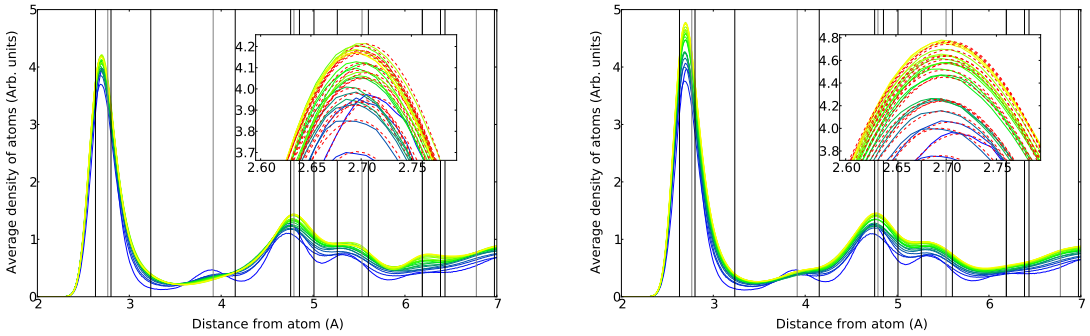

(a) **(b)**

Figure 6.18: *Pt-Pt RDFs for nanoparticles created from Pt_5Sr in the hexagonal structure with a shell of about 1 nm. a) For the full particle b) For the outermost three layers. The grey lines denote the Pt bulk values, and the black lines are bulk Pt_5Sr-hex values for the Pt-Pt distance. The insets show the gaussian fit at the top of the first peak.*

the Pt-Pt RDF's for Pt_5Sr in the hexagonal structure, one for the whole particle, the other for only the shell. The vertical lines are again the bulk values, but there are now many more lines due to the lower symmetry of this structure. The two plots are seemingly very similar, with the same overall features. In both cases the first peak falls between the distances of bulk Pt_5Sr-hex and Pt. The difference is mostly that the first peak is both higher and broader when looking at only the outermost three layers.

The mean Pt-Pt distances from these plots are collected in figure 6.19 on the facing page, together with Pt_5Sr in the fcc and dhcp structures and Pt_3Sr. Despite Sr being slightly bigger than Y, and these alloys having correspondingly larger lattice parameters, the average Pt-Pt distance is generally slightly smaller in this case. It is even more surprising that Pt_3Sr has consistently shorter Pt-Pt distances, compared to the three Pt_5Sr phases. This suggests that all of these alloys would be very good ORR catalysts. The bulk Pt-Pt distances of the alloys are either much too large (Pt_3Sr and dhcp phase) or much too small (fcc and hexagonal phases) to fit in figure 6.19 on the next page. See tables 6.2 and 6.4 on page 61 for the exact values.

In figure 6.20 on the next page we show the average compression for 9-coordinated atoms in Pt_5Sr and the frequency of 9-coordinated atoms with a compression between 0 and 4 %. While the average compression is significantly lower, indicating a higher activity than pure Pt, the number of atoms in the interesting interval is also consistently lower, making it hard to draw a definite conclusion. Nevertheless, this shows that Pt_5Sr-hex nanoparticles should be interesting to investigate further.

In figure 6.21 on page 72 we show the average compression of 9-coordinated atoms and the frequency of 9-coordinated atoms with a compression in the relevant range. It is very much like the equivalent figure for Pt_xY, figure 6.13 on page 67, with Pt_xSr exhibiting slightly lower average compression, but also a slightly lower frequency of atoms in the interesting range, indicating that there could be some of the 9-coordinated surface atoms which are compressed so much that they fall outside the interesting range.

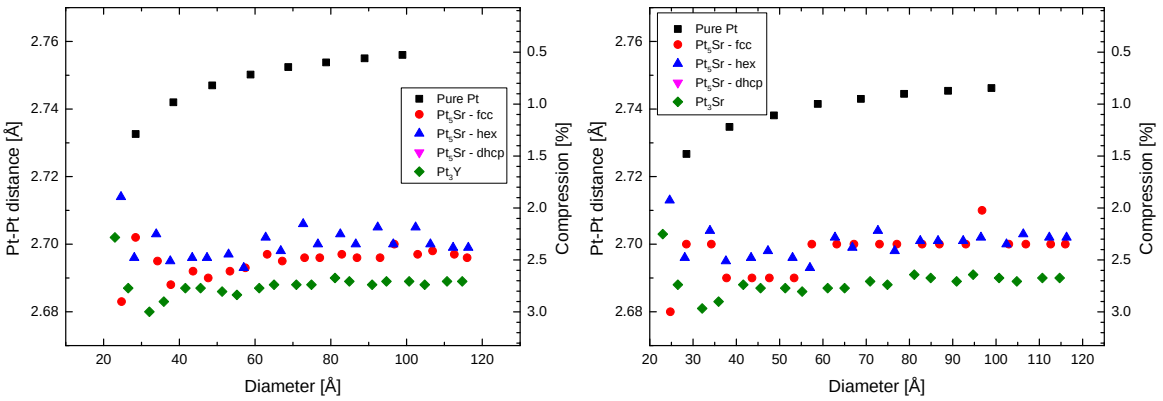

(a) **(b)**

Figure 6.19: *Mean Pt-Pt distance for nanoparticles created from the four Pt_xSr structures, together with Pt nanoparticles. For the full nanoparticles in a) and only the three outermost layers in b). Compression is with reference to bulk Pt.*

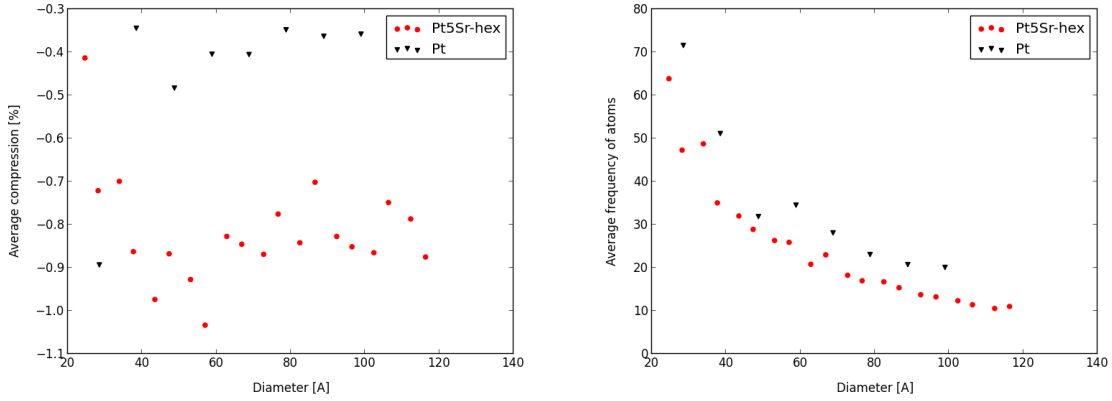

(a) **(b)**

Figure 6.20: *a) The average compression of the 9-coordinated surface atoms as a function of size. b) The frequency of 9-coordinated surface atoms with a compression between 0 and 4 %, normalised to the total number of atoms. Here is shown data only for Pt_5Sr in the hexagonal structure.*

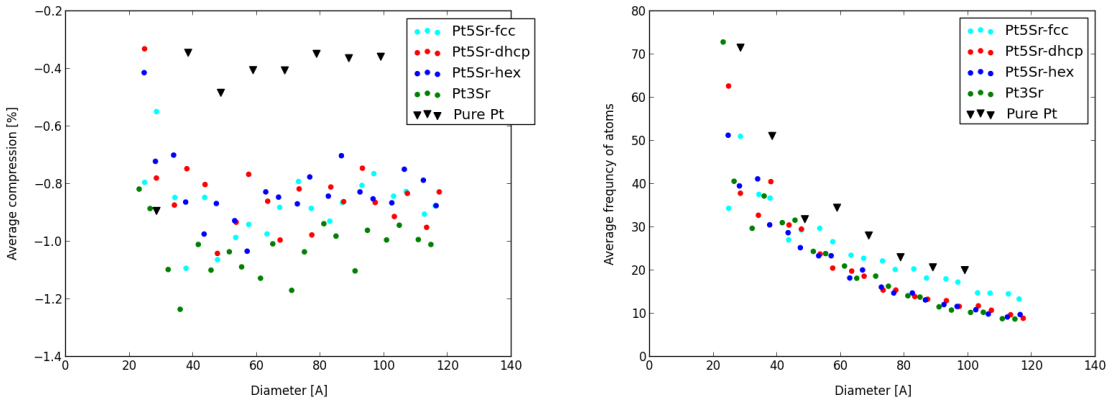

(a) (b)

Figure 6.21: *a) Average compression for 9-coordinated surface atoms for all Pt_xSr alloy structures and compared to pure Pt. b) Frequency of 9-coordinated surface atoms with a compression between 0 and 4 % for all Pt_xSr alloy structures and compared to pure Pt. In both cases are the Pt_5Sr-hex data the same as in figure 6.20 on the previous page.*

6.5.1 Structure of the core of Pt_5Sr-hex nanoparticles

As we have changed both the crystal structure and minority element used in constructing the nanoparticles, when compared to the Pt_xY analysis in section 6.4.2, we will do the analysis also for the Pt_5Sr-hex nanoparticles. In figure 6.22 on the facing page we show RDF's for the Pt-Sr and Sr-Sr elemental pairs. In this case, the Pt_2Sr-like peak for Sr-Sr is much more pronounced than the corresponding one for Y-Y, and here we also see the third peak coming up for the larger particles. The second peak is harder to describe, as both the hexagonal Pt_5Sr and Pt_2Sr has a line at the same value here. For the Pt-Sr distances, the peaks seem more aligned with the bulk values than for Pt-Y, but it is hard to deduce anything specific because both structures have their bulk peaks so close together. All in all it seems that there is quite a lot of restructuring going on, perhaps even a form of phase segregation into Pt_2Sr and pure Pt.

However, visual inspection, with a few examples shown in figure 6.23 on the next page, tells a different story. The core of the shell-particle in figure 6.23a on the facing page seems fairly ordered, more than would be expected if there had been phase segregation going on. The explanation for the appearance of the Sr-Sr peak at low distances, seems to be that the Sr atoms pairwise move close together, creating Pt_2Sr-like dimers. This effect is even more pronounced in the shell-less particle shown in figure 6.23b on the next page, where the core is very ordered, but every other row of Sr atoms have moved in one direction, and the rest in the opposite.

6.6 Trends across elements in Pt_5M alloys

In order to study the effect of the specific element on the Pt-Pt distances, we show in figure 6.24 on page 74 the mean Pt-Pt distance for the five different Pt_5M alloys, all initiated in the hex structure. It is very interesting how there seems to be an inverse relationship

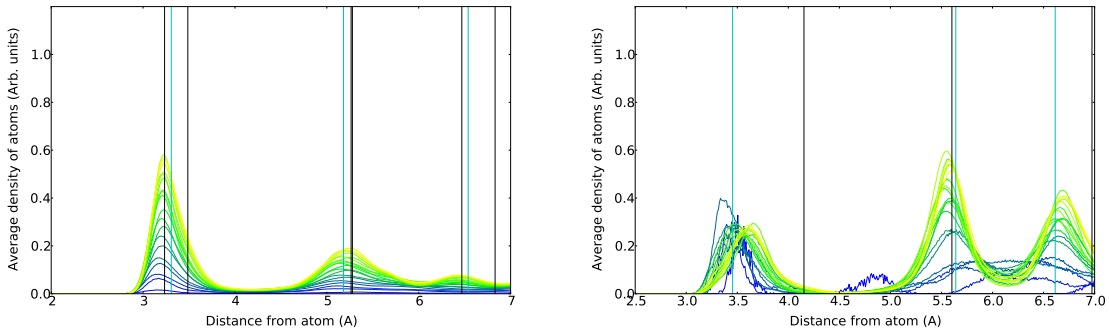

(a) **(b)**

Figure 6.22: *RDF's for Pt_5Sr-hex nanoparticles with a shell of approximately 1 nm: a) Pt-Sr distances and b) Sr-Sr distances. Black lines denote the bulk Pt_5Sr-hex values and cyan denote bulk Pt_2Sr.*

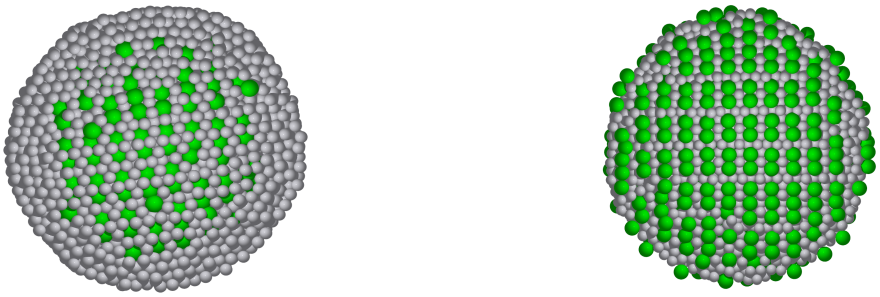

(a) **(b)**

Figure 6.23: *Representative Pt_5Sr-hex nanoparticles with a diameter of about 7 nm: a) with a shell of about 1 nm, and b) without a shell.*

between the size of the minority element and the Pt-Pt distance in the shell. The two alloys with Pt-Pt distances closest to pure Pt are also those with the smallest covalent radii[63].

As before, we take a closer look at the catalytically relevant 9-coordinated surface atoms, where we plot the average compression and frequency of 9-coordinated surface atoms with a compression in the interesting range. The average compression in figure 6.25a on the next page is generally lower than for pure Pt, with Pt_5Ca and Pt_5Sr being fairly consistent. However, for Pt_5Y the scatter is much larger, with some of the points having the largest average compression, while others are very close to pure Pt. This is probably the same phenomenon as was seen in figure 6.10 on page 64, confirming that there is some special behaviour in hexagonal Pt_5Y.

6.7 Trends across elements in Pt_3M alloys

To further explore the dependence of the Pt-Pt distance in the Pt overlayer on the size of the minority element used to construct the nanoparticles, we show in figure 6.26 on page 75 the Pt-Pt distances in the full particle and shell of nanoparticles constructed using Pt_3M alloys in the $L1_2$ structure. Here the effect seen in the previous section is even more pronounced

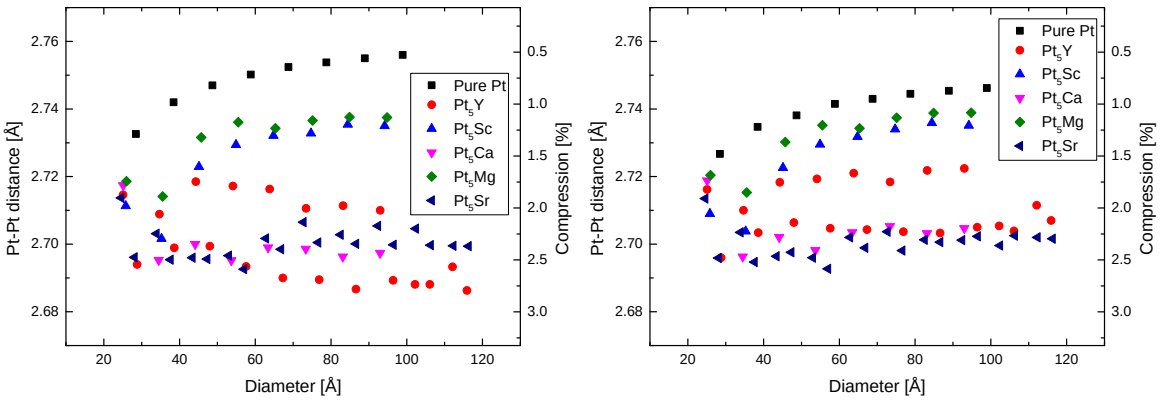

(a) **(b)**

Figure 6.24: *Mean Pt-Pt distance for particles of the five Pt_5M alloys. a) Full nanoparticle and b) outermost three layers. Compression is with reference to bulk Pt. Pt_5Y and Pt_5Sr data have already been presented in figures 6.10 and 6.19.*

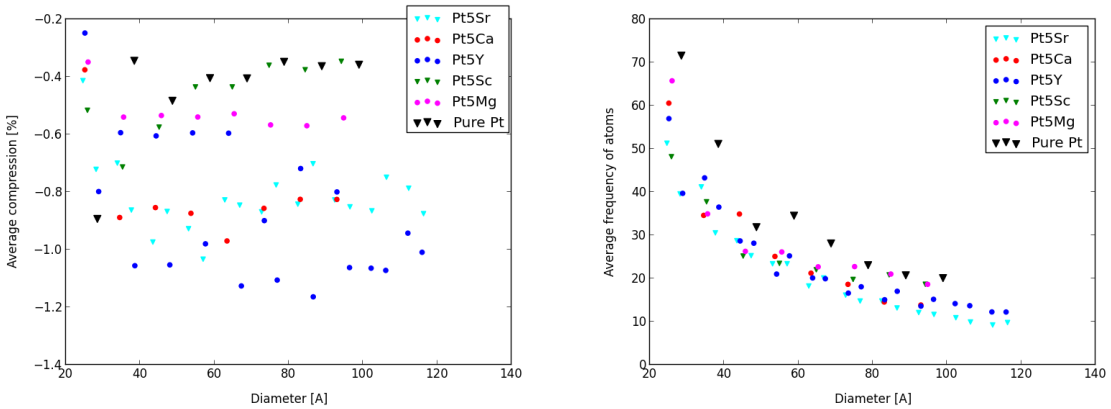

(a) **(b)**

Figure 6.25: *a) Average compression for 9-coordinated surface atoms for all Pt_5M alloys in the hexagonal structure and compared to pure Pt. b) Frequency of 9-coordinated surface atoms with a compression in the interesting region for all Pt_5M alloys in the hexagonal structure and compared to pure Pt. In both cases are the Pt_5Y data the same as in figure 6.13 and Pt_5Sr as in figure 6.21 and 6.20.*

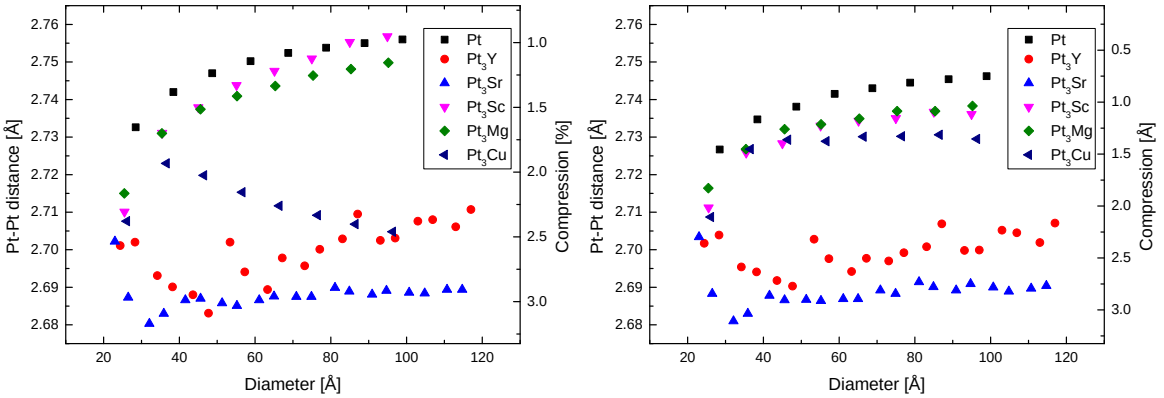

Figure 6.26: *Mean Pt-Pt distance for particles of the six Pt_3M alloys. a) Calculated for the full nanoparticle. b) Calculated only for the outermost three layers. Compression is relative to bulk Pt. Pt_3Y and Pt_3Sr data have already been presented in figures 6.10 and 6.19.*

with Pt_3Sr having a significantly more compressed overlayer than Pt_3Y, with both of them much more compressed than the alloys with smaller lattice parameters. This is especially surprising considering that Pt_3Cu has a much smaller lattice parameter compared to Pt, but it lies fairly close to pure Pt, together with Pt_3Sc and Pt_3Mg, which both have lattice parameters close to pure Pt. Especially for Pt_3Cu, there is also a significant difference between the full nanoparticle and the shell; in the full nanoparticle there is a clear downward trend with increasing size, due to the bulk-like core becoming comparatively larger, while the Pt-Pt distance in the shell is constant with size.

In figure 6.27 we plot the average compression of 9-coordinated surface atoms and their frequency with a compression between 0 and 4 %. For the average compression in figure 6.27a there is a clear separation between Pt, Pt_3Mg and Pt_3Sc, and the others. It is interesting to note that Pt_3Mg and Pt_3Sc have lattice parameters which are close to pure Pt, while Pt_3Cu is much smaller, and Pt_3Y and Pt_3Sr are much larger. Even so, the latter three result in an average compression of the 9-coordinated surface atoms. In figure 6.27b there is no clear separation, as they all are clearly lower than pure Pt, though Pt_3Sr seems to be slightly higher than the others. The interesting question is then, once again, whether the much higher average compression or the frequency is the more important parameter.

6.7.1 Structure of the Pt_3M core

Pt_3Y and Pt_3Sr both show very promising average compressions and it is therefore interesting to take a closer look at what goes on in the core in an attempt to deduce the reason for this behaviour. In figure 6.28 on the following page we show RDF's for the Y-Y and Sr-Sr distances in the two types of nanoparticles. It shows that there are two very different situations in the cores of the particles. While Pt_3Sr shows a very clear peak at the Pt_2Sr value, and basically nothing at the first Pt_3Sr value, Pt_3Y show marked peaks for the Pt_3Y values, except for the smallest particles. This shows that the Pt_3Sr nanoparticles have a high degree of restructuring, while the Pt_3Y nanoparticles show a much greater tendency to stay in the original crystal structure. This is further validated by the example nanoparticles shown in figure 6.29 where there is almost no discernible $L1_2$ structure visible for Pt_3Sr, while Pt_3Y

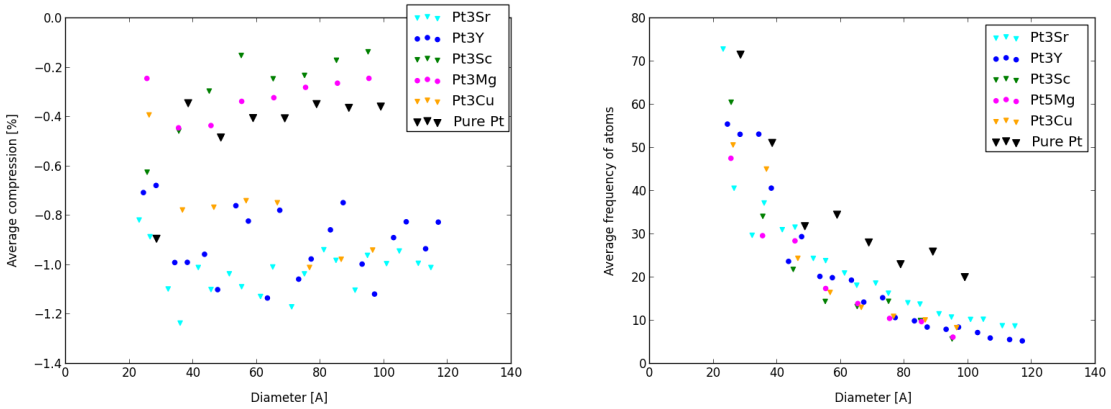

(a) **(b)**

Figure 6.27: *a) Average compression for 9-coordinated surface atoms for all Pt_3M alloys and compared to pure Pt. b) Frequency of 9-coordinated surface atoms with a compression in the interesting region for all Pt_3M alloys and compared to pure Pt. In both cases are the Pt_3Y data the same as in figure 6.13 and Pt_3Sr as in figure 6.21.*

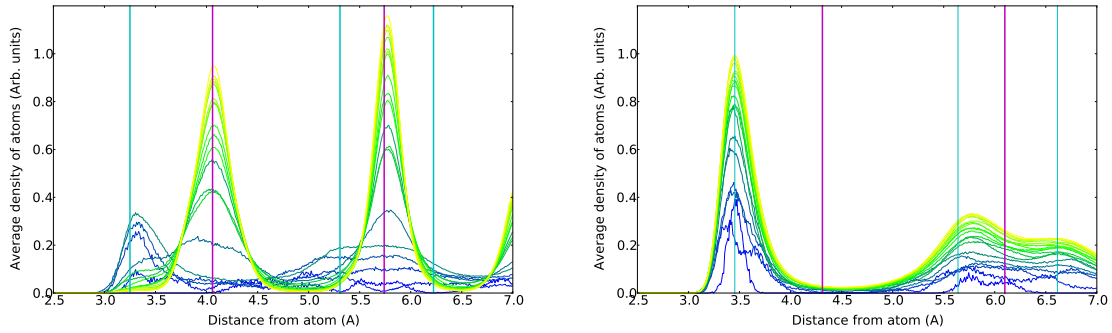

(a) **(b)**

Figure 6.28: *M-M RDF's for Pt_3M nanoparticles with a shell of approximately 1 nm: a) Y-Y distances, and b) Sr-Sr distances. Magenta lines denote the bulk Pt_3M values and cyan denote bulk Pt_2M.*

exhibits a large crystalline core. As mentioned earlier, we have found Pt_3Sr only in a proposed phase diagram, and we have not been able to find crystallographic data, indicating that it might not be a stable phase.

6.8 Influence of shell thickness

As a final exercise, we will look at the effect of the induced shell thickness on the Pt-Pt distance. In this case we look at Pt_5Sc prepared from the hexagonal structure, but, as mentioned earlier, it is difficult to know what has happened in the core during the simulation. The initial shell is either 0, 5, 10, 15 or 20 Å thick, but for the analysis purposes, it is defined

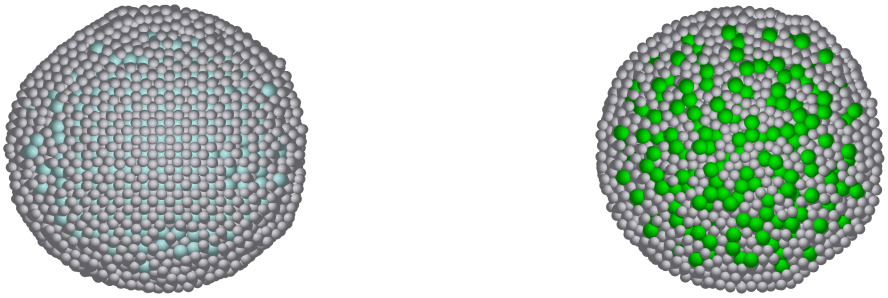

(a) (b)

Figure 6.29: *Representative Pt_3M nanoparticles with a diameter of about 8 nm: a) Pt_3Y and b) Pt_3Sr.*

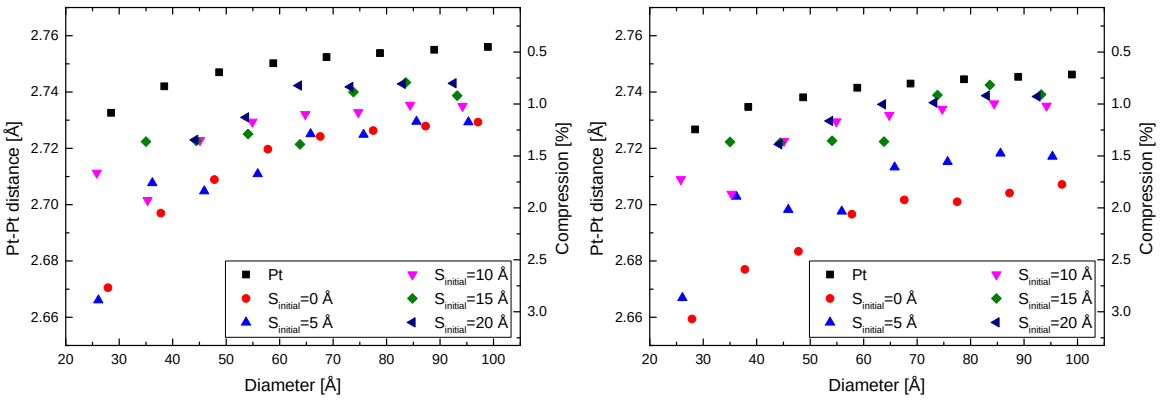

(a) (b)

Figure 6.30: *Mean Pt-Pt distance for Pt_5Sc particles initiated in the hexagonal structure, with five different induced shell thicknesses, S_{initial}. Compression is relative to bulk Pt. a) Calculated for the full nanoparticle. b) Calculated for the outermost three layers. The data for shell thickness of 10 Å have already been presented in figure 6.24.*

as the outermost 3 layers in all cases. The results are shown in figure 6.30. For initial shells of 0 and 5 Å, the mean Pt-Pt distance is quite low in both the full particle and the shell. This is obviously because the bulk Pt_5Sc structure is quite dominant in these cases. For initial shells of 10 Å and greater, there is more difference between the two plots, as the three outermost layers are now, more or less, devoid of Sc. However, it seems there is very little effect of increasing the initial shell thickness in this case. This is probably due to a quick convergence towards the value for pure Pt, and we would probably see a more gradual change for an alloy with a larger minority atom, such as Sr or Y.

6.9 Chapter summary and discussion

In this chapter we have presented the results of our Molecular Dynamics simulations on nanoparticles made from alloys of Pt and various other metals. We have shown how the Pt-Pt distance varies as a function of size for the various alloys and crystal structures used

to construct the nanoparticle. We have shown how minority elements which are both larger and smaller than Pt can cause a significant compression of the Pt-Pt distances on the surface of the nanoparticle. We speculate that this is caused by a disruption of the crystal symmetry at the interface between the Pt overlayer and the alloy core, allowing the surface atoms to contract unhampered by symmetry. We cannot rule out that some of these effects might be artefacts of the EMT description of the system, which is not as accurate as DFT. However, simulations like these are currently practically impossible to do with DFT.

The results in this chapter indicate that the Pt-Pt distance at the surface is less coupled to the core structure than previously believed. This indicates that the important feature of a Pt alloy in the nanoparticulate form is the mismatch between the core structure and pure Pt, if ORR activity is to be optimised. However, we speculate that this mismatch is also inherently a destabilising influence, and further work is needed to understand how we can optimise both activity and stability at the same time. Based on these results, it seems that Pt_3Y has a good mix of core stability and compressed Pt-Pt distance at the surface.

The present method of creating the nanoparticles results in rather spherical particles. It could be relevant to define a method which uses a Wulff-like construction as the starting point, and see if this makes any difference in the results.

Chapter 7

Conclusion and Outlook

7.1 Conclusion

The overall aim of thesis has been to investigate various aspects of the activity and stability of Pt alloys as catalysts for the Oxygen Reduction Reaction (ORR). This has been done to further our understanding of these systems, aiding in the effort to develop new catalysts for the ORR with higher activity than pure Pt, without sacrificing stability. This is necessary if fuel cell cars are to become a widespread technology. In this thesis we have investigated phenomena related to Pt alloys in the form of bulk alloys, extended surfaces and nanoparticles, as they can all contribute to our understanding of this class of materials as a catalyst.

We have investigated the bulk diffusion of the minority element in A_3M alloys and shown how the barrier for vacancy diffusion scales with the alloying energy of the alloy for both Pt_3M, Pd_3M and Al_3M in the $L1_2$ structure. We used an energy difference along the chosen diffusion path as a descriptor for the full barrier to extend the number of systems we could treat. These results support the notion that alloys of Pt and and early transition metals should be more stable under reaction conditions due to the high alloying energy; we show that they should be less prone to diffusion related degradation mechanisms.

The surface of the catalyst is exposed to the corrosive conditions of the electrolyte where the reaction takes place, and it is important that this surface is stable under these conditions. However, we have shown that for some adsorbates, there is a correlation between the adsorption energy and the stability of the Pt surface layer, setting a limit for the stability of the surface if a given adsorption energy is necessary for optimal activity. We also show that this correlation is qualitatively different between adsorbates which bind through the same atom, indicating that it might be possible to bend the scaling relation between their adsorption energies through the right combination of strain and ligand effects.

For Pt alloys in the nanoparticulate form, we have shown how the Pt-Pt distance at the surface, which is essential for the catalytic activity, depends on the specific alloy phase used to construct the nanoparticle. We have shown how the smallest Pt-Pt distance at the surface is found for nanoparticles constructed from alloy phases with a minority element which is either much larger, or much smaller than Pt. The former is true even if it forms a phase where the bulk crystal distances are much larger than equilibrium Pt; the Pt-Pt distance at the surface is still much smaller than equilibrium Pt. We speculate that the large lattice mismatch at the interface between the alloy core and the pure Pt overlayer decouples the two phases. This frees the Pt overlayer to contract in order to satisfy the loss of electron density at the surface, unhampered by an underlying crystal symmetry governing the interatomic distances.

7.2 Outlook

While this thesis has furthered our understanding of Pt alloys as ORR catalysts, there are still questions to be asked and answered. Our work on diffusion has so far been limited to the well-defined bulk of the $L1_2$ structure. It would be very beneficial if we could extend it all the way to the surface and also take the electrolyte into account, giving a more complete picture of the dealloying process. It would also be an improvement if we can find a method to describe diffusion in more complex structures, such as those for Pt_5M that was introduced in chapter 6. The main challenge here is to find and define one or more diffusion processes which are relevant and computationally practical. A third avenue of improvement would be to work explicitly with dealloying in nanoparticles, combining the work presented in chapters 4 and 6. However, this is hampered by the underestimation of barriers by EMT.

The nanoparticulate form is the form most relevant for catalytic purposes, and it is therefore of special interest to investigate all relevant phenomena on this scale. However, this is hampered by the fact that even small nanoparticles are too big for DFT-based methods to be practical. This makes it very difficult to include the electrolyte explicitly and it is therefore a significant challenge to develop methods which incorporates more of the system and still rest on a solid theoretical foundation.

Bibliography

[1] R. K. Pachauri and L. A. Meyer, editors. *IPCC, 2014: Climate Change 2014: Synthesis Report. Contribution of Working Groups I, II and III to the Fifth Assessment Report of the Intergovernmental Panel on Climate Change*. IPCC, Geneva, Switzerland.

[2] F. Birol and R. Priddle. *Energy and Climate Change*. Technical report (2015).

[3] British Petroleum. *BP Statistical Review of World Energy June 2015*. Technical report (2015).

[4] C. A. Hall, R. Powers, and W. Schoenberg. *Peak Oil, EROI, Investments and the Economy in an Uncertain Future*. In *Biofuels, Sol. Wind as Renew. Energy Syst. Benefits Risks*, pp. 109–132 (2008). ISBN 978-1-4020-8653-3.

[5] *HDI, Energy Consumption and CO2 Emissions*.
URL `http://www.thewatt.com/node/170`

[6] International Energy Agency. *World Energy Outlook 2014 - Executive Summary*. Technical report (2014).

[7] *World Population Graphs* (2015).
URL `http://esa.un.org/unpd/wpp/Graphs/`

[8] S. Safarkhanlou, editor. *Wind power to combat climate change*. ISBN 9788790707651.

[9] *Naturvidenskabeligt Grundforløb - Transport - Elbiler*.
URL `http://sustainable.dk/naturvidenskabeligt-grundforlob/transport/4-elbiler/`

[10] *Hydrogen Storage - Fuel Cell Technologies Office - U.S. Department of Energy*.
URL `http://energy.gov/eere/fuelcells/hydrogen-storage`

[11] Duracell. *Technical Bulletin - Zinc-air batteries* (2009).

[12] Y. Hori, A. Murata, and R. Takahashi. *Formation of hydrocarbons in the electrochemical reduction of carbon dioxide at a copper electrode in aqueous solution*. J. Chem. Soc. Faraday Trans. 1, **85(8)**, p. 2309 (1989).

[13] A. A. Peterson, F. Abild-Pedersen, F. Studt, J. Rossmeisl, and J. K. Nørskov. *How copper catalyzes the electroreduction of carbon dioxide into hydrocarbon fuels*. Energy Environ. Sci., **3(9)**, p. 1311 (2010).

[14] A. A. Peterson and J. K. Nørskov. *Activity descriptors for CO2 electroreduction to methane on transition-metal catalysts*. J. Phys. Chem. Lett., **3**, pp. 251–258 (2012).

[15] Y.-J. Zhang and A. A. Peterson. *Oxygen-induced changes to selectivity-determining steps in electrocatalytic CO 2 reduction.* Phys. Chem. Chem. Phys., **17(6)**, pp. 4505–4515 (2015).

[16] J. H. Montoya, C. Shi, K. Chan, and J. K. Nørskov. *Theoretical Insights into a CO Dimerization Mechanism in CO2 Electroreduction.* J. Phys. Chem. Lett., **6(11)**, pp. 2032–2037 (2015).

[17] M. Karamad, H. A. Hansen, J. Rossmeisl, and J. K. Nørskov. *Mechanistic Pathway in the Electrochemical Reduction of CO 2 on RuO 2.* ACS Catal., **5(7)**, pp. 4075–4081 (2015).

[18] R. Frydendal. *Improving performance of catalysts for water electrolysis : The MnOx case.* Ph.D. thesis, Technical University of Denmark (2015).

[19] Honda. *FCX Clarity - Fuel cells comparison* (2015).
URL `http://automobiles.honda.com/fcx-clarity/fuel-cell-comparison.aspx`

[20] U.S. Department of Energy's Office of Energy Efficiency and Renewable Energy. *Where the Energy Goes: Gasoline Vehicles* (2015).
URL `http://www.fueleconomy.gov/feg/atv.shtml`

[21] M. Escudero-Escribano. *Electrocatalysis and surface nanostructuring : atomic ensemble effects and non-covalent interactions.* Ph.D. thesis, Universidad Autónoma de Madrid Departamento (2011).

[22] H. A. Gasteiger, S. S. Kocha, B. Sompalli, and F. T. Wagner. *Activity benchmarks and requirements for Pt, Pt-alloy, and non-Pt oxygen reduction catalysts for PEMFCs.* Appl. Catal. B Environ., **56(1-2)**, pp. 9–35 (2005).

[23] I. E. L. Stephens, A. S. Bondarenko, U. Grønbjerg, J. Rossmeisl, and I. Chorkendorff. *Understanding the electrocatalysis of oxygen reduction on platinum and its alloys.* Energy Environ. Sci., **5(5)**, p. 6744 (2012).

[24] P. C. K. Vesborg and T. F. Jaramillo. *Addressing the terawatt challenge: scalability in the supply of chemical elements for renewable energy.* RSC Adv., **2(21)**, p. 7933 (2012).

[25] U. Eberle, B. Müller, and R. von Helmolt. *Fuel cell electric vehicles and hydrogen infrastructure: status 2012.* Energy Environ. Sci., **5(10)**, p. 8780 (2012).

[26] Y. Nie, L. Li, and Z. Wei. *Recent advancements in Pt and Pt-free catalysts for oxygen reduction reaction.* Chem. Soc. Rev., pp. 2168–2201 (2015).

[27] M. Pourbaix. *Atlas of electrochemical equilibria in aqueous solutions.* National Association of Corrosion Engineers (1974).

[28] I. Chorkendorff and J. W. Niemantsverdriet. *Concepts of Modern Catalysis and Kinetics.* Wiley-VCH Verlag GmbH, second edition (2007).

[29] *"CatalysisScheme". Licensed under Public Domain via Commons.*
URL `https://commons.wikimedia.org/wiki/File:CatalysisScheme.png{\#}/media/File:CatalysisScheme.png`

[30] J. K. Nørskov, J. Rossmeisl, A. Logadottir, L. Lindqvist, J. R. Kitchin, T. Bligaard, and H. Jónsson. *Origin of the Overpotential for Oxygen Reduction at a Fuel-Cell Cathode.* J. Phys. Chem. B, **108(46)**, pp. 17886–17892 (2004).

[31] G. S. Karlberg, J. Rossmeisl, and J. K. Nørskov. *Estimations of electric field effects on the oxygen reduction reaction based on the density functional theory.* Phys. Chem. Chem. Phys., **9(37)**, pp. 5158–5161 (2007).

[32] J. Rossmeisl, G. S. Karlberg, T. F. Jaramillo, and J. K. Nørskov. *Steady state oxygen reduction and cyclic voltammetry.* Faraday Discuss., **140**, pp. 337–346 (2008).

[33] I. E. L. Stephens, A. S. Bondarenko, F. J. Perez-Alonso, F. Calle-Vallejo, L. Bech, T. P. Johansson, A. K. Jepsen, R. Frydendal, B. P. Knudsen, J. Rossmeisl, and I. Chorkendorff. *Tuning the activity of Pt(111) for oxygen electroreduction by subsurface alloying.* J. Am. Chem. Soc., **133(14)**, pp. 5485–91 (2011).

[34] J. Rossmeisl, A. Logadottir, and J. K. Nørskov. *Electrolysis of water on (oxidized) metal surfaces.* Chem. Phys., **319(1-3)**, pp. 178–184 (2005).

[35] F. Abild-Pedersen, J. Greeley, F. Studt, J. Rossmeisl, T. Munter, P. Moses, E. Skúlason, T. Bligaard, and J. K. Nørskov. *Scaling Properties of Adsorption Energies for Hydrogen-Containing Molecules on Transition-Metal Surfaces.* Phys. Rev. Lett., **99(1)**, p. 016105 (2007).

[36] D. Friebel, D. J. Miller, D. Nordlund, H. Ogasawara, and A. Nilsson. *Degradation of bimetallic model electrocatalysts: an in situ X-ray absorption spectroscopy study.* Angew. Chem. Int. Ed. Engl., **50(43)**, pp. 10190–2 (2011).

[37] B. Hammer and J. K. Nørskov. *Electronic factors determining the reactivity of metal surfaces.* Surf. Sci., **343**, pp. 211–220 (1995).

[38] B. Hammer and J. K. Norskov. *Why gold is the noblest of all the metals.* Nature, **376**, pp. 238–240 (1995).

[39] B. Hammer, Y. Morikawa, and J. K. Nørskov. *CO chemisorption at metal surfaces and overlayers.* Phys. Rev. Lett., **76(12)**, pp. 2141–2144 (1996).

[40] A. Ruban, B. Hammer, P. Stoltze, H. L. Skriver, and J. K. Nørskov. *Surface electronic structure and reactivity of transition and noble metals.* J. Mol. Catal. A Chem., **115(3)**, pp. 421–429 (1997).

[41] M. Mavrikakis, B. Hammer, and J. K. Nørskov. *Effect of Strain on the Reactivity of Metal Surfaces.* Phys. Rev. Lett., **81(13)**, pp. 2819–2822 (1998).

[42] T. V. W. Janssens, B. S. Clausen, B. Hvolbæk, H. Falsig, C. H. Christensen, T. Bligaard, and J. K. Nørskov. *Insights into the reactivity of supported Au nanoparticles: combining theory and experiments.* Top. Catal., **44(1-2)**, pp. 15–26 (2007).

[43] J. R. Kitchin, J. K. Nørskov, M. A. Barteau, and J. G. Chen. *Modification of the surface electronic and chemical properties of Pt(111) by subsurface 3d transition metals.* J. Chem. Phys., **120(21)**, pp. 10240–6 (2004).

[44] F. Calle-Vallejo, J. I. Martínez, J. M. García-Lastra, J. Rossmeisl, and M. T. Koper. *Physical and Chemical Nature of the Scaling Relations between Adsorption Energies of Atoms on Metal Surfaces.* Phys. Rev. Lett., **108(11)**, p. 116103 (2012).

[45] S. Mukerjee and S. Srinivasan. *Enhanced electrocatalysis of oxygen reduction on platinum alloys in proton exchange membrane fuel cells.* J. Electroanal. Chem., **357(1-2)**, pp. 201–224 (1993).

[46] S. Mukerjee, S. Srinivasan, M. Soriaga, and J. Mcrreen. *Role of Structural and Electronic Properties of Pt and Pt Alloys on Electrocatalysis of Oxygen Reduction.* J. Electrochem. Soc., **142(5)**, p. 1409 (1995).

[47] S. Mukerjee and J. McBreen. *Effect of particle size on the electrocatalysis by carbon-supported Pt electrocatalysts: an in situ XAS investigation.* J. Electroanal. Chem., **448(2)**, pp. 163–171 (1998).

[48] T. Toda, H. Igarashi, H. Uchida, and M. Watanabe. *Enhancement of the electroreduction of Oxygen on Pt alloys with Fe, Ni, and Co.* J. Electrochem. Soc., **146(10)**, pp. 3750–3756 (1999).

[49] S. Chen, H. A. Gasteiger, K. Hayakawa, T. Tada, and Y. Shao-Horn. *Platinum-Alloy Cathode Catalyst Degradation in Proton Exchange Membrane Fuel Cells: Nanometer-Scale Compositional and Morphological Changes.* J. Electrochem. Soc., **157(1)**, p. A82 (2010).

[50] K. J. J. Mayrhofer, K. Hartl, V. Juhart, and M. Arenz. *Degradation of carbon-supported Pt bimetallic nanoparticles by surface segregation.* J. Am. Chem. Soc., **131(45)**, pp. 16348–16349 (2009).

[51] H. L. Xin, J. A. Mundy, Z. Liu, R. Cabezas, R. Hovden, L. F. Kourkoutis, J. Zhang, N. P. Subramanian, R. Makharia, F. T. Wagner, and D. A. Muller. *Atomic-resolution spectroscopic imaging of ensembles of nanocatalyst particles across the life of a fuel cell.* Nano Lett., **12(1)**, pp. 490–7 (2012).

[52] C. Baldizzone, S. Mezzavilla, H. W. P. Carvalho, J. C. Meier, A. K. Schuppert, M. Heggen, C. Galeano, J.-D. Grunwaldt, F. Schüth, and K. J. J. Mayrhofer. *Confined-Space Alloying of Nanoparticles for the Synthesis of Efficient PtNi Fuel-Cell Catalysts.* Angew. Chem. Int. Ed. Engl., pp. 14250–14254 (2014).

[53] B. Han, C. E. Carlton, A. Kongkanand, R. S. Kukreja, B. R. Theobald, L. Gan, R. O'Malley, P. Strasser, F. T. Wagner, and Y. Shao-Horn. *Record activity and stability of dealloyed bimetallic catalysts for proton exchange membrane fuel cells.* Energy Environ. Sci., **8(1)**, pp. 258–266 (2015).

[54] C. Chen, Y. Kang, Z. Huo, Z. Zhu, W. Huang, H. L. Xin, J. D. Snyder, D. Li, J. A. Herron, M. Mavrikakis, M. Chi, K. L. More, Y. Li, N. M. Marković, G. A. Somorjai, P. Yang, and V. R. Stamenkovic. *Highly crystalline multimetallic nanoframes with three-dimensional electrocatalytic surfaces.* Science, **343(6177)**, pp. 1339–43 (2014).

[55] X. Huang, Z. Zhao, L. Cao, Y. Chen, E. Zhu, Z. Lin, M. Li, A. Yan, A. Zettl, Y. M. Wang, X. Duan, T. Mueller, and Y. Huang. *High-performance transition metal-doped Pt3Ni octahedra for oxygen reduction reaction.* Science (80-.)., **348(6240)**, pp. 1230–1234 (2015).

[56] L. Dubau, M. Lopez-Haro, L. Castanheira, J. Durst, M. Chatenet, P. Bayle-Guillemaud, L. Guétaz, N. Caqué, E. Rossinot, and F. Maillard. *Probing the structure, the composition and the ORR activity of Pt3Co/C nanocrystallites during a 3422h PEMFC ageing test.* Appl. Catal. B Environ., **142-143**, pp. 801–808 (2013).

[57] A. Ohma, K. Shinohara, A. Iiyama, T. Yoshida, and A. Daimaru. *Membrane and Catalyst Performance Targets for Automotive Fuel Cells by FCCJ Membrane, Catalyst, MEA WG.* ECS Trans., **41(1)**, pp. 775–784 (2011).

[58] A. Marcu, G. Toth, and R. J. Behm. *Electrochemical Test Procedures for Accelerated Evaluation of Fuel Cell Cathode Catalyst Degradation.* Fuel Cells, **14(3)**, pp. 378–385 (2014).

[59] J. Greeley, I. E. L. Stephens, A. S. Bondarenko, T. P. Johansson, H. A. Hansen, T. F. Jaramillo, J. Rossmeisl, I. Chorkendorff, and J. K. Nørskov. *Alloys of platinum and early transition metals as oxygen reduction electrocatalysts.* Nat. Chem., **1(7)**, pp. 552–556 (2009).

[60] I. E. L. Stephens, A. S. Bondarenko, L. Bech, and I. Chorkendorff. *Oxygen Electroreduction Activity and X-Ray Photoelectron Spectroscopy of Platinum and Early Transition Metal Alloys.* ChemCatChem, **4(3)**, pp. 341–349 (2012).

[61] M. Escudero-Escribano, A. Verdaguer-Casadevall, P. Malacrida, U. Grønbjerg, B. P. Knudsen, A. K. Jepsen, J. Rossmeisl, I. E. L. Stephens, and I. Chorkendorff. *Pt5Gd as a highly active and stable catalyst for oxygen electroreduction.* J. Am. Chem. Soc., **134(40)**, pp. 16476–9 (2012).

[62] P. Malacrida, M. Escudero-Escribano, A. Verdaguer-Casadevall, I. E. L. Stephens, and I. Chorkendorff. *Enhanced activity and stability of Pt–La and Pt–Ce alloys for oxygen electroreduction: the elucidation of the active surface phase.* J. Mater. Chem. A, **2(12)**, p. 4234 (2014).

[63] B. Cordero, V. Gómez, A. E. Platero-Prats, M. Revés, J. Echeverría, E. Cremades, F. Barragán, and S. Alvarez. *Covalent radii revisited.* Dalton Trans., **(21)**, pp. 2832–8 (2008).

[64] U. G. Andersen. *Modelling of structure and reactivity of Platinum alloys as catalysts for the Oxygen Reduction Reaction.* Ph.D. thesis, Technical University of Denmark (2012).

[65] V. R. Stamenkovic, B. S. Mun, K. J. J. Mayrhofer, P. N. Ross, and N. M. Marković. *Effect of surface composition on electronic structure, stability, and electrocatalytic properties of Pt-transition metal alloys: Pt-skin versus Pt-skeleton surfaces.* J. Am. Chem. Soc., **128(27)**, pp. 8813–9 (2006).

[66] M. Escudero-Escribano, P. Malacrida, U. G. Vej-Hansen, V. Tripkovic, J. Schiøtz, J. Rossmeisl, I. E. L. Stephens, and I. Chorkendorff. *Using the lanthanide contraction to engineer the activity and stability of Pt-based oxygen reduction electrocatalysts.* Prep. (2015).

[67] B. Han, C. E. Carlton, J. Suntivich, Z. Xu, and Y. Shao-Horn. *Oxygen Reduction Activity and Stability Trends of Bimetallic Pt 0.5 M 0.5 Nanoparticle in Acid.* J. Phys. Chem. C, **119(8)**, pp. 3971–3978 (2015).

[68] F. Masini, P. Hernández-Fernández, D. Deiana, C. E. Strebel, D. N. McCarthy, A. Bodin, P. Malacrida, I. E. L. Stephens, and I. Chorkendorff. *Exploring the phase space of time of flight mass selected PtxY nanoparticles.* Phys. Chem. Chem. Phys., **16(48)**, pp. 26506–13 (2014).

[69] P. Hernandez-Fernandez, F. Masini, D. N. McCarthy, C. E. Strebel, D. Friebel, D. Deiana, P. Malacrida, A. Nierhoff, A. Bodin, A. M. Wise, J. H. Nielsen, T. W. Hansen, A. Nilsson, I. E. L. Stephens, and I. Chorkendorff. *Mass-selected nanoparticles of PtxY as model catalysts for oxygen electroreduction.* Nat. Chem., **6(8)**, pp. 732–8 (2014).

[70] A. Velázquez-Palenzuela, F. Masini, A. F. Pedersen, M. Escudero-Escribano, D. Deiana, P. Malacrida, T. W. Hansen, D. Friebel, A. Nilsson, I. E. L. Stephens, and I. Chorkendorff. *The enhanced activity of mass-selected PtxGd nanoparticles for oxygen electroreduction.* J. Catal., **328**, pp. 297–307 (2015).

[71] F. J. Perez-Alonso, D. N. McCarthy, A. Nierhoff, P. Hernandez-Fernandez, C. E. Strebel, I. E. L. Stephens, J. H. Nielsen, and I. Chorkendorff. *The Effect of Size on the Oxygen Electroreduction Activity of Mass-Selected Platinum Nanoparticles.* Angew. Chemie Int. Ed., **51(19)**, pp. 4641–4643 (2012).

[72] D. Sayers, E. Stern, and F. Lytle. *New technique for investigating noncrystalline structures: Fourier analysis of the Extended X-Ray Absorption Fine Structure.* Phys. Rev. Lett., **27(18)** (1971).

[73] A. Filipponi, A. D. Cicco, and C. Natoli. *X-ray-absorption spectroscopy and n-body distribution functions in condensed matter. I. Theory.* Phys. Rev. B, **52(21)**, pp. 122–134 (1995).

[74] E. Stern. *Musings about the development of XAFS.* J. Synchrotron Radiat., **8**, pp. 49–54 (2001).

[75] F. de Groot. *High-resolution X-ray emission and X-ray absorption spectroscopy.* Chem. Rev., **101(6)**, pp. 1779–808 (2001).

[76] J. Kohanoff. *Electronic Structure Calculations for Solids and Molecules.* Cambridge University Press (2006). ISBN 0-521-81591-6.

[77] P. Hohenberg and W. Kohn. *Inhomogeneous electron gas.* Phys. Rev., **136(3B)**, pp. 864–871 (1964).

[78] W. Kohn and L. Sham. *Self-consistent equations including exchange and correlation effects.* Phys. Rev., **140(4A)**, pp. 1133–1138 (1965).
URL `http://link.aps.org/doi/10.1103/PhysRev.140.A1133`

[79] J. P. Perdew. *Jacob's ladder of density functional approximations for the exchange-correlation energy.* In *AIP Conf. Proc.*, volume 577, pp. 1–20. AIP (2001). ISBN 0735400164.

[80] J. Perdew, K. Burke, and M. Ernzerhof. *Generalized Gradient Approximation Made Simple.* Phys. Rev. Lett., **77(18)**, pp. 3865–3868 (1996).

[81] J. Wellendorff, K. Lundgaard, A. Møgelhøj, V. Petzold, D. Landis, J. K. Nørskov, T. Bligaard, and K. W. Jacobsen. *Density functionals for surface science: Exchange-correlation model development with Bayesian error estimation.* Phys. Rev. B, **85(23)**, p. 235149 (2012).

[82] B. Hammer, L. Hansen, and J. K. Nørskov. *Improved adsorption energetics within density-functional theory using revised Perdew-Burke-Ernzerhof functionals.* Phys. Rev. B, **59(11)**, pp. 7413–7421 (1999).

[83] J. P. Perdew, A. Ruzsinszky, G. I. Csonka, O. A. Vydrov, G. E. Scuseria, L. A. Constantin, X. Zhou, and K. Burke. *Restoring the Density-Gradient Expansion for Exchange in Solids and Surfaces.* Phys. Rev. Lett., **100(13)**, p. 136406 (2008).

[84] J. Perdew, S. Kurth, A. Zupan, and P. Blaha. *Accurate Density Functional with Correct Formal Properties: A Step Beyond the Generalized Gradient Approximation.* Phys. Rev. Lett., **82(25)**, pp. 5179–5179 (1999).

[85] A. D. Becke. *A new mixing of Hartree–Fock and local density-functional theories.* J. Chem. Phys., **98(2)**, p. 1372 (1993).

[86] J. J. Mortensen, L. Hansen, and K. W. Jacobsen. *Real-space grid implementation of the projector augmented wave method.* Phys. Rev. B, **71(3)**, p. 035109 (2005).

[87] J. Enkovaara, C. Rostgaard, J. J. Mortensen, J. Chen, M. Dułak, L. Ferrighi, J. Gavnholt, C. Glinsvad, V. Haikola, H. A. Hansen, H. H. Kristoffersen, M. Kuisma, A. H. Larsen, L. Lehtovaara, M. Ljungberg, O. Lopez-Acevedo, P. G. Moses, J. Ojanen, T. Olsen, V. Petzold, N. A. Romero, J. Stausholm-Møller, M. Strange, G. A. Tritsaris, M. Vanin, M. Walter, B. Hammer, H. Häkkinen, G. K. H. Madsen, R. M. Nieminen, J. K. Nørskov, M. Puska, T. T. Rantala, J. Schiøtz, K. S. Thygesen, and K. W. Jacobsen. *Electronic structure calculations with GPAW: a real-space implementation of the projector augmented-wave method.* J. Phys. Condens. matter, **22(25)**, p. 253202 (2010).

[88] S. Bahn and K. W. Jacobsen. *An object-oriented scripting interface to a legacy electronic structure code.* Comput. Sci. Eng., pp. 56–66 (2002).

[89] D. Vanderbilt. *Soft self-consistent pseudopotentials in a generalized eigenvalue formalism.* Phys. Rev. B, **41(11)**, pp. 7892–7895 (1990).

[90] P. Blöchl. *Projector augmented-wave method.* Phys. Rev. B, **50(24)**, pp. 17953–17979 (1994).

[91] P. Blöchl, C. Först, and J. Schimpl. *Projector augmented wave method: ab initio molecular dynamics with full wave functions.* Bull. Mater. Sci., **26(1)**, pp. 33–41 (2003).

[92] A. H. Larsen, M. Vanin, J. J. Mortensen, K. S. Thygesen, and K. W. Jacobsen. *Localized atomic basis set in the projector augmented wave method.* Phys. Rev. B, **80(19)**, p. 195112 (2009).

[93] M. F. Ashby and D. R. H. Jones. *Engineering Materials I: An introduction to Properties, Applications and Design.* Elsevier (2005). ISBN 9780080545653.

[94] C. A. Menning and J. G. Chen. *Theoretical Prediction and Experimental Verification of Stability of Pt–3d–Pt Subsurface Bimetallic Structures: From Single Crystal Surfaces to Polycrystalline Films.* Top. Catal., **53(5-6)**, pp. 338–347 (2010).

[95] G. Mills and H. Jónsson. *Quantum and thermal effects in H_ {2} dissociative adsorption: Evaluation of free energy barriers in multidimensional quantum systems.* Phys. Rev. Lett., **72(7)**, pp. 1124–1128 (1994).

[96] G. Mills, H. Jónsson, and G. Schenter. *Reversible work transition state theory: application to dissociative adsorption of hydrogen.* Surf. Sci., **324**, pp. 305–337 (1995).

[97] H. Jónsson, G. Mills, and K. W. Jacobsen. *Nudged elastic band method for finding minimum energy paths of transitions.* pp. 385–404 (1998).

[98] G. Henkelman, B. P. Uberuaga, and H. Jónsson. *A climbing image nudged elastic band method for finding saddle points and minimum energy paths.* J. Chem. Phys., **113(22)**, p. 9901 (2000).

[99] G. Henkelman and H. Jónsson. *Improved tangent estimate in the nudged elastic band method for finding minimum energy paths and saddle points.* J. Chem. Phys., **113(22)**, p. 9978 (2000).

[100] G. L. Kellogg and P. J. Feibelman. *Surface self-diffusion on Pt(001) by an atomic exchange mechanism.* Phys. Rev. Lett., **64(26)**, pp. 3143–3146 (1990).

[101] C. Chen and T. T. Tsong. *Displacement distribution and atomic jump direction in diffusion of Ir atoms on the Ir(001) surface.* Phys. Rev. Lett., **64(26)**, pp. 3147–3150 (1990).

[102] S. Smidstrup, A. Pedersen, K. Stokbro, and H. Jónsson. *Improved initial guess for minimum energy path calculations.* J. Chem. Phys., **140(21)** (2014).

[103] J. N. Brønsted. *Acid and Basic catalysis.* Chem. Rev., **5(3)**, pp. 231–338 (1928).

[104] M. G. Evans and M. Polanyi. *Inertia and driving force of chemical reactions* (1938).

[105] T. P. Johansson, E. T. Ulrikkeholm, P. Hernandez-Fernandez, M. Escudero-Escribano, P. Malacrida, I. E. L. Stephens, and I. Chorkendorff. *Towards the elucidation of the high oxygen electroreduction activity of PtxY: surface science and electrochemical studies of Y/Pt(111).* Phys. Chem. Chem. Phys., **16(27)**, pp. 13718–25 (2014).

[106] N. Schumacher, K. Andersson, L. C. Grabow, M. Mavrikakis, J. Nerlov, and I. Chorkendorff. *Interaction of carbon dioxide with Cu overlayers on Pt(1 1 1).* Surf. Sci., **602(3)**, pp. 702–711 (2008).

[107] J. Tang, J. Lawrence, and J. Hemminger. *Structure and valence of the Ce/Pt (111) system.* Phys. Rev. B, **48(20)**, pp. 15342–15353 (1993).

[108] P. Vanýsek. *Handbook of Chemistry and Physics - Electrochemical Series* (2015).

[109] G. Jóhannesson, T. Bligaard, A. Ruban, H. L. Skriver, K. W. Jacobsen, and J. K. Nørskov. *Combined Electronic Structure and Evolutionary Search Approach to Materials Design.* Phys. Rev. Lett., **88(25)**, p. 255506 (2002).

[110] V. R. Stamenkovic, B. S. Mun, K. J. J. Mayrhofer, P. N. Ross, N. M. Marković, J. Rossmeisl, J. Greeley, and J. K. Nørskov. *Changing the activity of electrocatalysts for oxygen reduction by tuning the surface electronic structure.* Angew. Chem. Int. Ed. Engl., **45(18)**, pp. 2897–2901 (2006).

[111] V. R. Stamenkovic, B. Fowler, B. S. Mun, G. Wang, P. N. Ross, C. A. Lucas, and N. M. Marković. *Improved oxygen reduction activity on Pt3Ni(111) via increased surface site availability.* Science (80-.)., **315**, pp. 493–497 (2007).

[112] M. Du, L. Cui, Y. Cao, and A. J. Bard. *Mechanoelectrochemical Catalysis of the Effect of Elastic Strain on a Platinum nanofilm for the ORR Exerted by a Shape Memory Alloy Substrate.* J. Am. Chem. Soc., pp. 7397–7403 (2015).

[113] V. A. Sethuraman, D. Vairavapandian, M. C. Lafouresse, T. A. Maark, N. Karan, S. Sun, U. Bertocci, A. A. Peterson, G. R. Stafford, and P. R. Guduru. *Role of Elastic Strain on Electrocatalysis of Oxygen Reduction Reaction on Pt.* J. Phys. Chem. C, **119(33)**, pp. 19042–19052 (2015).

[114] Y. Yang, T. A. Maark, A. A. Peterson, and S. Kumar. *Elastic strain effects on catalysis of a PdCuSi metallic glass thin film.* Phys. Chem. Chem. Phys., **17**, pp. 1746–1754 (2015).

[115] A. S. Bandarenka, A. S. Varela, M. Karamad, F. Calle-Vallejo, L. Bech, F. J. Perez-Alonso, J. Rossmeisl, I. E. L. Stephens, and I. Chorkendorff. *Design of an active site towards optimal electrocatalysis: overlayers, surface alloys and near-surface alloys of Cu/Pt(111).* Angew. Chem. Int. Ed. Engl., **51(47)**, pp. 11845–8 (2012).

[116] A. Schlapka, M. Lischka, A. Groß, U. Käsberger, and P. Jakob. *Surface Strain versus Substrate Interaction in Heteroepitaxial Metal Layers: Pt on Ru(0001).* Phys. Rev. Lett., **91(1)**, p. 016101 (2003).

[117] J. R. Kitchin, J. K. Nørskov, M. A. Barteau, and J. G. Chen. *Role of strain and ligand effects in the modification of the electronic and chemical Properties of bimetallic surfaces.* Phys. Rev. Lett., **93(15)**, pp. 4–7 (2004).

[118] A. K. Jepsen. *Stability and Activity of New Alloy catalysts for the Oxygen Reduction Reaction under Acidic Conditions - Master Thesis* (2012).

[119] H. Monkhorst and J. Pack. *Special points for Brillouin-zone integrations.* Phys. Rev. B, **13(12)**, pp. 5188–5192 (1976).

[120] F. D. Murnaghan. *The Compressibility of Media under Extreme Pressures.* Proc. Natl. Acad. Sci. U. S. A., **30(9)**, pp. 244–247 (1944).

[121] A. Alchagirov, J. Perdew, J. Boettger, R. Albers, and C. Fiolhais. *Energy and pressure versus volume: Equations of state motivated by the stabilized jellium model.* Phys. Rev. B, **63(22)**, p. 224115 (2001).

[122] L. Eldén, L. Wittmeyer-Koch, and H. B. Nielsen. *Introduction to Numerical Computation.* Studentlitteratur (2004). ISBN 978-91-44-03727-1.

[123] G. Papoian, J. K. Nørskov, and R. Hoffmann. *A comparative theoretical study of the hydrogen, methyl, and ethyl chemisorption on the Pt(111) surface.* J. Am. Chem. Soc., **122(17)**, pp. 4129–4144 (2000).

[124] S. Badescu, K. Jacobi, Y. Wang, K. Bedürftig, G. Ertl, P. Salo, T. Ala-Nissila, and S. Ying. *Vibrational states of a H monolayer on the Pt(111) surface.* Phys. Rev. B, **68(20)** (2003).

[125] B. Fowler, C. A. Lucas, A. Omer, G. Wang, V. R. Stamenkovic, and N. M. Marković. *Segregation and stability at Pt3Ni(111) surfaces and Pt75Ni25 nanoparticles.* Electrochim. Acta, **53(21)**, pp. 6076–6080 (2008).

[126] T. P. Johansson, E. T. Ulrikkeholm, P. Hernandez-Fernandez, P. Malacrida, H. A. Hansen, A. S. Bandarenka, J. K. Nørskov, J. Rossmeisl, I. E. L. Stephens, and I. Chorkendorff. *Pt Skin Versus Pt Skeleton Structures of Pt3Sc as Electrocatalysts for Oxygen Reduction.* Top. Catal., **57(1-4)**, pp. 245–254 (2013).

[127] U. G. Vej-hansen, M. Escudero-Escribano, P. Malacrida, J. Rossmeisl, I. E. L. Stephens, I. Chorkendorff, and J. Schiøtz. *New Platinum alloy catalysts based on abundant alkaline earth metals.* Prep. (2015).

[128] A. I. Liechtenstein, V. I. Anisimov, and J. Zaanen. *Density-functional theory and strong interactions: Orbital ordering in Mott-Hubbard insulators.* Phys. Rev. B, **52(8)**, pp. 5467–5471 (1995).

[129] S. L. Dudarev, S. Y. Savrasov, C. J. Humphreys, and A. P. Sutton. *Electron-energy-loss spectra and the structural stability of nickel oxide: An LSDA+U study.* Phys. Rev. B, **57(3)**, pp. 1505–1509 (1998).

[130] P. Strasser, S. Koh, T. Anniyev, J. Greeley, K. More, C. Yu, Z. Liu, S. Kaya, D. Nordlund, H. Ogasawara, M. F. Toney, and A. Nilsson. *Lattice-strain control of the activity in dealloyed core-shell fuel cell catalysts.* Nat. Chem., **2(6)**, pp. 454–60 (2010).

[131] P. Mani, R. Srivastava, and P. Strasser. *Dealloyed binary PtM3 (M=Cu, Co, Ni) and ternary PtNi3M (M=Cu, Co, Fe, Cr) electrocatalysts for the oxygen reduction reaction: Performance in polymer electrolyte membrane fuel cells.* J. Power Sources, **196(2)**, pp. 666–673 (2011).

[132] R. Yang, P. Strasser, and M. F. Toney. *Dealloying of Cu 3 Pt (111) Studied by Surface X-ray Scattering.* J. Phys. Chem. C, **115(18)**, pp. 9074–9080 (2011).

[133] L. Han, H. Liu, P. Cui, Z. Peng, S. Zhang, and J. Yang. *Alloy Cu$_3$Pt nanoframes through the structure evolution in Cu-Pt nanoparticles with a core-shell construction.* Sci. Rep., **4**, p. 6414 (2014).

[134] M. P. Allen and D. J. Tildesley. *Computer Simulation of Liquids.* Oxford University Press, paperback edition (1987). ISBN 978-0-19-855645-9.

[135] K. W. Jacobsen, J. K. Nørskov, and M. Puska. *Interatomic interactions in the effective-medium theory.* Phys. Rev. B, **35(14)**, pp. 7423–7442 (1987).

[136] K. W. Jacobsen. *Bonding in metallic systems: An effective medium approach.* Comments Condens. Matter Phys., **14(3)**, pp. 129–161 (1988).

[137] K. W. Jacobsen, P. Stoltze, and J. K. Nørskov. *A semi-empirical effective medium theory for metals and alloys.* Surf. Sci., **366**, pp. 394–402 (1996).

[138] S. H. Brodersen, R. E. Chrstiansen, U. G. Vej-hansen, K. W. Jacobsen, and J. Schiøtz. *A modernized Effective Medium Theory potential for metals and intermetallics.* Prep. (2015).

[139] H. Gould and J. Tobochnik. *Statistical and Thermal Physics - With computer applications.* Princeton University Press (2010). ISBN 978-0-691-13744-5.

[140] H. Jónsson and H. C. Andersen. *Icosahedral ordering in the Lennard-Jones liquid and glass* (1988).

[141] J. D. Honeycutt and H. C. Andersen. *Molecular Dynamics Study of Melting and Freezing of Small Lennard- Jones Clusters.* J. Phys. Chem., **91(24)**, pp. 4950–4963 (1987).

[142] A. S. Clarke and H. Jónsson. *Structural changes accompanying densification of random hard-sphere packings.* Phys. Rev. E, **47(6)**, pp. 3975–3984 (1993).

[143] D. Faken and H. Jónsson. *Systematic analysis of local atomic structure combined with 3D computer graphics.* Comput. Mater. Sci., **2(2)**, pp. 279–286 (1994).

[144] E. B. Saff and A. B. J. Kuijlaars. *Distributing many points on a sphere.* Math. Intell., **19(1)**, pp. 5–11 (1997).

[145] G. Wulff. *Zur Frage der Geschwindigkeit des Wachsthums und der Auflösung der Krystallflächen.* Zeitschrift für Krist. - Cryst. Mater., **34(1-6)**, pp. 20449–530 (1901).

[146] C. Herring. *Some Theorems on the Free Energies of Crystal Surfaces.* Phys. Rev., **82(1)**, pp. 87–93 (1951).

[147] S. H. Brodersen. *Theoretical modelling of nanoparticles with applications to catalysis and sustainable energy.* Ph.D. thesis, Technical University of Denmark (2013).

[148] S. Foiles, M. Baskes, and M. Daw. *Embedded-atom-method functions for the fcc metals Cu, Ag, Au, Ni, Pd, Pt, and their alloys.* Phys. Rev. B, **33(12)**, pp. 7983–7991 (1986).

[149] F. Ercolessi, M. Parrinello, and E. Tossati. *Simulation of gold in the glue model.* Philos. Mag. A - Phys. Condens. Matter Struct. Defects Mech. Prop., **58(1)**, pp. 213 – 226 (1988).

[150] R. Gupta. *Lattice relaxation at a metal surface.* Phys. Rev. B, **23(12)**, pp. 6265–6270 (1981).

[151] M. W. Finnis and J. E. Sinclair. *A simple empirical N-body potential for transition metals.* Philos. Mag. A - Phys. Condens. Matter Struct. Defects Mech. Prop., **50(1)**, pp. 45 – 55 (1984).

[152] T. Rasmussen. *Simulation of misfit dislocation loops at the Ag/Cu (111) interface.* Phys. Rev. B, **62(19)**, pp. 664–667 (2000).

[153] N. P. Bailey, J. Schiøtz, and K. W. Jacobsen. *Simulation of Cu-Mg metallic glass: Thermodynamics and structure.* Phys. Rev. B - Condens. Matter Mater. Phys., **69**, pp. 1–11 (2004).

[154] A. Paduraru, A. Kenoufi, N. P. Bailey, and J. Schiøtz. *An Interatomic Potential for Studying CuZr Bulk Metallic Glasses.* Adv. Eng. Mater., **9(6)**, pp. 505–508 (2007).

[155] W. Bronger and W. Klemm. *Darstellung von Legierungen des Platins mit unedlen Metallen.* Zeitschrift für Anorg. und Allg. Chemie, **319**, pp. 58–81 (1962).

[156] H. H. Stadelmaier and W. K. Hardy. *Ternäre Kohlenstofflegierungen Von Palladium Und Platin Mit Magnesium, Aluminium, Zink, Gallium, Germanium, Kadmium, Indium, Zinn, Quecksilber, Thallium Und Blei.* Zeitschrift Fur Met., **52(6)**, pp. 391–396 (1961).

[157] T. Heumann and M. Kniepmeyer. *A5B-Phasen vom Typ Cu5Ca und Lavesphasen in den Systemen des Strontiums mit Palladium, Platin, Rhodium und Iridium.* Zeitschrift für Anorg. und Allg. Chemie, **290**, pp. 191–204 (1957).

[158] N. Krikorian. *The reaction of selected lanthanide carbides with platinum and iridium.* J. Less Common Met., **23**, pp. 271–279 (1971).

[159] A. Schneider and U. Esch. *The copper-platinum system.* Zeitschrift für elektrochemie und Angew. Phys. chemie, **50**, pp. 290–301 (1944).

[160] A. E. Dwight, J. W. Downey, and R. A. Conner. *Some AB3 compounds of the transitiom metals.* Acta Crystallogr., **14(1)**, pp. 75–76 (1961).

[161] T. Geballe, B. Matthias, V. Compton, E. Corenzwit, G. Hull, and L. Longinotti. *Superconductivity in Binary Alloy Systems of the Rare Earths and of Thorium with Pt-Group Metals.* Phys. Rev., **137(1962)**, pp. A119–A127 (1965).

[162] T. Massalski, H. Okamoto, P. R. Subramanian, and L. Kacprzak. *Binary alloy phase diagrams.* ASM International (1990). ISBN 0-87170-403-X.

[163] I. Syôzi. *Statistics of Kagomé Lattice.* Prog. Theor. Phys., **6(3)**, pp. 306–308 (1951).

[164] V. B. Compton and B. T. Matthias. *Laves phase compounds of rare earths and hafnium with noble metals.* Acta Crystallogr., **12(9)**, pp. 651–654 (1959).

[165] K. H. Lieser and H. Witte. *Untersuchungen in den ternären Systemen Magnesium-Kupfer-Zink, Magnesium-Nickel-Zink und Magnesium-Kupfer-Nickel.* Zeitschrift Fur Met., **43(11)**, pp. 396–401 (1952).

[166] R. F. Berger, S. Lee, J. Johnson, B. Nebgen, and A. C.-Y. So. *Laves Phases, γ - Brass, and 2x2x2 Superstructures: A New Class of Quasicrystal Approximants and the Suggestion of a New Quasicrystal.* Chem. - A Eur. J., **14(22)**, pp. 6627–6639 (2008).

[167] J. Aufrecht, W. Baumann, a. Leineweber, V. Duppel, and E. Mittemeijer. *Layer-stacking irregularities in C36-type Nb–Cr and Ti–Cr Laves phases and their relation with polytypic phase transformations.* Philos. Mag., **90(23)**, pp. 3149–3175 (2010).

[168] H. Lueken and W. Bronger. *Zusammenhänge zwischen Struktur und magnetischen Eigenschaften bei LnPt5-Phasen.* Zeitschrift für Anorg. und Allg. Chemie, **395**, pp. 203–206 (1973).

[169] B. Predel. *Ca-Pt (Calcium-Platinum) - Phase diagram and Crystal structure.* In O. Madelung, editor, *Landolt-Börnstein - Gr. IV Phys. Chem. 5c* (1993).

[170] E. A. Wood and V. B. Compton. *Laves-phase compounds of alkaline earths and noble metals.* Acta Crystallogr., **11(6)**, pp. 429–433 (1958).

Appendix A

Included papers

Paper I

Correlation between diffusion barriers and alloying energy in binary alloys

Ulrik Grønbjerg Vej-Hansen, Jan Rossmeisl, Ifan E. L. Stephens and Jakob Schiøtz

Accepted, Physical Chemistry Chemical Physics, 2015

Physical Chemistry Chemical Physics

PCCP

Correlation between diffusion barriers and alloying energy in binary alloys

Journal:	*Physical Chemistry Chemical Physics*
Manuscript ID:	CP-ART-08-2015-004694
Article Type:	Paper
Date Submitted by the Author:	07-Aug-2015
Complete List of Authors:	Vej-Hansen, Ulrik; Technical University of Denmark, Physics Rosmeisl, Jan; University of Copenhagen, Department of Chemistry; Technical University of Denmark, Physics Stephens, Ifan; Technical University of Denmark, CINF, Institute of Physics Schiøtz, Jakob; Technical University of Denmark, DTU Physics

Journal Name

ARTICLE TYPE

Cite this: DOI: 10.1039/xxxxxxxxxx

Correlation between diffusion barriers and alloying energy in binary alloys

Ulrik Grønbjerg Vej-Hansen,[ab] Jan Rossmeisl,[bc], Ifan E. L. Stephens,[a] and Jakob Schiøtz*[ab]

Received Date
Accepted Date

DOI: 10.1039/xxxxxxxxxx

www.rsc.org/journalname

In this paper, we explore the notion that a negative alloying energy may act as a descriptor for long term stability of Pt-alloys as cathode catalysts in low temperature fuel cells. Using density functional theory calculations, we show that there is a correlation between the alloying energy of an alloy, and the diffusion barriers of the minority component. Alloys with a negative alloying energy may show improved long term stability, despite the fact that there is typically a greater thermodynamic driving force towards dissolution of the solute metal over alloying. In addition to Pt, we find that this trend also appears to hold for alloys based on Al and Pd.

1 Introduction

Intermetallics with good resistance against diffusion have a number of important technological applications. An almost classical example is the use of Ni_3Al based "superalloys" in the aviation industry, for instance for turbine blades in jet engines, where the high diffusion barrier in the material, combined with ingenious design of the microstructure, reduce creep deformation[1]. Creep is the mechanism by which a material slowly changes shape under load, a problem that is strongly aggravated in jet engine turbines due to the high temperature combined with a very high mechanical tension due to centrifugal forces. A characteristic feature of these superalloys is that they have very negative alloying energies.

Similar design principles have been used for designing alloys in other harsh environments, one such example being the Oxygen Reduction Reaction (ORR) catalyst in low-temperature Polymer Electrolyte Membrane Fuel Cells (PEMFCs). For instance, alloys of Pt and late transition metals such as Ni, Cu, Co and Fe are often employed as cathode catalysts in Polymer Electrolyte Membrane Fuel cells. The catalysts are typically in nanoparticulate form, and need to withstand a very chemically aggressive environment, with a high oxidation potential and low pH. This class of catalysts was first implemented in PEMFCs over two decades ago[2–5].

When commercial catalysts based on these alloys are implemented in fuel cells, they tend to degrade over time. The solute metal will tend to diffuse to the surface and dissolve into the electrolyte. This process is known as dealloying, and results in the catalytic activity decreasing towards that of pure Pt[6–9].

Such degradation limits the lifetime of PEMFCs with Pt alloys as cathode catalysts. Even so, there are numerous recent reports of novel forms of Pt-Ni based catalysts which show exceptionally high activity and stability, at least in accelerated degradation tests[10–13]. Nevertheless, it remains to be seen whether these catalysts will be able to maintain their superior performance over long periods of time[14].

In the search for new Pt-alloys for oxygen reduction, an earlier paper[15], co-authored by some of us, proposed that the alloying energy, or the enthalpy of formation, could also be used as a descriptor for stability for Pt alloys under PEMFC conditions. Some Pt rare earth alloys have exceptionally negative alloying energies, which could make them less susceptible to dealloying under PEMFC conditions. We discovered numerous ORR catalysts with negative alloying energies; in particular Pt_xY and Pt_xGd exhibit activity amongst the highest ever reported, both in the bulk polycrystalline and nanoparticulate form[15–19].

We note that although compounds such as Pt_3Y have a highly

[a] DNRF Center for Individual Nanoparticle Functionality (CINF), Department of Physics, Technical University of Denmark, DK-2800 Kgs. Lyngby, Denmark; E-mail: schiotz@fysik.dtu.dk
[b] Center for Atomic-scale Materials Design (CAMD), Department of Physics, Technical University of Denmark, DK-2800 Kgs. Lyngby, Denmark.
[c] Department of Chemistry, University of Copenhagen, DK-2100 København Ø, Denmark.

negative alloying energy, they are thermodynamically more unstable than alloys such as Pt_3Ni under operating conditions. Indeed, the alloying energy tends to scale linearly with the dissolution potential of the transition metal[20]. This leads us to to question whether it is the dissolution potential or the alloying energy that is more important in controlling the long term stability of Pt alloy catalysts in fuel cells.

In order to explore this notion experimentally, the catalysts would need to be tested over the long term in a PEMFC[14]. However, thus far, no synthesis method has been devised for alloys of Pt and rare earths that would yield a sufficient quantity of the catalyst for it to be tested in PEMFCs. The fact that similar compounds have already been produced leads us to take the view that this should eventually be possible[21–23].

On the contrary, in the current paper, we explore the notion with theoretical methods. We show that the alloying energy correlates strongly with the diffusion barrier of the alloying element. This implies that the high stability of the alloy would work as a kinetic barrier towards the dissolution of the highly reactive second component of the Pt alloy. We validate this assumption by showing that the diffusion barriers for vacancy diffusion scales with the alloying energy of the alloy.

2 Methods

We assume that solute metals transport from a Pt-alloy particle to the shell via diffusion. Interactions with adsorbed oxygen, either as a 2D adsorbate or as a 3D oxide phase, will only induce solute metal segregation between neighbouring atoms[24]. For example, it is unlikely that in a 3 nm particle adsorbed O or OH at the surface of the particle would interact directly with a solute metal atom in the core.

Usually, the dominant diffusion mechanism in metals is by vacancy diffusion along grain boundaries and dislocations, and there is no reason to believe that this is different in the alloys investigated in this work. In this work we investigate vacancy diffusion in defect-free, single-crystalline systems, as we take the view that any trend found here applies equally well to more realistic diffusion paths for larger systems. Furthermore, commercial Pt-based catalysts are often single crystalline[25], in which case bulk vacancy diffusion is likely to be the most relevant process.

Although most of the alloys under consideration have a relatively simple $L1_2$ crystal structure, modelling the diffusion process is computationally very demanding. For this reason, we only calculate the full diffusion path for a small number of alloys, and show that the diffusion barrier is well described by the energy of a characteristic configuration along the diffusion path, an energy that can be calculated with an order of magnitude lower computational cost. In these very stable alloys a significant energy is gained when the two different elements are next to each other, and conversely, a sizeable amount of energy is lost when this atomic arrangement is broken during the diffusion process.

We look at a vacancy diffusion path by exchanging the position of an atom of the alloying element with a vacancy. The simplest such diffusion path consists of six steps, involving a total of three atoms changing their lattice site. When all 6 steps have been completed, the crystal has regained its initial configuration, when translational symmetry is taken into account. The proposed diffusion path is shown in figure 1. It should be noted that the path is symmetric, with the 6 steps being pairwise mirror images of each other.

We have calculated the barrier for each step using the Nudged Elastic Band method[26–28], with the total barrier simply being the energy difference between the initial state and the transition state with the highest energy along the path. Two examples of the energies along the path are shown alongside the diffusion path in figure 1.

The interatomic interactions are described within the Density Functional Theory[29], using the PBE exchange-correlation functional[30]. The calculations were done using the GPAW DFT code[31] and the Atomic Simulation Environment (ASE)[32]. Due to the size of the calculations, the Kohn-Sham wavefunctions were described using a localized basis set within the Linear Combination of Atomic Orbitals (LCAO) formalism[33], using a Double-Zeta Polarised (dzp) basis set, from GPAW setups version 0.9.9672. The barriers were calculated in a 3 x 3 x 2 supercell, with the path being in the xy-plane. We used a 5 x 5 x 5 Monkhost-Pack grid[34] for sampling the k-space when doing calculations for the supercell used for calculating the barriers. The validity of the LCAO approximation was tested by calculating a few key energy differences using a full grid-based basis set, using a grid spacing of 0.18 Å. We calculated the total energy of the configurations A and B, as well as the one in the middle between them, in the LCAO geometry for Pt_3Y and Pt_3Cu, and found the shift in the total energy to be the same for the three configurations, within 140 meV for Pt_3Y and 14 meV for Pt_3Cu, indicating that the error in the barrier from using LCAO mode compared to FD, was on that order.

For all the alloys, we also calculated the alloying energy and the equilibrium lattice constant. The alloying energy is calculated with reference to bulk fcc Pt and the other metal in its most stable crystalline form. Here the number of k-points used depended on the element and its structural unit cell, but was never less than 6 x 6 x 6, and usually at least 8 x 8 x 8, for a unit cell with at least 2 atoms. In all cases it was a result of a convergence test. Any calculation involving at least one of V, Cr, Mn, Fe, Co or Ni was spin-polarised. This resulted in a shift of as much as 350 meV per atom in the alloying energy compared to spin-paired calculations.

As the full diffusion path is demanding to calculate, we have calculated the barrier for a handful of alloys, chosen to be diverse with regard to alloying energy and lattice parameter. We expect that these two most important parameters are influencing diffu-

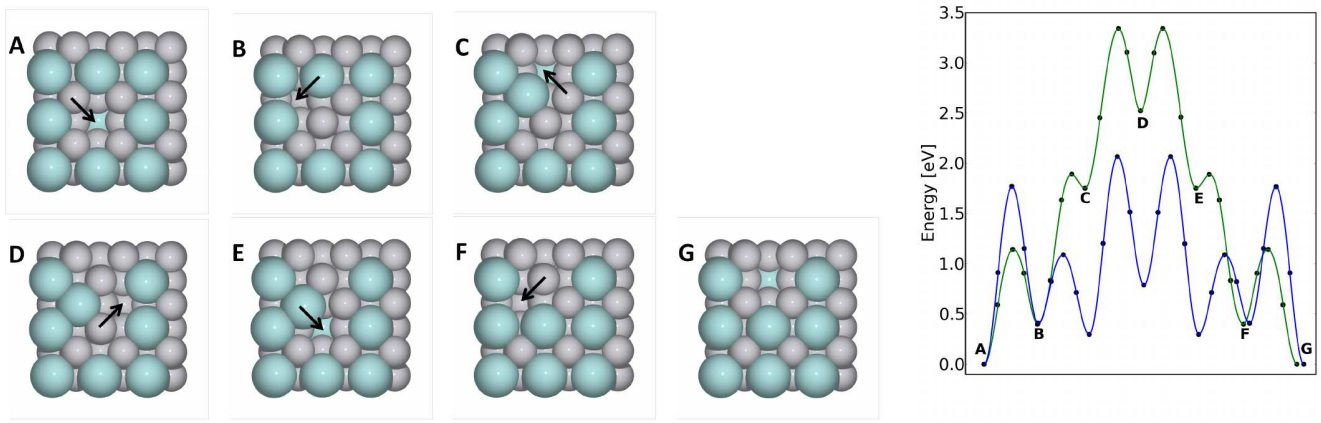

Fig. 1 The overall diffusion path. Here a top view of the computational unit cell is shown, which has a depth of two crystal unit cells. Here is shown Pt_3Y specifically, but it is equivalent for all alloys. To the right, the energy along the diffusion path is shown for both Pt_3Y in green and for Pt_3Cu in blue.

sion: the alloying energy describes the strength of the interaction between the atoms, whereas the lattice parameter describes the space between the atoms along the diffusion path.

When atoms diffuse across surfaces, the lowest diffusion barriers often occur during the concerted motion of several atoms[35,36]. It is possible that something similar could occur here, i.e. that several of the fundamental steps in figure 1 occur simultaneously. To investigate this, we set up a large Nudged Elastic Band calculation with configuration A and D as the starting and ending point, and the three involved atoms moving simultaneously as the initial guess for the path. Since such a simulation is exceedingly demanding, we could only perform two calculations; we chose Pt_3Y and Pt_3Cu as two extreme cases, both with respect to alloying energy and size of the atoms. In both cases, the NEB calculations automatically split the motion into the three separate parts considered in this work, confirming that concerted motion of the atoms does not occur.

Finally, we investigated the "direct" diffusion path, where the alloying atom moves directly from configuration A to G in figure 1 without a corresponding diffusive motion of the Pt atoms. For geometric reasons, we would only expect this to be possible for the smallest alloying atoms. Even in these cases, the barrier for direct diffusion is prohibitive. For example in Pt_3Cu, the direct diffusion barrier is 3.641 eV, whereas the barrier for the diffusion path in figure 1 is only 2.067 eV. Using a 3 x 3 x 3 supercell did not change this.

3 Results

We plot the barrier as a function of alloying energy and of the lattice parameter in figure 2. It is clearly seen that there is a significant correlation between the diffusion barrier and both the alloying energy and the lattice constant. As both the alloying energy and the size of the alloying atom and thus the lattice constant vary systematically through the periodic table, the two are clearly correlated, and it is *a priori* difficult to distinguish if the alloying energy or the lattice constant is the quantity that correlates most strongly with the diffusion barrier, and is thus the best predictor. In principle, this could be more rigorously investigated by performing the full diffusion barrier calculation on a large number of alloys: however, such an operation would be computationally too expensive. For this reason, on figure 3 we plot the energy difference, $E_{A\to D}$, between the initial configuration and the middle of the diffusion path (labeled A and D in figure 1). There is a strong correlation, suggesting that $E_{A\to D}$ is a major contributor to the diffusion barrier. The remainder of the diffusion barrier will then be the barrier between configurations C and D in figure 1. Furthermore, it turns out that the barrier height scales with the energy of the final state. This is commonly known as a Brønsted-Evans-Polanyi relation, and is ubiquitous in chemistry[37,38]

The strong correlation between $E_{A\to D}$ and the barrier height allows us to estimate the barrier height on a much larger number of alloys, using around an order of magnitude less computational time than if we were to perform the full barrier height calculation on each of the alloys. The correlations between this energy difference and the alloying energy and the lattice constant are shown in figure 4(a) and 5, respectively.

Figure 4(a) shows that there is indeed a correlation between the alloying energy for the alloy and the specified energy difference. There is a significant amount of scatter, indicating that the alloying energy is not the only parameter determining the barrier height, as expected. Nevertheless, the alloying energy correlates with the diffusion barrier, making it a sensible predictor for the stability of the alloy. The barriers of self-diffusion are included in the figures as star-shaped points.

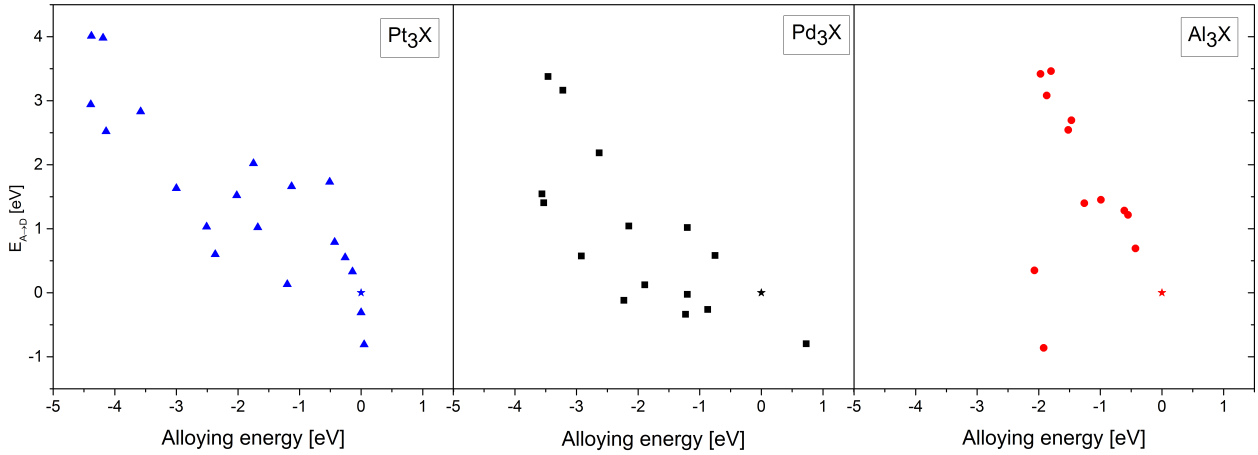

Fig. 4 The energy difference describing the diffusion barrier correlated with the alloying energy for Pd_3X (squares), Al_3X (circles) and Pt_3X (triangle) alloys. The autodiffusion for each main element is shown as a star and is by definition zero in this plot. In all three cases, we see a clear correlation. The outliers in the Al_3X set are Al_3Ir and Al_3Pt.

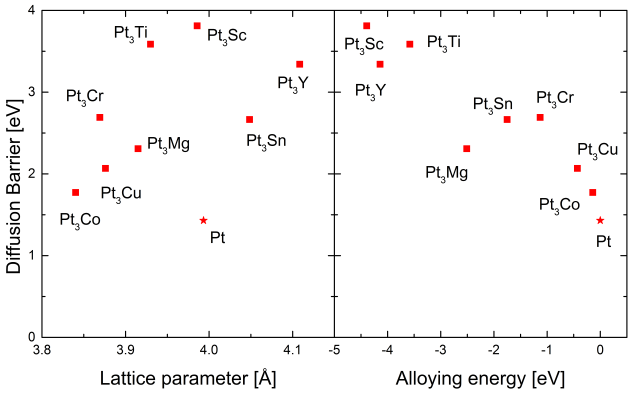

Fig. 2 Plot of the total barrier height vs. the lattice parameter of the alloy (left) and the alloying energy (right).

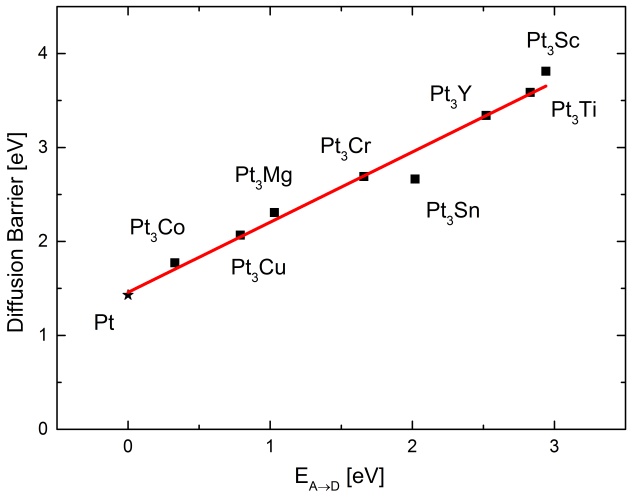

Fig. 3 The barrier height as a function of the energy difference between the initial and middle configurations on the diffusion path. These are shown as A and D in figure 1. The red line is a best linear fit with a slope of 0.75 ± 0.04 and an intercept of 1.46 ± 0.08 eV. It is seen that the correlation is very clear, indicating that this energy difference is a good descriptor for the barrier.

Figure 5 shows the relationship between $E_{A\to D}$ and the lattice parameter of the alloy; we see no clear correlation. This indicates that the diffusion barrier is not significantly determined by the size of the atoms and the space in the lattice.

To investigate if the trends observed here are specific to platinum alloys or represent a more general tendency, we extended the calculations to Pd_3X and Al_3X alloys, chosen because palladium is chemically very similar to platinum whereas aluminium is very different, and yet both form a significant number of 3:1 alloys. We selected alloys where the structure is either $L1_2$, or very similar to $L1_2$ (similar in the sense that the two kinds of atoms have the same first coordination shell as in the $L1_2$ structure, but in a different Bravais lattice, in much the same way that hcp and fcc are similar, both being closed-packed structures). In all cases, the calculations are done in the $L1_2$ structure. The results are

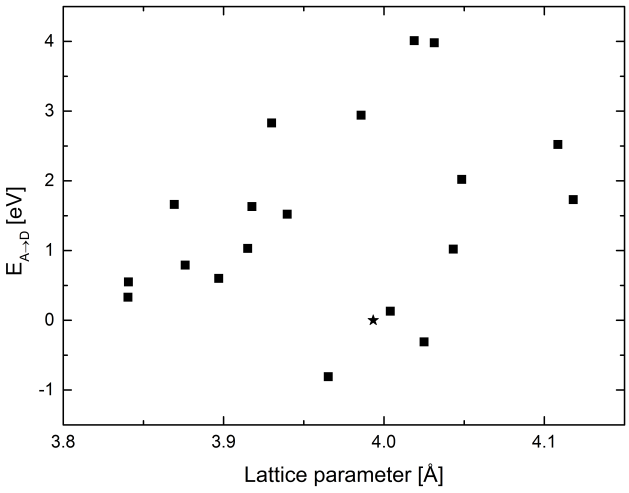

Fig. 5 The energy difference $E_{A\to D}$ vs. the lattice parameter of the alloy.

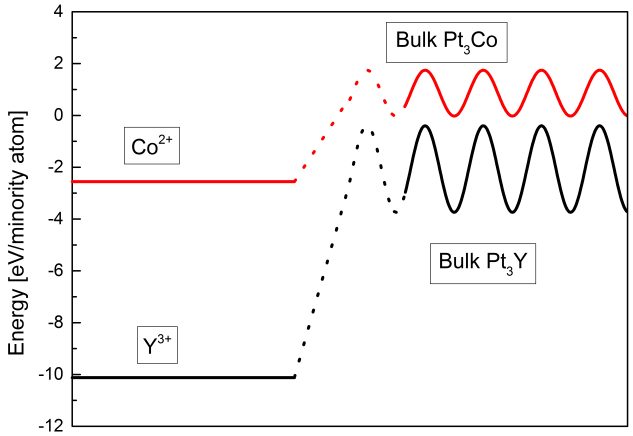

Fig. 6 Schematic overview of the energetics of the dealloying process in a PEM fuel cell with an electrode potential of 1 V vs. RHE. The focus of this work is the diffusion energy barrier in the metal. The energy barriers in the alloy, and the energy difference between the alloy and the dissolved atom are shown to scale. The energies of intermediate configurations relating to the dissolution process itself and passage through the near-surface region are unknown, as indicated by the dotted part of the lines. Everything else is under standard conditions with the standard reduction potential from ref. [42].

shown in figure 4. We indeed see the same trends in these families of alloys. In the palladium alloys the trend is slightly less pronounced, whereas it is significantly stronger in the aluminium alloys with the exception of Al_3Ir and Al_3Pt, which for reasons unknown are complete outliers.

4 Discussion and experimental evidence

These calculations have been performed for one of the simplest possible crystal structures for ordered alloys. Nevertheless, we conjecture that the correlation between alloying energy and diffusion barrier is a general principle, also applicable to similar families of alloys with other crystal structures. This is analogous to the experimentally observed strong correlation between the barrier for autodiffusion of a pure metal and its melting point, where the ratio between the activation energy and the melting point is approximately the same for almost all simple metals [1].

Our results are consistent with the experimental work of Johansson *et al.* [39] and Schumacher *et al.* [40] They deposited metals on a single crystalline Pt substrate under ultra-high vacuum conditions, and investigated at which temperature the metal diffused away from the surface. Y on Pt(111) went subsurface at 800 K [39] while Cu went subsurface already at 460 K on Pt(111) [40]. In both cases the bulk crystal was pure Pt instead of an alloy as in our case, which could cause an additional geometric contribution to the barrier of Y compared to Cu. A similar experiment was carried out by Tang et al [41] for Ce on Pt(111), a system with an equivalent alloying energy as Y/Pt(111), where they found that Ce alloyed with Pt at 770 K.

We illustrate the overall dissolution process of a Pt_3X alloy in figure 6. In order to be dissolved, the alloying element must first reach the surface, that implies overcoming both the diffusion barrier in the bulk alloy itself, and in the Pt overlayer. Once the atom reaches the surface, it is oxidised in a complicated process, the details of which are beyond the scope of this paper. Even so, we anticipate that the barrier for diffusion is comparable, if not greater than the barriers associated with the segregation of the solute metal to the surface and its subsequent dissolution [24].The initial diffusion barrier provides the alloy with kinetic stability, in spite of the strong thermodynamic driving force toward oxidation. This barrier correlates with the alloying energy of the alloy; this causes the alloys of Pt and the early transition metals to be at more stable toward diffusion-related degradation than the alloys with the late transition metals. This opens the possibility that they may display at least comparable stability under realistic operating conditions, in spite of the greater driving force for oxidation.

5 Conclusion

We have shown that the barrier for vacancy diffusion of the minority element in Pt_3X, Pd_3X and Al_3X alloys correlate with the alloying energy of the alloy. This validates the use of the alloying energy as a key parameter when searching for alloys that are stable against diffusion related degradation. A central example is the discovery of Pt_3Y and Pt_5Y alloys as electrocatalysts for the oxygen reduction reaction in fuel cells [15,16], where Pt_3Y was predicted to be active while having a large alloying energy, and subsequently shown in electrochemical experiments to be both active and stable. In this case a protective overlayer of pure Pt is formed at the surface of the alloy. A high alloying energy turns out to be more important than the thermodynamic driving force

for oxidative corrosion of the minority element. This is because the diffusion of the alloying element to the surface is kinetically hindered by the large diffusion barrier.

Experimental alloying energies are known for many compounds, and can be calculated relatively easily and accurately for new materials[43]. Consequently, we confirm the notion that the alloying energy will be useful as a key search parameter when searching for new alloys for applications where the diffusive stability of the alloy is of importance.

6 Acknowledgements

For funding of this work we gratefully acknowledge The Danish National Research Foundation's Center for Individual Nanoparticle Functionality (DNRF54) .

References

1 M. F. Ashby and D. R. H. Jones, *Engineering Materials I: An introduction to Properties, Applications and Design*, Elsevier, 2005.

2 S. Mukerjee and S. Srinivasan, *J. Electroanal. Chem.*, 1993, **357**, 201–224.

3 S. Mukerjee, S. Srinivasan, M. P. Soriaga and J. McBreen, *J. Electrochem. Soc.*, 1995, **142**, 1409–1422.

4 S. Mukerjee and J. McBreen, *J. Electroanal. Chem.*, 1998, **448**, 163–171.

5 T. Toda, H. Igarashi, H. Uchida and M. Watanabe, *J. Electrochem. Soc.*, 1999, **146**, 3750–3756.

6 S. Chen, H. A. Gasteiger, K. Hayakawa, T. Tada and Y. Shao-Horn, *J. Electrochem. Soc.*, 2010, **157**, A82.

7 K. J. J. Mayrhofer, K. Hartl, V. Juhart and M. Arenz, *J. Am. Chem. Soc.*, 2009, **131**, 16348–16349.

8 H. A. Gasteiger, S. S. Kocha, B. Sompalli and F. T. Wagner, *Appl. Catal. B Environ.*, 2005, **56**, 9–35.

9 H. L. Xin, J. A. Mundy, Z. Liu, R. Cabezas, R. Hovden, L. F. Kourkoutis, J. Zhang, N. P. Subramanian, R. Makharia, F. T. Wagner and D. A. Muller, *Nano Lett.*, 2012, **12**, 490–7.

10 C. Baldizzone, S. Mezzavilla, H. W. P. Carvalho, J. C. Meier, A. K. Schuppert, M. Heggen, C. Galeano, J.-D. Grunwaldt, F. Schüth and K. J. J. Mayrhofer, *Angew. Chem. Int. Ed. Engl.*, 2014, 14250–14254.

11 B. Han, C. E. Carlton, A. Kongkanand, R. S. Kukreja, B. R. Theobald, L. Gan, R. O'Malley, P. Strasser, F. T. Wagner and Y. Shao-Horn, *Energy Environ. Sci.*, 2015, **8**, 258–266.

12 C. Chen, Y. Kang, Z. Huo, Z. Zhu, W. Huang, H. L. Xin, J. D. Snyder, D. Li, J. A. Herron, M. Mavrikakis, M. Chi, K. L. More, Y. Li, N. M. Markovic, G. A. Somorjai, P. Yang and V. R. Stamenkovic, *Science*, 2014, **343**, 1339–1343.

13 X. Huang, Z. Zhao, L. Cao, Y. Chen, E. Zhu, Z. Lin, M. Li, A. Yan, A. Zettl, Y. M. Wang, X. Duan, T. Mueller and Y. Huang, *Science*, 2015, **348**, 1230–1234.

14 L. Dubau, M. Lopez-Haro, L. Castanheira, J. Durst, M. Chatenet, P. Bayle-Guillemaud, L. Guétaz, N. Caqué, E. Rossinot and F. Maillard, *Appl. Catal. B Environ.*, 2013, **142-143**, 801–808.

15 J. Greeley, I. E. L. Stephens, A. S. Bondarenko, T. P. Johansson, H. A. Hansen, T. F. Jaramillo, J. Rossmeisl, I. Chorkendorff and J. K. Nørskov, *Nat. Chem.*, 2009, **1**, 552–556.

16 I. E. L. Stephens, A. S. Bondarenko, L. Bech and I. Chorkendorff, *ChemCatChem*, 2012, **4**, 341–349.

17 M. Escudero-Escribano, A. Verdaguer-Casadevall, P. Malacrida, U. Grønbjerg, B. P. Knudsen, A. K. Jepsen, J. Rossmeisl, I. E. L. Stephens and I. Chorkendorff, *J. Am. Chem. Soc.*, 2012, **134**, 16476–9.

18 P. Hernandez-Fernandez, F. Masini, D. N. McCarthy, C. E. Strebel, D. Friebel, D. Deiana, P. Malacrida, A. Nierhoff, A. Bodin, A. M. Wise, J. H. Nielsen, T. W. Hansen, A. Nilsson, I. E. L. Stephens and I. Chorkendorff, *Nat. Chem.*, 2014, **6**, 732–738.

19 A. Velázquez-Palenzuela, F. Masini, A. F. Pedersen, M. Escudero-Escribano, D. Deiana, P. Malacrida, T. W. Hansen, D. Friebel, A. Nilsson, I. E. L. Stephens and I. Chorkendorff, *J. Catal.*, 2015, **328**, 297–307.

20 B. Han, C. E. Carlton, J. Suntivich, Z. Xu and Y. Shao-Horn, *J. Phys. Chem. C*, 2015, **119**, 3971–3978.

21 K. W. Lux and E. J. Cairns, *J. Electrochem. Soc.*, 2006, **153**, A1139.

22 D. Saha, E. D. Bojesen, K. M. O. Jensen, A.-C. Dippel and B. B. Iversen, *J. Phys. Chem. C*, 2015, 13357–13362.

23 C. Yan and M. J. Wagner, *Nano Lett.*, 2013, 1–4.

24 C. A. Menning and J. G. Chen, *Top. Catal.*, 2010, **53**, 338–347.

25 L. C. Gontard, L. Y. Chang, C. J. D. Hetherington, A. I. Kirkland, D. Ozkaya and R. E. Dunin-Borkowski, *Angew. Chemie - Int. Ed.*, 2007, **46**, 3683–3685.

26 H. Jónsson, G. Mills and K. W. Jacobsen, *Class. Quantum Dyn. Condens. Phase Simulations*, World Scientific, 1998, ch. 16, pp. 385–404.

27 G. Henkelman, B. P. Uberuaga and H. Jónsson, *J. Chem. Phys.*, 2000, **113**, 9901.

28 G. Henkelman and H. Jónsson, *J. Chem. Phys.*, 2000, **113**, 9978.

29 W. Kohn and L. Sham, *Phys. Rev.*, 1965, **140**, 1133–1138.

30 J. Perdew, K. Burke and M. Ernzerhof, *Phys. Rev. Lett.*, 1996, **77**, 3865–3868.

31 J. J. Mortensen, L. Hansen and K. W. Jacobsen, *Phys. Rev. B*, 2005, **71**, 035109.

32 S. R. Bahn and K. W. Jacobsen, *Comput. Sci. Eng.*, 2002, 56–66.

33 A. H. Larsen, M. Vanin, J. J. Mortensen, K. S. Thygesen and K. W. Jacobsen, *Phys. Rev. B*, 2009, **80**, 195112.

34 H. Monkhorst and J. Pack, *Phys. Rev. B*, 1976, **13**, 5188–5192.

35 G. L. Kellogg and P. J. Feibelman, *Phys. Rev. Lett.*, 1990, **64**, 3143–3146.

36 C. Chen and T. T. Tsong, *Phys. Rev. Lett.*, 1990, **64**, 3147–3150.

37 J. N. Brønsted, *Chem. Rev.*, 1928, **5**, 231–338.

38 M. G. Evans and M. Polanyi, *Inertia and driving force of chemical reactions*, 1938.

39 T. P. Johansson, E. T. Ulrikkeholm, P. Hernandez-Fernandez, M. Escudero-Escribano, P. Malacrida, I. E. L. Stephens and I. Chorkendorff, *Phys. Chem. Chem. Phys.*, 2014, **16**, 13718–25.

40 N. Schumacher, K. Andersson, L. C. Grabow, M. Mavrikakis, J. Nerlov and I. Chorkendorff, *Surf. Sci.*, 2008, **602**, 702–711.

41 J. Tang, J. Lawrence and J. Hemminger, *Phys. Rev. B*, 1993, **48**, 15342–15353.

42 P. Vanýsek, *Handbook of Chemistry and Physics - Electrochemical Series*, 2015.

43 G. Jóhannesson, T. Bligaard, A. Ruban, H. L. Skriver, K. W. Jacobsen and J. K. Nørskov, *Phys. Rev. Lett.*, 2002, **88**, 255506.

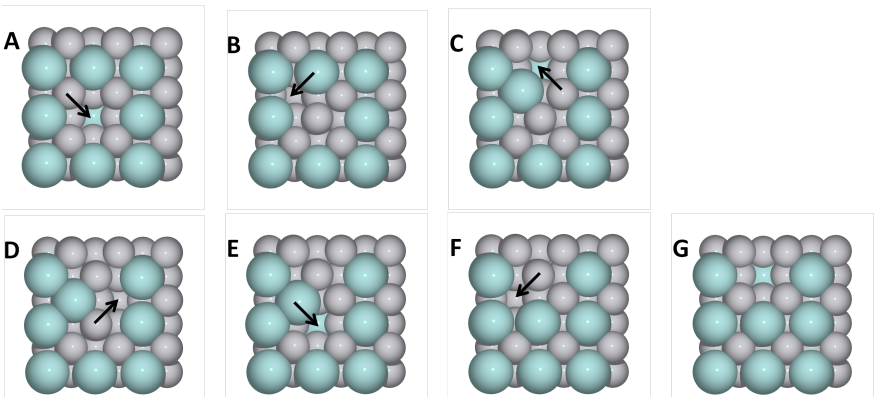
A
B
C
D
E
F
G

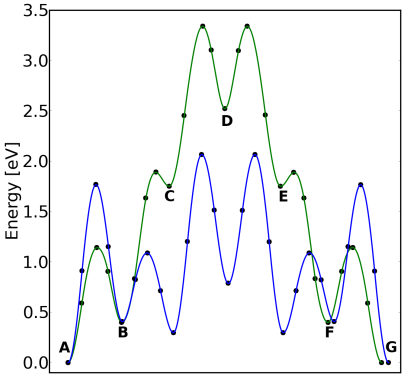
Energy [eV]
3.5
3.0
2.5
2.0
1.5
1.0
0.5
0.0
A
B
C
D
E
F
G

Paper II

A modernized Effective Medium Theory potential for metals and intermetallics

S. H. Brodersen, Ulrik Grønbjerg Vej-Hansen, R. E. Christiansen, K. W. Jacobsen, and J. Schiøtz

In preparation, 2015

A modernized Effective Medium Theory potential for metals and intermetallics

S. H. Brodersen,[1] U. G. Vej-Hansen,[1] R. E. Christiansen,[1,2] K. W. Jacobsen,[3] and J. Schiøtz[1,*]

[1] *DNRF Center for Individual Nanoparticle Functionality (CINF), Dept. of Physics, DTU Building 307, DK-2800 Kongens Lyngby, Denmark*

[2] Present address: *Dept. of Mechanical Engineering, DTU Building 404, DK-2800 Kongens Lyngby, Denmark*

[3] *Center for Atomic-scale Materials Design (CAMD), Dept.of Physics, DTU Building 307, DK-2800 Kongens Lyngby, Denmark*

(Dated: November 17, 2015)

In this paper we present a modernised implementation of the Effective Medium Theory (EMT) interatomic potential, where we correct minor weaknesses in the original definition, and have refitted all parameters in the potential for the original metals to material properties. This gives a significantly better description of these metals, in particular when it comes to surface energies, which were significantly underestimated in the original EMT. The Effective Medium theory is a computationally efficient description of interatomic interactions in closed packed metals, suitable for large-scale molecular dynamics with millions of atoms.

I. INTRODUCTION

When modeling various properties of metals at the atomic scale, the accuracy of the description necessarily depends on the size of the system being considered. For example, Density Functional Theory (DFT)[1,2] provides a very accurate but computationally expensive description of most of the periodic system, and is routinely used to describe systems with up to a few hundred atoms. For larger systems, more approximately and often (semi-)empirically based interatomic potentials are used. These potentials have been used for molecular dynamics simulations with hundreds of millions of atoms[3–5]. Clearly, such applications remain out of the range of DFT based methods, and there is a need for reliable and transferable interatomic potentials. A family of these potentials has proved to be highly useful for modeling late transition metals and simple metals having the face-centered cubic (fcc) crystal structure. This family of potential includes the Embedded Atom Method (EAM)[6], the glue model[7], the Gupta potential[8,9], the Finnis-Sinclair potential[10] and the Effective Medium Theory (EMT)[11,12].

In this paper we present an adjustment to the well-established EMT class of potentials, and a refitting of the parameters to a larger class of metals and their alloys. The main motivation for this, is the way cutoffs are handled in the original version. EMT is a short range potential, typically including interactions up to third nearest neighbors in closed-packed crystals. The interactions are described by exponentially decaying functions, cut off by a Fermi function. This may introduce two problems. First, the derivative of the interaction functions acquire a small peak at the cutoff distance. Second, the Fermi function is itself an exponentially decaying function without compact support, so eventually a "hard" cutoff is reached where the neighboring atoms are no longer included on neighbor lists, and a tiny discontinuity in the interaction occurs. This discontinuity is so small that it is unlikely to have any negative effects in real-life simulations. The peak in the derivative is, however, slightly more worrying, and is the reason that the cutoff in the original EMT is placed between the third and fourth shell in the fcc crystal: If a cutoff distance was chosen that was equal to an interatomic distance occurring in the equilibrium crystal, a small distortion of the crystal would occur.

The goal of this paper is fourfold: First, we wish to address a number of choices in the original formulation of EMT that time has shown to be less than optimal. Second, we improve the description of the supported metals through refitting the parameters of the potential, and present parameters for metals not previously described by EMT (although still limited to metals with a closed packed crystal structure). Third, we demonstrate how a set of parameters can be obtained for the pure metals that also describe alloys between these with reasonable accuracy. Fourth, we demonstrate how an optimized potential for a specific alloy can be made to improve upon the more general potential.

II. THE FUNCTIONAL FORM

In this modernized formulation of the EMT potential, we cut off the exponentially decaying interactions by subtracting a linear function instead of using a Fermi function. This ensures that the interaction and its derivative are both zero at the cutoff distance, and that the latter does not acquire a peak. This cutoff introduces a small perturbation of the interaction function at shorter distances, and therefore requires a refitting of all parameters of the potential. For Cu the relative perturbation is in the order of 10^{-3} at the nearest neighbor distance. The old and new way to cut off the interactions are shown in Fig. 1.

In the following, we describe the revised functional form of the EMT potential using the notation of Ref. 12. There are seven describing parameters E_0, s_0, V_0, η_2, κ, λ and n_0 for each element. Contrary to many other similar potentials interactions between atoms of unlike elements are described by the parameters of the two pure ele-

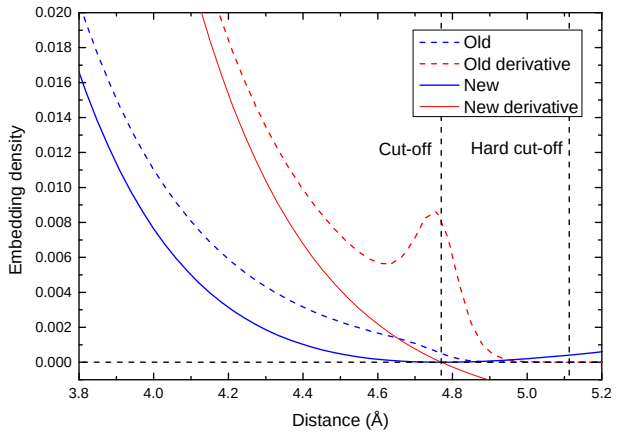

FIG. 1: Comparison of the original (dotted lines) and the new (full lines) cutoff implementations. The blue lines show the exponentially decaying interaction function f_1 with cutoff, and the red lines show its absolute derivative. The original parameters for Cu is used.

ments, without introducing extra parameters. The EMT parameters does therefore not need extra indexing and the index are also synonym for the atomic number, i.e. $E_{0,i} \equiv E_{0,Z_i}$.

The total energy of the system is described as a sum over all atoms, where the energy of a given atom is a sum of two contributions. The *cohesive function* $E_{c,i}$ is sensitive to the local density around atom i, and is responsible for the material's resistance to volume changes, i.e. it determines the bulk modulus. It is the energy the atom would have had if it had been in a face-centered cubic crystal (the *reference system*) with the same average electron density. The *atomic sphere correction* $E_{as,i}$ is the difference between a pair potential in the real system and in the reference system, it is responsible for the material's resistance to shape changes, i.e. it determines the shear modulus. We therefore write the total energy as

$$E_{tot} = \sum_i \left(E_{c,i} + E_{as,i}\right). \tag{1}$$

where the two contributions to the energy of the atom i are

$$E_{c,i} = E_{0,i}\big(\lambda_i(s_i - s_{0,i}) + 1\big)\exp\big(-\lambda_i(s_i - s_{0,i})\big), \tag{2}$$

and

$$E_{as,i} = 6V_i^0\left(\exp\big(-\kappa_i(s_i - s_{0,i})\big) - \frac{\sigma_{2,i}}{\sigma_{2,i}^{\mathrm{ref}}}\right). \tag{3}$$

The neutral-sphere radius s_i for atom i is given by

$$s_i = s_{0,i} - \frac{1}{\beta\eta_{2,i}}\ln\left(\frac{\sigma_{1,i}}{\sigma_{1,i}^{\mathrm{ref}}}\right), \tag{4}$$

the two σ_α variables are sums over contributions from all the neighboring atoms, and the σ^{ref} variables are the values that the σ's would have in a perfect fcc lattice at the equilibrium lattice spacing. The σ_α sums are defined as (for $\alpha = 1, 2$):

$$\sigma_{\alpha,i} = \sum_{j\neq i} n_{0,j}\left[f_{\alpha,j}(r_{ij}) - l_{\alpha,i,j}(r_{ij})\right], \tag{5}$$

where

$$f_{1,j}(r) = \exp\left(-\eta_{2,j}r + \beta\eta_{2,j}s_{0,j}\right), \tag{6}$$

$$f_{2,j}(r) = \exp\left(-\frac{\kappa_j}{\beta}r + \kappa_j s_{0,j}\right), \tag{7}$$

and

$$l_{\alpha,i,j}(r) = f'_{\alpha,j}(r_{i,j}^{\mathrm{cut}})(r - r_{i,j}^{\mathrm{cut}}) + f_{\alpha,j}(r_{i,j}^{\mathrm{cut}}), \tag{8}$$

The function $f_{1,j}$ gives the normalized contribution to the average electron density around atom i from the atom j, to get the contribution to the actual electron density one multiply with $n_{0,j}$. The EMT parameter $\eta_{2,Z}$ describes how fast the electron density from an atom with atomic number Z decays (the physical interpretation of these decay lengths are discussed further in Ref. 12). The function $-V_{0,i}f_{2,j}$ is the pair-potential used in the atomic sphere correction. Both of these functions are cut off by subtracting a linear function, l_1 and l_2 respectively. It is of course important that only terms with $r_{ij} < r_{i,j}^{\mathrm{cut}}$ are included in the sum in Eq. (5), as this kind of cutoff ensures that the function and its derivative are zero at the cut-off point, but not beyond it.

The parameters $\sigma_{1,Z}^{\mathrm{ref}}$ and $\sigma_{2,Z}^{\mathrm{ref}}$ are the values of σ_1 and σ_2 in an fcc crystal of element number Z with lattice constant $\beta s_{0,Z}$, calculated using up to the third nearest neighbors.

$$\begin{aligned}\sigma_{0,i}^{\mathrm{ref}} =& 12n_{0,i}\left(f_{1,i}(\beta s_{0,i}) - l_{1,i,i}(\beta s_{0,i})\right)\\ &+ 6n_{0,i}\left(f_{1,i}(\sqrt{2}\beta s_{0,i}) - l_{1,i,i}(\sqrt{2}\beta s_{0,i})\right)\\ &+ 24n_{0,i}\left(f_{1,i}(\sqrt{3}\beta s_{0,i}) - l_{1,i,i}(\sqrt{3}\beta s_{0,i})\right),\end{aligned} \tag{9}$$

and $\sigma_{2,i}^{\mathrm{ref}}$ is defined the same way using f_2 and l_2. Here it has been used that an atom has six second-nearest neighbors and 24 third-nearest neighbors in an fcc crystal.

This form of the potential is close to the original formulation[12], and retains the same seven EMT parameters for each element. All other parameters entering the equations above can be calculated from these parameters as already shown, with the exception of the cutoff distance. Where the original formulation of EMT operated with a common cutoff distance for all interactions in a simulation, we have a cutoff distance for each pair of element types. We somewhat arbitrarily choose to set the cutoff distance to halfway between the third and fourth nearest neighbor distance in the fcc lattice, and get $r_{i,i}^{\mathrm{cut}} = \frac{1}{2}\left(\sqrt{3}+2\right)\beta s_{0,i}$ for interactions between atoms of the same element. For interactions between unlike atoms, we choose to set $r_{i,j}^{\mathrm{cut}}$ to be the maximum of the cutoffs of the two elements.

III. OPTIMIZING THE POTENTIAL

In the original formulation of EMT, some potential parameters were calculated directly from DFT calculations (such as the decay length of the contribution to the electron density from an atom, η_2). Other were calculated from experimental data, mainly lattice parameters and elastic constants under the approximation that only nearest neighbors contribute to the potential (see Ref. 12). Contributions from further neighbors meant that not all quantities were reproduced perfectly, for example were all lattice constants a few percent too low.

In this work, we fit all parameters to a combination of experimental data and electronic structure calculations at the DFT level. We follow a procedure close to the one of Bailey *et al.*[13] and Păduraru *et al.*[14], and aim at at generating as general a parameter set as possible for as many elements as possible. In this case parameters were first fitted for the pure elements, and in a second step some of the parameters of all elements were adjusted to give reasonable values for alloy quantities such as formation energies and lattice constants of ordered alloys. Simultaneous fitting to many different alloy compositions by necessity results in a compromise potential since EMT does not contain parameters for each combination of elements, but only for the pure elements, as discussed below. As an example of this fitting strategy, we present a general potential applicable to NN metallic elements and their alloys.

An alternative fitting strategy would be to generate specialized potentials for specific applications. In this case parameters are optimized to a single or a few chemical compositions, and a significantly better potential can be obtained, although with less general applicability. We will illustrate this in a later publication.

The EMT potential is described by seven parameters for each element, but they do leave some room for adjusting the parameters to alloy properties without impairing the properties of the pure element. First, the parameter n_0 does not enter into interactions between atoms of the same element, whereas the ratio of the n_0 parameters is important for the description of interactions between atoms of different elements. Second, most properties of pure elements are to first order insensitive to changes of the parameters V_0 and κ if the change preserves the value of $V_0 \cdot (\beta\eta_2 - \kappa)$ (see Ref. 12). This naturally leads to a fitting procedure where first six parameters (excluding n_0) are fitted for each element independently (using only data for pure elements); then in a second phase the parameters n_0, κ and V_0 are optimized simultaneously for all elements, fitting to both pure-element and alloy data. We choose not to fit the cutoff distances, as fitting these risks leading to very long-ranged and computationally expensive potentials.

The actual parameter fitting is done by minimizing an error function

$$f(\mathbf{P}) = \sum_i w_i \left(\frac{C_i^{\mathrm{EMT}}(\mathbf{P}) - C_i^{\mathrm{target}}}{C_i^{\mathrm{target}}} \right)^2 \qquad (10)$$

where $\mathbf{P}$ is the set of parameters being optimized. C_i^{EMT} and C_i^{target} are properties being used in the optimization, with the former being values calculated with the potential and the latter being target values from experiment or DFT calculations. The weights w_i can be used to adjust the relative importance of the various quantities being fitted. Ideally, these weights should reflect relative uncertainties on the target values, but in reality they have to reflect that certain properties are harder to fit than others, and that a larger misfit must be allowed for such quantities. The weights can also be adjusted if a good descriptions of some properties are considered more important than others.

To minimizing the error function (Eq. 10) we use a minimization algorithm resembling basin-hopping[15]. A Monte Carlo procedure is used to construct a random walk in parameter space and at each step a local minimization is performed with the Nelder Mead simplex algorithm[16]. The Monte Carlo procedure is started with the parameter values from the original EMT implementation[12], and at each step the last accepted parameters, $\mathbf{P}$, are changed by random factors drawn from a Gaussian distribution with a width 0.1 and a mean 1.0. The new set of parameters, $\mathbf{P}'$, are after the local minimization accepted with the probability

$$A = \min\left\{1, \exp\left(-\frac{f(\mathbf{P}) - f(\mathbf{P}')}{T\, f(\mathbf{P})}\right)\right\}. \qquad (11)$$

Here we use the relative change in error function as a measure of the acceptance probability, since we want to make moves between two large error function values equally probable as moves between small error function values. In the same manner as minimizing the potential energy a "temperature", T, is used to adjust acceptance rate. A temperature of 0.144 is chosen, which result in a 50 % chance of accepting a relative increase of 10 % of the error function.

After finding parameters for the each of the pure elements separately, the potentials are further optimized with respect to alloy properties. Now the n_0, V_0 and κ of all elements are allowed to vary simultaneously, while keeping other parameters constant. The error function (Eq. 10) now includes both the pure-element properties of all the elements and quantities relating to alloys, such as heats of formation of ordered alloys. Finally, a single Nelder-Mead optimization is done while all parameters of all metals are allowed to vary.

It is important to monitor all steps of the optimization procedure carefully, both to insure that acceptable potentials are found for all elements in the initial steps, and to insure that the later optimizations do not "sacrifice" the properties of a single element to give better results for the others.

TABLE I: Revised EMT potential parameters. **DRATFT VALUES — MAY CHANGE IN FINAL VERSION.**

Metal	E_0 (eV)	s_0 (Å^{-1})	V_0 (eV)	η_2 (Å^{-1})	κ (Å^{-1})	λ (Å^{-1})	n_0 (Å^{-3})
Ag	-2.86327	1.66504	2.01388	1.93853	2.94300	3.36962	0.04145
Al	-3.22459	1.68471	1.95940	1.57457	2.45458	2.56372	0.03703
Au	-3.66341	1.65832	2.64664	1.71984	2.61161	3.57633	0.04176
Ca	-1.78388	2.29503	2.61428	1.62087	2.70302	2.23144	0.02900
Cu	-3.38904	1.48553	2.55628	2.15650	3.38210	3.39056	0.04423
Mg	-1.50895	1.77483	1.76222	2.93783	4.85189	3.25047	0.04276
Ni	-4.29999	1.45897	3.91950	2.19528	3.50270	3.42161	0.05303
Pb	-2.02919	1.93209	1.13348	2.44066	3.83930	3.30891	0.01046
Pd	-3.64416	1.61554	3.20470	1.76375	2.68297	3.46943	0.04615
Pt	-5.46902	1.63191	4.50140	1.58293	2.41782	3.23959	0.05460
Ru	-6.73743	1.48982	2.94632	3.92075	6.23962	4.10673	0.04438
Sc	-3.07795	2.17315	5.05400	1.23824	2.03161	2.06617	0.05941
Sr	-1.67041	2.49188	2.22683	1.51657	2.49294	2.04637	0.02534
Y	-3.58255	2.38967	5.01972	1.09226	1.78623	1.77614	0.06358
Zr	-4.97575	2.12487	6.57236	1.09563	1.78277	1.89956	0.08365

IV. A GENERAL SET OF EMT PARAMETERS

In this section we present a general set of EMT parameters, applicable to a large set of metals crystallizing in the closed-packed crystal structures (fcc and hcp). EMT potentials and related interatomic potentials such as EAM all favor closed-packed crystal structures, and although it is possible to fit parameters that stabilize the more open body-centered cubic (bcc) structure, such a potential is unlikely to give a good, transferable description of these metals. For that reason, we limit ourselves to the closed-packed structures. As the number of parameters to be fitted grows linearly with the number of elements, and the number of alloy properties to be fitted to grow quadratically with the number of elements, it was not feasible to fit all elements simultaneously. Instead, we split up the elements in two "tiers", where tier-1 contains the same six elements as the original EMT potential (Ni, Cu, Pd, Ag, Pt and Au), for which the good performance of EMT has been established over the years. Tier-2 contains six new elements that do not form part of the original potential. We then fit the tier-1 elements first, and later the tier-2 elements while keeping all tier-1 element parameters fixed, but including alloys between tier-1 and tier-2 element in the fitting of tier-2.

We fit the potential to lattice constants, cohesive energies, elastic constants, surface energies and intrinsic stacking fault energies.

Target values for lattice constants and elastic moduli are preferably from experimentally measured references obtained at 0 K, since temperature effects are not included in the fitting procedure, so it is essentially done at 0 K. The majority of these lattice constants are obtained by a publication by Haas *et al.*[?] , where they use the data to evaluate different exchange-correlation potentials commonly used with DFT. For that purpose, they correct the experimental lattice constant by removing the contribution from the zero-point motion of the nuclei. As zero-point motion is not included in classical molecular dynamics simulations, we find it more appropriate to use the uncorrected values for this work, in order to reproduce the correct lattice constant in simulations. If lattice constants are not available at 0K, we as far as possible extrapolate them from room temperature using the thermal expansion coefficient. Since the thermal expansion coefficient is itself temperature dependent, and is approximately proportional to temperature, a factor $\frac{1}{2}$ is included in the extrapolation. We have verified for the cases where both room temperature and 0K data are available that this extrapolation gives a more accurate result than either using the room temperature lattice constant directly, or using values calculated using DFT.

Cohesive energies measured at 0 K and 1 atm are readily known form experiments[17,18] and these are therefore used.

Single-crystal elastic constants are known form experiments at room-temperature[19?,?] and for some metals also at at 0 K[17?,?] . When experimental values at 0 K are not available, we prefer to use room temperature values rather than values calculated with DFT, since the difference between DFT and 0 K values typically are larger than the one between room-temperature and 0 K values[20]. For strontium and calcium, the single-crystal elastic constants can be found in Smithells handbook of metals and in some solid-state physics textbooks, but these values are inconsistent with the polycrystalline data. When tracking down the original litterature, it turns out that these values are from old electronic structure and Morse-potential calculations. For these two metals, we have calculated the single-crystal elastic constants using DFT and the PBEsol exchange-correlation potential, finding values that agree well with the polycrystalline experimental data. When fitting the elastic constants, we fit for FCC metals the bulk modulus $B = \frac{1}{3}(C_{11} + 2C_{12})$, the shear modulus C_{44} (which is different from the polycrystalling shear modulus G), and with lower weight the elastic anisotropy

TABLE II: Target values for the used material properties and the results from the fitted EMT potentials for the FCC metals.

Property		Ag	Al	Au	Ca	Cu	Ni	Pb	Pd	Pt	Sr
a											
	Target	4.07	4.03	4.07	5.57	3.60	3.52	4.92	3.88	3.92	6.05
	This work	4.07	4.02	4.07	5.59	3.60	3.51	4.90	3.88	3.91	6.05
	Orig. EMT	4.06	3.99	4.06	—	3.59	3.49	—	3.88	3.92	—
B											
	Target	108.70	79.40	180.30	17.60	142.00	187.60	48.80	195.40	288.40	12.60
	This work	109.02	73.50	184.08	16.96	139.00	182.68	49.69	189.92	273.29	12.14
	Orig. EMT	100.17	40.19	173.86	—	134.78	181.34	—	180.66	278.69	—
C_{11}											
	Target	131.50	114.30	201.60	23.40	176.20	261.20	55.50	234.10	358.00	17.40
	This work	123.86	81.13	197.46	23.60	163.06	220.20	61.62	211.82	298.02	17.64
	Orig. EMT	125.88	54.04	196.51	—	172.95	243.04	—	217.59	318.58	—
C_{12}											
	Target	97.30	61.90	169.70	16.10	124.90	150.80	45.40	176.10	253.60	9.80
	This work	101.61	69.68	177.39	13.64	126.98	163.92	43.72	178.98	260.92	9.39
	Orig. EMT	87.31	33.26	162.54	—	115.69	150.50	—	162.20	258.75	—
C_{44}											
	Target	51.10	31.60	45.40	23.80	81.80	131.70	19.40	71.20	77.40	16.70
	This work	49.31	24.06	46.35	19.42	78.28	119.96	27.80	68.82	72.06	15.94
	Orig. EMT	54.20	36.56	47.02	—	89.71	147.40	—	74.51	79.48	—
E_{coh}											
	Target	2.95	3.39	3.81	1.84	3.49	4.44	2.03	3.89	5.84	1.72
	This work	2.96	3.38	3.80	1.83	3.50	4.47	2.03	3.89	5.86	1.72
	Orig. EMT	2.96	3.28	3.80	—	3.51	4.44	—	3.90	5.85	—
γ_{111}											
	Target	0.45	0.45	0.45	0.41	0.54	0.78	0.21	0.70	0.79	0.37
	This work	0.57	0.48	0.73	0.38	0.61	0.86	0.25	0.91	1.22	0.39
	Orig. EMT	0.24	0.30	0.23	—	0.36	0.55	—	0.27	0.31	—
γ_{100}											
	Target	0.58	0.60	0.63	0.47	0.71	1.01	0.31	0.89	1.07	0.43
	This work	0.69	0.57	0.90	0.44	0.73	1.01	0.32	1.09	1.47	0.45
	Orig. EMT	0.32	0.36	0.31	—	0.45	0.68	—	0.36	0.42	—
$\gamma_{111}/\gamma_{100}$											
	Target	0.78	0.74	0.71	0.89	0.77	0.77	0.67	0.79	0.74	0.86
	This work	0.83	0.84	0.81	0.85	0.84	0.85	0.78	0.83	0.83	0.86
	Orig. EMT	0.77	0.84	0.74	—	0.80	0.81	—	0.75	0.74	—
γ_{sf}											
	Target	0.02	0.13	0.03	0.01	0.04	0.16	0.04	0.17	0.32	0.01
	This work	0.02	0.03	0.03	0.00	0.03	0.05	-0.00	0.05	0.08	0.00
	Orig. EMT	0.01	0.05	0.00	—	0.03	0.05	—	0.01	0.01	—

$A = (C_{11} - C_{12})/C_{44}$, rather than fitting C_{11} and C_{12} directly, as the bulk modulus is often more important for the applications. For HCP metals, we fit the bulk modulus $B = XXX$ and the elastic constants C_{11}, C_{12}, C_{13}, C_{33}, and C_{44}.

Surface energies of solids are exceedingly difficult to measure, and reliable values are not available, we therefore turn to DFT calculations. Since Schimka *et al.*[21] have shown that PBEsol gives a reasonable description of surface energies, at the price of giving a worse description of chemical reactivity of surfaces and molecules, we again use that exchange-correlation potential for the DFT calculations. The surface energies (γ) to which we fit are the closed-packed (111)-surface and the more open (100)-surface. We chose to fit directly to the former and only to include the latter through the ratio $\gamma_{100}/\gamma_{111}$, as the ratio between surface energies is often more important than the absolute value, for example when the potential is used to determine the shape of nanoparticles[22?] . For HCP metals we only fit the closed-packed surface energy $\gamma_{(0001)}$.

For FCC metals we fit the energy of the (111) and (with higher weight) the ratio between the (100) and (111) surface energies, rather than fitting the two surface energies separately, as the ratio between surface energies is more important than the absolute values e.g. for the shape of nanoparticles.

The target values are listed in Table II and we refer to the Appendix for calculation details. XXX

After fitting each element separately, we use these parameters as a starting point when fitting alloy data. The properties of a pure element does not depend on the

EMT parameter $n0$, and only weakly on V_0 and κ if $\delta = V_0(\beta\eta_2 - \kappa)$ is kept constant. For this reason, we fit the alloy properties allowing these three parameters to vary, but keeping the remaining four parameters fixed. We fit the potential to alloys with all combination of elements in the $L1_2$ ($AuCu_3$) and $L1_0$ (AuCu) structures. For the cubic $L1_2$ structure, we fit to the lattice constant, the bulk modulus and the alloying energy. For the tetragonal $L1_0$ structure, we fit to the two lattice constants and the alloying energy. In the fitting procedure, all pure-element quantities are still calculated, to prevent damaging the pure-element properties. As a final step, the parameters are optimized with all parameters of all elements allowed to vary simultaneously, but in this step no Monte Carlo search is done in parameter space, only a minimization using the Nelder-Mead simplex algorithm. As not all of these alloys are stable in nature, we have chosen to fit to values calculate using DFT in the PBEsol approximation.

The potential parameters resulting from the fitting are shown in Table I, the fitted values for the material properties are shown in the appendix. Figure 2 show the quality of the fit, i.e. the deviation between target and fitted value, and compares it to the original EMT parameters. It is seen that the refitting improves almost all quantities, but most dramatically the surface energies, which were not fitted in the original formulation. Such an improvement of surface energies when they are included in the fit has also been reported by Rasmussen[23,24]. The fitted lattice constants and cohesive energies are in excellent agreement with their target values, and the fitted bulk modulus and shear modulus only deviate a little from the target values. The elastic constants C_{11} and C_{12} have opposite deviations form the target values, since this results in good values for the bulk modulus. This indicates that the elastic anisotropy of the fcc metals is slightly underestimated by these potentials. The stacking fault energy is difficult to describe correctly in an EMT style potential, as all nearest neighbors and second-nearest neighbors are in the same distance as in the FCC structure, and as there are no angular-dependent terms in the potential. For most metals, the stacking fault energy is severely underestimated, for Pb it even has a small negative value.

The quality of the fit to the alloy parameters is shown in Fig. 4, where XXXX.

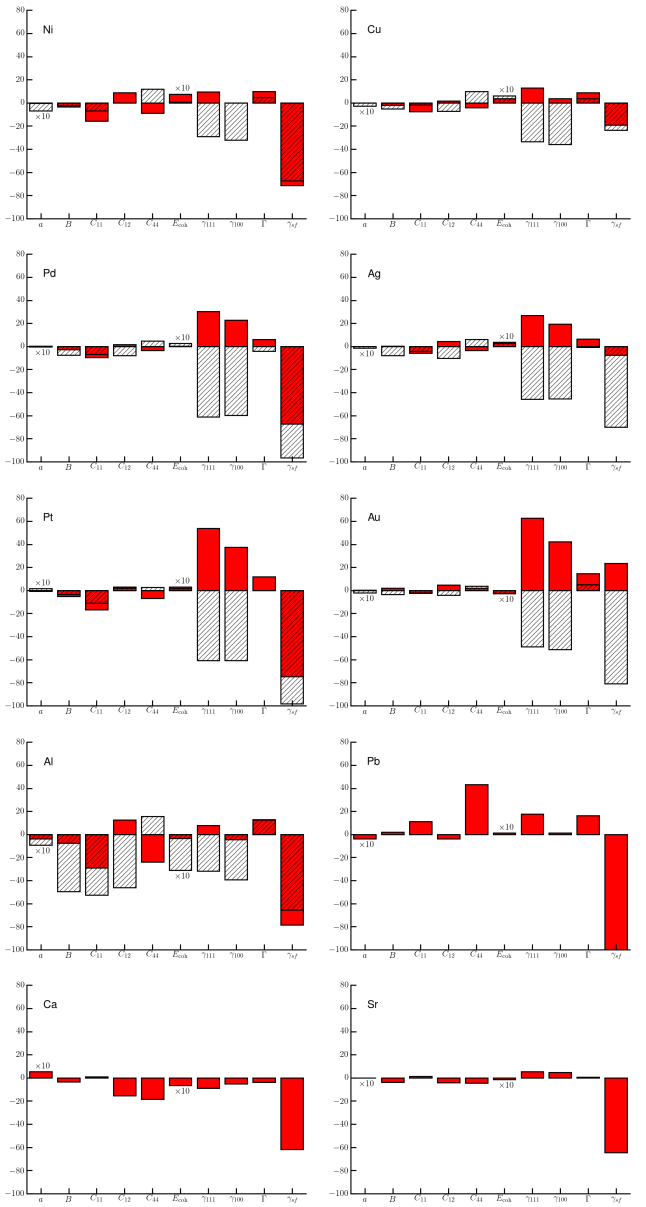

FIG. 2: Deviation of the materials properties of the metals described with the new (red) and old (striped) EMT potential. In general the new potentials are more accurate than the old ones, in particular when it comes to the surface energies. This is mainly due to the old potentials not being optimized for these.

V. SPECIALIZED PARAMETERS FOR PLATINUM ALLOYS

An all-purpose potential as the one presented in the previous section is by necessity a compromise between the many properties fitted. More specialized potentials can (and should) be fitted for specific purposes. In this section, we present a potential fitted for a series of platinum alloys of particular interest for the oxygen evolution reaction in polymer electrolyte membrane fuel cells. We are particularly interested in the properties of alloys with the composition Pt_3X and Pt_5X, where X is a rare-earth or alkaline earth metal. As we are only interested in alloys containing platinum, and not in alloys between the other element, the fitting can be focused on the platinum alloys without worrying about having a proper fit of the irrelevent alloys. We start with the same pure-element parameters as before, but this time we fit to alloys in the $L1_2$ and $L1_0$ structure as before, in the compositions

TABLE III: EMT parameters fitted for Platinum alloys.

Metal	E_0 (eV)	s_0 (Å^{-1})	V_0 (eV)	η_2 (Å^{-1})	κ (Å^{-1})	λ (Å^{-1})	n_0 (Å^{-3})
Ca	-1.72226	2.41028	1.57827	1.54112	2.32870	2.03554	0.01146
Mg	-1.28192	1.96830	0.79162	1.88179	2.11410	2.99732	0.01124
Pt	-5.46902	1.63191	4.50140	1.58293	2.41782	3.23959	0.05460
Sc	-3.36073	2.07250	1.35025	1.64560	1.83222	2.33563	0.01445
Sr	-1.61779	2.56585	1.56429	1.59853	2.46517	1.86187	0.00943
Y	-3.66086	2.33797	1.26263	1.55387	1.52622	2.00561	0.01074

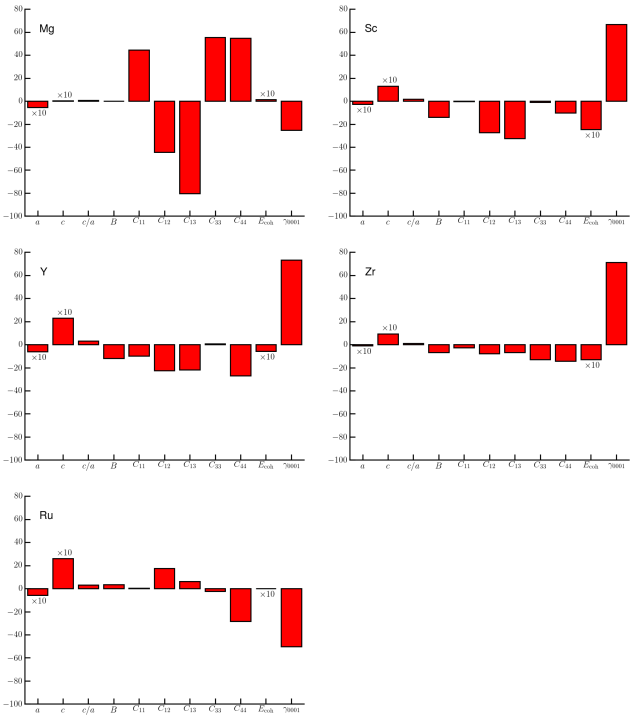

FIG. 3: Deviation of the materials properties of the metals described with the new (red) and old (striped) EMT potential. In general the new potentials are more accurate than the old ones, in particular when it comes to the surface energies. This is mainly due to the old potentials not being optimized for these.

MISSING FIGURE

FIG. 4: Alloy data.

Pt_3X, PtX and PtX_3; but also to Pt_5X alloys in the hexagonal $CaCu_5$ phase, where we fit to the two lattice parameters and to the alloying energy. All parameters for Pt are retained from the general potential, as this insures that region in the simulation cell with pure Pt are consistent with results obtained with the general potential, and as it did not give noticably better results to allow the Pt parameters to vary. All parameters of the alloying elements are allowed to vary, and pure-element properties are part of the fitting procedure. As we only attempt to describe binary alloys between Pt and one other element, the elements can be fitted independently.

The results of the fitting procedure are shown in Table III

VI. CONCLUSION

We have presented a modernized version of the EMT potential, that eliminates the need for a "hard" cutoff of the interaction function and the derivative peak in the original version. In addition, we have refitted all potential parameters, yielding an improvement of the description of almost all quantities tested with respect to the original EMT potential.

VII. APPENDIX

The following gives a short description of the methods used to calculate the lattice constants and surface energies. The GPAW[25] DFT code has been used with the PBEsol exchange-correlation potential[26]. In the calculations has both a plane wave and grid-based representation been used.

A. Lattice constants

The equilibrium lattice constants are found by a minimization of the energy with respect to the lattice parameters. For a cubic crystal with only one lattice constant this is done by calculating the energy for a range of different lattice constants spanning 0.5 % on each side of the equilibrium, and then finding the minimum based on a third order inverse polynomial fit to the volume[27]. For a hexagonal crystal the same principle can be applied in two dimensions, but since the number of energy calculations goes quadratically with the number of lattice parameters in the mentioned range this is unfeasible. Instead we turn to a minimization of the energy with respect to the energy using the Nealder-Mead downhill simplex algorithm[16].

The calculations are carried out in plane wave mode with a plane wave cutoff of 1000 eV and a k-point sampling with 12 points in all directions.

B. Surface energies

The surface energies were calculated based on the method by Fiorentini and Methfessel[28], where the surface energies are extrapolated using a linear fit to a set of slab energies.

The DFT calculations are carried out on slabs with 3, 5, 7 and 9 layers using grid mode with a grid spacing of 0.15 Å and a k-point sampling of 12 in the two in plane directions with periodic boundary conditions. The vacuum above and below the slab was at minimum 6.0 Å and have been fitted, so the total height of the cell was dividable with the grid spacing. This was done to have an integer number of grid points, keeping the atoms positions relative to the grid points fixed when the slab thickness increases. The two outer most layers were only relaxed on one side until the maximum force was below 0.05 eV/Å^2, assuming a symmetric relaxation on both sides.

* Electronic address: schiotz@fysik.dtu.dk

[1] P. Hohenberg and W. Kohn, Physical Review **136**, B864 (1964).
[2] W. Kohn and L. J. Sham, PhysRev **140**, A1133 (1965).
[3] J. Schiøtz and K. W. Jacobsen, Science **301**, 1357 (2003).
[4] X. W. Gu, C. N. Loynachan, Z. Wu, Y.-W. Zhang, D. J. Srolovitz, and J. R. Greer, Nano Letters **12**, 6385 (2012).
[5] E. Bringa, A. Caro, Y. Wang, M. Victoria, J. McNaney, B. Remington, R. Smith, B. Torralva, and H. Van Swygenhoven, Science **309**, 1838 (2005).
[6] S. M. Foiles, M. I. Baskes, and M. S. Daw, Physical Review B **33**, 7983 (1986).
[7] F. Ercolessi, M. Parrinello, and E. Tosatti, Philosophical Magazine A **58**, 213 (1988).
[8] R. Gupta, Physical Review B **23**, 6265 (1981).
[9] V. Rosato, M. Guillope, and B. Legrand, Philosophical Magazine A **59**, 321 (1989).
[10] M. W. Finnis and J. E. Sinclair, Philosophical Magazine A **50**, 45 (1984).
[11] K. W. Jacobsen, J. Norskov, and M. Puska, Physical Review B Condensed Matter **35**, 7423 (1987).
[12] K. W. Jacobsen, P. Stoltze, and J. Nørskov, Surface Science **366**, 394 (1996).
[13] N. Bailey, J. Schiøtz, and K. Jacobsen, Physical Review B Condensed Matter **69**, (2004).
[14] A. Paduraru, A. Kenoufi, N. P. Bailey, and J. Schiøtz, Advanced Engineering Materials **9**, 505 (2007).
[15] D. J. Wales and H. A. Scheraga, Science (New York, N.Y.) **285**, 1368 (1999).
[16] W. H. Press, S. A. Teukolsky, W. T. Vetterling, and B. P. Flannery, *Numerical Recipes in C* (Cambridge University Press, Cambridge, 1995), 5th ed.
[17] C. Kittel, *Introduction to solid state physics* (John Wiley & Sons, 2005), 8th ed.
[18] L. Brewer, Tech. Rep. 2, Lawrence Berkeley National Laboratory (LBNL), Berkeley, CA (1975).
[19] K. Gschneidner, Solid State Physics **16**, 275 (1964).
[20] S. H. Brodersen, Ph.D. thesis, Technical University of Denmark (2013).
[21] L. Schimka, J. Harl, A. Stroppa, A. Grüneis, M. Marsman, F. Mittendorfer, and G. Kresse, Nature materials **9**, 741 (2010).
[22] G. Wulff, Z. kristallogr **34**, 449 (1901).
[23] T. Rasmussen, *private communications*.
[24] T. Rasmussen, Physical Review B **62**, 12664 (2000).
[25] J. Enkovaara, C. Rostgaard, J. J. Mortensen, J. Chen, M. Duak, L. Ferrighi, J. Gavnholt, C. Glinsvad, V. Haikola, H. A. Hansen, et al., Journal of physics. Condensed matter : an Institute of Physics journal **22**, 253202 (2010).
[26] J. Perdew, A. Ruzsinszky, G. Csonka, O. Vydrov, G. Scuseria, L. Constantin, X. Zhou, and K. Burke, Physical review letters **100**, 136406 (2008).
[27] A. Alchagirov, J. Perdew, J. Boettger, R. Albers, and C. Fiolhais, Physical Review B **67**, 026103 (2003).
[28] V. Fiorentini and M. Methfessel, Journal of Physics: Condensed Matter **8**, 6525 (1996).

Paper III

Pt_xGd alloy formation on Pt(111): Preparation and structural characterization

Elisabeth T. Ulrikkeholm, Anders F. Pedersen, Ulrik G. Vej-Hansen, Maria Escudero-Escribano, Ifan E. L. Stephens, Daniel Friebel, Apurva Mehta, Jakob Schiøtz, Robert K. Feidenhansl', Anders Nilsson and Ib Chorkendorff

Submitted, 2015

Pt_xGd alloy formation on Pt(111): Preparation and structural characterization

Elisabeth T. Ulrikkeholm[a,*], Anders F. Pedersen[a,*], Ulrik G. Vej-Hansen[b], Maria Escudero-Escribano[a], Ifan E. L. Stephens[a], Daniel Friebel[c], Apurva Mehta[d], Jakob Schiøtz[b], Robert K. Feidenhansl'[e], Anders Nilsson[c], Ib Chorkendorff[a,**]

[a]*Department of Physics, Center for Individual Nanoparticle Functionality, Building 312, Technical University of Denmark, 2800 Lyngby, Denmark*
[b]*Department of Physics, Center for Atomic-scale Materials Design, Building 307, Technical University of Denmark, 2800 Lyngby, Denmark*
[c]*Department of Chemical Engineering, SUNCAT Center for Interface Science and Catalysis, Stanford University, Stanford, CA, USA*
[d]*Stanford Synchrotron Light Source, SLAC National Laboratory, 2575 Sand Hill Road, 94025, Menlo Park, CA, USA*
[e]*Niels Bohr Institute, University of Copenhagen, DK-2100 Copenhagen*

Abstract

Pt_xGd single crystals have been prepared in ultra high vacuum (UHV). This alloy shows promising catalytic properties for the oxygen reduction reaction. The samples were prepared by using vacuum deposition of a thick layer of Gd on a sputtercleaned Pt(111) single crystal, resulting in a ~63 nm thick alloy layer. Subsequently the surfaces were characterized using low energy electron diffraction (LEED), ion scattering spectroscopy (ISS) and temperature programmed desorption (TPD) of CO. A Pt terminated alloy was observed upon annealing the sample to 600 °C. The LEED and XRD experiments have shown that a slightly compressed (2×2) alloy appear. This structure is sometimes rotated 30° with respect to the Pt substrate. The TPD spectra show a well-defined peak shifted down 200 °C in temperature. The crystal structure of the alloy was investigated using ex-situ x-ray diffraction experiments, which revealed an in-plane compression and a complicated stacking sequence. The crystallites in the crystal are very small, and a high degree of merohedral twinning was observed.

Keywords: Platinum alloys, Single crystals, X-ray diffraction, Alloy formation

1. Introduction

One of the most promising technologies for utilizing the energy stored in hydrogen is the low temperature polymer electrolyte membrane fuel cell (PEMFC). However, as a consequence of a large potential loss on the cathode these devices require a large amount of Pt to catalyze the Oxygen Reduction Reaction (ORR). To lower the Pt loading and improve the activity, Pt based alloys can be used instead of pure Pt. [1–6]. However, bimetallic alloys tend to dealloy in the acidic environment in a fuel cell, causing the catalyst to degrade [7–9]. Bimetallic systems based on platinum and lanthanide metals have shown high catalytic activity for the ORR. Due to their large, negative heat of formation, these alloys may not be as prone to electrochemical dealloying [10–12]. Pt_xGd exhibit an exceptionally high activity for oxygen reduction, both in the polycrystalline form and the nanoparticulate form [12–14]. Gd modified Pt(111) single crystals have been investigated in order to understand the origin of the enhanced activity of this alloy. This article contains a thorough description of the alloy prepared in UHV combined with investigations of the crystal structure. The ideal catalyst for ORR will have a slightly weaker reactivity than Pt(111), and bind oxygen 0.2 eV weaker [15, 16]. To probe the reactivity of the surface, CO temperature programmed desorption experiments have been performed. Yates was amongst the pioneers of this techniques, which his group used on single crystals to study to study the dynamics of molecules, the effect of steps on the reactivity of Pt(112) [17], and reaction pathways on Ni(111) [18].

X-ray diffraction experiments made on polycrystalline Pt_5Gd have shown that this alloy has a large unit cell with a complicated stacking [19, 20]. Furthermore, these studies never found the crystal structure for Pt_5Gd using powder samples. In this article, we demonstrate how we can determine the space group, unit cell, and

*These authors contributed equally to this work.
**Corresponding author.
Email address: ibchork@fysik.dtu.dk (Ib Chorkendorff)

structural motifs behind a Pt-Pt compression using a 3-dimensional diffraction pattern. Due to the complicated stacking expected for this alloy, single crystal diffraction is essential, since it provides much more structural information than powder diffraction.
Understanding and characterizing this alloy system is imperative, since it is the precursor for a highly active surface for the ORR. We publish this work in memory of John T. Yates and his great contribution to the field of surface science.

2. Experimental setup

The sample preparation and the UHV characterization were performed in a vacuum chamber with a base pressure of $1.0{\cdot}10^{-10}$ Torr. The chamber is equipped with standard UHV surface science techniques; x-ray photoelectron spectroscopy (XPS), ion scattering spectroscopy (ISS), low energy electron diffraction, and a quadrupole mass spectrometer for temperature programmed desorption (TPD). ISS is performed using He^+ ions accelerated over an acceleration voltage of 1.25 kV. The XPS experiments were performed using K_α radiation from a Mg anode (1253.4 eV).
The sample, a Pt(111) single crystal, 5 mm in diameter and 3 mm thick, was supplied by MaTecK, GmbH, Germany. The sample was mounted in a hairpin shaped tungsten wire which is then mounted onto the feedthrough on the manipulator end [21]. The temperature is measured using a type K thermocouple. The sample can be resistively heated using a PID controller, and cooled to $T = -190°$C using liquid nitrogen. The main chamber is equipped with a water cooled metal Gd evaporator and a Quartz Crystal Microbalance (QCM), which makes it possible to evaporate Gd on the surface of the sample at a well known evaporation rate. The evaporator was made by cutting flakes of a Gd foil and attaching them to a coil shaped 0.25 mm 99.95 % tungsten wire. The Gd flakes were cut from a 0.127 mm 99.9 % Gd foil supplied by Alfa Aesar.

After the Gd/Pt(111) single crystal was made with a thick alloy in the UHV chamber at DTU, it was transported to the Stanford Synchrotron Radiation Lightsource (SSRL) where the diffraction experimentes were carried out at beam line 7-2. This beam line is equipped with a Huber six-circle (4+2) diffractometer and a Dectris Pilatus 300K imaging detector. The diffractometer stage was equipped with a goinimeter head that allowed the crystal surface normal to be aligned to the phi rotation axis using a laser. All the data was acquired at a fixed incidence angle of 0.2° to maximize surface sensitivity, and the photon energy was set to 11.0 keV to avoid fluorescence background from the Pt. A sketch of the setup is seen in Figure 1 [22]. At each detector position a circular diffraction pattern from a polycrystalline LaB_6 sample was recorded, so that the position of the detector could be calculated. Data was acquired by rotating the crystal in steps of 0.2°, and a rocking scan was performed in each spot. This was repeated using 6 different positions of the detector. The acquired diffraction data was stitched together to form a 3 dimensional image of parts of the Q-space, and the intensity has been corrected for the Lorentz factor, polarization, and geometrical effects using MatLab scripts developed by the authors.

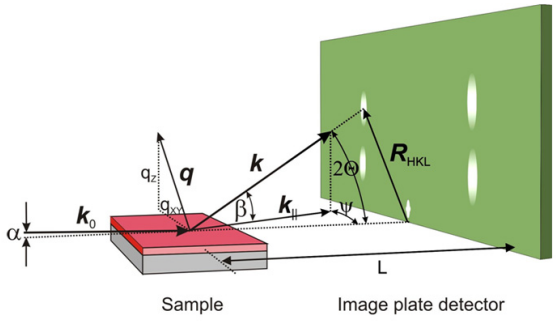

Figure 1: *A sketch of the experimental setup used for the x-ray diffraction measurements. The incidence angle was fixed at $\alpha = 0.2°$ for all measurements. The whole reciprocal space is reconstructed by rotating the sample around its surface normal and stitching each slice of data. The image is from [22].*

3. Results

3.1. Alloy formation

Earlier experiments have shown that it is possible to prepare a well-organized crystalline structure by vacuum deposition of monolayers of lanthanide metals on a sputter cleaned Pt single crystal [23–26]. Our experiments with deposition of thick layers of Y on Pt(111) have shown that it is possible to simulate a crystal that behaves like a single crystal [27]. On the basis of these promising results, we initiated experiments on Gd modified Pt(111) single crystals.

3.1.1. Creating a near surface alloy

To probe whether Gd and Pt would form an alloy, a thin layer of 2 nm Gd was deposited on a sputter cleaned, annealed Pt(111) surface. XPS measurements performed after the deposition showed that the Gd was

oxidized, see Appendix A. To remove traces of gadolinium oxide, the sample was gently sputtered using Ar ions for 10 min. The composition of the atoms in the surface of the sample was subsequently probed using ISS. The sample was then heated in steps of 25 °C and the composition of the surface was evaluated after each heating step. ISS spectra for representative temperatures can be seen in Figure 2. At $T = 200$ °C the spectrum is dominated by Gd, at $T = 500$ °C the Pt signal becomes visible, and at $T = 800$ °C the surface is completely dominated by Pt, indicating a formation of a Pt_xGd alloy terminated by a Pt overlayer.

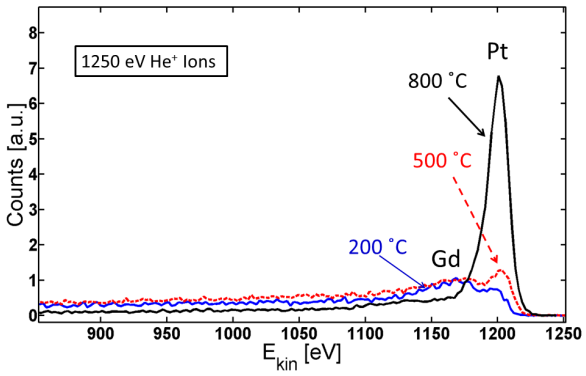

Figure 2: *ISS spectra measured at different temperatures. At $T = 200$ °C the sample is dominated by Gd and only a small amount of Pt can by seen, at $T = 500$ °C the platinum signal becomes more pronounced, and at $T = 800$ °C the Pt signal becomes dominating indicating the formation of a Pt overlayer.*

In Figure 3 the relative intensity of the Gd signal can be seen as a function of temperature. It can be seen that the amount of Gd in the surface drops rapidly at $T = 450$ °C, and at temperatures above $T = 500$ °C, the spectra are dominated by Pt, indicating inter-diffusion of Gd and the formation of a Pt overlayer. The alloying process is sketched in Figure 4.

XPS was performed to verify that the Gd has merged to the subsurface layer, and that the decrease in the Gd intensity is not a consequence of He^+ sputtering of the gadolinium atoms in the surface during the ISS experiment, see Figure 5. The quantification of the different elements in the sample can be seen in Table 1, and an overview spectrum can be seen in Appendix A. From the XPS spectra, it can be seen that the gadolinium is still present, indicating that it has merged to the subsurface region and has created a near surface alloy (NSA). It is possible to calculate the stoichiometry of the alloy under the assumption that the surface is terminated by a

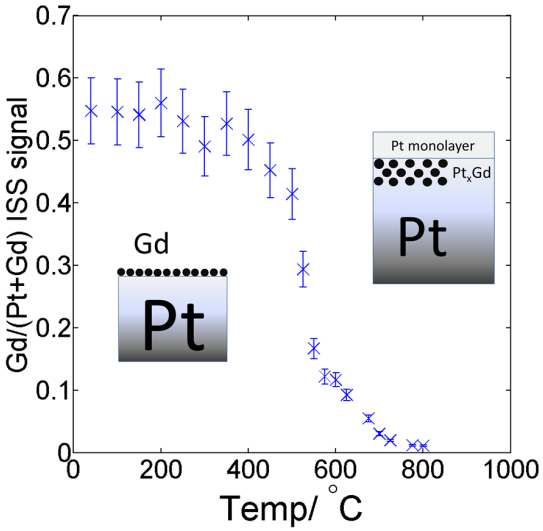

Figure 3: *The 'Gd' to the 'Gd+Pt' ratio probed with ISS as a function of temperature. The intensities have been found by comparing the peak intensities. No sensitivity factors have been used and hence the ratio can only be considered qualitatively. At $T = 450$ °C the amount of Gd decreases significantly indicating alloy formation terminated by a Pt overlayer.*

single layer of platinum [28]. The quantification of the XPS spectrum can be seen in Table 1

Pt [%]	Gd [%]	x for Pt/Pt_xGd
89.7	10.3	6.9

Table 1: Concentrations of the different elements in the Gd/Pt(111) quantified with XPS after the gadolinium deposition and annealing to 800 °C.

To probe the reactivity of thin Pt_xGd alloy terminated by Pt, CO TPD was performed on a CO saturated surface. $2.0 \cdot 10^{-7}$ torr CO was dosed for 30 minutes while the sample was cooled from 400 °C to -190 °C, corresponding to a dosage of 360 L. The sample was heated at a constant rate of 2 °C/s during the TPD experiments. The CO TPD can be seen in Figure 6 where it is compared to a CO TPD made on a CO saturated Pt(111) surface. The experiment was performed several times, and has shown a high degree of reproducibility. This indicates that there were no dissociation of CO.
In the CO TPD made on the Gd/Pt(111) sample a sharp peak appears at $T = -10$ °C. This peak has a shoulder to higher temperatures at $T = 0$ °C, and a less pronounced shoulder to lower temperatures at $T = -60$ °C. The integrated intensity of the desorption peaks were calculated to evaluate the amount of CO molecules ad-

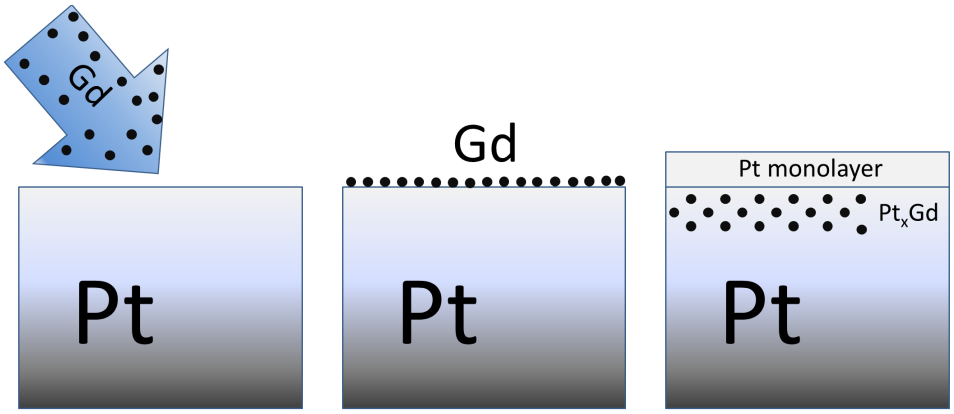

Figure 4: *The deposition process. Gd is deposited on the surface of a Pt(111) a room temperature. At this temperature the Gd is not mobile. After heating up the crystal Gd becomes mobile and migrate to the subsurface region and a Pt overlayer is formed.*

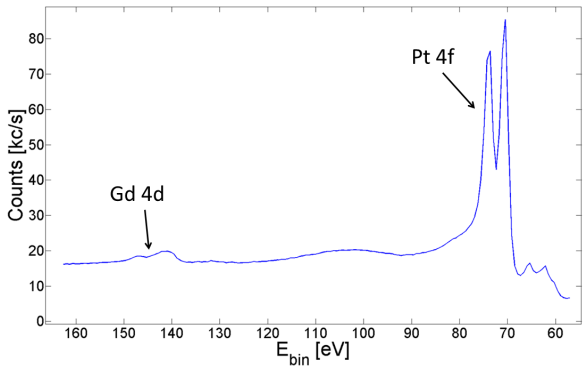

Figure 5: *XPS performed after Gd deposition and annealing to 800 °C.*

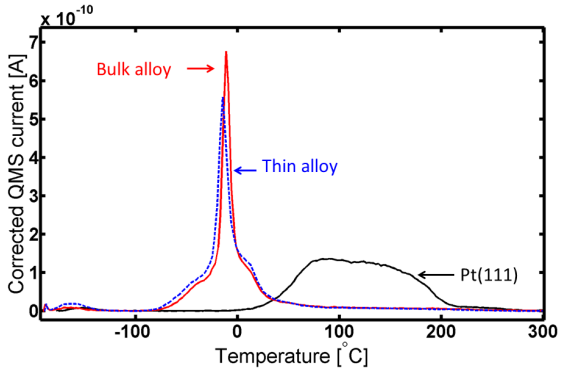

Figure 6: *TPDs on CO saturated surfaces. Blue curve: TPD made on the thin, near surface alloy of Gd/Pt(111) alloy, red curve TPD made on the bulk alloy, black curve TPD made on a sputter cleaned, annealed Pt(111) surface. The TPDs are made at a constant heating rate of 2 °C/s.*

sorbed to the surface during the TPD experiments. The coverage of the sample can be evaluated by comparing this value to the integrated intensity of the desorption peak from the Pt(111) sample, since the behavior of CO on clean Pt(111) surfaces has been studied extensively over the last decades [29–33]. For a perfect Pt(111) single crystal the CO saturation coverage is $\theta = 0.68$ [30]. By comparing the integrated desorption peaks we determine the a CO saturation coverage of $\theta = 0.54 \pm 0.03$ on Gd/Pt(111).

3.1.2. Simulating a bulk alloy

To simulate the behavior of a bulk alloy, a thick layer of Gd was deposited on a sputtercleaned, annealed Pt(111) surface. A thick layer of (200 ± 50) Å Gd was deposited on a sample heated to a temperature of 800 °C. This temperature is well above the mobility temperature and hence we anticipate that a platinum overlayer will form instantaneously which will protect the Gd from oxidation. The stoichiometry of the alloy was evaluated using XPS, see Table 2. Traces of oxygen were seen in the XPS spectra, see Figure 7, indicating the formation of gadolinium oxide. To remove this, the sample was sputtered gently using Ar-ions while the sample was kept at 800 °C. The amounts of oxygen and gadolinium have decreased significantly after the sputtering, which implies that a layer of gadolinium oxide has been formed on the surface during the evaporation, and that the sputtering procedure has removed this. The stoichiometry of the alloy has been evaluated assuming that the platinum skin consists of a single layer of atomic platinum of thickness $d = 2.28$ Å [28, 34], see Table 2.

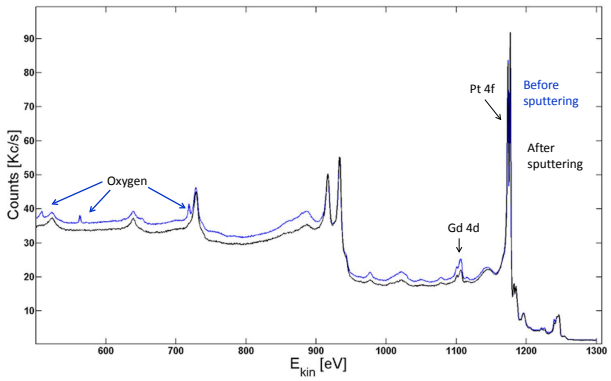

Figure 7: *Blue: XPS spectrum made after the deposition of gadolinium at 800 °C. Oxygen can be seen in this spectrum indicating the formation of gadolinium oxide. Black: XPS spectrum made on the sample after a light sputtering at 800 °C. After the sputtering, the oxygen signal is close to the detection limit.*

	Pt [%]	Gd [%]	O [%]	x for Pt/Pt$_x$Gd
Before	74.0	17.4	8.5	3.2
After	87.4	12.5	0.1	5.5

Table 2: Concentrations of the different elements in the Gd/Pt(111) quantified with XPS after the gadolinium deposition. The measurements were made before and after Ar sputtering at 800 °C.

From the calculated Gd concentration, it is most likely that the crystal has formed Pt_5Gd, which is the most platinum rich, stable Pt_xGd alloy [35]. The composition of the surface layer was measured using ISS, see Figure 8. Gd was not seen in the ISS spectrum after the deposition, indicating the formation of a Pt overlayer.

The reactivity of this surface was probed using CO

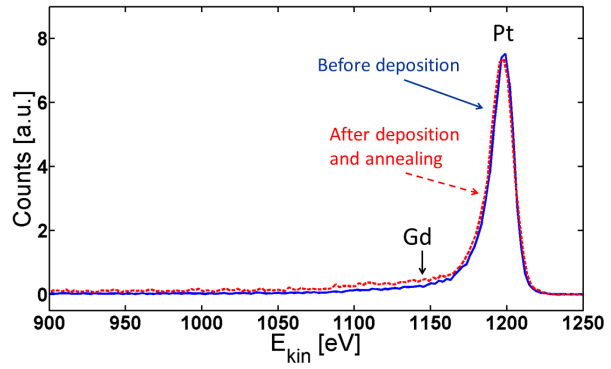

Figure 8: *ISS before and after the deposition. Gd was not seen in the spectrum measured after the deposition, indicating the existence of a Pt overlayer.*

TPD experiments using the same experimental conditions as for the thin alloy. The sample was saturated with CO, cooled using liquid nitrogen, and heated using a constant heating rate of 2 °C/s, see Figure 6. The TPD experiments were repeated several times showing a high degree of reproducibility. From the integrated intensity of the desorption peak the CO saturation coverage of this surface is $\theta = 0.58 \pm 0.02$.

LEED was performed to evaluate the crystal struc-

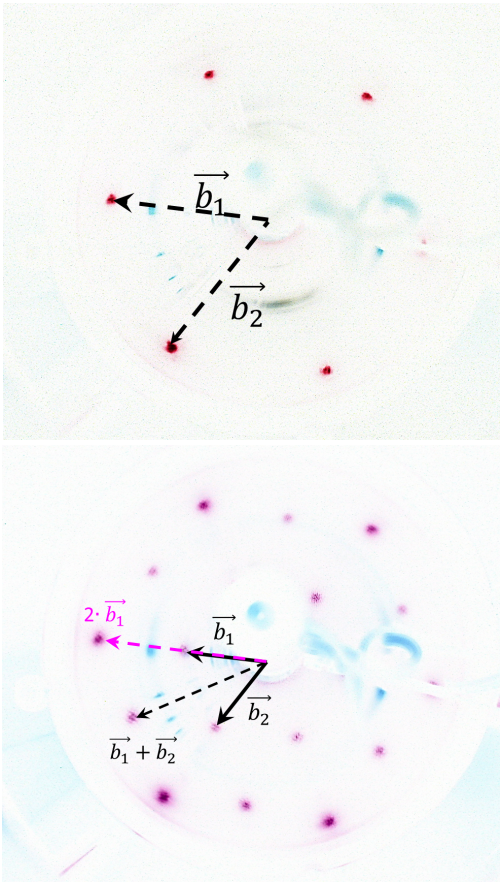

Figure 9: *Top: A LEED pattern made on a sputter cleaned, annealed Pt(111) surface. Bottom: LEED pattern made on the prepared Gd/Pt(111) sample. The colors have been inverted for clarity. The surface structure forms a (1.90 × 1.90) structure not rotated with respect to the Pt substrate.*

ture of the Gd/Pt(111) sample. This was made on the clean Pt(111) surface before the Gd deposition, and after the deposition and annealing, see Figure 9. A well-defined diffraction pattern appears after the deposition of Gd, indicating that a well-defined, crystalline surface has been formed. The structure of the Gd/Pt(111) surface is hexagonal and show a (1.90×1.90) structure, not rotated with respect to the platinum substrate. The po-

sition of the diffraction peak can be estimated within a resolution of 2 %. Gd/Pt(111) samples have been prepared using this procedure 5 times. The lattice constant of the observed structures are always the same, but the rotation could vary; sometimes a rotation of 30° was observed, and sometimes the structure was not rotated with respect to the Pt substrate, see Appendix B. This indicates that these two configurations are equivalent or extremely close in energy. We will consider this further in the discussion section.

3.2. X-ray diffraction experiments

The 3-dimensional Q-space was investigated, and it was immediately seen that the alloy has a hexagonal symmetry in the plane of the crystal surface. Figure 10 shows the diffraction pattern integrated along the L-direction, the surface normal. The arrows show the in-plane H and K crystal lattice vectors, and the L lattice vector is perpendicular to the figure plane. The red circles show the diffraction peaks from the Pt_xGd alloy, whereas the black circles show the diffraction peaks from the Pt(111) substrate. The single Pt overlayer may have a different crystal structure than the rest of the alloy, but the sensitivity of this XRD experiment is not high enough to detect a single monolayer. A large number of super-spots are seen, indicating a high degree of twinning. Besides the merohedral twinning (overlapping diffraction spots) indicated by the super-spots some non-merohedral twins are present, since many of the diffraction spots are split into 3 spots. This peak splitting indicating domains in the alloy is more clearly seen in Figure 11, showing a zoom of the white square in Figure 10. This non-merohedral twinning shows a small rotation around the surface normal, and are caused by separate domains in the alloy only, since the Pt(111) substrate do not show any splitting. Unfortunately these non-merohedral twinned peaks are too close to rigorously separate, and in the further data processing they have all been included in a single integrated intensity.

The hexagonal unit cell dimensions was found by fitting a pseudo-Voigt peak shape to the positions of the brightest alloy peaks. These positions in Q-space were then calibrated using the Pt(111) substrate diffraction peaks, and small corrections on the order of 1% were made, since the detector positioning method using the LaB_6 sample is not perfect. In the hexagonal unit cell the parameters are $a = 5.3309 \pm 0.0008$ Å and $c = 40.358 \pm 0.012$ Å. Furthermore from the width (full width at half max, FWHM) of the peaks the crystallite sizes are estimated using Scherrer's formula [36], and using a shape factor of 1 the in-plane size is estimated to be 22 nm and out-of-plane size 12 nm. This small crystallite size is consistent with the high number of super-

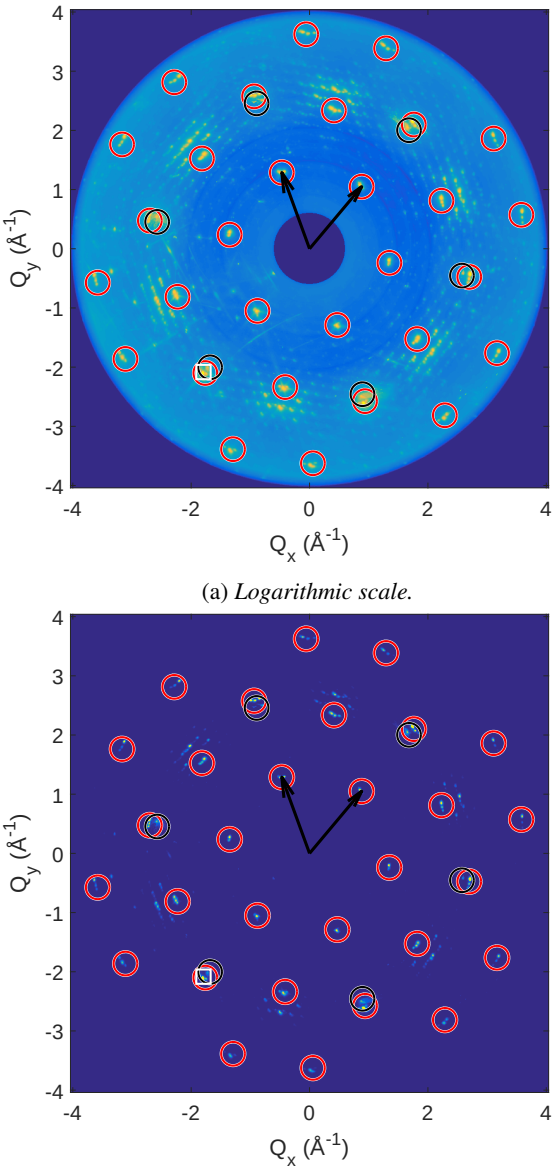

(a) *Logarithmic scale.*

(b) *Linear scale.*

Figure 10: *The XRD intensity integrated along the surface normal, along the L lattice vector. The arrows show the in-plane crystal lattice vectors H and K, the red circles show the diffraction peaks from the Pt_xGd alloy, and the black circles show the diffraction peaks from the Pt(111) substrate. Many super-spots are seen, indicating a high degree of twinning. Furthermore non-merohedral twinning is seen as the spots are split in 3, and this is shown by a zoom of the white square in Figure 11. In (a) the color scale is logarithmic to show more features, and the intensity ranges 4 orders of magnitude. In (b) the color scale is linear and the maximum is set to 1/4 of the maximum intensity of the peaks.*

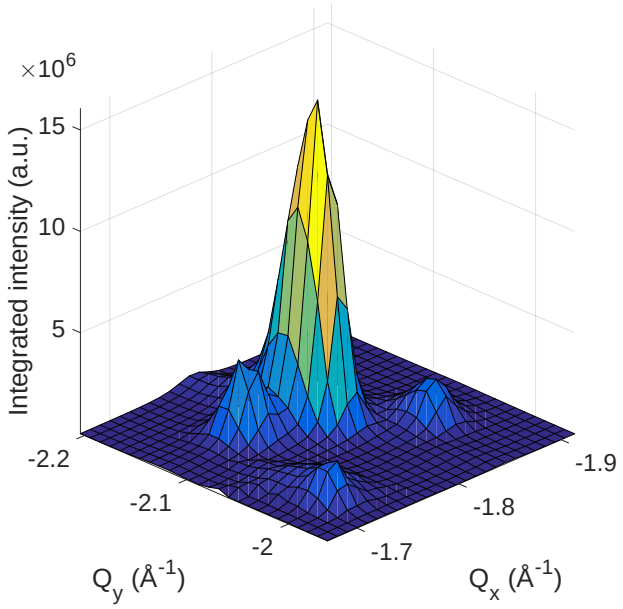

Figure 11: *The alloy splitting in 3 domains is clearly seen in this surface plot, showing a zoom in of the white square in Figure 10. The 3 large peaks are from the alloy and the weak peak closest is the Pt(111) substrate. The substrate peak does show some broadening in the left-right direction, but there is no splitting as seen in the alloy.*

spots seen, since a typical beam coherence length on the order of a μm will illuminate a large number of domains coherently. The broadening of the peaks from the beam coherence has not been taken into account, since the crystal broadening is much larger.

The main alloy diffraction peaks were indexed, and the intensity was integrated by summing the voxels around each diffraction peak. The noise was assumed to be 10 counts (out of a maximum count of 1,000,000) per voxel. Integrated intensity of the peaks was calculated by summing the intensities in the voxels around the area covering the brightest peak and a depth large enough to cover all 3 domains. Uncertainty on the intensity measurement were estimated as the square root of 10 times the number of voxels contributing to the integrated peak. The range of diffraction peaks in-plane was from (H,K) = (1,0) to (2,1), and the out-of-plane range was L = 1 to 24. Due to the low incidence angle the specular diffraction spots are unavailable, and for the ⟨10L⟩ peaks the maximum L was 21 or 22. This leads to a total of 705 diffraction peaks indexed. The measured intensities and the estimated uncertainties from noise are found in Appendix C, where H and K are multiples of the two reciprocal lattice vectors shown in Figure 10 and L is multiple a the reciprocal lattice vector pointing out of the plane in the same figure.

Space group determination was done using the program SHELXT, part of the SHELX crystal structure determination and refinement package [37]. The best fit to the presented data is R3m, spacegroup 160, which has a rhombohedral symmetry. In here, we use the hexagonal axes to represent the rhombohedral lattice to make comparison to the Pt(111) substrate more intuitive. With inspiration from the high temperature Pd_5Ce [38] and Cu_5Ca [20] structures, an initial guess was made. The height of the unit cell (c axis) is consistent with 18 Pt(111) like atomic layers. The rhombohedral symmetry reduces the asymmetric cell to 1/3 c axis height, i.e., 6 Pt(111) like layers. The initial guess for the asymmetric cell is shown in Figure 12. The lines show the unit cell in-plane, and the z-value indicates the relative z-coordinate of the given layer. In this structure three different types of layers are seen. Gd atoms are only located in the 2nd and the 6th layers (H_1 and H_3) and they are ordered with Pt in 2:1 (Pt_2Gd), and 1:2 ($PtGd_2$) ratio. The layers above or below the Gd containing layers, i.e., 1st, 3rd, and the 5th layers, have vacancies in the hexagonal net just above or below the Gd atom, forming a "kagome" like net (K_1, K_2, and K_3). The 4th layer in the asymmetric cell (H_2) is Pt only hexagonal net with no vacancies. The atoms in the kagome layers are on a 9b Wyckoff site; whereas the atoms of both types of the hexagonal layers are on a 3a Wyckoff site. There are 12 unique atoms in the asymmetric unit cell with 15 refinable position parameters, and the full unit cell has 54 atoms. Ordering of the Gd atoms and the corresponding vacancies in the adjacent kagome layers presumably helps to accommodate the larger Gd ion.

To optimize the guessed structure the program SHELXL was used, which was used with a least-squared fitting routine. As an input it takes the unique atomic positions and optimizes them against the measured peaks. Out of the 705 measured peaks, 55 unique peaks were found for this space group. The program has an option for handling simple twinning, but it was not possible to get any stable fits considering different kind of twins, both 60° rotated twins and obverse/reverse rhombohedral twinning was attempted. Assuming the trial structure described above, the structure factors for a 60° rotated twin was calculated and all peaks that contribute to this twin were removed from the raw data. A total of 235 diffraction peaks were removed, leaving 470 peaks of which 47 are unique. Because of the complexity of structure and relatively few unique reflections, first set of refinements were performed by fixing the Debye-Waller factors isotropic and 0.02 $Å^2$, and constraining Pt-Pt distances to be approximately equal. In the subsequent refinements, Pt-Pt distance constrains

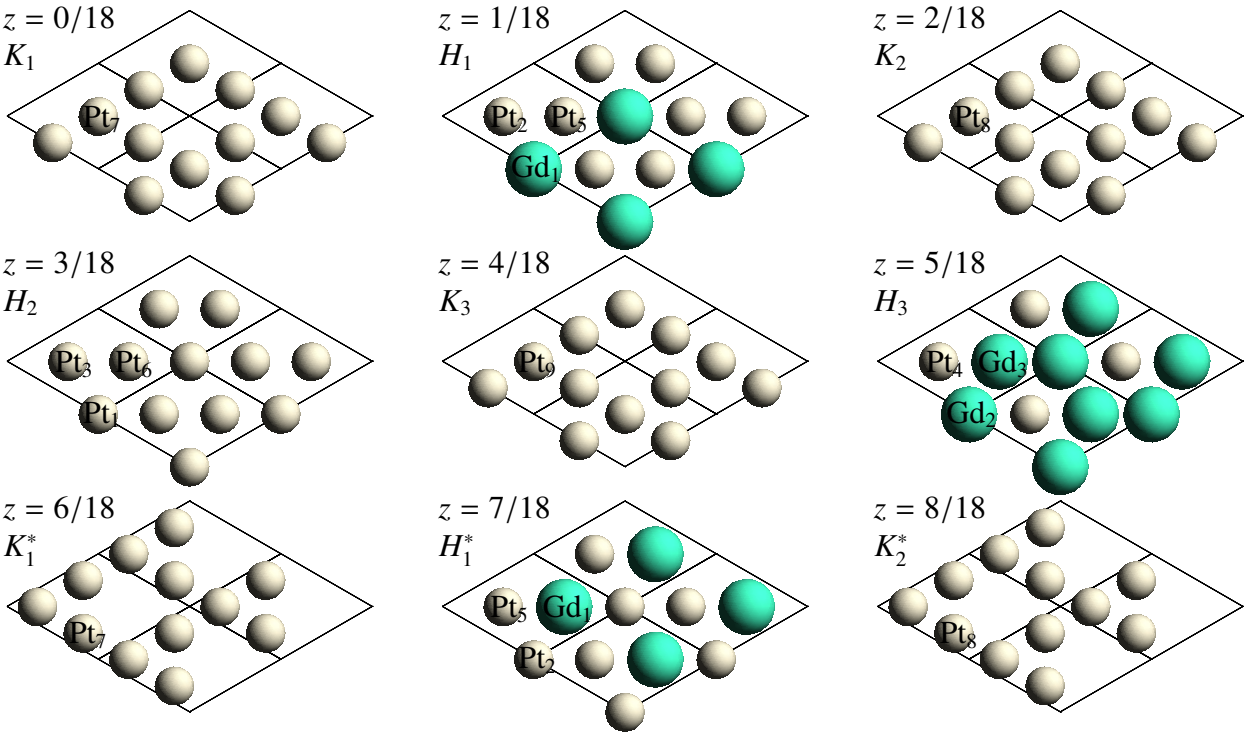

Figure 12: *The first 9 layers out of 18 of the initial structure guess, the grey spheres are Pt and green spheres are Gd. Due to the rhombohdral symmetry the 6 first layers repeat above, but are shifted by one atom, as shown here. The lines show the unit cell in-plane, and the z-coordinate gives the relative z-position of the given layer. Three types of layers are seen, the first layer is a kagome type layer consisting only of Pt, and it has a void that can accomodate the larger Gd in layer above or below. The other layers are hexagonal and are either pure Pt (H_2) or have a varying Pt-Gd stoichiometry. To distiguish the layers the kagome layers are labeled by K and the hexagonal layers are labeled H, and the * denotes symmetrically equivalent plane. The unique atoms in the asymmetrical unit cell have been labeled as well.*

were removed, to achieve a stable refinement with R1 of 0.57 (0 being a perfect fit). To understand the reason for the relatively large R-factor, the calculated and measured structure factors were plotted against the scattering vector Q, see Figure C.18. The fit is mostly good for the weaker reflections, whereas strong reflections are fitted poorly, and we speculate that perhaps the misfits arise from incomplete separation of intensities from various twins still present in the data.

The fitted structure has the same layers as the intial guess, although the layers have become somewhat disordered. The in-plane structure is not changed due to the symmetry of the special sites. A side view of the structure is seen in Figure 13. The structure is seen along the a-axis of the unit cell, and the kagome layers have been shown with black lines. The atomic layers are no longer equidistant, and the structure is more disordered than the initial guess. The hexagonal layers have become significantly buckled, and the Gd atoms have moved closer to the voids in the kagome layers. That also shows as the two neighboring Gd atoms are displaced in opposite directions, just as seen in the Pd_5Ce structure. The Pt atom in the hexagonal layer with the two Gd atoms have moved down very close to the Pt atoms in the kagome layer below, and are unphysically close. A Fourier different map comparing the measured and calculated electron densities does show that this Pt atom should be higher. Otherwise the rest of the interatomic distances are more reasonable, although varying more than expected. Table 3 sums up the structure with the until cell and atomic positions of the 12 unique atoms.

The fitted structure is somewhat disordered, and in order to understand atomic displacement in great detail anisotropic Debye-Waller factors were fitted while fixing the atomic positions. With the amount of data available these Debye-Waller factors are not expected to represent physical atomic motion, but rather comparing them with Fourier difference maps they can indicate particular disorder and potential broken symmetry. The anisotropic Debye-Waller factors are sketched in Figure 14, showing an asymmetrical unit cell. It is seen that Pt_1

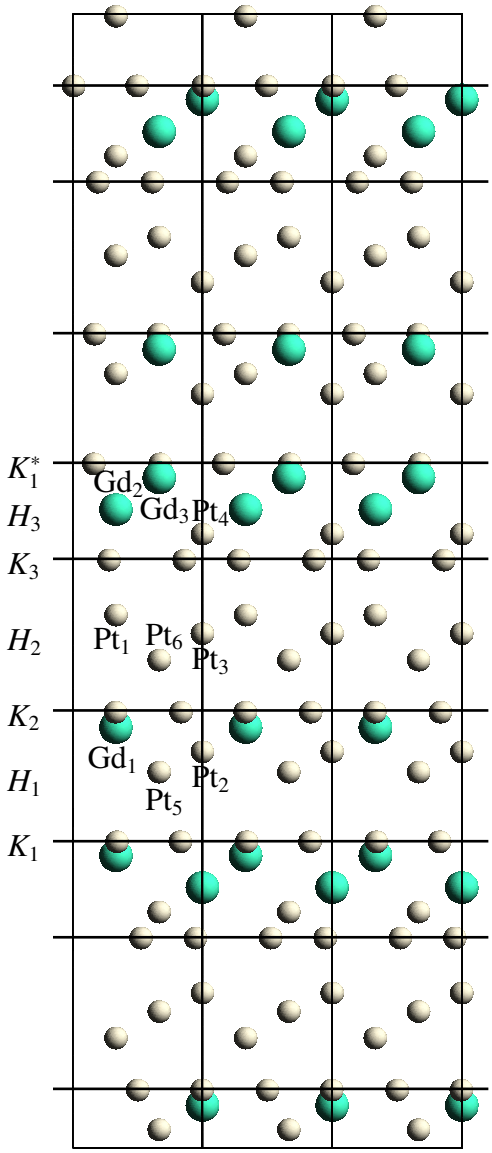

Figure 13: *The final stable structure fit is shown, and the grey spheres are Pt and the green spheres are Gd. The structure is seen along the a-axis, and the black lines are placed on the kagome layers as a guide. Some of the layers have been labeled as in Figure 12, and the atoms in the hexagonal layers have been labeled as well. It is seen that the kagome layers are no longer equally spaced, and the hexagonal layers have become strongly buckled. The neighboring Gd atoms have displaced in opposite directions, increasing the interatomc distance, jsut as seen in the Pd_5Ce structure. The Pt in the same hexagonal layer as the two Gd atoms have moved down, and is unphysically close to the other Pt atoms in the kagome layer below. Otherwise the interatomic distances in the rest of the structure are more reasonable.*

has a strong disorder along the z-axis, and also that the K_1 layer has a large degree of disorder in-plane, which is shown in Figure 15.

Space group	a (α)	b (β)	c (γ)
R3m	5.3309 Å	5.3309 Å	40.358 Å
160	90°	90°	120°
Atom	x	y	z
Gd_1	0	0	0.0380
Gd_2	0	0	0.2302
Gd_3	0	0	0.9250
Pt_1	0	0	0.1372
Pt_2	0	0	0.3500
Pt_3	0	0	0.4542
Pt_4	0	0	0.5520
Pt_5	0	0	0.6654
Pt_6	0	0	0.7642
Pt_7	0.5039	0.0078	0.9373
Pt_8	0.4983	0.9967	0.0516
Pt_9	0.4735	0.9470	0.1857

Table 3: *The unit cell parameters and positions of the 12 atomic positions of the final refined structure model. The atomic coordinates are given in relative units to the unit cell.*

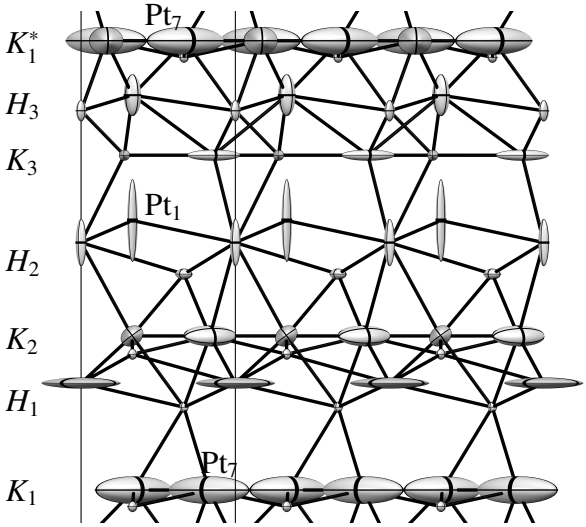

Figure 14: *The anisotropic Debye-Waller factors are sketched in the asymmetrical unit cell. The plot is seen along the a-axis of the structure. Interpreting the Debye-Waller factors as a measure of disorder it is seen that some sites show either disorder in the z-direction or in-plane. As an example Pt_1 shows strong disorder in the z-direction only, whereas Pt_7 shows most disorder in the xy-plane.*

4. Discussion

In this paper we have studied Gd modified Pt(111) single crystals. Gd has been deposited on a sputter-cleaned Pt(111) surface. From the ISS measurements it could be seen that a Pt overlayer forms after annealing the sample to temperatures above 550 °C. By deposition of 200 Å Gd on a sample heated to 800 °C, it was

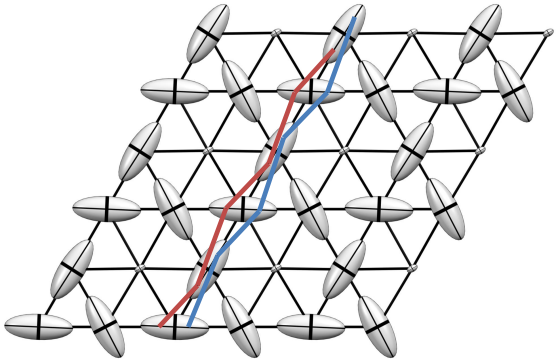

Figure 15: *The anisotropic Debye-Waller factors is sketched for the K_1 kagome type layer. This particular disorder could indicate a broken symmetry in which 1 or 2 of the Pt atoms move closer to the center of the void (in which a Gd atom is seen). Such a symmetry breaking disorder is indicated by the blue and red lines. This might help alleviate the strain within the kagome layer by increasing the Pt-Pt distance, and could also produces a large number of twins.*

possible to prepare a thick alloy with a stoichiometry close to Pt_5Gd.

The crystal structure of the sample was investigated using LEED and surface sensitive X-ray diffraction. It was seen that the alloy was sometimes rotated by 30° compared to the Pt(111) substrate. Based on the crystal structure it is highly likely that the interface between the alloy and the Pt(111) substrate is a kagome layer. We speculate that the energy of rotated or not rotated strained kagome layer on top of a non-strained Pt(111) layer is very similar. From the LEED pattern, it could be seen that the Gd/Pt(111) sample had formed a 1.90×1.90 structure, corresponding to a 2×2 structure with (5±1) % compressive strain. This is in accordance with powder XRD experiments performed on Pt_5Gd that shows a strain of 4.8 % [14]. CO TPDs have been made to evaluate the reactivity of the sample. The shape of the desorption peak becomes more well-defined after the deposition of the thick Gd layer, indicating that a more well-ordered surface has been created. The shape of the desorption peak bares many similarities to CO TPDs made on Y/Pt(111) [27]. The desorption peak is extremely sharp, indicating strong attractive interactions between the CO molecules on the surface. It is beyond the scope of this article to understand the origin of interactions that lead to the shape of this desorption peak.

A large downshift in the desorption temperature was observed. The change in the desorption temperature compared to the desorption temperature for the Pt(111) surface is $\Delta T = 200$ °C, see Figure 6. This decrease in reactivity is expected for Pt surfaces under compressive strain. A compression of the Pt atoms in the surface will result in a downshift in their d-band center which will cause a weakning of the binding energy of the surface [39–41].

The strain seen in the LEED images is in good aggreement with the unit cell of the alloy determined by the XRD patterns, and compared to a 2×2 reconstruction the single crystal alloy is compressed by 3.9 % in-plane. Furthermore the XRD experiments also reveal that the c-axis is compressed around 1 % compared to 18 layers of pure Pt. It is counterintuitive that the alloy has a closer packing than pure Pt, considering that Gd atoms are significantly larger than Pt atoms. We expect the real structure to have a number of vacancies to accomodate the compression. However, the location of the vacancies could not be determined, they may contribute to the large number of twins. The X-ray diffraction measurements have revealed that the alloy does not behave like an ideal single crystal. The alloy forms a rather complicated stacking sequence, as evidenced by the large c-axis. Furthermore the crystallites are very small, giving a large number of twins. All the measured diffraction peaks have been analyzed, except the superspots, which are expected to appear because of the small crystallites. However, many similar structures could give rise to merohedral twins. Other potential structures could also have a different c-axis, being either 2, 3, 6, or 9 atomic layers thick will give rise to diffraction spots that are completely overlapping with the diffraction peaks from the described structure. This could explain why the fitting procedure underestimates certain diffraction peaks. Nonetheless, since most peaks are descibed fairly well, this structure is dominant in the alloy. The measuring technique using the rocking scans does not provide the most accurate intensities. Although both factor into the poor structure fit, the twinning is most likely more severe than the measurement error.

The strong buckling seen in the hexagonal layers and the inplane rotational disorder, shown in Figure 15, of the proposed structure may be a way of alleviating the in-plane strain, due to the compression discussed above. The key for the in-plane compression observed in this alloy seems to be the structural motif consisting of a kagome layer stabilized by neighboring Gd atoms; the hexagonal layers are buckling to reduce the strain.

5. Conclusion

- A thin layer of Gd was deposited on a Pt(111) surface. An alloy terminated by a Pt overlayer was

formed after heating the sample to 550 °C.

- A 63 nm thick single crystal alloy of Pt_5Gd was prepared by depositing a thick layer of Gd on a Pt(111) single crystal heated to 800 °C.

- XPS was used to determine the stoichiometry to be close to Pt_5Gd, and ISS measurements showed that the alloy was terminated by a single atomic layer of Pt.

- Both LEED images and bulk XRD measurements show an in-plane compression of 4-5 % of the alloy compared to Pt(111). This value is in good agreement with experimental values reported from Pt_5Gd powders and polycrystalline samples [12, 14, 20].

- CO TPD experiments showed that a downshift in the desorption temperature of 200 °C compared to that of pure Pt(111), indicating a decreased reactivity of the Gd/Pt(111).

- The bulk alloy structure had a high degree of merohedral twinning and a detailed structure determination was difficult, but a slightly distorted structure was found having a hexagonal unit cell with the parameters $a = 5.3309 \pm 0.0008$ Å and $c = 40.358 \pm 0.012$ Å, and a crystal symmetry of R3m (space group 160).

- The key to the compressed structure is the combination of kagome type layers stabilized by larger Gd atoms.

- The decreased binding to CO, as probed by TPD, is consistent with the compressive strain we measure using LEED and XRD [39]. Assuming perfect scaling between the intermediates of oxygen reduction and adsorbed CO, this surface would interact too weakly with OH for optimal activity [15]. However, we do not anticipate that the structured herein is the active phase for oxygen reduction. Gd will dissolve, relaxing the strain to a lower value [12].

6. Acknowledgement

For funding of this work we gratefully acknowledge The Danish National Research Foundations Center for Individual Nanoparticle Functionality. Use of the Stanford Synchrotron Radiation Lightsource, SLAC National Accelerator Laboratory, is supported by the U.S. Department of Energy, Office of Science, Office of Basic Energy Sciences under Contract No. DE-AC02-76SF00515. The Danish Ministry of Higher Education and Science is acknowledged for an EliteForsk travel grant making an extended stay at SLAC possible.

References

[1] V. R. Stamenkovic, B. S. Mun, K. J. J. Mayrhofer, P. N. Ross, N. M. Markovic, Effect of surface composition on electronic structure, stability, and electrocatalytic properties of Pt-transition metal alloys: Pt-skin versus Pt-skeleton surfaces, Journal of the American Chemical Society 128 (2006) 8813–8819.

[2] V. R. Stamenkovic, B. Fowler, B. S. Mun, G. Wang, P. N. Ross, C. A. Lucas, N. M. Markovic, Improved oxygen reduction activity on $Pt_3Ni(111)$ via increased surface site availability, Science 315 (2007) 493–497.

[3] T. Toda, H. Igarashi, H. Uchida, M. Watanabe, Enhancement of the electroreduction of oxygen on Pt alloys with Fe, Ni, and Co, Journal of the Electrochemical Society 146 (1999) 3750–3756.

[4] C. Chen, Y. Kang, Z. Huo, Z. Zhu, W. Huang, H. L. Xin, J. D. Snyder, D. Li, J. A. Herron, M. Mavrikakis, M. Chi, K. L. More, Y. Li, N. M. Markovic, G. A. Somorjai, P. Yang, V. R. Stamenkovic, Highly Crystalline Multimetallic Nanoframes with Three-Dimensional Electrocatalytic Surfaces, Science 343 (2014) 1339–1343.

[5] I. Spanos, J. J. K. Kirkensgaard, K. Mortensen, M. Arenz, Investigating the activity enhancement on PtxCo1-x alloys induced by a combined strain and ligand effect, Journal of Power Sources 245 (2014) 908–914.

[6] N. Todoroki, Y. Asakimori, T. Wadayama, Effective shell layer thickness of platinum for oxygen reduction reaction alloy catalysts, Physical Chemistry Chemical Physics 15 (2013) 17771–17774.

[7] R. Srivastava, P. Mani, P. Strasser, In situ voltammetric dealloying of fuel cell catalyst electrode layer: A combined scanning electron microscope/electron probe micro-analysis study, Journal of Power Sources 190 (2009) 40–47. 11th Ulm Electro-Chemical Talks, Neu Ulm, GERMANY, JUN 11-12, 2008.

[8] S. Chen, H. A. Gasteiger, K. Hayakawa, T. Tada, Y. Shao-Horn, Platinum-Alloy Cathode Catalyst Degradation in Proton Exchange Membrane Fuel Cells: Nanometer-Scale Compositional and Morphological Changes, Journal of the Electrochemical Society 157 (2010) A82–A97.

[9] H. L. Xin, J. A. Mundy, Z. Liu, R. Cabezas, R. Hovden, L. F. Kourkoutis, J. Zhang, N. P. Subramanian, R. Makharia, F. T. Wagner, D. A. Muller, Atomic-Resolution Spectroscopic Imaging of Ensembles of Nanocatalyst Particles Across the Life of a Fuel Cell, Nano Letters 12 (2012) 490–497.

[10] P. Malacrida, M. Escudero-Escribano, A. Verdaguer-Casadevall, I. E. L. Stephens, I. Chorkendorff, Enhanced activity and stability of Pt-La and Pt-Ce alloys for oxygen electroreduction: the elucidation of the active surface phase, J. Mater. Chem. A 2 (2014) 4234–4243.

[11] U. Vej-Hansen, J. Rosmeisl, I. Stephens, J. Schiøtz, Correlation between diffusion barriers and alloying energy in binary alloys, Physical Chemistry Chemical Physics (2015).

[12] M. Escudero-Escribano, A. Verdaguer-Casadevall, P. Malacrida, U. Grønbjerg, B. P. Knudsen, A. K. Jepsen, J. Rossmeisl, I. E. L. Stephens, I. Chorkendorff, Pt_5Gd as a Highly Active and Stable Catalyst for Oxygen Electroreduction, Journal of the American Chemical Society 134 (2012) 16476–16479.

[13] A. Velzquez-Palenzuela, F. Masini, A. F. Pedersen, M. Escudero-Escribano, D. Deiana, P. Malacrida, T. W. Hansen, D. Friebel, A. Nilsson, I. E. L. Stephens, I. Chorkendorff, The enhanced activity of mass-selected PtxGd nanoparticles for oxygen electroreduction, Journal of Catalysis 328 (2015) 297–307.

[14] M. Escudero-Escribano, P. Malacrida, M. H. Hansen, U. G. Vej-Hansen, A. Velazquez-Palenzuela, V. Tripkovic, J. Schiøtz, J. Rossmeisl, I. E. L. Stephens, I. Chorkendorff, To be submitted, - (2015).

[15] J. K. Nørskov, J. Rossmeisl, A. Logadottir, L. Lindqvist, J. R. Kitchin, T. Bligaard, H. Jonsson, Origin of the overpotential for oxygen reduction at a fuel-cell cathode, Journal fo Physical Chemistry B 108 (2004) 17886–17892.

[16] J. Rossmeisl, G. S. Karlberg, T. Jaramillo, J. K. Nørskov, Steady state oxygen reduction and cyclic voltammetry, Faraday Discussions 140 (2008) 337–346.

[17] H. R. Siddiqui, X. Gou, I. Chorkendorff, J. T. Yates, CO adsorption site exchange between step and terrace sites on Pt(112)., Surface Science 191 (1987) L813–L818.

[18] P. L. Hagans, I. Chorkendorff, J. T. Yates, Scanning kinetic spectroscopy and temperature-programmed desorption studies of the adsorption and decomposition of hydrogen cyanide on the nickel(111) surface, Journal of Physical Chemistry (1896-1996) 92 (1988) 471–476.

[19] N. Baenziger, J. L. Moriarty, Gadolinium and Dysprosium Intermetallic Phases .1. Crystal Structures of DyGa and GdPt and their realted compounds, Acta Crystallographica 14 (1961) 946–947.

[20] W. Bronger, Preparation and X-Ray investigation af platinum alloys with rare-earth metals (Pt5Ln and Pt3Ln phases), Journal of the less-common metals 12 (1967) 63–68.

[21] J. Yates, Experimental Innovations in Surface Science: A Guide to Practical Laboratory Methods and Instruments, Aip-Press Series, AIP Press, 1998.

[22] http://www-ssrl.slac.stanford.edu/toneygroup/node/10, ????

[23] A. Kildemo, A. Juel, S. Raaen, Properties of Tm-Pt(111) surface alloys, Surface Science 581 (2005) 133–141.

[24] J. Tang, J. M. Lawrence, J. C. Hemminger, Structure and valence of the Ce/Pt(111) system, Physical Review B 48 (1993) 15342–15352.

[25] A. Ramstad, S. Raaen, N. Barrett, Electronic structure of the La-Pt(111) surface alloy, Surface Science 448 (2000) 179–186.

[26] A. Ramstad, S. Raaen, Formation of and CO adsorption on an inert La-Pt(111) surface alloy, Physical Review B 59 (1999) 15935–15941.

[27] T. P. Johansson, E. T. Ulrikkeholm, P. Hernandez-Fernandez, M. Escudero-Escribano, P. Malacrida, I. E. L. Stephens, I. Chorkendorff, Towards the elucidation of the high oxygen electroreduction activity of PtxY: surface science and electrochemical studies of Y/Pt(111)., Physical Chemistry Chemical Physics 16 (2014) 13718–13725.

[28] D. Briggs, P. Seah, Practical Surface Analysis, Auger and X-ray Photoelectron Spectroscopy, Practical Surface Analysis, Wiley, 1990.

[29] G. Ertl, M. Neumann, K. M. Streit, Chemisorption of CO on Pt(111) Surface, Surface Science 64 (1977) 393–410.

[30] E. K. Vestergaard, P. Thostrup, T. An, E. Laegsgaard, I. Stensgaard, B. Hammer, F. Besenbacher, Comment on "High pressure adsorbate structures studied by scanning tunneling microscopy: CO on Pt(111) in equilibrium with the gas phase", Physical Review Letters 88 (2002) –.

[31] J. C. Davies, R. M. Nielsen, L. B. Thomsen, I. Chorkendorff, A. Logadottir, Z. Lodziana, J. K. Norskov, W. X. Li, B. Hammer, S. R. Longwitz, J. Schnadt, E. K. Vestergaard, R. T. Vang, F. Besenbacher, CO Desorption Rate Dependence on CO Partial Pressure over Platinum Fuel Cell Catalysts, FUEL CELLS 4 (2004) 309–319.

[32] S. R. Longwitz, J. Schnadt, E. K. Vestergaard, R. T. Vang, I. Stensgaard, H. Brune, F. Besenbacher, High-Coverage Structures of Carbon Monoxide Adsorbed on Pt(111) Studied by High-Pressure Scanning Tunneling Microscopy, The Journal of Physical Chemistry B 108 (2004) 14497–14502.

[33] G. Ertl, M. Neumann, K. Streit, Chemisorption of {CO} on the Pt(111) surface, Surface Science 64 (1977) 393–410.

[34] E. T. Ulrikkeholm, Single crystal studies of platinum alloys for oxygen reduction electrodes., Ph.D. thesis, Center for Individual Nanoparticle Functionality, Department of Physics, Technical University of Denmark, 2014.

[35] B. Predel, Gd-Pt (Gadolinium-Platinum), Landolt-Börnstein - Group IV Physical Chemistry, volume 5f, Springer-Verlag, 1996.

[36] J. I. Langford, A. Wilson, Scherrer after sixty years: A survey and some new results in the determination of crystallite size, Journal of applied crystallography 11 (1978) 102–113.

[37] G. M. Sheldrick, A short history of *SHELX*, Acta Crystallographica Section A Foundations of Crystallography 64 (2008) 112–122.

[38] M. Itakura, Y. Hisatsune, H. Sato, N. Kuwano, K. Oki, Crystal Structures of H-Pd5ce and Pd5la and Their Electrical Resistivities at Low Temperatures, Japanese Journal of Applied Physics 27 (1988) 684.

[39] B. Hammer, J. K. Nørskov, Electronic factors determining the reactivity of metal surfaces, Surface Science 343 (1995) 211–220.

[40] B. Hammer, J. K. Nørskov, Theoretical surface science and catalysis - Calculations and concepts, in: Gates, B. C. and Knozinger, H. (Ed.), Advances in Catalysis, VOL 45: Impact of Surface Science on Catalysis, volume 45 of *Advances in Catalysis*, 2000, pp. 71–129.

[41] M. Mavrikakis, B. Hammer, J. K. Nørskov, Effect of Strain on the Reactivity of Metal Surfaces, Physical Review Letters 81 (1998) 2819–2822.

Appendix A. XPS pattern after Gd deposition

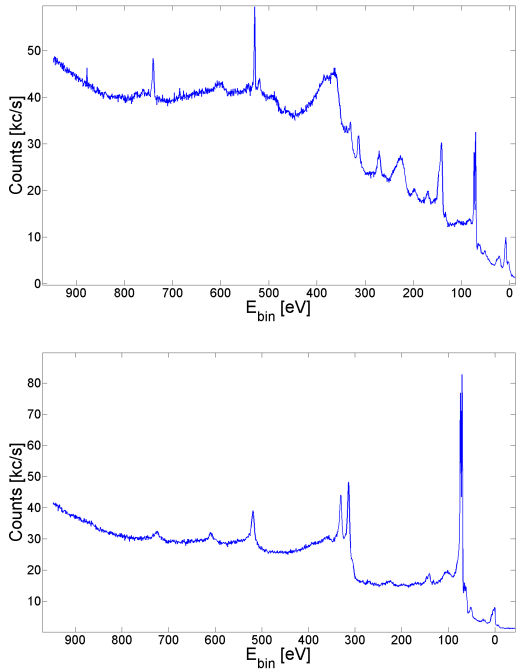

Figure A.16: *TOP: XPS spectrum made after deposition of Gd. The Gd is strongly oxidized. Bottom: XPS made on the sample after Gd deposition, a light sputtering, and annealing to 800 °C.*

Appendix B. LEED patterns

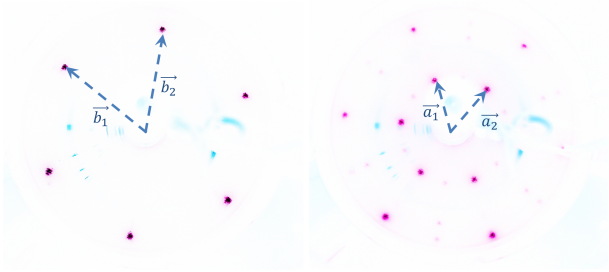

Figure B.17: *Left: A LEED pattern made on a sputter cleaned, annealed Pt(111). Right: LEED pattern made on the prepared Gd/Pt(111) sample. The sample forms a (1.90 × 1.90) structure rotated 30° with respect to the Pt substrate.*

Appendix C. List of diffraction peaks

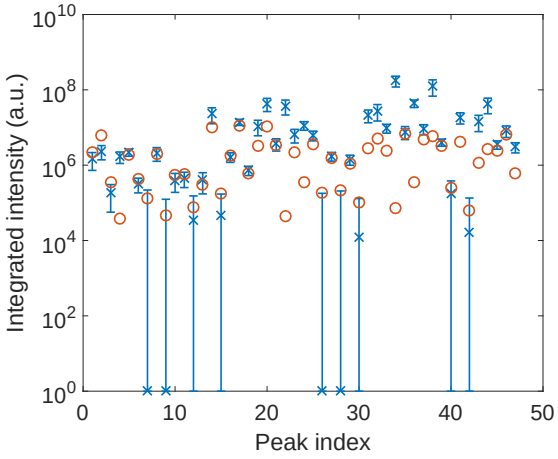

(a) *Peak intensity vs. peak index.*

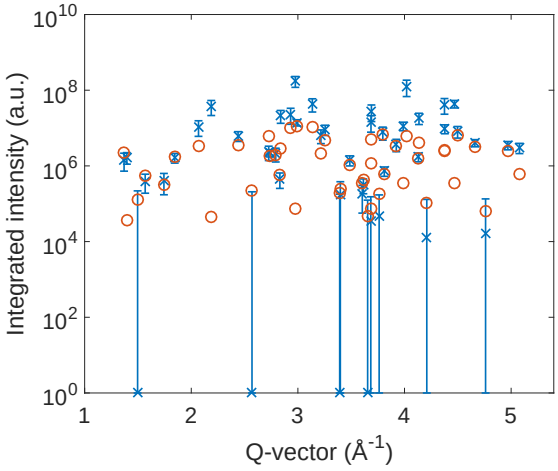

(b) *Peak intensity vs. Q-vector.*

Figure C.18: *The measured intensity of the 47 unique diffraction peaks is shown as blue crosses, and the standard deviation of the intensity has been calculated by SHELXL from the equivalent peaks. The calculated intensities are shown as orange circles. In general it is seen that many of the brightest peaks are not fitted very well. In (a) the peaks are plotted against their index. In (b) the unique peaks have been plotted as a function of their scattering vector length, Q. There is no Q-dependence of the mismatch between the measured and calculated diffraction peaks.*

H	K	L	F^2	$\sigma(F^2)$
-1	0	1	1.75	0.46
-1	0	2	0.41	0.46
-1	0	3	0	0.46
-1	0	4	0.02	0.46
-1	0	5	0.13	0.46
-1	0	6	0	0.46
-1	0	7	4.54	0.46
-1	0	8	0.86	0.46
-1	0	9	0.03	0.46
-1	0	10	69.64	0.46
-1	0	11	12.28	0.46
-1	0	12	0.01	0.46
-1	0	13	42.68	0.46
-1	0	14	0	0.46
-1	0	15	0.01	0.46
-1	0	16	208.89	0.46
-1	0	17	97.11	0.46
-1	0	18	0.06	0.46
-1	0	19	53.17	0.46
-1	0	20	0.02	0.46
-1	0	21	0	0.46
-1	0	22	30.57	0.46
1	0	1	3.24	0.52
1	0	2	1.89	0.52
1	0	3	0.01	0.52
1	0	4	0	0.52
1	0	5	0.57	0.52
1	0	6	0	0.52
1	0	7	1.23	0.52
1	0	8	3.24	0.52
1	0	9	0	0.52
1	0	10	19.31	0.52
1	0	11	68.22	0.52
1	0	12	1.29	0.52
1	0	13	11.17	0.52
1	0	14	0	0.52
1	0	15	0.41	0.52
1	0	16	36.55	0.52
1	0	17	202.54	0.52
1	0	18	0.51	0.52
1	0	19	16.49	0.52
1	0	20	0	0.52
1	0	21	0.24	0.52

H	K	L	F^2	$\sigma(F^2)$
0	-1	1	0.95	0.47
0	-1	2	3.65	0.47
0	-1	3	0	0.47
0	-1	4	0	0.47
0	-1	5	1.09	0.47
0	-1	6	0.06	0.47
0	-1	7	0.38	0.47
0	-1	8	8.09	0.47
0	-1	9	0.14	0.47
0	-1	10	4.8	0.47
0	-1	11	90.95	0.47
0	-1	12	0.11	0.47
0	-1	13	4.76	0.47
0	-1	14	0.01	0.47
0	-1	15	0	0.47
0	-1	16	8.39	0.47
0	-1	17	181.02	0.47
0	-1	18	0.17	0.47
0	-1	19	7.84	0.47
0	-1	20	0.18	0.47
0	-1	21	0.49	0.47
0	-1	22	20.51	0.47
1	-1	1	1.61	0.49
1	-1	2	3.36	0.49
1	-1	3	0	0.49
1	-1	4	0	0.49
1	-1	5	0.98	0.49
1	-1	6	0	0.49
1	-1	7	0.45	0.49
1	-1	8	3.02	0.49
1	-1	9	0	0.49
1	-1	10	14.57	0.49
1	-1	11	80.27	0.49
1	-1	12	0.19	0.49
1	-1	13	17.44	0.49
1	-1	14	0	0.49
1	-1	15	0.98	0.49
1	-1	16	35.58	0.49
1	-1	17	272.04	0.49
1	-1	18	0.33	0.49
1	-1	19	15.17	0.49
1	-1	20	0.6	0.49
1	-1	21	0.09	0.49

H	K	L	F^2	$\sigma(F^2)$
-1	1	1	0.25	0.48
-1	1	2	4.85	0.48
-1	1	3	0	0.48
-1	1	4	0	0.48
-1	1	5	0.86	0.48
-1	1	6	0	0.48
-1	1	7	0.17	0.48
-1	1	8	6.35	0.48
-1	1	9	0	0.48
-1	1	10	2.82	0.48
-1	1	11	87.58	0.48
-1	1	12	0	0.48
-1	1	13	4.47	0.48
-1	1	14	0	0.48
-1	1	15	0	0.48
-1	1	16	11.13	0.48
-1	1	17	350.36	0.48
-1	1	18	0.03	0.48
-1	1	19	5.39	0.48
-1	1	20	1.23	0.48
-1	1	21	0	0.48
-1	1	22	3.36	0.48
0	1	1	0.89	0.44
0	1	2	2.21	0.44
0	1	3	0.01	0.44
0	1	4	0	0.44
0	1	5	0.49	0.44
0	1	6	0.03	0.44
0	1	7	0.14	0.44
0	1	8	1.67	0.44
0	1	9	0.03	0.44
0	1	10	12.17	0.44
0	1	11	40.05	0.44
0	1	12	0	0.44
0	1	13	28.11	0.44
0	1	14	0	0.44
0	1	15	1.39	0.44
0	1	16	208.42	0.44
0	1	17	65.65	0.44
0	1	18	0.26	0.44
0	1	19	63.39	0.44
0	1	20	0	0.44
0	1	21	0	0.44

Table C.4: *List of the measured diffraction peaks.*

H	K	L	F^2	$\sigma(F^2)$
1	1	1	0	0.51
1	1	2	0	0.51
1	1	3	3.25	0.51
1	1	4	0	0.51
1	1	5	0	0.51
1	1	6	8.21	0.51
1	1	7	0.01	0.51
1	1	8	0	0.51
1	1	9	676.43	0.51
1	1	10	0	0.51
1	1	11	0	0.51
1	1	12	17.38	0.51
1	1	13	0.05	0.51
1	1	14	0.02	0.51
1	1	15	1.32	0.51
1	1	16	0	0.51
1	1	17	0.04	0.51
1	1	18	605.77	0.51
1	1	19	0.01	0.51
1	1	20	0	0.51
1	1	21	209.84	0.51
1	1	22	0.01	0.51
1	1	23	0.01	0.51
1	1	24	2.64	0.51
2	-1	1	0	0.59
2	-1	2	0	0.59
2	-1	3	4.03	0.59
2	-1	4	0	0.59
2	-1	5	0	0.59
2	-1	6	10.42	0.59
2	-1	7	0	0.59
2	-1	8	0	0.59
2	-1	9	999.99	0.59
2	-1	10	0	0.59
2	-1	11	0.01	0.59
2	-1	12	22.22	0.59
2	-1	13	0	0.59
2	-1	14	0.09	0.59
2	-1	15	1.54	0.59
2	-1	16	0	0.59
2	-1	17	0.01	0.59
2	-1	18	826.53	0.59
2	-1	19	0.03	0.59
2	-1	20	0.01	0.59
2	-1	21	225.1	0.59
2	-1	22	0	0.59
2	-1	23	0	0.59
2	-1	24	2.34	0.59

H	K	L	F^2	$\sigma(F^2)$
1	-2	1	0	0.49
1	-2	2	0	0.49
1	-2	3	3.72	0.49
1	-2	4	0	0.49
1	-2	5	0	0.49
1	-2	6	9.91	0.49
1	-2	7	0	0.49
1	-2	8	0	0.49
1	-2	9	404.78	0.49
1	-2	10	0	0.49
1	-2	11	0	0.49
1	-2	12	20.67	0.49
1	-2	13	0	0.49
1	-2	14	0.06	0.49
1	-2	15	1.55	0.49
1	-2	16	0	0.49
1	-2	17	0.02	0.49
1	-2	18	584.36	0.49
1	-2	19	0.02	0.49
1	-2	20	0	0.49
1	-2	21	222.91	0.49
1	-2	22	0	0.49
1	-2	23	0.02	0.49
1	-2	24	2.65	0.49
-1	-1	1	0	0.58
-1	-1	2	0	0.58
-1	-1	3	2.34	0.58
-1	-1	4	0	0.58
-1	-1	5	0	0.58
-1	-1	6	6.43	0.58
-1	-1	7	0	0.58
-1	-1	8	0.01	0.58
-1	-1	9	351.95	0.58
-1	-1	10	0	0.58
-1	-1	11	0	0.58
-1	-1	12	12.98	0.58
-1	-1	13	0.01	0.58
-1	-1	14	0.01	0.58
-1	-1	15	0.83	0.58
-1	-1	16	0	0.58
-1	-1	17	0.06	0.58
-1	-1	18	496.58	0.58
-1	-1	19	0.08	0.58
-1	-1	20	0	0.58
-1	-1	21	144.24	0.58
-1	-1	22	0.01	0.58
-1	-1	23	0.02	0.58
-1	-1	24	2.05	0.58

H	K	L	F^2	$\sigma(F^2)$
-2	1	1	0	0.59
-2	1	2	0	0.59
-2	1	3	1.75	0.59
-2	1	4	0	0.59
-2	1	5	0	0.59
-2	1	6	4.97	0.59
-2	1	7	0	0.59
-2	1	8	0	0.59
-2	1	9	320.44	0.59
-2	1	10	0	0.59
-2	1	11	0	0.59
-2	1	12	10.97	0.59
-2	1	13	0.04	0.59
-2	1	14	0.07	0.59
-2	1	15	0.82	0.59
-2	1	16	0.01	0.59
-2	1	17	0.02	0.59
-2	1	18	411.17	0.59
-2	1	19	0.04	0.59
-2	1	20	0	0.59
-2	1	21	126.96	0.59
-2	1	22	0.01	0.59
-2	1	23	0	0.59
-2	1	24	1.45	0.59
-1	2	1	0	0.5
-1	2	2	0	0.5
-1	2	3	2.52	0.5
-1	2	4	0	0.5
-1	2	5	0	0.5
-1	2	6	6.97	0.5
-1	2	7	0.04	0.5
-1	2	8	0.02	0.5
-1	2	9	377.32	0.5
-1	2	10	0	0.5
-1	2	11	0.01	0.5
-1	2	12	14.81	0.5
-1	2	13	0	0.5
-1	2	14	0.01	0.5
-1	2	15	1.14	0.5
-1	2	16	0	0.5
-1	2	17	0.01	0.5
-1	2	18	499.95	0.5
-1	2	19	0	0.5
-1	2	20	0	0.5
-1	2	21	161.46	0.5
-1	2	22	0.03	0.5
-1	2	23	0.05	0.5
-1	2	24	1.59	0.5

Table C.5: *List of the measured diffraction peaks.*

H	K	L	F^2	$\sigma(F^2)$
2	0	1	2.57	0.45
2	0	2	3.98	0.45
2	0	3	0.04	0.45
2	0	4	3.39	0.45
2	0	5	1.16	0.45
2	0	6	0.79	0.45
2	0	7	20.86	0.45
2	0	8	24.42	0.45
2	0	9	1.27	0.45
2	0	10	71.38	0.45
2	0	11	11.67	0.45
2	0	12	0.24	0.45
2	0	13	0	0.45
2	0	14	2.72	0.45
2	0	15	0.85	0.45
2	0	16	44.12	0.45
2	0	17	14.27	0.45
2	0	18	0.73	0.45
2	0	19	174.4	0.45
2	0	20	34.43	0.45
2	0	21	0.07	0.45
2	0	22	58.1	0.45
2	0	23	13.83	0.45
2	0	24	1.19	0.45
2	-2	1	4.7	0.47
2	-2	2	6.08	0.47
2	-2	3	0.76	0.47
2	-2	4	4.17	0.47
2	-2	5	0.92	0.47
2	-2	6	0	0.47
2	-2	7	41.22	0.47
2	-2	8	53	0.47
2	-2	9	0.17	0.47
2	-2	10	82.48	0.47
2	-2	11	1.7	0.47
2	-2	12	0	0.47
2	-2	13	0	0.47
2	-2	14	3.34	0.47
2	-2	15	0.19	0.47
2	-2	16	51.99	0.47
2	-2	17	6.91	0.47
2	-2	18	0	0.47
2	-2	19	231.85	0.47
2	-2	20	2.32	0.47
2	-2	21	1.27	0.47
2	-2	22	75.31	0.47
2	-2	23	0	0.47
2	-2	24	0	0.47

H	K	L	F^2	$\sigma(F^2)$
0	-2	1	1.27	0.42
0	-2	2	2.29	0.42
0	-2	3	0.06	0.42
0	-2	4	5.02	0.42
0	-2	5	0.36	0.42
0	-2	6	0	0.42
0	-2	7	13.12	0.42
0	-2	8	13.91	0.42
0	-2	9	0.07	0.42
0	-2	10	36.57	0.42
0	-2	11	1.83	0.42
0	-2	12	0.74	0.42
0	-2	13	0	0.42
0	-2	14	0.96	0.42
0	-2	15	0	0.42
0	-2	16	58.81	0.42
0	-2	17	2.07	0.42
0	-2	18	0.01	0.42
0	-2	19	128.39	0.42
0	-2	20	7.51	0.42
0	-2	21	0.03	0.42
0	-2	22	81.21	0.42
0	-2	23	0.65	0.42
0	-2	24	0	0.42
-2	0	1	0.51	0.38
-2	0	2	6.28	0.38
-2	0	3	0	0.38
-2	0	4	0.45	0.38
-2	0	5	3.19	0.38
-2	0	6	0	0.38
-2	0	7	8.86	0.38
-2	0	8	17.36	0.38
-2	0	9	0.03	0.38
-2	0	10	14.06	0.38
-2	0	11	48.75	0.38
-2	0	12	0	0.38
-2	0	13	0	0.38
-2	0	14	10.04	0.38
-2	0	15	0	0.38
-2	0	16	6.32	0.38
-2	0	17	75.92	0.38
-2	0	18	0	0.38
-2	0	19	41.83	0.38
-2	0	20	182.91	0.38
-2	0	21	0	0.38
-2	0	22	17.86	0.38
-2	0	23	0	0.38
-2	0	24	0.01	0.38

H	K	L	F^2	$\sigma(F^2)$
-2	2	1	2.05	0.35
-2	2	2	1.95	0.35
-2	2	3	0	0.35
-2	2	4	3.29	0.35
-2	2	5	0.29	0.35
-2	2	6	0	0.35
-2	2	7	32.67	0.35
-2	2	8	14.3	0.35
-2	2	9	0	0.35
-2	2	10	67.97	0.35
-2	2	11	4.22	0.35
-2	2	12	0	0.35
-2	2	13	0	0.35
-2	2	14	1.29	0.35
-2	2	15	0	0.35
-2	2	16	72.49	0.35
-2	2	17	6.49	0.35
-2	2	18	0	0.35
-2	2	19	278.41	0.35
-2	2	20	18.2	0.35
-2	2	21	0	0.35
-2	2	22	85.39	0.35
-2	2	23	8.66	0.35
-2	2	24	0	0.35
0	2	1	1.96	0.37
0	2	2	2.68	0.37
0	2	3	0.16	0.37
0	2	4	1.83	0.37
0	2	5	1.04	0.37
0	2	6	0	0.37
0	2	7	5.2	0.37
0	2	8	24.6	0.37
0	2	9	0.02	0.37
0	2	10	35.43	0.37
0	2	11	18.16	0.37
0	2	12	0	0.37
0	2	13	0	0.37
0	2	14	6.53	0.37
0	2	15	0	0.37
0	2	16	11.99	0.37
0	2	17	62.81	0.37
0	2	18	0	0.37
0	2	19	37.17	0.37
0	2	20	135.36	0.37
0	2	21	0	0.37
0	2	22	9.72	0.37
0	2	23	0	0.37
0	2	24	0	0.37

Table C.6: *List of the measured diffraction peaks.*

H	K	L	F^2	$\sigma(F^2)$
2	1	1	0.11	0.41
2	1	2	0.94	0.41
2	1	3	0	0.41
2	1	4	0	0.41
2	1	5	0.11	0.41
2	1	6	0	0.41
2	1	7	0.03	0.41
2	1	8	1.4	0.41
2	1	9	0.04	0.41
2	1	10	2.78	0.41
2	1	11	11.02	0.41
2	1	12	0.13	0.41
2	1	13	2.05	0.41
2	1	14	0	0.41
2	1	15	0.19	0.41
2	1	16	11.59	0.41
2	1	17	23.52	0.41
2	1	18	0.03	0.41
2	1	19	7.7	0.41
2	1	20	0	0.41
2	1	21	0.07	0.41
2	1	22	6.95	0.41
2	1	23	0.62	0.41
2	1	24	0	0.41
3	-2	1	0.07	0.48
3	-2	2	1.35	0.48
3	-2	3	0	0.48
3	-2	4	0	0.48
3	-2	5	0.14	0.48
3	-2	6	0	0.48
3	-2	7	0.05	0.48
3	-2	8	2.45	0.48
3	-2	9	0.06	0.48
3	-2	10	1.14	0.48
3	-2	11	22.82	0.48
3	-2	12	0.11	0.48
3	-2	13	2.56	0.48
3	-2	14	0.09	0.48
3	-2	15	0.27	0.48
3	-2	16	2.76	0.48
3	-2	17	72.54	0.48
3	-2	18	0	0.48
3	-2	19	6.22	0.48
3	-2	20	0.03	0.48
3	-2	21	0	0.48
3	-2	22	3.07	0.48
3	-2	23	5.06	0.48
3	-2	24	0	0.48

H	K	L	F^2	$\sigma(F^2)$
1	-3	1	0.07	0.33
1	-3	2	1.3	0.33
1	-3	3	0	0.33
1	-3	4	0	0.33
1	-3	5	0.17	0.33
1	-3	6	0	0.33
1	-3	7	0	0.33
1	-3	8	2.79	0.33
1	-3	9	0	0.33
1	-3	10	0.26	0.33
1	-3	11	22.06	0.33
1	-3	12	0.18	0.33
1	-3	13	0.9	0.33
1	-3	14	0	0.33
1	-3	15	0.09	0.33
1	-3	16	4.69	0.33
1	-3	17	58.84	0.33
1	-3	18	0	0.33
1	-3	19	4.11	0.33
1	-3	20	0	0.33
1	-3	21	0.01	0.33
1	-3	22	4.55	0.33
1	-3	23	1.4	0.33
1	-3	24	0	0.33
-2	-1	1	0.3	0.32
-2	-1	2	0.13	0.32
-2	-1	3	0	0.32
-2	-1	4	0	0.32
-2	-1	5	0.03	0.32
-2	-1	6	0	0.32
-2	-1	7	0.27	0.32
-2	-1	8	0.49	0.32
-2	-1	9	0	0.32
-2	-1	10	12.08	0.32
-2	-1	11	3.16	0.32
-2	-1	12	0	0.32
-2	-1	13	4.76	0.32
-2	-1	14	0.02	0.32
-2	-1	15	0	0.32
-2	-1	16	36.87	0.32
-2	-1	17	11.83	0.32
-2	-1	18	0	0.32
-2	-1	19	12.57	0.32
-2	-1	20	0	0.32
-2	-1	21	0	0.32
-2	-1	22	9.97	0.32
-2	-1	23	0.56	0.32
-2	-1	24	0	0.32

H	K	L	F^2	$\sigma(F^2)$
-3	2	1	0	0.4
-3	2	2	1.06	0.4
-3	2	3	0	0.4
-3	2	4	0	0.4
-3	2	5	0.13	0.4
-3	2	6	0	0.4
-3	2	7	0	0.4
-3	2	8	2.09	0.4
-3	2	9	0	0.4
-3	2	10	0.17	0.4
-3	2	11	22.54	0.4
-3	2	12	0.24	0.4
-3	2	13	0.33	0.4
-3	2	14	0.08	0.4
-3	2	15	0	0.4
-3	2	16	0.61	0.4
-3	2	17	84.42	0.4
-3	2	18	0	0.4
-3	2	19	1.16	0.4
-3	2	20	0.23	0.4
-3	2	21	0.1	0.4
-3	2	22	0.59	0.4
-3	2	23	9.02	0.4
-3	2	24	0	0.4
-1	3	1	1.41	0.37
-1	3	2	0.03	0.37
-1	3	3	0	0.37
-1	3	4	0.01	0.37
-1	3	5	0.01	0.37
-1	3	6	0	0.37
-1	3	7	0.38	0.37
-1	3	8	0.15	0.37
-1	3	9	0	0.37
-1	3	10	14.49	0.37
-1	3	11	0.4	0.37
-1	3	12	0	0.37
-1	3	13	6.87	0.37
-1	3	14	0	0.37
-1	3	15	0	0.37
-1	3	16	53.02	0.37
-1	3	17	1.13	0.37
-1	3	18	0	0.37
-1	3	19	19.1	0.37
-1	3	20	0	0.37
-1	3	21	0.01	0.37
-1	3	22	18.44	0.37
-1	3	23	0.02	0.37
-1	3	24	0	0.37

Table C.7: *List of the measured diffraction peaks.*

H	K	L	F^2	$\sigma(F^2)$
1	2	1	0.14	0.39
1	2	2	0.67	0.39
1	2	3	0	0.39
1	2	4	0.01	0.39
1	2	5	0.07	0.39
1	2	6	0	0.39
1	2	7	0.01	0.39
1	2	8	0.93	0.39
1	2	9	0.06	0.39
1	2	10	0	0.39
1	2	11	11.1	0.39
1	2	12	0.05	0.39
1	2	13	2.24	0.39
1	2	14	0	0.39
1	2	15	0.15	0.39
1	2	16	0.89	0.39
1	2	17	42.38	0.39
1	2	18	0.09	0.39
1	2	19	7.16	0.39
1	2	20	0	0.39
1	2	21	0	0.39
1	2	22	5.59	0.39
1	2	23	2.47	0.39
1	2	24	0	0.39
3	-1	1	1.18	0.47
3	-1	2	0.19	0.47
3	-1	3	0	0.47
3	-1	4	0	0.47
3	-1	5	0.04	0.47
3	-1	6	0	0.47
3	-1	7	0.28	0.47
3	-1	8	0.75	0.47
3	-1	9	0.01	0.47
3	-1	10	9.4	0.47
3	-1	11	4.79	0.47
3	-1	12	0.07	0.47
3	-1	13	4.46	0.47
3	-1	14	0.01	0.47
3	-1	15	0.08	0.47
3	-1	16	20.56	0.47
3	-1	17	33.07	0.47
3	-1	18	0	0.47
3	-1	19	6.64	0.47
3	-1	20	0	0.47
3	-1	21	0.04	0.47
3	-1	22	2.91	0.47
3	-1	23	5.35	0.47
3	-1	24	0	0.47

H	K	L	F^2	$\sigma(F^2)$
2	-3	1	0.4	0.37
2	-3	2	0.5	0.37
2	-3	3	0	0.37
2	-3	4	0	0.37
2	-3	5	0.07	0.37
2	-3	6	0	0.37
2	-3	7	0.08	0.37
2	-3	8	0.95	0.37
2	-3	9	0	0.37
2	-3	10	3.55	0.37
2	-3	11	13.17	0.37
2	-3	12	0	0.37
2	-3	13	2.49	0.37
2	-3	14	0	0.37
2	-3	15	0.14	0.37
2	-3	16	1.07	0.37
2	-3	17	56.69	0.37
2	-3	18	0	0.37
2	-3	19	3.93	0.37
2	-3	20	0.1	0.37
2	-3	21	0	0.37
2	-3	22	1	0.37
2	-3	23	6.22	0.37
2	-3	24	0	0.37
-1	-2	1	0.18	0.37
-1	-2	2	0.79	0.37
-1	-2	3	0.01	0.37
-1	-2	4	0	0.37
-1	-2	5	0.1	0.37
-1	-2	6	0	0.37
-1	-2	7	0.1	0.37
-1	-2	8	1.76	0.37
-1	-2	9	0.01	0.37
-1	-2	10	2.24	0.37
-1	-2	11	18.08	0.37
-1	-2	12	0	0.37
-1	-2	13	1.3	0.37
-1	-2	14	0.08	0.37
-1	-2	15	0.02	0.37
-1	-2	16	5.46	0.37
-1	-2	17	81.39	0.37
-1	-2	18	0	0.37
-1	-2	19	2.41	0.37
-1	-2	20	0.35	0.37
-1	-2	21	0.09	0.37
-1	-2	22	0.81	0.37
-1	-2	23	10.66	0.37
-1	-2	24	0	0.37

H	K	L	F^2	$\sigma(F^2)$
-3	1	1	0.52	0.35
-3	1	2	0.04	0.35
-3	1	3	0	0.35
-3	1	4	0	0.35
-3	1	5	0.01	0.35
-3	1	6	0	0.35
-3	1	7	0.52	0.35
-3	1	8	0.18	0.35
-3	1	9	0	0.35
-3	1	10	18	0.35
-3	1	11	1.14	0.35
-3	1	12	0	0.35
-3	1	13	6.99	0.35
-3	1	14	0	0.35
-3	1	15	0	0.35
-3	1	16	56.72	0.35
-3	1	17	5.38	0.35
-3	1	18	0	0.35
-3	1	19	17.78	0.35
-3	1	20	0	0.35
-3	1	21	0.06	0.35
-3	1	22	15.51	0.35
-3	1	23	0.59	0.35
-3	1	24	0	0.35
-2	3	1	0.02	0.42
-2	3	2	0.93	0.42
-2	3	3	0	0.42
-2	3	4	0	0.42
-2	3	5	0.07	0.42
-2	3	6	0	0.42
-2	3	7	0	0.42
-2	3	8	1.23	0.42
-2	3	9	0	0.42
-2	3	10	0.79	0.42
-2	3	11	16.08	0.42
-2	3	12	0	0.42
-2	3	13	0.9	0.42
-2	3	14	0	0.42
-2	3	15	0.03	0.42
-2	3	16	2.16	0.42
-2	3	17	57.25	0.42
-2	3	18	0	0.42
-2	3	19	2.03	0.42
-2	3	20	0.06	0.42
-2	3	21	0	0.42
-2	3	22	1.07	0.42
-2	3	23	5.27	0.42
-2	3	24	0	0.42

Table C.8: *List of the measured diffraction peaks.*